University of Sussex

Testing CPT conservation using the NuMI neutrino beam with the MINOS experiment

David John Auty

Submitted for the degree of Doctor of Philosophy

University of Sussex

March 2010

Abstract

The MINOS experiment was designed to measure neutrino oscillation parameters with muon neutrinos. It achieves this by measuring the neutrino energy spectrum and flavour composition of the man-made NuMI neutrino beam 1 km after the beam is formed and again after 735 km. By comparing the two spectra it is possible to measure the oscillation parameters.

The NuMI beam is made up of 7.0 % $\overline{\nu}_\mu$, which can be separated from the ν_μ because the MINOS detectors are magnetised. This makes it possible to study $\overline{\nu}_\mu$ oscillations separately from those of muon neutrinos, and thereby test CPT invariance in the neutrino sector by determining the $\overline{\nu}_\mu$ oscillation parameters and comparing them with those for ν_μ, although any unknown physics of the anti-neutrino would appear as a difference in oscillation parameters. Such a test has not been performed with beam $\overline{\nu}_\mu$ before. It is also possible to produce an almost pure $\overline{\nu}_\mu$ beam by reversing the current through the magnetic focusing horns of the NuMI beamline, thereby focusing negatively, instead of positively charged particles.

This thesis describes the analysis of the 7 % $\overline{\nu}_\mu$ component of the forward horn current NuMI beam. The $\overline{\nu}_\mu$ of a data sample of 3.2×10^{20} protons on target analysis found 42 events, compared to a CPT conserving prediction of $58.3^{+7.6}_{-7.6}$(stat.)$^{+3.6}_{-3.6}$(syst.) events. This corresponds to a 1.9 σ deficit, and a best fit value of $\Delta\overline{m}^2_{32} = 18 \times 10^{-3}$ eV^2 and $\sin^2 2\overline{\theta}_{23} = 0.55$.

This thesis focuses particularly on the selection of $\overline{\nu}_\mu$ events, and investigates possible improvements of the selection algorithm. From this a different selector was chosen, which corroborated the findings of the original selector. The thesis also investigates how the systematic errors affect the precision of $\Delta\overline{m}^2_{32}$ and $\sin^2 2\overline{\theta}_{23}$. Furthermore, it describes a study to determine the gains of the PMTs

via the single-photoelectron spectrum. The results were used as a crosscheck of the gains determined at higher intensities by an LED-based light-injection system.

Declaration

I hereby declare that this thesis, either in the same or different form, has not been previously submitted to this or any other University for a degree.

Signature:

David John Auty

Acknowledgements

There have been many people that have help me through my time as a DPhil student and producing this thesis. I would like to thank first off my supervisor Dr Elisabeth Falk for accepting me onto the course and all the help and guidance, along with my second supervisor Dr Jeffery Hartnell. Also STFC (formerly PPARC) for funding me for 3 of the years I worked on MINOS. I also like to thank the many post-docs that have helped me in my time at Sussex: Dr Chris Smith; Dr Cristian Bungau; Dr Jeanne Wilson Hawke; Dr Jamie Dawson who all helped me at various times with my ROOT exploits and made me into the coder that I am today! I would like to give special thanks to Dr Marta Artamendi Tavera; Dr Andrew Blake; Dr Jim Grozier; Dr Gwenaëlle Lefeuvre; Dr Christina Potter, who have all helped me through the thesis writing process.

The students that I have spent my time with at Sussex that have gone through the highs and lows of the DPhil: Andrew Baxter; Nicholas Devenish; Shakeel Fernandes; Dr Christopher Reeve; Paul Wahnon and Rajiv Ramasawmy.

The MINOS collaboration for making me feel welcome and especially the Cambridge group (Andy Blake, John Marshall, Jess Mitchell and others).

Also a thanks needs to go out to Rob Grant and Doug Naylor for creating possibly the best T.V. show ever shown. In homage to this, I have written some of my favourite quotes from each series at the start of each chapter.

Finally my parents for supporting me, no matter what I've decided today.

Contents

List of Tables

List of Figures

UNIVERSITY OF SUSSEX

DAVID JOHN AUTY, DOCTOR OF PHILOSOPHY

TESTING CPT CONSERVATION USING THE NUMI NEUTRINO BEAM WITH THE MINOS EXPERIMENT

SUMMARY

The MINOS experiment was designed to measure neutrino oscillation parameters with muon neutrinos. It achieves this by measuring the neutrino energy spectrum and flavour composition of the man-made NuMI neutrino beam 1 km after the beam is formed and again after 735 km. By comparing the two spectra it is possible to measure the oscillation parameters.

The NuMI beam is made up of 7.0 % $\overline{\nu}_\mu$, which can be separated from the ν_μ because the MINOS detectors are magnetised. This makes it possible to study $\overline{\nu}_\mu$ oscillations separately from those of muon neutrinos, and thereby test CPT invariance in the neutrino sector by determining the $\overline{\nu}_\mu$ oscillation parameters and comparing them with those for ν_μ, although any unknown physics of the anti-neutrino would appear as a difference in oscillation parameters. Such a test has not been performed with beam $\overline{\nu}_\mu$ before. It is also possible to produce an almost pure $\overline{\nu}_\mu$ beam by reversing the current through the magnetic focusing horns of the NuMI beamline, thereby focusing negatively, instead of positively charged

particles.

This thesis describes the analysis of the 7 % $\overline{\nu}_\mu$ component of the forward horn current NuMI beam. The Main[Backup] $\overline{\nu}_\mu$ analysis of a data sample of 3.2 $\times$ 10^{20} protons on target found 42[50] events, compared to a CPT conserving prediction of $58.3^{+7.6}_{-7.6}$(stat.)$^{+3.6}_{-3.6}$(syst.)[$65.1^{+8.1}_{-8.1}$(stat.)($^{+3.9}_{-3.9}$(syst.)] events. This corresponds to a 1.9 σ[1.7 σ] deficit, and a best fit value of $\Delta\overline{m}^2_{32}$ = 18 $\times$ 10^{-3} eV^2 and $\sin^2 2\overline{\theta}_{23}$ = 0.55[$\Delta\overline{m}^2_{32}$ = 101.2 $\times$ 10^{-3} eV^2, $\sin^2 2\overline{\theta}_{23}$ = 0.73].

This thesis focuses particularly on the selection of $\overline{\nu}_\mu$ events, and investigates possible improvements of the selection algorithm. From this a different selector was chosen, which corroborated the findings of the original selector. The thesis also investigates how the systematic errors affect the precision of $\Delta\overline{m}^2_{32}$ and $\sin^2 2\overline{\theta}_{23}$. Furthermore, it describes a study to determine the gains of the PMTs via the single-photoelectron spectrum. The results were used as a crosscheck of the gains determined at higher intensities by an LED-based light-injection system.

Chapter 1

Introduction

> “ Lister, if you must know, what I did was, I wrote a discourse on power circuits which was simply too *radical*, too *unconventional*, too *mould-breaking* for the examiners to accept.”
>
> “Yeah. You said you were a fish.” (Arnold Judas Rimmer BSc SSc, David Lister - Series 1 The End)

The neutrino (ν) is one of the most elusive of the Standard Model (SM) particles even though it is the most abundant, after the photon. First suggested about 80 years ago, there are still many things that are unknown about the neutrino: What is its mass? How many different flavours are there? What are the mass differences and mixing angles between flavours? Much progress has been made in the last decade or so in the area of ν mixing measurement, but we still do not know the third mixing angle θ_{13}. Is the neutrino its own anti-particle? Are the mass differences and mixing angles the same for neutrinos and anti-neutrinos? Chapter 2 describes how neutrinos fit into the SM, with a brief discussion on how to extend the standard model to incorporate CPT-violation within a effective field theory that includes gravity. Chapter 3 gives an overview of how our knowledge of the neutrino has evolved, paying particular attention to the oscillation experiments. Chapter 4 introduces the MINOS experiment. The MINOS detectors calibration system is explained in chapter 5 which also presents a study to verify the gains of the PMTs using single-photo electron spectra. Chapter 6 describes the MINOS physics results that have been produced to date and brief descriptions

of the the beam oscillation analyses. The main analysis of this thesis namely that of $\overline{\nu}_\mu$ charged-current events, is described in chapters 7, 8, 9 and 10, which discuss in turn the $\overline{\nu}_\mu$ events selection, the extrapolation of the $\overline{\nu}_\mu$ spectrum from the near to the far detector, the systematic errors and the $\overline{\nu}_\mu$ oscillation result. The result of this analysis tries to address two of the fundamental questions regarding neutrinos. What is the mass difference $\Delta\overline{\text{m}}^2_{32}$ and is this the same as Δm^2_{32}? Although any difference in the found $\Delta\overline{\text{m}}^2_{32}$ and Δm^2_{32} is down to any unpredicted physics not just CPT-violation. Finally chapter 11 gives a brief summary of the main points of this thesis.

The author of this thesis has been a member of the MINOS collaboration between 2005 and 2010. The work presented here was carried out in collaboration with members of the $\overline{\nu}_\mu$ analysis and calibration working groups. The author's efforts in the $\overline{\nu}_\mu$ analysis have focused on the following topics: investigating whether the best selector was chosen? Exploring the robustness of the extrapolation. Determining how the systematic uncertainties affect the measured oscillation parameters for different $\Delta\overline{\text{m}}^2_{32}$. To investigate whether the best selector was chosen various studies were carried out by the author. Section 7.3.1 investigates how changing the values of the cut on parameters in the Main Selector change the sensitivity. Changing how the charge-current, neutral-current particle identifier (CC/NC PID) training was studied in section 7.3.2. A Backup Selector was created as detailed in section 7.3.3 to use the same CC/NC PID as the 2008 MINOS ν_μ-CC analysis [1] and use fewer cuts. How the lack of taus in the extrapolation of the near detector data to the far detector affects the measured oscillation parameters was studied by the author in section 8.3. The author investigated how changing the Main Selector cuts in the near detector affects the far detector spectrum in section 8.4. In section 8.5 the author compares the differences between how Monte Carlo and data differs for different regions of the near detector. The author investigated how much the five largest systematic errors affect the measured oscillation parameters for CPT conserving and CPT non-conserving $\Delta\overline{\text{m}}^2_{32}$ in section section 9.2. The author investigated a different way of calculating the muon track energy from curvature by using the response of the highest and lowest toroid rather than the response of the median response toroid with a 2 % error

added in section 9.3. Section 9.4 explored how not knowing the exact alignment of the scintillator strips would affect the measured best fit parameters and how it would affect other reconstructed values. The study of the PMT gains with the single-photoelectron spectra in section 5.3 is also the author's work.

Chapter 2

The Standard Model of Particle Physics

> "We are talking jape of the decade. We are talking April, May, June, July and August fool. That's right. I am Queeg." (Holly - series 2 Queeg)

The Standard Model (SM) of particle physics is a gauge theory that has been hugely successful in explaining particle interactions to a high degree of precision. This theory, is built upon 12 spin-half particles (section 2.1.2) arranged into three generations and four integer-spin particles that carry three forces (section 2.1.1). Mass is introduced to the theory by spontaneous symmetry breaking, which produces a heavy boson (section 2.2), the Higgs boson, which is yet to be discovered. In the SM the neutrino is massless, as only left-handed neutrinos interact via weak charged currents. However, experimental evidence shows that neutrinos change flavour, which is possible only if neutrinos have mass. Furthermore, experiments have shown that the mass of the neutrino, although not yet measured, must be at least seven orders of magnitude smaller than that of the lightest of the other particles, the electron. This suggests that it gains its mass in a different way to the other particles. The most plausible mechanism for this is the see-saw mechanism (section 2.2.2). The experimentally overwhelming favoured model for neutrino flavour change is neutrino oscillation (section 2.3). The oscillation parameters for neutrinos and anti-neutrinos are expected to be the same in the SM by CPT conservation but experiments to date have only loosely constrained them

(section 2.3.2).

This chapter discusses general theory and unless specifically stated the information was taken from [2].

2.1 The Standard Model

Our understanding of nature's smallest building block is best described by the Standard Model (SM) of particle physics developed more than 40 years ago by Glashow [3], Salam [4] and Weinberg [5]. It relates the results of experiments to 17 fundamental particles and three fundamental forces (**Strong Nuclear force, Weak Nuclear force** and **Electromagnetic force**) via a $SU(3)_C \times SU(2)_L \times U(1)_Y$ symmetry group, where C is colour charge L is left-handed parity and Y is the weak hypercharge. In the SM, the particles are split into two groups: fermions and bosons, where fermions are the half-interger spin particles that make up matter, and bosons are the integer-spin particles that transmit the forces. Despite the power of the SM to accurately describe the world we live in, it has known problems : it does not include gravity; it has 19 free parameters that must be found experimentally; it does not explain why there are three generations of fermions. These problems suggest that there must be a higher order theory of which the SM is a low energy approximation. Most importantly, for this thesis, in the SM neutrinos are massless while experiments show that neutrinos have mass, giving the first evidence of physics beyond the Standard Model.

2.1.1 Bosons

Bosons are integer-spin particles and so obey Bose-Einstein statistics[1] [6][7]. Gauge bosons are the particles that transmit the forces (table 2.1).

The electromagnetic force is mediated by photons (γ), which are known to be massless. As a result of the photon having no mass, the range of the electromagnetic force is infinite and its strength follows the inverse square law. Even though

[1] Bose-Einstein statistics describe the distribution of the energy of particles that are indistinguishable when in thermal equilibrium.

Boson	charge (Q)	Spin	Colour	Mass (GeV)	Interaction
g	0	1	r,b,g	0	strong
γ	0	1	0	0	electromagnetic
$W^{\pm}$	$\pm$1	1	0	80.4	weak
Z^0	0	1	0	91.2	weak
H^0	0	0	0	114$<$ m $<$170	-

Table 2.1: *The bosons of the Standard Model with some of their fundamental properties.*

the photon has no charge itself, it couples proportionally to a particle's charge. Thus, only charged particles feel the electromagnetic force.

The strong nuclear force comes in three "colour charges", red (r), blue (b) and green (g), and is mediated via the massless gluon (g). Gluons are produced with a colour and an anti-colour, which means that there are eight different combinations of gluon pairs. Although the mediating particle is massless, the strong nuclear force is not infinite, as the gluons carry colour charge themselves. This colour charge on the gluons means that they interact with each other causing the confinement of quarks. This causes the force to grow as the distance between particles that feel the strong force grows, until 10^{-15} m at which point there is enough energy in the field that new particles are formed in colour anti-colour pairs. So at low energies colour-charged particles are not seen in isolation[2]. The third force is the weak nuclear force, which has three mediating particles: the two charged W^+ and W^- and a neutral Z^0. Unlike mediators of the strong nuclear force and electromagnetic force, the weak force bosons are massive; therefore the weak nuclear force acts only over a short range (10^{-18} m).The weak nuclear force is also unlike the other forces as it is felt by all left-handed fermions (right-handed anti-fermions). The charge current interactions, which exchange $W^{\pm}$ bosons, change the flavour of the fermion it interacts with. The neutral cur-

[2]All non-Abelian gauge theories are asymptotically free; that is, the coupling goes to 0 as the distance between the separation becomes small. A non-Abelian gauge theory is one in which the Lagrangian is invariant under transformations of a non-Abelian group. A non-Abelian group is a group where at least 2 elements do not commute: $a \times b \neq b \times a$

rent interaction, which exchanges the Z^0 boson, does not change the flavour of the fermion as it is neutral but it couples to the weak isospin and charge. Another property unique to the $W^{\pm}$ interaction is that it violates parity. It only couples to left-handed particles and right-handed anti-particles.

Also the Standard Model predicts the existence of a further gauge boson that is responsible for giving the $W^{\pm}$ and Z^0 and the fermions mass, the Higgs Boson. This boson has not been discovered yet but is predicted to be found in the next few years in the energy range that will be explored by the Large Hadron Collider.

2.1.2 Fermions

Fermions are half integer-spin particles, obey Fermi-Dirac statistics[3] [8] [9] [10] describe and make up matter (table 2.2). Elemental fermions can be split into two further categories: quarks (feel the strong force) and leptons (do not feel the strong force).

2.1.2.1 Quarks

There are 6 different quarks (q), arranged in three generations, that feel all four forces. They have fractional charges: top (t), charm (c) and up (u) have a charge of +2/3 of the charge of an positron (e) and bottom (b), strange (s) and down (d) have a charge of -1/3 e. Individual quarks have a colour charge of red, blue or green but bind together to form colourless particles called hadrons. The overall colour charge for hadrons is zero for reasons that will be explained in section 2.1.1 and their electric charge is integer. To achieve this, quarks arrange themselves in one of two ways, either in $q\bar{q}$ pairs of the same colour to form hadrons called mesons (from the Greek mesos for middle) or in groups of three (qqq) where each has a different colour: red; blue; green. These qqq particles are called baryons (from the Greek barys meaning heavy).

[3] Fermi-Dirac statistics describe the distribution of the energy of particles that are indistinguishable when in thermal equilibrium that obey the Pauli Exclusion Principle.

Generation	Flavour	Q	T_3	Colour	Mass (MeV)	life time (s)
1	u	$+\frac{2}{3}$	$+\frac{1}{2}$	r,b,g	1.5 - 3.0	-
	d	$-\frac{1}{3}$	$-\frac{1}{2}$	r,b,g	3 - 7	-
	ν_e	0	$+\frac{1}{2}$	-	$<$ 0.00000022	-
	e	-1	$-\frac{1}{2}$	-	0.511	$> 4.6 \times 10^{26}$
2	c	$+\frac{2}{3}$	$+\frac{1}{2}$	r,b,g	1250	1×10^{-13}
	s	$-\frac{1}{3}$	$-\frac{1}{2}$	r,b,g	95	1×10^{-8}
	ν_μ	0	$+\frac{1}{2}$	-	$<$ 0.17	-
	μ	-1	$-\frac{1}{2}$	-	105.7	2.20×10^{-6}
3	t	$+\frac{2}{3}$	$+\frac{1}{2}$	r,b,g	170900	1×10^{-25}
	b	$-\frac{1}{3}$	$-\frac{1}{2}$	r,b,g	4200	1×10^{-12}
	ν_τ	0	$+\frac{1}{2}$	-	$<$15.5	-
	τ	-1	$-\frac{1}{2}$	-	1776.99	291×10^{-15}

Table 2.2: *The fermions of the Standard Model with some of their fundamental properties [11]. Masses shown are the experimentally measured masses.*

2.1.2.2 Leptons

Unlike quarks, the leptons do not feel the strong force, so are not bound together and can exist individually. Like the quarks, leptons have six particles arranged into three generations. There are three charged leptons: tauon (τ), muon (μ) and electron (e), each having a single negative charge. There are also three charge-less leptons called neutrinos; these are named for the charged lepton that is produced when the neutrinos interact via the charged weak-nuclear force: tau-neutrino (ν_τ); muon-neutrino (ν_μ) and electron-neutrino (ν_e). Leptons comes from the Greek word lepto, which means light.

2.2 Mass in the Standard Model

In the Standard Model the neutrino is massless. The reason it was given no mass is because the neutrino only interacts via the weak force: as it is a lepton it feels no colour charge and it has no electromagnetic charge. It was seen experimentally

that the flavour of neutrinos is related to a specific charged lepton flavour. As the weak force only couples to left-handed particles, the right-handed neutrino would not couple to any other particle. If neutrinos had mass, then they would travel slower than the speed of light so it would be possible to travel in a frame of reference where the angular momentum would be in the same direction as the direction of travel. This would mean that the neutrino would become right-handed. This can be tested in such reactions as the beta decay of polarised cobalt

$$^{60}Co \rightarrow^{60} Ni^{*} + e^{-} + \overline{\nu}_{e}. \tag{2.1}$$

In this reaction, the outgoing neutrino is always observed going in the opposite direction with respect to the polarisation of the cobalt [12]. If the neutrino could be boosted to being right-handed then some times it would be observed going in the same direction.

Quantum Field theory defines particles in terms of their fields. If a gauge symmetry is imposed on the fermion field then a conserved quantity can be defined. This conserved quantity is the “charge” associated with a boson field involved. If we consider a Lagrangian for a free fermion field:

$$\mathcal{L} = \overline{\psi}(x)(i\overleftrightarrow{\partial} - m)\psi(x) \tag{2.2}$$

where ψ is the fermion field describing the particle and m is the mass, then force a local U(1) symmetry on the field:

$$\psi(x) \rightarrow \psi'(x) = e^{i\alpha(x)Q}\psi(x) \tag{2.3}$$

where ψ' is a transformation of the fermion field and $\alpha(x)$ is a constant, this leads to the Lagrangian for Quantum Electrodynamics:

$$\mathcal{L} = \overline{\psi}(x)(i\overleftrightarrow{\partial} - m)\psi(x) - e\overline{\psi}(x)\gamma^{\mu}Q\psi(x)A^{\mu} - \frac{1}{4}F_{\mu\nu}F^{\mu\nu} \tag{2.4}$$

where A^{μ} is identified as the photon field and is required to preserve the invariance of the electromagnetic field tensor, $F^{\mu\nu} \equiv \delta^{\mu}A^{\nu} - \delta^{\nu}A^{\mu}$; Q is the charge operator, for which the eigenvalues are the conserved property of the symmetry, in this case electromagnetic charge; γ^{μ} is the Dirac matrix. The interaction term $-e\overline{\psi}(x)\gamma^{\mu}Q\psi(x)A^{\mu}$ between the fermion field ψ and the photon field A^{μ} arises

from applying the local gauge symmetry, and causes the strength of the coupling to be the strength of the conserved property Q.

This can be expanded to a $SU(2)_L \times U(1)_Y$ symmetry to account for the weak interaction, making it a unified Electroweak symmetry. The interaction term in the Lagrangian becomes

$$- g\overline{\chi}_L \gamma_\mu T \cdot \mathbf{W}^\mu \chi_L - g'\overline{\psi}\gamma_\mu \frac{Y}{2}\psi B^\mu \tag{2.5}$$

where $\mathbf{W}^\mu$ and B^μ are the vector fields that preserve the gauge invariance, T (weak isospin) and Y are the operators that are equivalent to Q in QED and whose eigenvalues need to be conserved. SU(2)$_L$ only acts on left-handed particles, thus resulting in a doublet for the left-handed particles and a singlet for right-handed particles.

$$\begin{array}{llll} Lepton & & Quarks & \\ \chi_L^l = \begin{pmatrix} \nu_e \\ e^- \end{pmatrix}_L & & \chi_L^q = \begin{pmatrix} u \\ d \end{pmatrix}_L & \\ \psi_R = e_R^- & & \psi_R = u_R, d_R & \end{array}$$

For quarks, the right-handed chiral state has both members of the generation while the lepton right-handed chiral state is only represented by the charged lepton and not the neutrino. Even though there are four gauge fields these are not the ones seen in nature. Renormalisation and gauge invariance demands $\mathbf{W}^\mu$ and B^μ to be massless. So to relate $\mathbf{W}^\mu$ and B^μ to the physical particles, spontaneous electroweak symmetry breaking needs to be introduced to the theory; this is known as the Higgs mechanism [13].

2.2.1 Spontaneous Symmetry Breaking

In order to give mass to the SM particles, Peter Higgs [13] introduced a way to spontaneously break the symmetry of the electroweak gauge field. The Lagrangian is invariant under symmetry transformation, but the ground state is not invariant. For this we consider four scalar particle fields ψ_i, with a gauge-invariant Lagrangian of

$$\mathcal{L} = \left| \left(i\delta - g\mathbf{T} \cdot \mathbf{W}_\mu - g'\frac{Y}{2}B_\mu \right) \phi \right|^2 \tag{2.6}$$

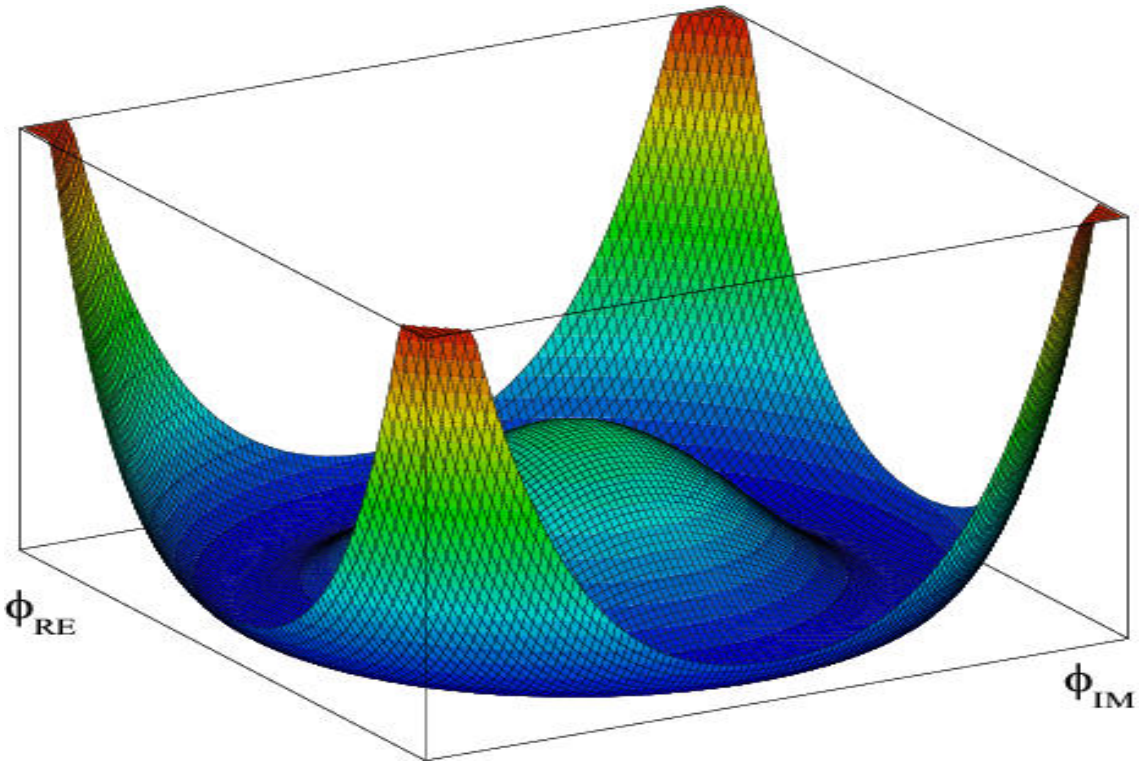

Figure 2.1: *The Higgs potential V(ϕ) for a fixed value of λ shown in real and imaginary parts. This is sometimes called the "Mexican-hat" or "Wine-bottle" profile.*

where $||^2 \equiv ()^\dagger()$. A potential V(ϕ) is added to achieve the requirements that the ground state of the symmetry is not invariant. This is the Higgs potential

$$V(\phi) = \frac{1}{2}\mu^2\phi^2 + \frac{1}{4}\lambda\phi^4 \tag{2.7}$$

which gives a maximum at ϕ = 0 and minima, when μ^2 <0 and λ >0. There are an infinite number of minima in a circle around the maximum, which give the "Mexican-hat" or "Wine-bottle" profile (figure 2.1). The scalar field acquires a non-zero expectation value in a vacuum.

By requiring the symmetry to be a gauge symmetry, a third degree of freedom is acquired by the gauge boson "eating" the Goldstone boson produced by the breaking of the symmetry, and so gives the bosons mass[4].

[4]A massless boson has two degrees of freedom. There are two degrees of freedom from the Goldstone boson, one is taken by the gauge boson (mass) and the remaining degree of freedom becomes the Higgs field

The scalar Higgs field (ϕ) can be represented by an SU(2) doublet:

$$\phi = \begin{pmatrix} \phi^+ \\ \phi^0 \end{pmatrix} = \frac{1}{\sqrt{2}} \begin{pmatrix} \phi_1 + i\phi_2 \\ \phi_3 + i\phi_4 \end{pmatrix}. \tag{2.8}$$

By choosing a true vacuum state the symmetry is broken:

$$\phi_0 = \frac{1}{\sqrt{2}} \begin{pmatrix} 0 \\ \nu \end{pmatrix}, \tag{2.9}$$

where $\nu = \sqrt{-\mu^2/\lambda}$.

In order to find the physical properties of the particles of the particles produced in the spontaneous symmetry of the $SU(2)_2 \times U(1)_Y$ to $U(1)_Q$ it is convenient to write Eq:2.8 as

$$\phi = \frac{1}{\sqrt{2}} e^{\left(\frac{i}{2\nu}\overline{\eta}\cdot\tau\right)} \begin{pmatrix} 0 \\ \nu + H \end{pmatrix}, \tag{2.10}$$

where $\overline{\eta}$ = (η_1, η_2, η_3) and H are four real scalar fields. The $\overline{\eta}$ can be rotated away by a gauge transformation and H field describes the Higgs boson as excitations above the natural Higgs field. The gauge transformation defines the unitary gauge and the Higgs doublet is now

$$\phi = \frac{1}{2\nu} \begin{pmatrix} 0 \\ \nu + H \end{pmatrix}. \tag{2.11}$$

Placing this in Eq:2.7 shows that the mass of the Higgs boson (m_H) is $\sqrt{2}\mu$. This leaves the kinetic term of the Lagrangian $(D_\mu\phi)^\dagger(D^\mu\phi)$. In the unitary gauge the covariant derivative acting on the Higgs doublet is

$$D_\mu\phi = \frac{1}{\sqrt{2}} \left(\partial_\mu + i\frac{g}{2} \begin{pmatrix} W_\mu^3 & \sqrt{2}W_\mu^1 \\ W_\mu^2 & W_\mu^3 \end{pmatrix} + i\frac{g'}{2}B_\mu \right) \begin{pmatrix} 0 \\ \nu + H \end{pmatrix}, \tag{2.12}$$

W_μ^3 and B_μ mix in such a way that the physical bosons are superpositions of these fields:

$$Z_\mu \equiv \cos\theta_W W_\mu^3 - \sin\theta_W B_\mu \tag{2.13}$$

$$A_\mu \equiv \cos\theta_W B_\mu + \sin\theta_W W_\mu^3, \tag{2.14}$$

where θ_W is the weak mixing angle. Although $\mathbf{W}$ and B are massive, A_μ is chosen so that the operator $Q = T^3 + \frac{Y}{2}$ and $Q_{\phi_0} = 0$. In doing this although there are four generators, only three Goldstone bosons are produced so this choice means that W^1_μ and W^2_μ are the massive W^+ and W^- gauge bosons and the Z_μ is the also massive Z^0, and A_μ is the physical particle γ, which is massless. The fourth degree of freedom is taken up by the Higgs Boson itself, thus acquiring mass. As well as giving the $W^\pm$ and Z^0 mass we can see how the Higgs scalar field interacts with the fermion fields. By coupling the left-handed doublet and the right-handed singlet fermion fields with the Higgs scalar field a fermionic mass term is produced in the Lagrangian. For the first generation of fermions:

$$\mathcal{L} = f^e \overline{\chi}^l_L \phi_0 e_R + f^d \overline{\chi}^q_L \phi_0 d_R + f^u \overline{\chi}^q_L \tilde{\phi}_0 u_R + h.c. \tag{2.15}$$

which can be written

$$\mathcal{L} = f^e \frac{\nu}{\sqrt{2}} \overline{e}_L e_R + f^d \frac{\nu}{\sqrt{2}} \overline{d}_L d_R + f^u \frac{\nu}{\sqrt{2}} \overline{u}_L u_R + h.c., \tag{2.16}$$

where $\tilde{\phi}_0 = i\tau_2 \phi^*_0$, and f^x is the Yukawa coupling. This gives the mass term for all the fermions to be $f^x \frac{\nu}{\sqrt{2}}$ except for the neutrino as it does not have a right-handed singlet in the Standard Model.

2.2.2 Theory of Neutrino Mass

Neutrino flavour oscillation has been experimentally measured to a high degree of accuracy, resulting in evidence for non-zero masses for at least two neutrinos. A detailed experimental discussion can be found in chapter 3. To integrate ν mass into the SM framework, they may have a Dirac mass[5] as described for the other fermions, or as the neutrino is neutral, it may have a Majorana mass term[6]. If the neutrino's mass is generated via the Dirac mechanism, then a right-handed neutrino SU(2) singlet ν_R needs to exist. This neutrino would have no other SM interactions so is described as "sterile". The fact that the neutrino's mass is so much smaller (10^6 times smaller) than the charged leptons, suggests that its mass is generated differently. In comparison, the surprisingly large mass of the top quark is 40 times the mass of the bottom quark.

[5] A Dirac mass is described by a 4-component spinor

[6] A Majorana mass is described by a 2-component spinor

In the following section, only one generation of neutrino is considered in order to simplify the equations but the argument can be expanded to three generations. The neutrino mass terms can be written as:

$$\begin{aligned} \mathcal{L}_D &= -m_D(\overline{\psi}_R\psi_L + \overline{\psi}_L\psi_R) = m_D\overline{\psi}\psi, \\ \mathcal{L}_M^L &= m_L(\overline{\psi_L^C}\psi_L + \overline{\psi_L}\psi_L^C) = m_L\overline{\xi}\xi \\ \mathcal{L}_M^R &= m_R(\overline{\psi_R^C}\psi_R + \overline{\psi_R}\psi_R^C) = m_R\overline{\omega}\omega \end{aligned} \tag{2.17}$$

where subscript D denotes Dirac mass and subscript M denotes Majorana masses. The L and R super/subscripts denote left and right-handed operators with the fields defined as:

$$\psi = \psi_L + \psi_R \tag{2.18}$$

$$\xi = \psi_L + \psi_L^C, \quad \xi^C = \xi \tag{2.19}$$

$$\omega = \psi_R + \psi_R^C, \quad \omega^C = \omega. \tag{2.20}$$

It is obvious from equations 2.18, 2.19, 2.20 that the Majorana fields are self-conjugating, thus the neutrino and anti-neutrino are the same particle.

The mass terms can be combined to form a matrix including both the Majorana and Dirac terms of the neutrino lagrangian:

$$\mathcal{L}_{M+D} = \mathcal{L}_D + \mathcal{L}_M^R + \mathcal{L}_M^L \tag{2.21}$$

$$\mathcal{L}_{M+D} = \begin{pmatrix} \overline{\xi} & \overline{\omega} \end{pmatrix} \begin{pmatrix} m_L & \frac{m_D}{2} \\ \frac{m_D}{2} & m_R \end{pmatrix} \begin{pmatrix} \xi \\ \omega \end{pmatrix}. \tag{2.22}$$

By diagonalising the matrix in Eq 2.22 the ν mass eigenstates can be found. If a state is considered where m_L = 0 and $m_D \ll m_R$, the nearly left-handed neutrino will have a mass given by $m_1 \sim m_D^2/m_R$ and the nearly right-handed neutrino will have mass $m_2 \sim m_R$. In many theories, the Majorana mass (m_R) is 10^{15} GeV, which is much larger than the Dirac mass. If $m_D \sim 100$ GeV, the left-handed neutrino mass is $\sim \mathcal{O}(10^{-2})$ eV. This is known as the see-saw mechanism. The mass of the neutrino has yet to be determined experimentally let alone whether

the neutrino is a Majorana or Dirac particle. With this in mind, it is presumed for the rest of this thesis that neutrinos are Dirac particles unless stated[7]. If, however, the neutrino is a Majorana particle it would allow phenomena such as neutrinoless double beta decay ${}^{A}_{Z}X \rightarrow {}^{A}_{Z+2}X + 2e^{-}$ to occur. Only a few isotopes allow double beta decay to happen; these have even numbers of protons and neutrons in the nucleus, which is two protons short of making the isobaric isotope of the highest binding energy. Most of the time it could decay to an intermediate state that has odd numbers of protons and neutrons. However sometimes this has a lower binding energy than the initial state so is forbidden as the nucleus would have to gain energy to turn into this "odd-odd" nucleus. To get to the highest binding energy the nucleus needs to emit two β^{-} particles at the same time otherwise it would need energy. This has been observed but only with neutrinos being emitted as well which are inferred by the "missing" energy that is taken by the neutrino. A signal for neutrinoless double beta decay is for the β particles to have all the energy. If observed the half life ($T^{0\nu}_{1/2}$) of this decay would relate to the neutrino mass by [14]:

$$\left(T^{0\nu}_{1/2}\right)^{-1} = G^{0\nu}\left|M^{0\nu}\right|^{2}\left(\frac{\langle m_{\nu_e}\rangle}{m_e}\right)^{2}, \tag{2.23}$$

where $G^{0\nu}$ is the two-body phase-space factor and $M^{0\nu}$ is the nuclear matrix element. This has yet to be observed, with the lowest limit on mass coming from the CUORICINO experiment [11, 15] which found no signal for a half life up to 3.0 $\times$ 10^{24} y which gives an effective mass of between 0.19 and 0.68 eV. If neutrinoless beta decay was discovered, as well as confirming the neutrino was Majorana, it would also set a scale for the absolute neutrino mass.

2.3 Neutrino Oscillation

From experiments (chapter 3) it has been shown that neutrinos change flavour during flight. To explain this it is required that at least two of the neutrinos have mass, which are different from each other and the weak flavour eigenstates are different to the mass eigenstates.This is also seen in the down type quark sector where the flavour and mass eigenstates are related via the 3 $\times$ 3 CKM matrix [16,

[7] Majorana mass term would add another rotational matrix that is not affected by oscillation

11]. A unitary matrix U relates the weak eigenstates $|\nu_\alpha > (\alpha = e, \mu, \tau)$ of the neutrino to the mass states $|\nu_i > (i = 1, 2, 3)$; and this is known as the Pontecorvo, Maki, Nakagawa and Sakata matrix (PMNS)[17, 11]:

$$|\nu_\alpha\rangle = \sum_{i=1}^{n} U_{\alpha i}|\nu_i\rangle. \tag{2.24}$$

The PMNS matrix may be expanded to a 6 $\times$ 6 matrix to include the Majorana terms. As the Majorana terms do not affect the oscillation they are ignored in this thesis.

2.3.1 Neutrino Oscillation in a Vacuum

In a vacuum, the mass ν states will evolve independently of one another, so state $|\nu_i >$ at a position $\mathbf{x}$ and momentum $\mathbf{p}$ evolves as

$$|\nu_i(\mathbf{x})\rangle = e^{-i\mathbf{p}_i\cdot\mathbf{x}}|\nu_i\rangle, \tag{2.25}$$

while the neutrino flavour eigenstate will evolve as

$$|\nu_\alpha(\mathbf{x})\rangle = \sum_{i=1}^{n} e^{-i\mathbf{p}_i\cdot\mathbf{x}} U_{\alpha i}|\nu_i\rangle, \tag{2.26}$$

where $n = 1, 2, 3$. Using the fact that U is unitary, Eq 2.24 may be inverted and inserted into Eq 2.26, so that the flavour eigenstate is

$$|\nu_\alpha(\mathbf{x})\rangle = \sum_{\beta=e}^{l} \left[\sum_{i=1}^{n} e^{-i\mathbf{p}_i\cdot\mathbf{x}} U_{\alpha i} U^*_{\beta i} \right] |\nu_{\beta i}\rangle, \tag{2.27}$$

where $l = e, \mu, \tau$. Assuming the energy of $|\nu_\alpha\rangle$ is shared by all mass eigenstates and that E $\gg$ m$_i$, the momentum component $\mathbf{p}_i = \sqrt{E^2 + m_i^2} \approx E - m_i^2/2p$. Since the neutrinos are ultra-relativistic, $t \approx L$ and so the phase factor of Eq 2.27 becomes

$$e^{-i(m_i^2/2E)L} \tag{2.28}$$

and with this substituted into Eq 2.27, the flavour eigenstate can be expressed as

$$|\nu_\alpha(\mathbf{x}) = \sum_{\beta=e}^{l} \left[\sum_{i=1}^{n} e^{-im_i^2 L/2E} U_{\alpha i} U^*_{\beta i} \right] |\nu_{\beta i}\rangle. \tag{2.29}$$

Equation 2.29 shows that the different $|\nu_i\rangle$ evolve at different rates, if they are different masses. After travelling a distance L, ν_α becomes a superposition of all flavour states if the off-diagonal components are not zero. It is now possible to calculate the probability of seeing a neutrino produced in flavour state ν_α as a ν_β by finding the square of the matrix element:

$$\begin{aligned} P(\nu_\alpha \to \nu_\beta) &= |\langle \nu_\beta | \nu_\alpha(L) \rangle|^2 \\ &= \sum_{i,j} U^*_{\alpha i} U_{\beta i} U_{\alpha j} U^*_{\beta j} e^{-i\Delta m^2_{ij} L/2E}, \end{aligned} \tag{2.30}$$

where $\Delta m^2_{ij} = m^2_i - m^2_j$ and i and j iterate over the mass eigenstates. By explicitly writing the real and imaginary parts, Eq 2.30 can be rewritten:

$$\begin{aligned} P(\nu_\alpha \to \nu_\beta) = \delta_{\alpha\beta} &- 4 \sum_{i>j} \Re(U^*_{\alpha i} U_{\beta i} U_{\alpha j} U^*_{\beta j}) \sin^2\left(\frac{\Delta m^2_{ij} L}{4E}\right) \\ &+ 2 \sum_{i>j} \Im(U^*_{\alpha i} U_{\beta i} U_{\alpha j} U^*_{\beta j}) \sin^2\left(\frac{\Delta m^2_{ij} L}{4E}\right). \end{aligned} \tag{2.31}$$

By inserting the units of $\hbar$ and c[8] the probability of ν oscillation may be directly related to the L,E and Δ m

$$\frac{\Delta m^2_{ij} L}{4E} \cong 1.27 \Delta m^2_{ij}(eV^2) \frac{L(\text{km})}{E(\text{GeV})}. \tag{2.32}$$

Equation 2.31 shows that the probability of ν oscillation is periodic with the distance travelled divided by the energy of the neutrino. Therefore, if the ν mass eigenstates are different, the probability of detecting a weak flavour eigenstate will oscillate during flight, but the total number of neutrinos will remain the same.

2.3.1.1 Three Flavour Neutrino Oscillation

The PMNS matrix (U) for three neutrino flavours and three mass states is given by

$$U = \begin{pmatrix} U_{e1} & U_{e2} & U_{e3} \\ U_{\mu 1} & U_{\mu 2} & U_{\mu 3} \\ U_{\tau 1} & U_{\tau 2} & U_{\tau 3} \end{pmatrix} \tag{2.33}$$

[8] $\hbar$ = c = 1 by assumption

can also be parameterised using three angles θ_{ij} and a CP violating phase δ as

$$U = \begin{pmatrix} c_{12}c_{13} & s_{12}c_{13} & s_{13}e^{-i\delta} \\ -s_{12}c_{23} - c_{12}s_{23}s_{13}e^{i\delta} & c_{12}c_{23} - s_{12}s_{23}s_{13}e^{i\delta} & s_{23}c_{13} \\ s_{12}s_{23} - c_{12}c_{23}s_{13}e^{i\delta} & c_{12}s_{23} - s_{12}c_{23}s_{13}e^{i\delta} & c_{23}c_{13} \end{pmatrix}, \tag{2.34}$$

where $c_{ij} = \cos\theta_{ij}$ and $s_{ij} = \sin\theta_{ij}$. The PMNS matrix can be shown to be the product of three separate rotational matrices:

$$U = \underbrace{\begin{pmatrix} 1 & 0 & 0 \\ 0 & c_{23} & s_{23} \\ 0 & -s_{23} & c_{23} \end{pmatrix}}_{atmosphere} \underbrace{\begin{pmatrix} c_{13} & 0 & s_{13}e^{-i\delta} \\ 0 & 1 & 0 \\ -s_{13}e^{i\delta} & 0 & c_{13} \end{pmatrix}}_{reactor} \underbrace{\begin{pmatrix} c_{12} & s_{12} & 0 \\ -s_{12} & c_{12} & 0 \\ 0 & 0 & 1 \end{pmatrix}}_{solar}. \tag{2.35}$$

Eq 2.35 aids in the visualisation of the regimes that different neutrino experiments concentrate on. The first matrix in Eq 2.35 is the regime that describes oscillations in atmospheric neutrinos and is the regime that the MINOS experiment works in. The second matrix in Eq 2.35 holds the CP violating phase so it is only here that neutrinos and anti-neutrinos are allowed to differ from one another. At the time of writing the angle θ_{13} associated with the matrix is yet to be observed although future experiments are expected to probe this regime[9] and further discussions of these are found in section 3.2.8. The third matrix in Eq 2.35 is associated with solar neutrinos and long baseline reactor experiments. Due to the extremely small mixing angle in the second matrix of Eq 2.35, the matrix is nearly diagonal and the difference in the Δm^2s make it possible to treat the other two regimes separately.

2.3.1.2 Two Flavour Neutrino Oscillation

As discussed earlier, the probability (P) for $\nu_\alpha \rightarrow \nu_\beta$ oscillation depends on distance L travelled by the neutrinos. More specifically it depends on Δm^2_{ij} L/E; so

[9] For example the MINOS experiment has seen a 1.5 σ excess of ν_e in the Far Detector suggesting $\nu_\mu \rightarrow \nu_e$ oscillation [18]. Currently MINOS has collected double this data set and will release new results in 2010.

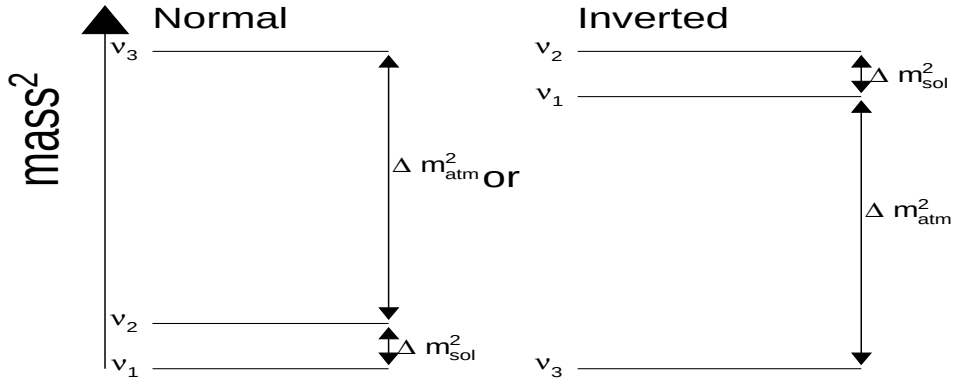

Figure 2.2: *The mass splitting for the three neutrinos (not to scale). The order of the solar mass splitting is known to be $\nu_2 > \nu_1$, while in the atmospheric mass splitting it is not known whether ν_3 is larger (normal hierarchy) or smaller (inverted hierarchy) than the other neutrino masses ν_1, ν_2*

that

$$\begin{aligned} \frac{\Delta m^2_{ij} L}{4E} &\ll 1, \quad P = 1 \\ \frac{\Delta m^2_{ij} L}{4E} &\sim \mathcal{O}(1), \quad P = \sin^2 2\theta \\ \frac{\Delta m^2_{ij} L}{4E} &\gg 1, \quad P = \frac{1}{2}\sin^2 2\theta \end{aligned} \tag{2.36}$$

Δm^2_{ij} L/E $\mathcal{O}(1)$ presents the best opportunity to measure the oscillation parameters as there is the largest change in probability of $\nu_\alpha \rightarrow \nu_\beta$. The distance that the ν travel and the energy of the ν can be chosen by the experiment. In accelerator experiments the detectors are a fixed distance away and the neutrino energy can be controlled. As the difference between the two mass splittings is so large (section 3.4) the different Δm^2s at a given experiment (figure 2.2) can be treated as only one. The independent treatment of Δm^2 is justified in many cases when analysing the data approximating the two-neutrino case. The PMNS matrix can then be simplified to

$$U = \begin{pmatrix} \cos\theta & \sin\theta \\ -\sin\theta & \cos\theta \end{pmatrix}, \tag{2.37}$$

where θ is the leptonic mixing angle. The columns in Eq 2.37 are the mass eigenstates and the rows are the weak eigenstates. When inserting matrix 2.37 into Eq 2.31, the probablity of the ν oscillation becomes

$$\begin{aligned} P(\nu_\alpha \rightarrow \nu_\beta) &= 4\cos^2\theta \sin^2\theta \sin^2\left(\frac{1.27\Delta m^2_{ij} L}{E}\right) \\ &= \sin^2(2\theta)\sin^2\left(\frac{1.27\Delta m^2_{ij} L}{E}\right). \end{aligned} \tag{2.38}$$

It is common for experiments to look at the survival of neutrino flavours, rather

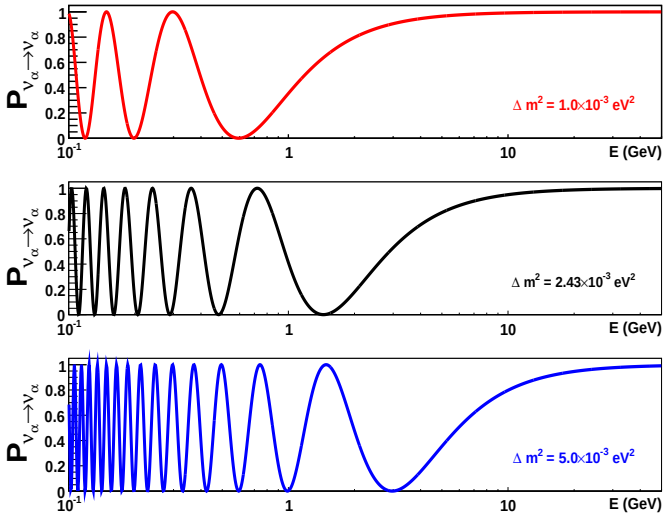

Figure 2.3: *The survival probability of a neutrino in a two-flavour model, for different* Δm^2 *(1.0, 2.43, 5.0)* $\times 10^{-3}$ *eV*^{2} *for the MINOS baseline 735 km and* $\sin^2 2\theta = 1$.

than the appearance of another neutrino flavour. The survival probability may be expressed as, $P(\nu_\alpha \rightarrow \nu_\alpha) = 1 - P(\nu_\alpha \rightarrow \nu_\beta)$. It is important to note that there is no room for a CP violating phase in Eq 2.38, as there are only two degrees of freedom. In addition, oscillation depends on θ, the values of which can vary so that $0 \leq \sin^2 2\theta \leq 1$. Thus, when $\theta = 0$ there is no ν flavour oscillation and when $\theta = \pi/4$ oscillation is maximised and all the neutrinos will have changed from α into β flavour states assuming $\Delta m^2 L/4E = \pi/2$. Experimental evidence for neutrino oscillation is the periodic change in neutrino flavour as a function of L/E. The mixing angle θ can be determined by measuring the amplitude of the oscillation and Δm can be determined by measuring the period of the oscillation.

The theoretical survival probability is shown as a function of energy in figure 2.3 for the MINOS baseline for various Δm^2_{32} with $\sin^2 2\theta$ = 1.

2.3.2 CPT Conservation in the Standard Model

Charge Parity Time (CPT) conservation is a fundamental part of the Standard Model and has so far been confirmed to a high degree of accuracy by experiment. Each individual symmetry can be broken but the entire CPT symmetry must be conserved in principle. C is the symbol given to charge conjugation, equivalent to exchanging a particle for its anti-particle, e.g.:

$$\psi(t,\mathbf{x}) \rightarrow \psi_C(t,\mathbf{x}) = C\overline{\psi}^T(t,\mathbf{x}) = i\gamma^2\gamma^0\overline{\psi}^T(t,\mathbf{x}), \tag{2.39}$$

where γ^2 and γ^0 are the Dirac matrices.

P is the symbol given to parity, the inversion of spatial coordinates, eg:

$$\psi(t,\mathbf{x}) \rightarrow \psi_P(t,-\mathbf{x}) = P\psi(t,\mathbf{x}) = \gamma^0\psi(t,\mathbf{x}), \tag{2.40}$$

The electrons emitted in β-decay of polarised ^{60}Co [12] were seen to have a preferred direction with respect to the ^{60}Co spin. It would be logical to think that CP symmetry, i.e. to exchange all particles with their anti-particles and to exchange right for left, would then be conserved. The standard electroweak model, however, does not respect the combined CP conservation, as shown in the K^0 sector, where

$$\begin{aligned} CP|K^0\rangle &= -C|K^0\rangle = |\overline{K}^0\rangle \\ CP|\overline{K}^0\rangle &= -C|\overline{K}^0\rangle = |K^0\rangle. \end{aligned} \tag{2.41}$$

Nevertheless it is possible to construct a CP K^0 eigenstate, where

$$\begin{aligned} |K_1\rangle &= \frac{1}{2}\sqrt{2}\left[|K^0 + \overline{K}^0\rangle\right] \quad \rightarrow CP|K_1\rangle = |K_1\rangle \\ |K_2\rangle &= \frac{1}{2}\sqrt{2}\left[|K^0 - \overline{K}^0\rangle\right] \quad \rightarrow CP|K_2\rangle = -|K_2\rangle. \end{aligned} \tag{2.42}$$

It was observed that there were two K^0, one that decayed into two pions and one that decayed into three:

$$\begin{aligned} K_S \rightarrow \pi + \pi \quad \tau &= (0.8953 \pm 0.0005) \times 10^{-10} \\ K_L \rightarrow \pi + \pi + \pi \quad \tau &= (5.084 \pm 0.023) \times 10^{-8}. \end{aligned} \tag{2.43}$$

As the mass of three pions is nearly the mass of the K, the K_L has a longer lifetime and it was thought that the K_S was equivalent to K_1 and K_L equivalent to K_2. However, in 1964 James Cronin and Val Fitch [19] showed that K_L is made up in part by K_1. They achieved this by producing a beam of K^0 and then after a distance long enough for the K_S decay, measuring the energies of two pions. A spectrum of pion energies was expected as the third pion could take a range of energies. However, a peak of energies that corresponded to the K mass was observed, proving that K_L is not a pure eigenstate, but a mixture given by

$$\begin{aligned} K_L &= K_2 + \varepsilon K_1 \\ K_S &= K_1 + \varepsilon K_2. \end{aligned} \tag{2.44}$$

This is known as indirect CP violation, as the violation was not observed in the decay but in the state of the particles decaying. It was not until 1999 that direct CP violation was observed for the K^0. Both forms have been detected for B mesons in BaBar[20][21] and Belle[22][23].

The final symmetry is T, time reversal symmetry, under which the laws of physics would be the same if time ran backwards:

$$\psi(t, \mathbf{x}) \rightarrow \psi_T(-t, \mathbf{x}) = T\psi^*(t, \mathbf{x}) = i\gamma^1\gamma^3\psi^*(t, \mathbf{x}), \tag{2.45}$$

where γ^1 and γ^3 are Dirac matrices. T violation has been observed in the K-meson by CPLEAR [24]. Another, non-K-meson, signal would be a non-zero Electric Dipole Moment (EDM) for the neutron. If the neutron EDM is non-zero it would show T violation as the EDM can define the z-axis while x and y are arbitrary. This would define the way the particle is spinning and so the direction of time. From the observed CP-violation in the kaon sector, the Standard Model predicts that there should be a neutron EDM of $10^{-32} - 10^{-33}\ e$ cm, while super-symmetric models give higher values. At the time of writing the experimental limit is $|d_n| < 2.9 \times 10^{-26} e$ cm [25] ruling out, many supersymetric models.

CPT is invariant, as long as locality, Hermiticity and Lorentz invariance holds and spacetime is flat. Each of C, P and T can be violated separately but the overall symmetry must hold [26]. The simplest test for CPT violation/conservation is comparing the masses of particles and their anti-particles. Currently the tightest

limit comes from the strangeness oscillation in the $\overline{K}^0$–K^0 system. The limit is

$$-5.1 \times 10^{-19}\,\text{GeV} < m_{\overline{K}^0} - m_{K^0} < 5.1 \times 10^{-19}\,\text{GeV at 95\% [11].} \quad (2.46)$$

2.3.2.1 CP Violation in Neutrino Oscillation

The anti-neutrino oscillation probability can be obtained from the neutrino probability, if CPT invariance is assumed to hold:

$$P(\overline{\nu}_\alpha \to \overline{\nu}_\beta) = P(\nu_\beta \to \nu_\alpha) \quad (2.47)$$

and by setting $\nu_\alpha \leftrightarrow \nu_\beta$ in Eq 2.31

$$P(\overline{\nu}_\alpha \to \overline{\nu}_\beta : U) = P(\nu_\alpha \to \nu_\beta : U^*). \quad (2.48)$$

Eq 2.48 shows that the anti-neutrino oscillation probability is the same as the neutrino oscillation probability, except where U is replaced with its complex conjugate U*. Consequently if the U matrix is complex the $\Im$ term in Eq 2.31 has the opposite sign for neutrinos and anti-neutrinos. In the PMNS matrix only the δ term is affected by this change in sign and hence is called the CP violating phase. The δ term only appears with θ_{13} in (Eq 2.35) and so θ_{13} must be measured for δ to be determined. Currently only an upper limit has been set on θ_{13}, as discussed in section 3.2.6. Disappearance experiments are not sensitive to δ, as Eq 2.31 shows that when $\beta = \alpha$, only the modulus squared appears, thus removing δ from the picture. The signal for CP violation with neutrinos would be a significant difference in the probability for oscillation of one neutrino flavour compared to its anti-neutrino, i.e.

$$P_{\alpha\beta}(L, E) \neq P_{\overline{\alpha}\overline{\beta}}(L, E), \quad \beta \neq \alpha. \quad (2.49)$$

This can be investigated by comparing signal measurements from $\nu_\mu \to \nu_e$ experiments with those from $\overline{\nu}_\mu \to \overline{\nu}_e$ experiments.

2.3.3 CPT Violation in Neutrino Oscillation

The Standard Model and supersymetric (SUSY) models are designed to incorporate CPT-invariance. However, these models do not include gravity. The Standard Model Extension (SME) [27, 28] is an effective field theory that incorporates

gravity with the SM, by way of introducing CPT-even and CPT-odd terms, SUSY can be extended in a similar manner. The fundamental scale of the SME is the Plank scale, $m_p \simeq 10^{19}$ GeV, which is about 17 orders of magnitude larger than electroweak scale m_w associated with the SM. This means any observable experimental signals would be suppressed by the ratio $r \approx m_w/M_p \simeq 10^{-17}$. The SME still contains gauge-invariance, energy conservation, and renormalisability and is symmetric under Lorentz transformation of the observer. However, it breaks symmetry in boost and rotations of particles. Due to the interferometric nature of neutrino oscillation this allows a way to probe physics at m_p. Neutrino oscillation in this model can be explained in three ways: massless Lorentz-violating models; hybrid Lorentz-violating models, which have a mass term for a subset of neutrinos; and massive neutrino Lorentz-violating models.

In the massless Lorentz-violating models all the observed neutrino oscillation is caused by nonzero Lorentz-violating coefficients. These coefficients combine via a Lorentz-seesaw mechanism to behave like mass terms for a range of energies [29]. The simplest of this model is the bicycle model [30], which has only two parameters. However, although describing the atmospheric oscillations well it does not account for the other oscillations seen.

In the hybrid Lorenz-violating models the neutrino oscillation is due to both Lorentz-violating coefficients and neutrino mass terms. An example of this is the tandem model [31]. In this model there are three parameters; one for mass; one coefficient for CPT even Lorentz-violation; and one for CPT odd Lorentz-violation. This model agrees with all neutrino oscillation experiments to date and also predicted the low energy excess for MiniBooNE [32], although not such a large excess as seen in the data.

Massive Lorentz-violating models have oscillations due to Lorentz-violating coefficients and neutrino terms. In these models the mixing due to mass is presumed to dominate over the Lorentz-violation. A example of this type of model is [33]. In this model the probability of $\nu_\mu \to \nu_\tau$ over a long baseline is given by;

$$P_{\mu\tau} \simeq P^{(0)}_{\mu\tau} + P^{(1)}_{\mu\tau}, \tag{2.50}$$

where $P^0_{\mu\tau}$ is the conventional mass oscillation probability between flavours and $P^{(1)}_{\mu\tau}$ is the pertubation due to Lorentz-violating and CPT-violating terms, where

$P^{(1)}_{\mu\tau}/P^{(0)}_{\mu\tau} << 1$. The asymmetry caused by CPT-violation can be defined as

$$\mathcal{A}^{CPT}_{ab} = \frac{P_{\nu_a\to\nu_b} - P_{\overline{\nu}_b\to\overline{\nu}_a}}{P_{\nu_a\to\nu_b} + P_{\overline{\nu}_b\to\overline{\nu}_a}}. \tag{2.51}$$

This asymmetry is dependant on the $(a_L)^{\alpha}_{ab}$ coefficient from [33] for Lorentz and CPT violation but independent of $(c_L)^{\alpha\beta}_{ab}$. To present the asymmetries, it is convenient to introduce the CPT-odd part of $(\delta h)^{CPT}_{\mu\tau}$ of the perturbative Hamiltonian $(\delta h)_{\mu\tau}$ with the coefficients expressed in the Sun-centred frame,

$$\begin{aligned}(\delta h)^{CPT}_{\mu\tau} &\equiv (\delta h)_{\mu\tau}\,|_{c_L\to 0} \\ &= (a_L)^T_{\mu\tau} - \hat{N}^Z(a_L)^Z_{\mu\tau} + (\hat{N}^Y(a_L)^X_{\mu\tau} - \hat{N}^X(a_L)^Y_{\mu\tau})\sin\omega_\oplus T_\oplus \\ &-(\hat{N}^X(a_L)^X_{\mu\tau} - \hat{N}^Y(a_L)^Y_{\mu\tau})\cos\omega_\oplus T_\oplus,\end{aligned} \tag{2.52}$$

where $(\hat{N}^X, \hat{N}^Y, \hat{N}^Z)$ represent the propagation direction and $T_\oplus$ is the local sidereal time for the neutrino detection. If $\left(\frac{\Delta m^2_{32}L}{4E}\right) \nsim 0$ the asymmetry for ν_μ disappearance is

$$\mathcal{A}^{CPT}_{\mu\mu} = \mathcal{A}^{CP}_{\mu\mu} \approx -2L\tan\left(\frac{\Delta m^2_{32}L}{4E}\right)\Re(\delta h)^{CPT}_{\mu\tau}, \tag{2.53}$$

where L is the distance that the neutrinos travel from production to measurement, $T_\oplus$ is the local sidereal time at the neutrino detection. Equation 2.53 shows that experiments with a longer baseline are more sensitive to the asymmetry even if they have the same Δm^2_{32} sensitivity, while equation 2.52 shows that the asymmetry varies with sidereal time and dependant on position.

Table 2.3 gives a selection of experimental limits on coefficients of the SME. These are a selected few experiments; a complete list with expected experimental limits can be found in [34].

2.4 Summary

The Standard Model of particle physics explains the properties of the fundamental particles, how they interact, and how they acquire mass. In this model mass is acquired via the Higgs mechanism, by a Higgs boson coupling to the left-handed doublet and right-handed singlet of fermions. The right-handed singlet of the neutrino would have no physical interactions, and thus be sterile. The simplest way to include the neutrino in the Standard Model is to assume that it is massless.

Expriment	SME coefficient	Results
Neutrino oscillations	a_L	$< 3.0 \times 10^{-20}$
Kaon oscillation	$\lvert\Delta a_{(1,2)}\rvert$	$< 9.2 \times 10^{-22}$
Clock comparisons	$\lvert(k^S_{\phi\phi})_{XX}\rvert, \lvert(k^S_{\phi\phi})_{YY}\rvert, \lvert(k^S_{\phi\phi})_{ZZ}\rvert$	$< 10^{-27}$
H Maser	$\lvert\tilde{b}_{(X,Y)}\rvert$	$< 2 \times 10^{-27}$
Neutrino Astronomy	$(c^{\nu_e}_L)_{00}$	$< 2 \times 10^{-11}$
g–2	b^μ_Z	$(1 \pm 1.1) \times 10^{-23}$
Muonium	$\sqrt{(\tilde{b}^{\mu^-}_X)^2 + (\tilde{b}{\mu^+}_Y)^2}$	$< 2.6 \times 10^{-23}$

Table 2.3: Some selected experimental limits on SME coefficients from [34]. These coefficients limit CPT-violation and Lorentz-violation.

However, neutrino mass can be incorporated into the Standard Model if the neutrino has both Majorana and Dirac masses. If the Majorana mass is 10^{15} GeV, and the Dirac mass $\sim$ 100 GeV, then a the left-handed neutrino mass would be of $\mathcal{O}(10^{-2})$ eV. It has been observed by experiments that neutrinos change flavour during flight, which is possible only if neutrinos have mass, and if the weak eigenstates for neutrinos are different from the mass eigenstates. This gives an elegant description of neutrino oscillations, the mechanism for neutrino flavour change with which all but one experiment to date are consistent. A unitary (PMNS) matrix relates the weak eigenstates to the mass eigenstates. Although CP violation is expected in the as yet unmeasured θ_{13} sector of the matrix, θ_{23} oscillation should conserve CPT in the Standard Model and thus ν_μ and $\overline{\nu}_\mu$ should oscillate with the same parameters. The Standard Model Extension gives an explanation to why CPT conservation may be violated.

Chapter 3

Neutrino Experiments

> "Oh smeg! What the smegging smeg has he smegging done? He's smegging killed me!" (Lister - series 3 Bodyswap)

The neutrino was first proposed as a solution to the unexpected shape of the β particle spectrum from radioactive decay in the 1930's. However, it was not until the 1950's that the neutrino was first detected. This chapter gives a brief overview of how our knowledge of the neutrino has evolved through a set of experiments, and also outlines future experiments. Since this first discovery it has been found that there are three types of neutrino, each with a distinct anti-neutrino (section 3.1).

Our local star, the Sun, burns through nuclear fusion (section 3.2.1), which should release a specific amount of neutrinos. A deficit in the number of these neutrinos was observed by the Homestake, KamiokaNDE and SNO experiments (section 3.2.2 and 3.2.3). In addition, ν from atmospheric sources were observed and an imbalance in the rates from above and below was recorded by KamiokaNDE, IMB and Soudan II expriments. To further probe these deficits and their possible causes, new experiments were proposed that used man-made ν sources.

The oscillation parameters associated with the solar neutrino deficit were investigated by setting a detector many miles away from many nuclear reactor in an experiment called KamLAND. The measured flux was then compared to the prediction from the well known reactor output (section 3.2.4). The atmospheric oscillation parameters were tested by firing a beam of neutrinos made by pion and

kaon decay and measuring the flux many miles away (section 3.2.5). By placing a detector near the beam source it was possible to compare with the un-oscillated neutrino flux. This is the method the MINOS experiment, which is the experiment at the heart of this thesis, uses.

As shown in chapter 2 there is expected to be another as yet unmeasured mixing angle.This angle will be probed by short-baseline oscillations in the neutrinos coming from nuclear reactor sources (section 3.2.6) or in long-baseline accelerator experiments discussed in section 3.2.8.

3.1 Neutrinos From Prediction to Discovery

The existence of the neutrino was first predicted by Wolfgang Pauli in 1930, in a letter to the "Group an Radioactivity" in Tübingen suggesting a desperate measure to help solve the problem of the energy spectrum of β^- particles from radioactive decay, which had been discovered by Henri Bequerel in 1896. In the reaction $X^A_Z \rightarrow Y^A_{Z+1} + e^-$, the ejected electron has a continuous energy spectrum, which apparently violates energy conservation. To solve this Pauli introduced a new particle that he called the "neutron", predicting this particle to be electrically neutral, have low mass (mass$_\nu$ $\sim$mass$_e$), and posses a small magnetic moment, and spin 1/2.

> "The continuous β spectrum would then become understandable by the assumption that in beta decay a neutron is emitted in addition to the electron such that the sum of the energies of the neutron and the electron is constant" [35].

He also postulated these neutrons must only interact weakly as they always escape detection, leading Pauli to say

> "I have done a terrible thing. I have invented a particle that cannot be detected".

In 1932 the particle that we know today as the neutron was discovered by James Chadwick [36]; the particle that was suggested by Pauli was renamed neutrino (little neutral one) by Enrico Fermi [37].

Although difficult to detect[1], it was realised neutrinos were not impossible to detect by using the combination of a large detector and a high number of neutrinos. The neutrino was finally detected 26 years after Pauli's proposal, by Reines and Cowan in 1956 [38]. The discovery was achieved by placing two tanks of ∼200 litres of water near the Savannah River nuclear reactor, and the $\bar{\nu}$ was detected by way of inverse β decay, p + $\bar{\nu} \rightarrow$ n + e^+. Both the extra neutrons and the γ rays from the positron annihilation with electrons in the water were detected. To prove these events were coming from neutrinos and not another source they were able to turn the reactor off and see no events. Discovering the ν earned Frederick Reines the 1995 Nobel Prize in Physics, and was closely followed by a rush of discoveries over the next few years. Goldhaber, Grodzins and Sunyar found in 1957 at Brookhaven that the neutrino is left-handed [39]; that the anti-neutrino is right-handed[2]. In 1962 Danby et al [40][3] showed that there were at least two different types of neutrino by using a neutrino beam produced by $\pi \rightarrow \mu$ + ν and K $\rightarrow \mu$ + ν. The ν produced here only ever produced a μ in the detector, never an e, and so must be different from the ν produced in β-reactions. This result earned Lederman, Schwartz and Steinberger the 1988 Nobel Prize. This solved the problem that had arisen from muon decay. In muon decay the muon decays into an electron and two neutrinos (ν and $\overline{\nu}$). This meant that the ν and $\overline{\nu}$ should annihilate, a reaction that was not detected. Finally, in the late 1980s the measurement of Z^0 decays at the L3 experiment at the Large ElectronPositron Collider (LEP) showed that there were only three light neutrinos that interact with the Z^0 [43]. More recently the third type of neutrino was directly observed. In 2000 the DONUT experiment at Fermilab discovered the neutrino associated with the tau charged lepton [44].

[1] It would on average take 300 light years of water to stop a single neutrino.

[2] If the neutrino is a Majorana particle, i.e., its own anti-particle, left- and right-handedness can be accounted for by viewing the (massive) neutrino in two different reference frames.

[3] The feasibility of the this type of experiment was suggested by Pontecorvo [41] and Schwartz [42] independently in 1960.

3.2 Neutrino Oscillation Experiments

3.2.1 Standard Solar Model

The first evidence for neutrino oscillations did not come from experiments that were investigating neutrino properties, but from experiments studing the nuclear fusion processes in the Sun. Models of the Sun were made by measuring its mass, radius, luminosity and chemical composition, and were entered into calculations which developed into the Standard Solar Model (SSM) [45]. Stars produce energy by fusion of light atomic nuclei into heavier nuclei. The main process by which fusion occurs in a 5 Gyr old dwarf star is the proton-proton (pp) chain (figure 3.1). However, the Carbon-Nitrogen-Oxygen (CNO) cycle occurs 1.7 $\%$ of the time. Both processes give;

$$4^1H + 2e^- \rightarrow^4_2 He + 2\nu_e + 26.7MeV. \tag{3.1}$$

The SSM gives precise predictions for the number of neutrinos reaching the Earth and their energy. Figure 3.2 shows the current best prediction of the neutrino flux coming from the Sun, where it can be seen that the dominant process for emitting neutrinos in the pp chain is the pp step, which account for 91 $\%$ of ν. The ^{7}Be step makes up a further 7 % and the ^{8}B events make up only 0.01 %. However, as the ^{8}B neutrinos are at a higher energy they are easier to detect. One of the major successes of the SSM was the prediction of the speed of sound in the Sun. The speed of sound in the Sun allows it to vibrate at certain frequencies, which were measured in the mid 1990s. The ability to predict the vibrations of the Sun suggests that the SSM is correct [46] and that any deficit in ν detected coming from the Sun is due to properties of the neutrino rather than a problem with the SSM[4].

[4] Although the SSM agreed with helioseismology in 2001 this was with a 1-D model of the Sun. The new updated 3-D model of the Sun has 30 – 40% less carbon than before, which affects the speed of sound in the Sun [47]. This means that now the helioseismology disagrees with the SSM model; however, neutrino oscillation is now accepted. The new measurement of carbon abundances disagrees with the accepted value of the age of the Sun.

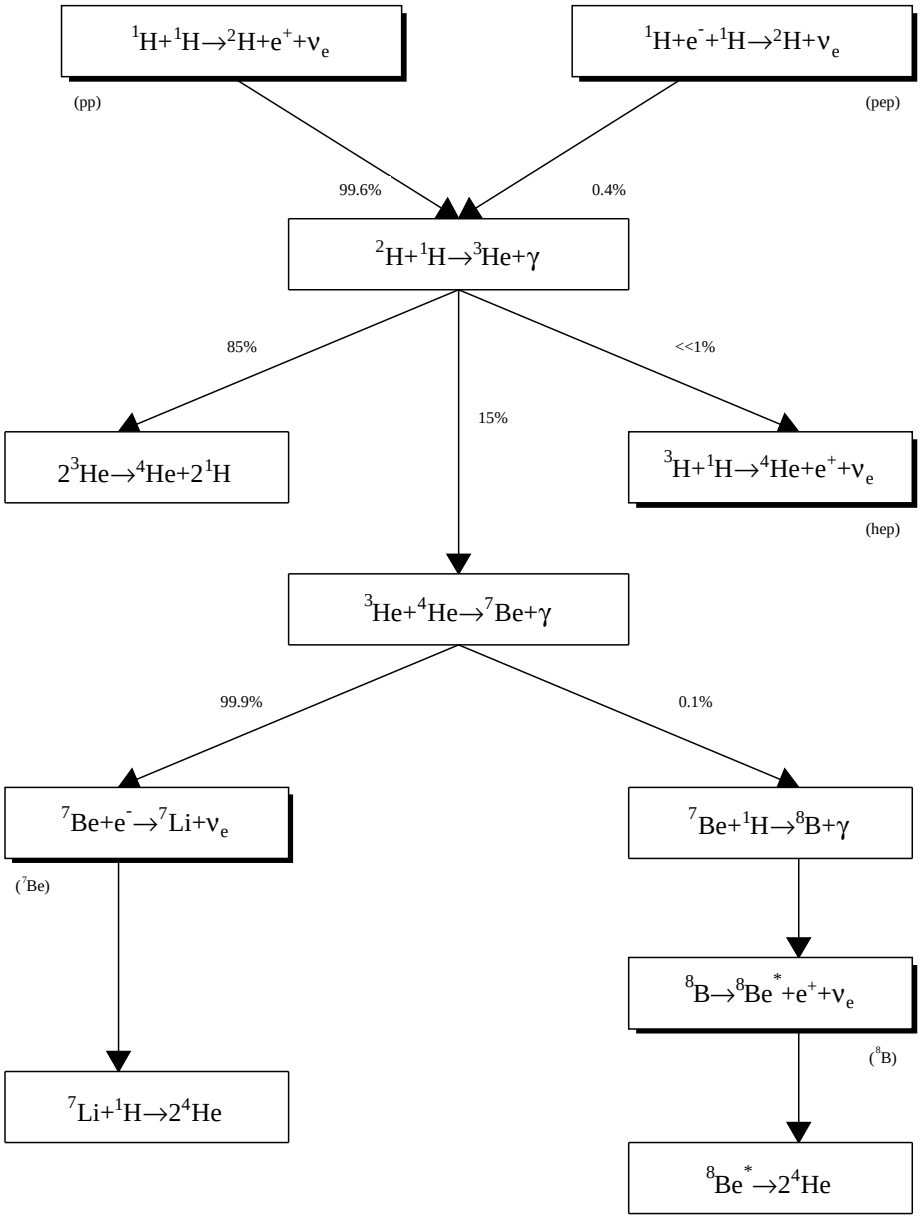

Figure 3.1: *The pp chain [48]. The shadowed boxes are the steps where neutrinos are produced and the percentages in the figure refer to the branching ratio. The pp step produces 91 % of the neutrinos, ^{7}Be step produces 7 %, pep step produces 0.7 %, ^{8}B produces 0.01 % and the hep step produces 0.000001 %. The rest of the neutrinos produced in the Sun is via other processes*

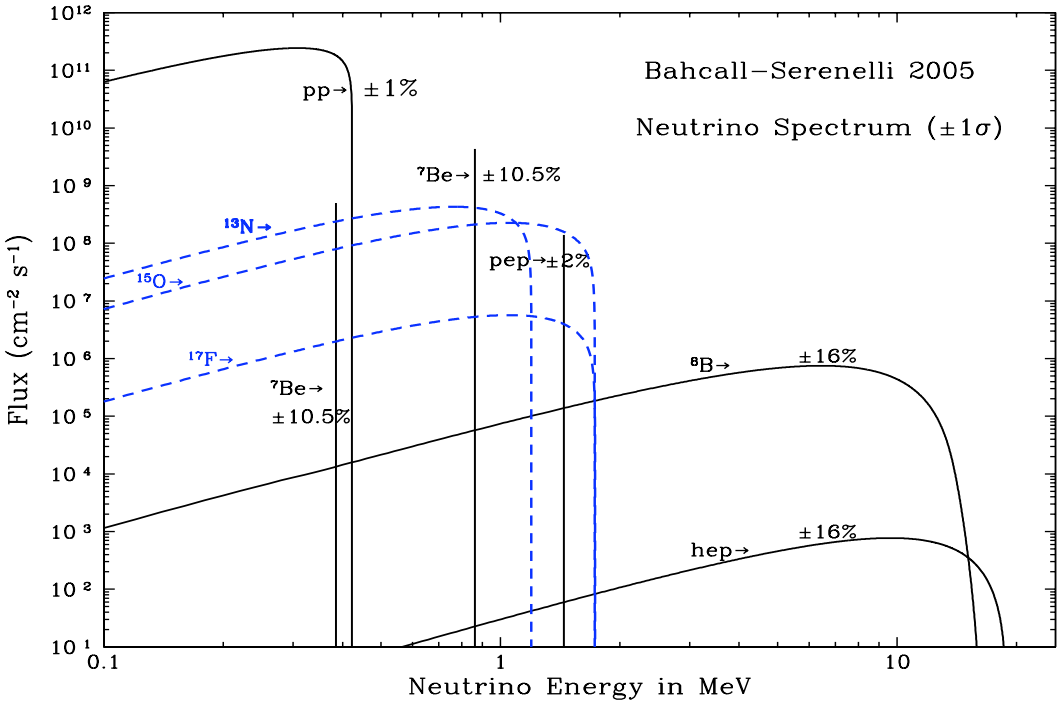

Figure 3.2: *The energy spectrum of neutrinos predicted by the Standard Solar Model. Black lines are fluxes from the pp chain, blue lines are from the CNO cycle. For continuum fluxes the flux is given as $cm^{-2}s^{-1}$ MeV^{-1} at a distance 1 Astronomical Unit (AU). The mono-energetic contributions to the flux are given in $cm^{-2}s^{-1}$ [45].*

3.2.2 Radio-Chemical Experiments

The first experiment to search for neutrinos originating from the Sun was designed by Davis [49] using a liquid chlorine detector in order to measure the solar neutrino flux predicted by Bahcall. Based 1478 m underground in the Homestake gold mine (South Dakota, USA), a 100,000 US gallon tank was filled with a common dry cleaning fluid (tetrachloroethylene C_2Cl_4). Tetrachloroethylene interacts with neutrinos that have an energy greater than 814 keV through the reaction

$$^{37}Cl + \nu_e \rightarrow ^{37} Ar + e^-. \tag{3.2}$$

The detector detected neutrinos from the ^{7}Be and ^{8}B stages. The Argon was detected by periodically flushing the detector, by bubbling Helium through the

experiment, and looking for the Auger electrons emitted as a result of the ^{37}Ar nucleus capturing an electron from the K-shell to form ^{37}Cl again. The cross-section for the neutrino being captured by the chlorine is very low, only one event per day was expected, and therefore each run lasted several months to let the ^{37}Ar accumulate. It was expected from the SSM [45] that the flux should be $8.5^{+1.8}_{-1.8}$ Solar Neutrinos Units (SNU)[5] for chlorine. The experiment found an average of 15 argon atoms per run which equates to a flux of $2.2^{+0.2}_{-0.2}$ SNU [49]. This deficit of neutrino flux detected at Earth was called the solar neutrino problem.

The initial step in the pp chain produces the majority (90 $\%$) of the neutrinos produced in the Sun, so in the 1990s two experiments were built to test the SSM prediction at neutrino energies that related to this step. SAGE and GALLEX used 50 and 30 tonnes of gallium respectively as the active compound as it has a lower threshold energy (233 keV) which should be sensitive to the pp step neutrinos. The exprimental signal was inverse beta decay;

$$^{71}Ga + \nu_e \rightarrow ^{71}Ge + e^-. \tag{3.3}$$

The SSM prediction for these experiments was 131^{+12}_{-10} SNU, while the result for SAGE was $70.8^{+5.3}_{-5.2}$(stat.)$^{+3.7}_{-3.2}$(syst.) SNU [50] and the GALLEX experiment saw $77.5^{+6.2}_{-6.2}$(stat.)$^{+4.3}_{-4.7}$(syst.) SNU [51]. These results are in agreement with the Homestake experiment, ruling out experimental error as a source of the disagreement with the SSM prediction.

3.2.3 Water Čerenkov Experiments

KamiokaNDE (Kamioka Nucleon Decay Experiment) was built in the early 1980s, located 1,000 m underground in Monzumi Mine in Hida's Kamioka area and was designed to look for proton decay [53], predicted by grand unified theories. Originally the experiment consisted of 3,000 tons of pure water and about 1000 photomultiplier tubes (PMTs), detecting the Čerenkov light which would be emitted from the positron produced in proton decay. It has since grown into the Super-KamiokaNDE experiment (Super-K), now comprising 50,000 tons of pure water

[5] A measurement of flux, where 1 SNU= 10^{-36} captures per target atom per second.

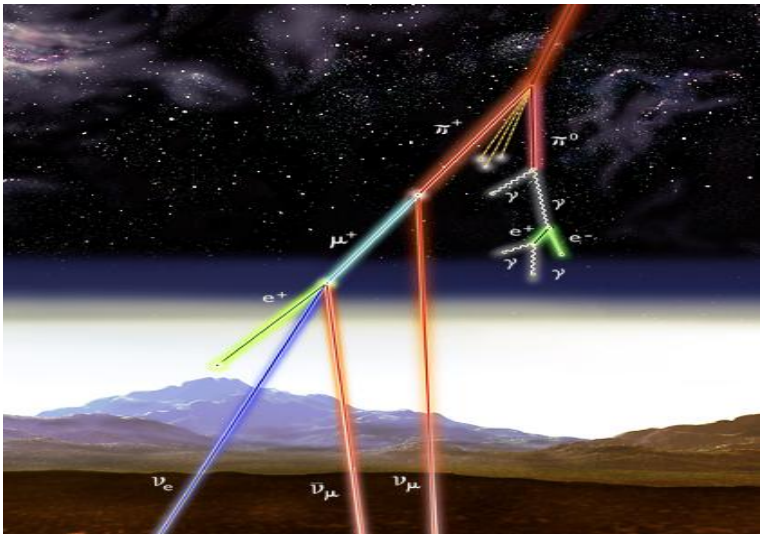

Figure 3.3: *Atmospheric neutrino production from cosmic rays [52]. It can be seen that two ν_μ are produced and one ν_e on per cosmic ray interaction.*

and around 11,000 PMTs and is still collecting data today. Proton decay is yet to be observed at the time of writing[6]; however, one of the backgrounds in the KamiokaNDE experiments has become a major source of study. Neutrinos that have an energy higher than the threshold energy of 768 keV (interact with the water, producing electrons that emit Čerenkov light away from the source of the neutrino. From this it was possible to work out which neutrinos came from the ^{8}B step from the Sun, and able to be detected the neutrinos in real time. This helped show that the solar neutrino problem was not the result of inefficient extraction of the radio-isotope in other experiments. KamiokaNDE was also able to look at neutrinos produced by cosmic rays interacting in the Earth's atmosphere. When a cosmic ray interacts with the atmosphere it produces a cascade of particles (figure 3.3). On average, the cascade produces a ratio of two muon neutrinos to one electron neutrino. When the data was compared to the MC simulation in the KamiokaNDE detector a deficit of ν_μ was found compared to ν_e. A deficit was also observed by the Irvine Michigan Brookhaven (IMB) [54] experiment in a 610 m deep zinc mine in Cleveland, which was also a water Čerenkov detector. The KamiokaNDE and IMB results suggested that there was a problem with atmospheric neutrinos similar to the solar neutrino problem. The deficit was not

[6]The constrant on the lifetime for the proton is mode dependent, $\tau > 10^{31}$ to 10^{33} years [11].

observed by the Frejus and Nusex experiments, which used iron calorimeters instead of water Čerenkov detectors. It was, however, confirmed by the Soudan II experiment, which was also an iron calorimeter designed to detect proton decay. It was located in the Soudan Mine Minnesota, USA. Two independent sources of neutrino disappearance was strong evidence of a flavour changing process.

The atmospheric problem was finally accepted to be a manifestation of neutrino flavour change in 1998 when Super-K released its results [56]. By plotting the number of neutrino events as a function of zenith angle (figure 3.4), they showed a deficit of muon-neutrinos having travelled through the Earth. The result is consistent with neutrino oscillation with $(0.5 < \Delta m^2_{32} < 6) \times 10^{-3}\,\text{eV}^2$. Convincing evidence of oscillations came when Super-K presented the same data as a function of L/E (figure 3.5), showing the characteristic dip-and-rise in the neutrino survival rate.

The Sudbury Neutrino Observatory (SNO) was another water Čerenkov detector, 2092 m underground in Sudbury (Ontario Canada). Like Super-K and other water Čerenkov detectors, having a energy threshold of 5 MeV it could detect ^{8}B neutrinos. However, the previous detectors could only observe the Elastic Scattering (ES) interactions. The ES interaction is $\nu_x + e^- \rightarrow \nu_x + e^-$ so is sensitive to all neutrino flavours, however, detection of ν_e is enhanced due to both the W and Z interactions being available, while for ν_μ and ν_τ interactions only the Z is available. SNO was filled with heavy water so that a further two interactions could be observed: the CC interaction $\nu_e + D \rightarrow p + p + e^-$, which is sensitive only to ν_e, but gives information about the neutrino energy; and the Neutral Current (NC) interaction $\nu_x + D \rightarrow \nu_x + p + n$, which does not give information about the energy of the neutrino but is equally likely for all types of neutrinos and thus allows measurement of the overall flux. The neutron in the NC reaction was measured by observing the 6 MeV gamma ray released via neutron capture. As expected, a deficit was observed in the CC and ES scattering events in comparison to the predicted amount from the SSM; however the NC interaction had the same rate as the prediction from the SSM. These results are plotted together with the Super-K solar result to find the total flux of electron neutrinos and muon/tau neutrinos, which can be compared to the SSM prediction (figure 3.6). All results

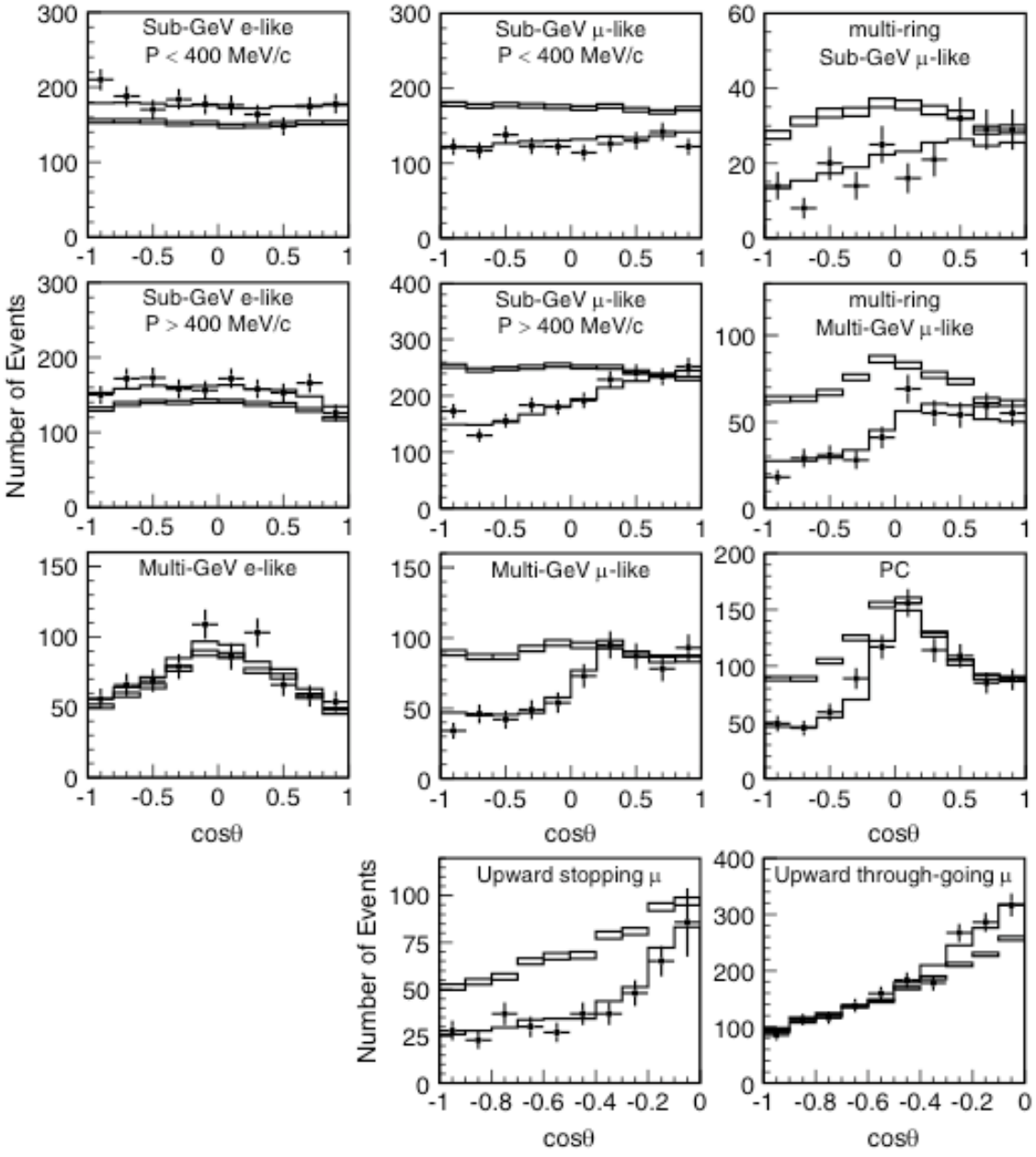

Figure 3.4: *Super-K ν_μ and ν_e events as a function of zenith angle, for fully contained 1-ring events, multi ring, partially contained events and upward muons respectively. The boxes show the MC unoscillated prediction and the points are the data. It can be seen that there are less data events coming from below the detector compared to MC but data and MC agree for events coming from above the detector. The solid line shows the best fit for $\nu_\mu \leftrightarrow \nu_\tau$ oscillation with $\Delta m^2 = 2.1 \times 10^{-3}$ eV^2 and $\sin^2 2\theta = 1.00$ [55].*

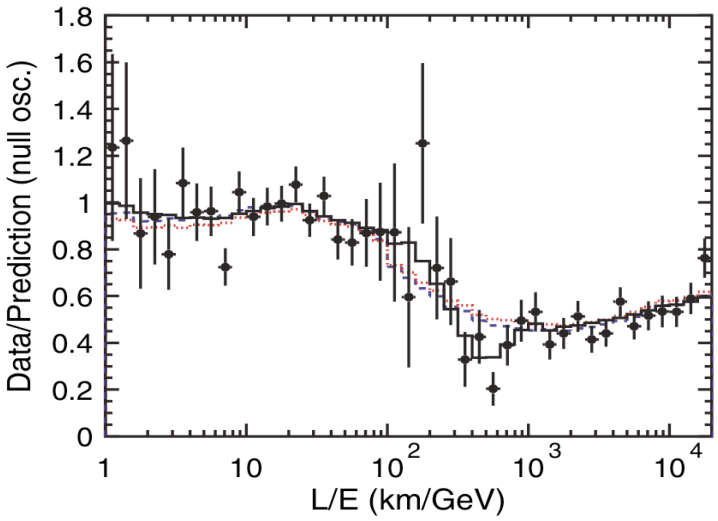

Figure 3.5: *Super-K's ratio of data to MC events without oscillation as a function of L/E shown as points. The best fit $\nu_\mu \rightarrow \nu_\tau$ oscillation is shown as the solid line. Best fit to neutrino decay is the dashed line and neutrino de-coherence is the dotted line [57].*

are in agreement with each other and the SSM. The results from the SNO data points to three possible regions of parameter space that could yield the results seen (figure 3.7). When the SNO result was combined with the other solar experiments (Super-K, SAGE, GALLEX and Homestake shown in figure 3.13) the large mixing angle MSW region was found to be the solution to the solar neutrino problem.

3.2.4 Long Baseline Reactor Experiment

Assuming the results of Super-K and SNO were the product of properties of the neutrino, and also that CPT conservation holds, then it should be possible to observe $\overline{\nu}_e$ disappearance from nuclear reactors. To do this the Kamioka Liquid Scintillator Anti-Neutrino Detector (KamLAND) experiment was built in the Kamiokande cavity. There are 55 nuclear reactors, producing an isotropic $\overline{\nu}_e$ flux, at 100 – 1000 km from the detector, which allow KamLAND to measure the oscillation at the mass difference suggested by the solar experiments. The exact flux was worked out by using reactor operation records provided by the electric-

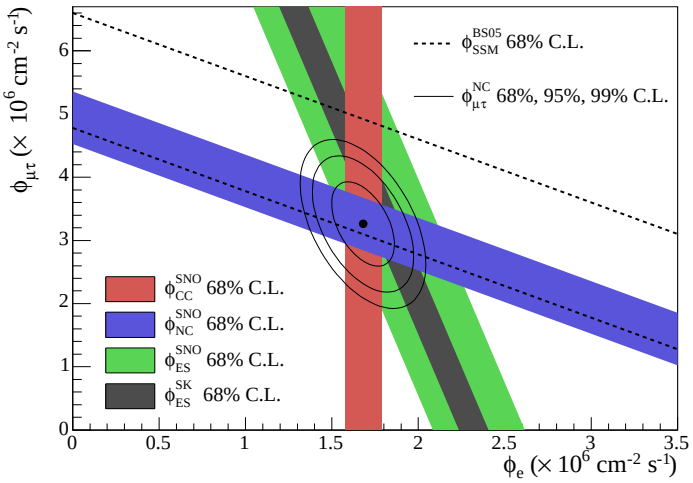

Figure 3.6: *Result from SNO showing the fluxes of $\nu_\mu + \nu_\tau$ versus the flux of ν_e [58].The filled bands represent CC, NC and ES flux, with the Super-Kamiokande ES result in the darker green [59].*

ity companies. The KamLAND detector is composed of a nylon balloon 13 m in diameter filled with 1,000 tons of scintillator, supported by purified oil, which also acted as a buffer to outside radiation. A larger stainless steel spherical vessel that holds 1879 PMTs contains the oil, outside which there is a 3.2 kton cylindrical water Čerenkov detector that acts as a muon veto. The anti-neutrinos were detected by inverse β-decay $\overline{\nu}_e + p \rightarrow e^+ + n$ with a threshold energy of 1.8 MeV. The energy of neutrino was calculated by $E_\nu = E_p + < E_n > + 0.8$ MeV, where E_p is the prompt event energy and $< E_n >$ is the average neutron recoil energy. After 200 μs the neutron was captured by a hydrogen nucleus, releasing a 2.2 MeV photon, which tagged the event as an inverse β-decay. The latest result [60] uses data from 9^{th} March 2002 to 12^{th} May 2007 giving 2.44 $\times$ 10^{32} proton yrs, in which time 2179 $\pm$ 89 (syst.) events were predicted to be detected in the absences of neutrino flavour changing. But only 1609 events were detected. Using information from the energy companies it was possible to predict the multiplicity and energy of neutrinos produced. When compared to the detected neutrinos, a deficit was again observed, which varies with the energy of the ν (figure 3.8(b)). The ν spectrum was used to compute the allowed values for $\Delta\, m^2_{21}$ and $\tan^2\theta_{12}$, which were then compared to the solar results. In figure 3.8(a) it can be seen that the two types

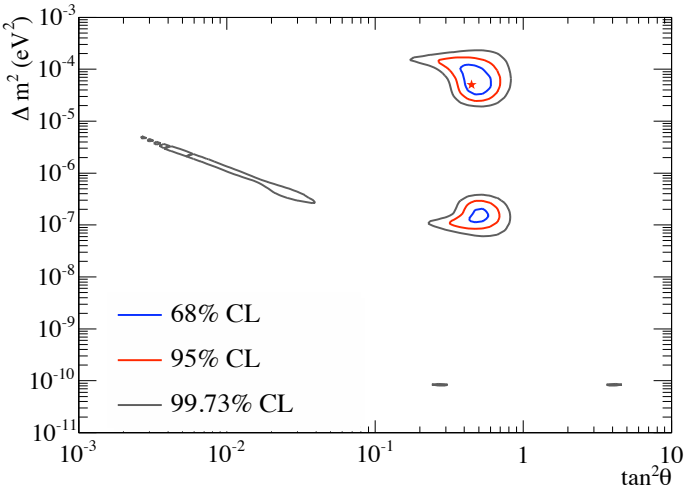

Figure 3.7: *The allowed regions of parameter space allowed using SNO data only. One σ (blue), two σ (red) and three σ (black) contours are shown. The star is the best fit.*

of experiments are complementary, as KamLAND has excellent Δm^2 resolution, while the solar experiments constrain $\tan^2\theta$ with greater precision. The combined best fit point is Δm^2_{21} of $7.59^{+0.21}_{-0.21} \times 10^{-5}$ eV^2 and a $\tan^2\theta_{12}$ of $0.47^{+0.06}_{-0.05}$. KamLAND is still taking data.

3.2.5 Long Baseline Accelerator Experiments

The atmospheric ν mass difference may also be investigated using a long baseline accelerator experiment. The first of these was the KEK to Kamioka (K2K) experiment. A beam of ν_μ was produced at the KEK facility from the KEK-PS accelerator and directed towards the Super-K detector. The beam was sampled by a 1 kt water Čerenkov detector and a fine grain detector system 300 m from the beam source, and again after 250 km, with the 50 kt Super-K water Čerenkov detector. The 1 kt detector was used to predict the spectrum in the Super-K detector. K2K was in operation from June 1999 to November 2004 and delivered 0.922×10^{20} Protons On Target (POT) for the physics analysis, producing a mean neutrino beam energy of 1.4 GeV. Of the $158.1^{+9.2}_{-8.6}$ beam events expected in the Super-K detector only 112 [61] were observed which gave a best fit value of the

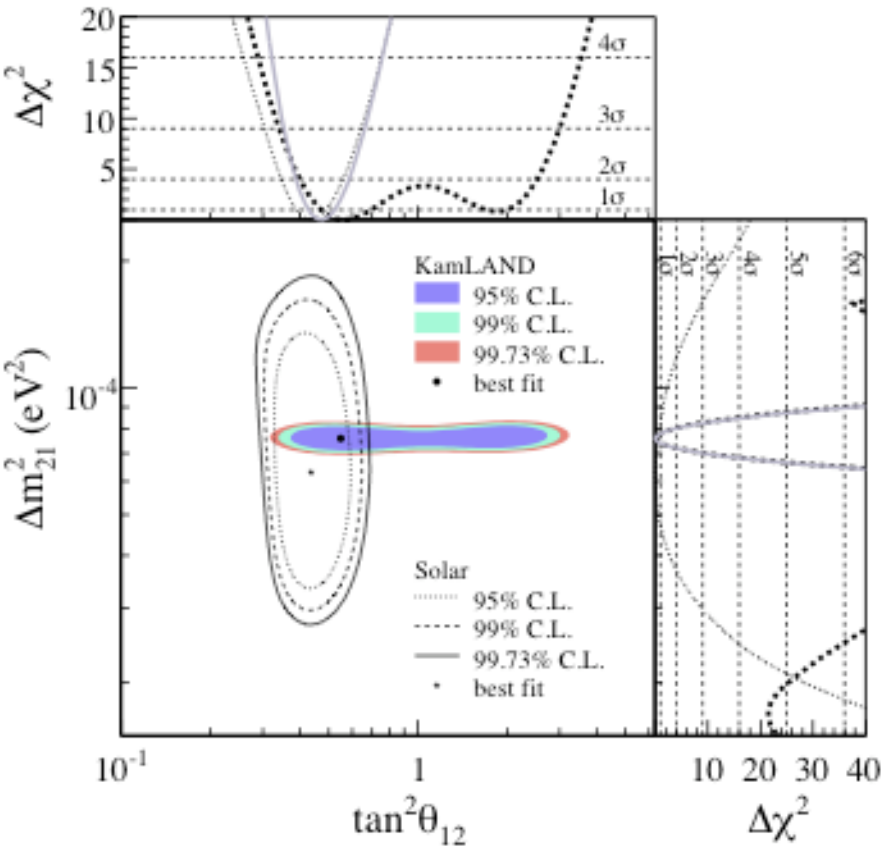

(a) KamLAND contour of Δm^2_{21} vs $\tan\theta_{12}$.

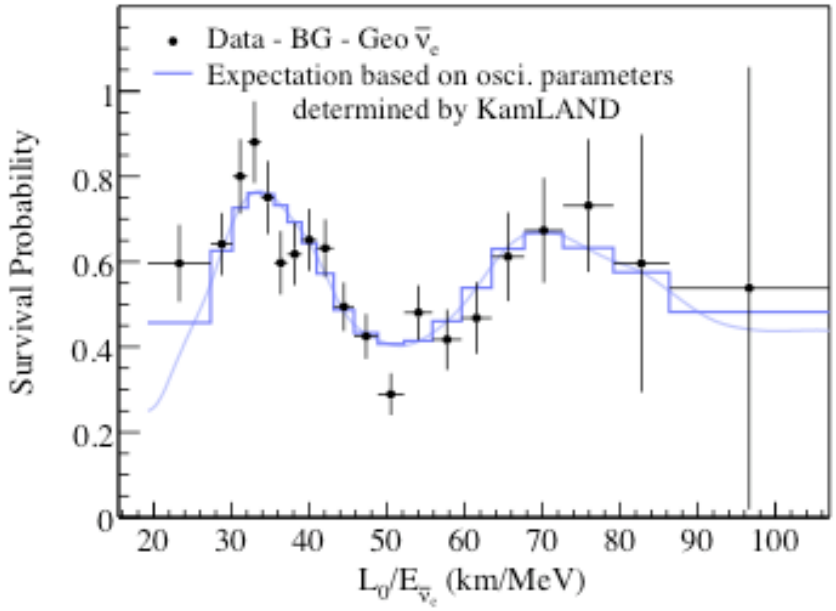

(b) KamLAND anti-neutrino energy spectrum (dots) with best fit oscillation spectrum (blue line).

Figure 3.8: *The KamLAND contour confirms the LMA MSW region for the solar neutrino oscillation [60].*

neutrino parameters of $\sin^2 2\theta = 1$ and Δm^2 = 2.8 $\times$ 10^{-3} eV^2. This is in agreement with the Super-K value for atmospheric neutrinos (figure 3.9). The MINOS experiment uses a similar concept, but has a three times longer baseline of 735 km and uses a beam that has higher intensity and variable energies. The MINOS experiment will be discussed in greater detail in chapter 4 and its results will be discussed in chapter 6.

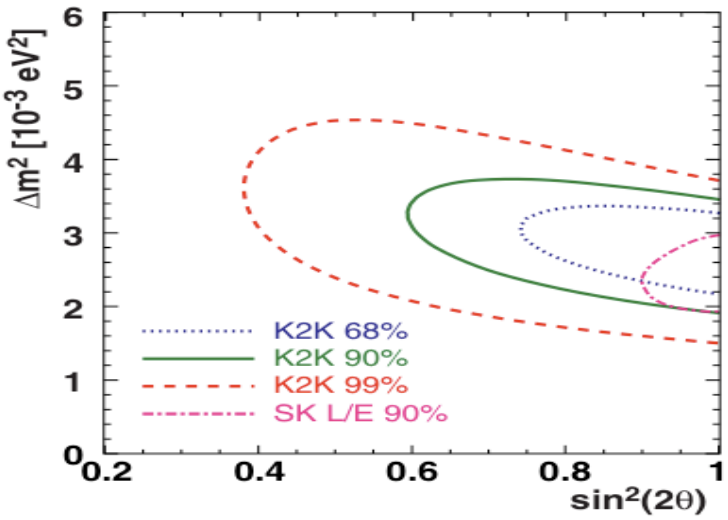

Figure 3.9: *Result from K2K compared to Super-K result [61]. K2K has a larger contour in both* $\sin^2 2\theta_{23}$ *and* Δm^2_{32}*, but is in agreement with Super-K.*

3.2.6 Short Baseline Reactor Experiments

The only mixing angle yet to be observed from the PMNS matrix is θ_{13}, which should present itself in short baseline reactor experiments[7]. The experiment that has given the best limit to date for θ_{13} is the Chooz experiment in northern France. The Chooz detector was built 1115 m and 995 m from the two reactors at the Chooz nuclear power station. It was a 5.5 m high by 5.5 m diameter cylinder, which had a central volume of 5 tons of scintillator doped with gadolinium which captured the $\bar{\nu}_e$. This was surrounded by 17 tonnes of scintillator to capture the electromagnetic energy. The scintillator was surrounded by 192 inward facing PMTs. The outer veto was 90 tonnes of scintillator which was used to veto cosmic

[7]The currently planned experiments can set limits on $\sin^2 \theta_{13}$ is > 0.001

rays. The CHOOZ detector was operational April 1997 to July 1998 with a live time of 8210 hours. The neutrino energy spectrum detected was consistent with no oscillation which set the limit in figure 3.10. The mass splitting is similar to the atmospheric mass difference, so the limit at Δm^2_{atm} for $\sin^2 2\theta_{13}$ is ¡ 0.15 at 90 $\%$ C.L..

3.2.7 Other Neutrino Oscillation Results

The Liquid Scintillator Neutrino Detector (LSND) experiment at Los Alamos Neutron Science Center found a Δm^2 of 0.2 – 10 eV^2 [63], which is significantly greater than the atmospheric and solar mass differences. In this experiment an intense proton beam of 798 MeV was directed to a fixed target, producing mainly π^+ and π^-. Most of the π^- were absorbed. This left the main neutrino source to be $\pi^+ \rightarrow \mu^+ + \nu_\mu$ and $\mu^+ \rightarrow e^+ + \nu_e + \overline{\nu}_\mu$. As most of the decays from pions and muons were at rest, it created a beam with a well defined energy spectrum. The lack of $\overline{\nu}_e$ in the beam, combined with the $\overline{\nu}_e$'s well known cross-section, meant that LSND could search for $\overline{\nu}_\mu \rightarrow \overline{\nu}_e$. The experiment ran from 1993 to 1998 and found an excess of $87.9^{+22.4}_{-22.4}$(stat.)$^{+6.0}_{-6.0}$(syst.) events. To explain this result, at least one more neutrino would need to be introduced. The measurement of the decay width of the Z^0 from the LEP experiments shows that there are only three light neutrinos that interact with the Z^0. Any new neutrino would not interact via the weak interaction; it would be "sterile". However, other short baseline experiments (KARMEN [63], Bugey [64]) have not found any evidence for this. With the release of the MiniBooNE result [65], the standard 4-neutrino model explanation has been disproved (figure 3.11).

3.2.8 Future Neutrino Oscillation Experiments

We have come a long way in the last 80 years, from a particle that was predicted to be undetectable to one that has been detected and found to exist in three flavours. Also, our idea of the neutrino has developed from having the mass of the electron to no mass then a small mass, although we still have not pinned

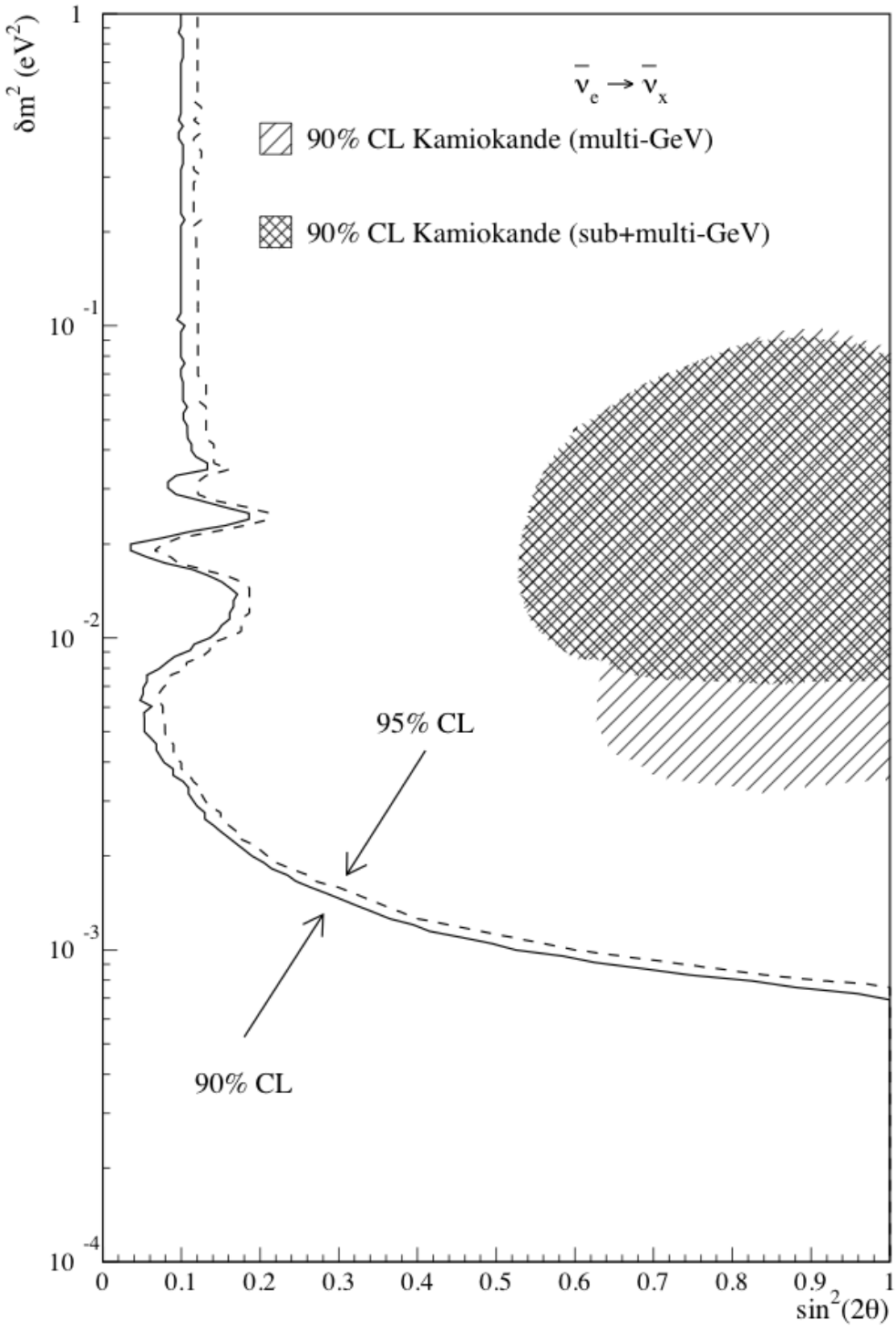

Figure 3.10: *CHOOZ 90 % and 95 % C.L. limit compared with Kamiokande results [62].*

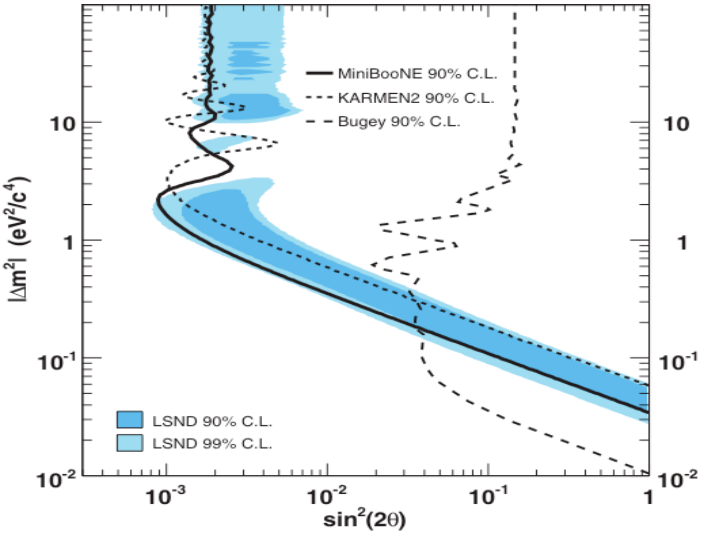

Figure 3.11: *The $|\Delta m^2|$ vs $\sin^2 2\theta$ for MiniBooNE, KARMEN2, Bugay and LSND. MiniBooNE [65] has excluded nearly all of the parameter space allowed by LSND.*

down all the properties of the neutrino. We do not know the value of the third mixing angle $theta_{13}$, is it 0? Also, it is not known whether mass state three is the largest mass or the smallest although in this thesis it is presumed that mass state three is the largest. A new generation of experiments are about to begin data-taking with the aim to search for evidence of a non-zero third mixing angle. These experiments are either reactor-based $\overline{\nu}_e$ disappearance at a long baseline or a search for appearance of ν_e in a ν_μ beam.

3.2.8.1 The Next Generation of Reactor Experiments

Double Chooz [66] is expected to be the first of the new reactor experiments. Double Chooz is expecting its first data in July 2010 [67]. It uses the same pit as the Chooz experiment, but with at larger detector at a distance of 1 km from the reactors. Double Chooz will also have a near detector 400 m from the reactors to measure the un-oscillated spectrum that is then extrapolated to the far detector, where oscillation due to θ_{13} is expected to take place. To reduce systematic errors, the two detectors will be almost identical. Both detectors will have a 10 m^3 fiducial volume, filled with organic scintillator doped with 1 g/l of gadolinium complex, to enhance neutrino capture. Double Chooz will be able to reduce the limit on $\sin^2 2\theta_{13}$ to 0.03 at 90 % C.L..

Daya Bay [68], will start taking data in mid 2011 [69], and follows a similar plan to Double Chooz, except it has two near detector sites, 1.1 km apart, each near two reactor cores[8]. At each near site, there are two detectors, while at the far site, which is 2 km from the near sites, there are four detectors. The detectors are designed to be moveable from one site to another to reduce the systematic error further. This will allow the Daya Bay experiment to set a limit on $\sin^2 2\theta_{13}$ to less than 0.01 at 90 % C.L.. These experiments will be sensitive to θ_{13} but will not be sensitive to the CP violating phase δ or matter effects.

3.2.8.2 The Next Generation of Accelerator Experiments

To measure the CP violating phase δ a ν_e appearance experiment is needed. For these experiments neutrino super-beams [70] are used. Super-beams are produced like conventional neutrino beams but have a higher intensity with a typical thermal power of 0.7 MW to 4 MW. This increases the number of events and thus allows off-axis measurements, which reduces the number of NC events which appear as a background to the ν_e appearance analysis. Tokai to Kamioka (T2K) [71], which has just started data taking[9], produces a beam of ν_μ neutrinos and will measure the flux 295 km away 2.5° off axis with the Super-K detector. Two near detectors, 280 m from beam production, are required, one on-axis to monitor the stability of the beam and one off-axis to extrapolate the energy spectrum to the far detector. T2K should be able to set a 90 % C.L. limit on $\sin^2 2\theta_{13}$ of 0.003.

The NuMI Off-Axis ν_e Appearance (NOνA) [73] experiment is also a long-baseline experiment that uses an off-axis far detector. NOνA will use the same, but upgraded, neutrino beam as the MINOS experiment. The NOνA far detector is 835 km from the NuMI beam target and is 0.8° off-axis. It will be made of liquid scintillator in a highly reflective PVC cell. The active mass of the far detector is 15 kT. The near detector is less massive, and is located 1 km from the NuMI target and 0.8° off-axis[10]. NOνA will be able to set a limit of $\sin^2 2\theta_{13}$ similar to that of

[8] A third pair of reactor cores will come online in 2011, between the two near sites.

[9] The first physics run has started and the first event has been observed in Super-K on the 25 February 2010 [72].

[10] The NOνA near detector will start operation on the surface and so 6° off axis.

T2K and will be able to test the mass hierarchy[11] if $\sin^2 2\theta_{13} > 0.05$. NO$\nu$A is expected to be operational by the end of 2013 [69].

Figure 3.12 shows an estimate of how the limit on $\sin^2 2\theta_{13}$ will improve over the coming years [69] with the planned and current experiments under the assumption that δ_{CP} = 0, and the mass hierarchy is normal. The uncertainties on the start dates and sensitivities of the these experiments are fairly large in some cases. None the less it is expected that the sensitivity to θ_{13} by an order of magnitude over the next five years or so.

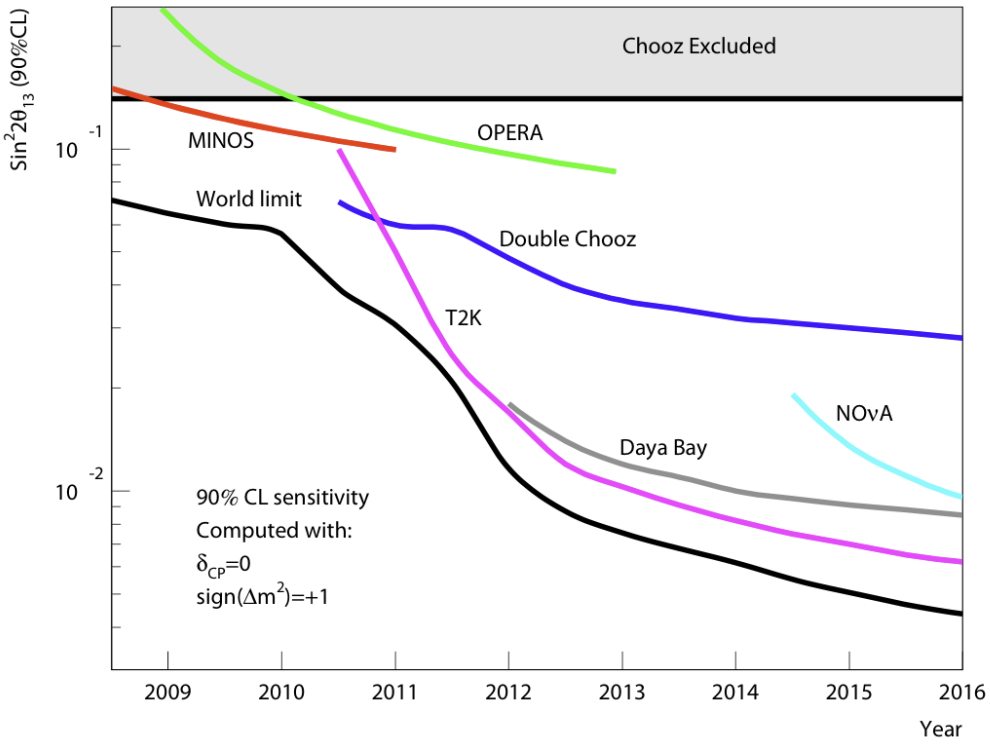

Figure 3.12: *Sensitivities to* $\sin^2 2\theta_{13}$*: different experiments and global [69].*

[11] The beam travels through the Earth's crust which is full of electrons. These electrons interact with the neutrinos propagating and the neutrinos can coherently forward scatter off the electrons. All neutrinos can scatter via interchange of the Z^0 while only the ν_e scatter via the interchange of W^+. Thus there will be a difference in the effective mass of ν_e and $\overline{\nu}_e$ and thus it is possible to work out the mass ordering

3.2.8.3 After the Next Generation of Experiments

Whether θ_{13} is discovered by the new and planned experiments will determine what experiments will be built beyond them. If θ_{13} is small, then a new type of experiment is needed. A neutrino factory [74] or β-beam [75] are ways of investigating lower $\sin^2\theta_{13}$. A β-beam is produced by accelerating heavy ions to a high γ factor. These ions then decay via β-decay to produce an anti-neutrino:

$$^{6}_{2}\mathrm{He}^{++} \rightarrow ^{6}_{3}\mathrm{Li}^{+++} + e^{-} + \overline{\nu}_{\mu} \tag{3.4}$$

The high γ factor reduces the transverse size of the beam by 1/γ and the neutrino energy is boosted by 2γ in the forward direction. The storage ring of the ions must have a straight section as long as possible to allow the ions to decay.

A neutrino factory has a similar design to a β-beam in that the storage ring needs a straight section for the muons to decay. These produce an intense neutrino beam of a single flavour and thus an advantage over super-beams as it reduces the uncertainty of contamination from mis-identified neutrinos by having a known flux of $\overline{\nu}_e$ (ν_e) and ν_μ ($\overline{\nu}_\mu$) of 50 % when the muon decays. In a super-beam the neutrino beam is produced by the decay of charged π and K which can decay via two-body decay (π^+ (K)$^+ \rightarrow \mu^+ + \nu_\mu$) or an uncertain amount of three-body decays ($\mathrm{K}^+ \rightarrow \pi^0 + e^+ + \nu_e$) that produce an electron-neutrino contamination. If the beam is of high enough energy there may be a tau-neutrino contamination from prompt decay of $\mathrm{D_s}$ ($\mathrm{D_s} \rightarrow \tau + \nu_\tau$). Muons have a lifetime of about 100 times longer than the charged pion lifetime, so a 20 GeV muon would have a decay length of 126 km. A storage ring with a long side pointing to the detectors would allow the muons to decay in the desired direction. While it would be relatively easy to check CP violation with a neutrino factory by using μ^- and μ^+, with a β-beam it would be more difficult as it is impossible to produce anti-helium at the moment. However, using a different atom that decays via e^+ it is possible to check. This would take advantage of the β-beam's lower energy and better focusing.

If θ_{13} is discovered by the latest experiments then a new focus of neutrino experiments would have to be taken. The experiments would be designed to look for small θ_{13} survival, to measure CP violation to high precision, determine the

mass hierarchy, and to investigate the θ_{23} octant degeneracy[12]

3.3 Testing CPT by experiment

CPT violation, as discussed in chapter 2 would manifest itself in the neutrino sector as a difference between θ_{ij} and $\overline{\theta}_{ij}$ and/or Δm^2_{ij} and $\Delta\overline{m}^2_{ij}$. Current upper limits on CPT violation from ν oscillation expriments are shown in Table 3.1. The

parameter	experiment	limit
$\lvert \sin^2\theta_{12} - \sin^2\overline{\theta}_{12}\rvert$	KamLAND [76]	$< 0.3^\circ$
$\lvert \Delta m^2_{21} - \Delta\overline{m}^2_{21}\rvert$	solar experiments [77, 78, 51, 79, 80]	$< 1.1 \times 10^{-4}$
$\lvert \sin^2 2\theta_{23}$- $\sin^2 2\overline{\theta}_{23}\rvert$	SuperK [56]	$< 0.45^\circ$
$\lvert \Delta m^2_{32}$- $\Delta\overline{m}^2_{32}\rvert$	K2K [81]	$< 1.1 \times 10^{-2}$
	MINOS [82]	
$\lvert \sin^2\theta_{13} - \sin^2\overline{\theta}_{13}\rvert$	CHOOZ [83]	$< 0.3^\circ$
	analysis of solar, accelerator	
	and atmospheric experiments [84]	

Table 3.1: *Limits on differences between the parameters for ν and $\overline{\nu}$ taken from [85]*

solar mixing parameter limits were calculated by combining KamLAND and solar neutrino experiments. Figure 3.8(a) shows there may be some tension between the anti-neutrino and neutrino oscillation parameters, as the solar neutrino best fit point is outside the 99.73 % C.L. contour of the KamLAND anti-neutrino analysis. Table 3.1 shows that this tension is insignificant at the moment. The atmospheric parameters were found by combining Super-K results with MINOS and K2K, while the CHOOZ experiment set the limit for the third mixing angle.

The MINOS experiment has already measured CPT in Δm^2_{32} using atmospheric neutrinos [86], and also by looking at $\overline{\nu}_\mu$ with the NuMI beam [87]; both sources yield results consistent with no CPT-violation. This thesis presents and expands on the 2009 $\overline{\nu}_\mu$ analysis [88], which builds on the technology used in [87].

[12] If $\sin^2 2\theta_{23}$ is not maximal different angles give the same answer. For example $\sin^2 2\theta_{23}$ = 0.96 $\rightarrow \sin^2\theta_{23}$ = 0.4 or 0.6.

3.4 Summary

Property	Experiments	Limit
δm^2	KamLAND + global solar [89]	$7.59^{+0.20}_{-0.20} \times 10^{-5}$ eV^2
Δm^2	MINOS [1]	$2.43^{+0.13}_{-0.13} \times 10^{-3}$ eV^2
$\sin^2 2\theta_{12}$	KamLAND + global solar [89]	$0.86^{+0.03}_{-0.04}$ C.L.90 %
$\sin^2 2\theta_{13}$	CHOOZ [83]	< 0.19 C.L. 90 %
$\sin^2 2\theta_{23}$	Super-K [55]	> 0.92 C.L. 90 %

Table 3.2: *Current limits for each difference in mass and mixing parameter [11].*

Neutrinos were first suggested 80 years ago and thought to be undetectable. They were first detected in 1954 and have since been shown to come in three flavours. When neutrinos were included in the Standard Model of particle physics they were believed to have no mass. However, experiments have since demonstrated that neutrinos undergo flavour oscillation, which is only possible if at least two neutrinos have mass and their masses are different from each other. The latest knowledge of the oscillation parameters is shown in figure 3.13 and summarised in table 3.2, where $\Delta m^2_{31} \approx \Delta|m^2_{32}| = \Delta m^2$ and $\Delta m^2_{21} = \delta m^2$. The generation of neutrino experiments about to start will search for the as yet unmeasured θ_{13} and will reduce the 90 % C.L. limit of $\sin^2 2\theta_{13}$ to 0.01 if very small or make a measurement of 5 σ if it is at the CHOOZ limit. If the value of $\sin^2 2\theta_{13} > 0.05$ then future experiments could search for and measure the CP violating phase δ.

CPT-violation has been well constrained in the quark sector by $\overline{K}^0$–K^0 oscillation. In the neutrino sector CPT-violation has not been yet to be observed, but has been less well constrained. MINOS has been able to improve the limits by observing $\overline{\nu}_\mu$ oscillations directly.

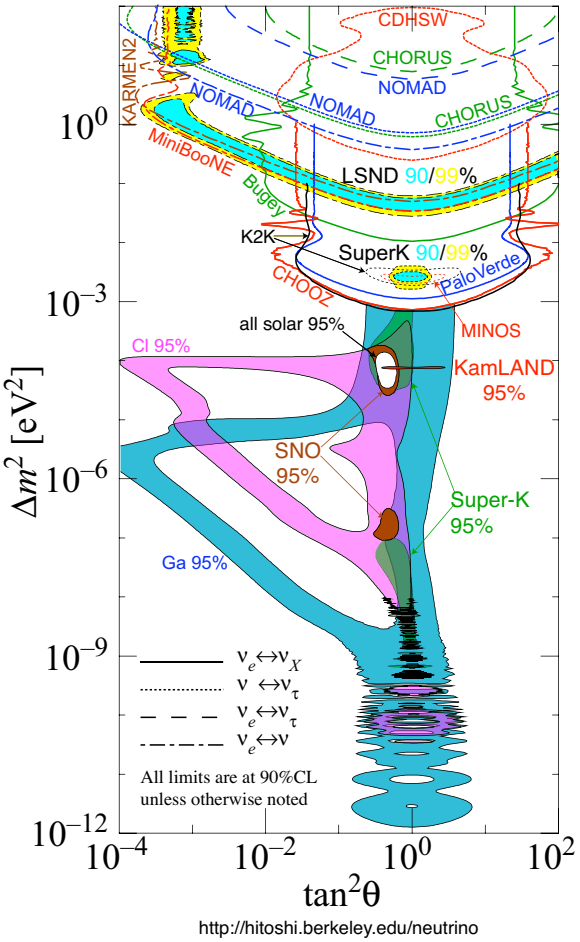

Figure 3.13: *The mass differences and* $\tan^2\theta$ *for all experiments[11]. The coloured shaded regions in a triangular shape are the regions covering the allowed oscillation parameters from radio chemical experiments measuring neutrinos from the Sun. The two brown shaded and green shaded regions are the allowed oscillation parameters for the SNO and Super-K solar neutrino analysis. The white region in these regions is where all these solar results agree. The red shaded region is the result from the measurement of anti-neutrinos from nuclear reactors detected by the KamLAND detector, which agrees with the solar neutrino results. The dotted lines are accelerator beam experiments; black outlines the allowed K2K oscillation parameters and red the MINOS. These agree with the atmospheric Super-K parameters, the shaded yellow and blue region with dotted outline. To the side and below the solid red line are the parameters allowed by the CHOOZ experiment. The yellow and blue region outlined by the dotted lines is the allowed region from LSND but only the regions below the red (MiniBooNE) and brown (KARMEN2) dashed line are allowed, which excludes most of the LSND region.*

Chapter 4

MINOS

> “Listen! Can anyone hear anything?”
>
> “No.”
>
> “Precisely. No one can hear anything! And you know WHY we can’t hear anything?”
>
> “Why?”
>
> “Because there are NO sounds to hear.” (Kryten 2X4B-523P,The Cat, Rimmer -series 4 Whitehole)

Main Injector Neutrino Oscillation Search (MINOS) is a long-baseline neutrino beam experiment, designed to measure the neutrino flavour-changing parameters in the “atmospheric neutrino regime” associated with ν_μ disappearance. MINOS is designed to search for neutrino oscillation, and it can also test other neutrino disappearance models. To do this the MINOS experiment receives a beam of ν_μ from the Neutrinos at the Main Injector (NuMI) beam line at Fermi National Accelerator Laboratory (Fermilab) near Chicago, Illinois, USA (section 4.1). The beam is directed towards the Soudan Underground Laboratory in Minnesota, USA. MINOS samples the beam at two points, once just after the beam is formed (1 km downstream of the primary beam target) with the Near Detector (ND) (section 4.4), and again at the Soudan Underground Laboratory (735 km from the primary beam target) with the Far Detector (FD) (section 4.3 figure 4.1). The ND neutrino energy spectrum is used to predict the un-oscillated neutrino energy

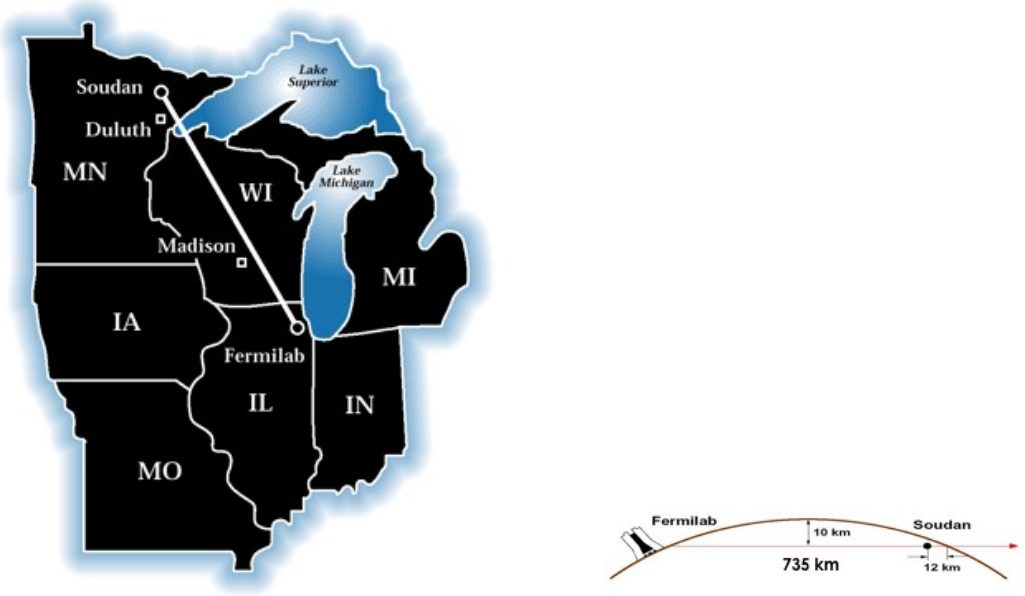

Figure 4.1: *The NuMI beam line fires a beam of ν from Fermilab Illinois 735 km through the Earth to the Soudan mine in Minnesota.*

spectrum at the FD. This prediction is compared to the actual neutrino energy spectrum measured at the FD. Any deficit of neutrino events in the FD data when compared to the prediction, combined with the difference in spectral shape, will give information about the mechanism for ν_μ disappearance and the associated physical parameters. This chapter describes the design of the beam and the detector. A more detailed description of the detectors can be found in [90].

4.1 NuMI Beam

4.1.1 NuMI Beam Production

The NuMI beam is produced by protons accelerated to 120 GeV in the Main Injector (MI) at Fermilab. The protons are extracted up to every 1.9 seconds[1] in spills that last 8.7 μs. Each spill contains around 2.4×10^{13} protons, which are directed 58 mrad downwards towards the FD. The protons are focused onto a long thin segmented graphite target, which is enclosed in an air-tight aluminium casing with beryllium windows at either end to allow the beam to enter and exit.

[1] 1.9 s is the design limit. The average extraction time is 2.4 secs.

The target is comprised of 47 segments, each 20 mm in length and separated by a 0.3 mm gap, giving a total target dimensions of 0.95 m $\times$ 0.0064 m $\times$ 0.018 m. The long and narrow shape allows the majority of protons to interact with the graphite while allowing the secondary particles, primarily pions and kaons, to escape through the sides of the target, so minimising re-absorption. The secondary particles are focused using two magnetic horns 10 m apart. Each horn is made of two conductors; the outer conductor is cylindrical while the inner conductor is parabolic. This shape causes focusing of charged particles that travel between the conductors. The horns are pulsed with up to 200 kA during beam spills. During normal running, the direction of the current is chosen so that positive particles are focused and negative particles are defocused. The secondary pions and kaons are directed into a pipe, starting 50 m from the target, of length 675 m long and diameter 2 m, where they decay into neutrinos. The decay pipe was evacuated to less than 1 torr for Run I (20/05/2005 – 26/02/2006) and Run II (12/09/06 – 16/07/2007). Helium was added to the decay pipe at 0.9 atm to reduce pressure on the aluminium window for Run III (17/11/2007 – 13/06/2009). At the end of the decay pipe is an absorber made from aluminium and steel and cooled by water. This stops any hadrons that have not decayed yet. After the absorber, 240 m of rock range out any $\mu^{\pm}$ produced in the meson decay before they enter the near detector hall. In front of the absorber is an ionisation detector that allows monitoring of the hadrons. A further three ionisation detectors are in alcoves in the rock to monitor the muons. These detectors provide information about the integrity of the target. Figure 4.2 shows a cartoon of the beam line.

4.1.2 NuMI Beam Composition

Since the positively charged secondaries are focused into the decay pipe, the dominant decay is π^+ (K)$^+ \rightarrow \mu^+ + \nu_\mu$ giving a beam of muon neutrinos. However, the beam also contains small components of $\overline{\nu}_\mu$ and ν_e from $\mu^+ \rightarrow e^+ + \overline{\nu}_\mu + \nu_e$ and K$^+ \rightarrow \pi^0 + e^+ + \nu_e$ and decays from any negative particles that were not defocused. This makes the final beam composition 91.7 % ν_μ, 7.0 % $\overline{\nu}_\mu$, 1.2 %, ν_e and 0.1% $\overline{\nu}_e$ [18], [92]. The energy spectrum of the neutrinos can be tuned by

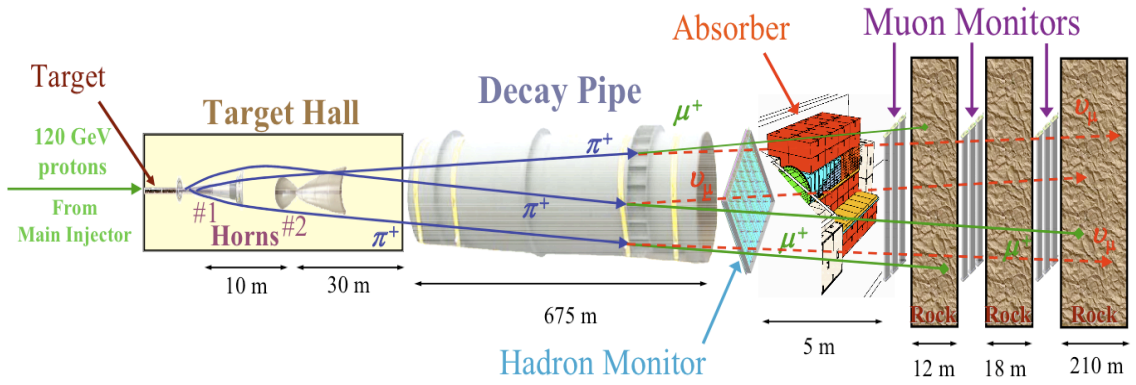

Figure 4.2: *A cartoon of the NuMI Beam line. A beam of ν are created by firing 120 GeV protons at a graphite target to created a shower of mesons. The horns focus positively charged particles into the decay pipe, where the mesons decay into ν_μ and μ^+. The absorber stops any hadrons that have not decayed, while the μ^+ range out in the rock before they reach the ND. Taken from [91].*

changing the distance between the target and the second horn. In practice, this is achieved by adjusting the position of the target or the position of the horn. Figure 4.3 shows the predicted spectra for three possible configurations of the NuMI beam: low energy (LE); medium energy (ME); high energy (HE). From the results from Super Kamiokande (discussed in section 3.2.3) for the $\Delta m^2_{32} - \sin^2 2\theta_{23}$ parameter space it was expected that a dip in the spectrum would occur around 3 GeV. To maximise the rate of neutrinos observed at this energy, most of the running has been carried out in the "LE-10" mode. In this configuration, the target is positioned 10 cm away from its lowest energy position and the horns are pulsed at 185 kA. More neutrinos are produced with the higher energy beams, but the neutrinos are at higher energies (figure 4.3) and thus not as sensitive to oscillations. Limited runs have however been carried out with higher-energy beams to understand the hadron production at higher energies. This helps with the modelling of the high-energy tail in the LE runs. Also, the higher energy running helps distinguish between neutrino oscillation and other neutrino disappearance models, which predict deficits at higher energies.

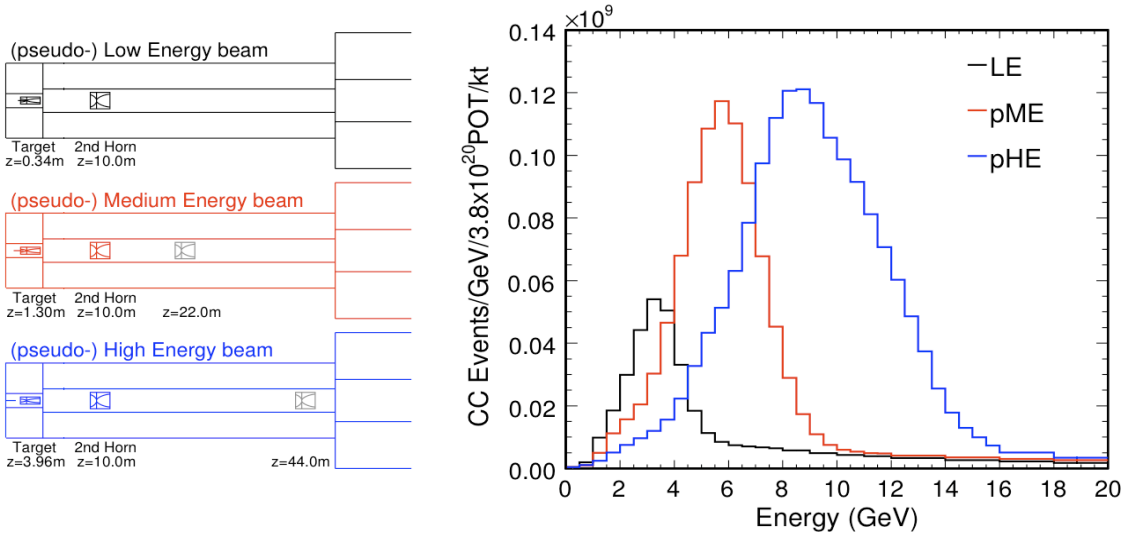

Figure 4.3: *The neutrino energy spectrum for three different horn and target positions. The greater the distance between the target and the second horn the higher the energy spectrum. When the change in spectrum is due to a change in only target position it is called pseudo.*

4.2 The MINOS Detectors

The MINOS experiment uses two detectors to sample the NuMI beam in two places, first 1 km downstream of the NuMI target and then again after 735 km. This allows a comparison of the un-oscillated neutrino spectrum to one obtained where the disappearance rate is predicted to be near its highest. The detectors are designed to be as functionally similar as possible, in order to reduce systematic errors associated with the neutrino-interaction cross-sections and the detector acceptance. Both detectors are steel-scintillator sampling calorimeters. Each detector is made up of a "sandwich" of planes, each comprising 2.54 cm thick steel attached to a layer of 1 cm thick strips of solid plastic scintillator followed by a 2.5 cm air gap. The planes are mounted with the strips oriented 45° to the horizontal and 90° to those of the previous plane. This gives a co-ordinate system based on the direction of the planes of U ($\frac{1}{\sqrt{2}}(x+y)$) or V ($\frac{1}{\sqrt{2}}(-x+y)$. This arrangement provides the ability to track charged particles in 3D. In order to identify the charge of the particles and therefore to enable the separation of

(a) Scintillator strip

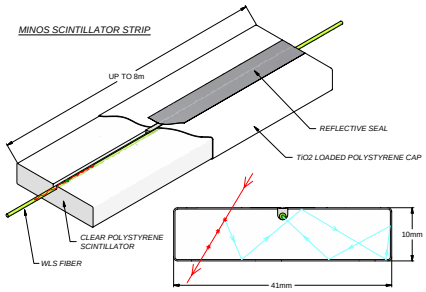

(b) Cartoon of light path in scintillator strip

Figure 4.4: *Short strip of scintillator co-extruded with TiO_2 coating to increase light collected by the WLS as shown in b). The strip in a) is being illuminated by a blue LED making the grove that holds the WLS visible.*

neutrinos from anti-neutrinos, the steel planes are magnetised with an average field of 1.3 T. In normal running the magnetic field points in the forward direction, which focuses μ^- towards the centre of the detector and defocuses μ^+. The field can be reversed to permit analysis of systematic errors associated with the field[2]. The magnetic field also allows the momentum of the muons to be worked out by the curvature of the path that they follow.

The scintillator strips are extruded polystyrene, each 4.1 cm wide, 1.0 cm thick and up to 8 m long. The polystyrene is doped with fluors PPO (1 % by weight) and POPOP (0.03% by weight). The strips are co-extruded with a 0.25 mm coating of TiO_2 to trap the light within the strip. Each strip is read out by 1.2 mm diameter wavelength-shifting fibre (WLS), which is inserted into a 2.3 mm deep groove cut into the "top" face of the strip (4.4). The WLS fibre is glued into the groove and sealed with an aluminised Mylar tape to maximise the light gathering of the WLS and keep the strips light tight. Wavelength shifting fibres absorb light at 420 nm and emit light at 470 nm, thus minimising the self-absorption of light in the fibre. The scintillator strips are laminated to an aluminium manifold, with each manifold holding either 20 or 28 strips. At the ends of each strip, the WLS fibres are connected to clear fibres, which have a longer attenuation length. The clear fibres are used to transmit the light signals over several metres to the multi-anode photo-

[2]This study has not been completed at the time of writing this thesis. To find any errors associated with the $\mathbf{B}$-field the ratio of the data/MC for forward and reverse field would be taken.

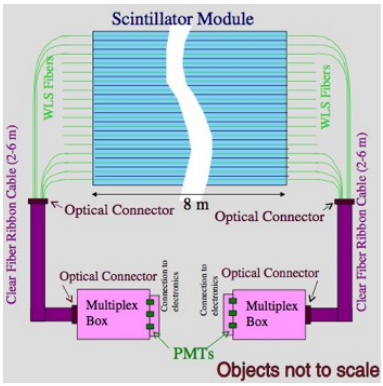

Figure 4.5: *A schematic of the FD optical readout. The light from the scintillation is guided out of the scintillator module by the WLS fibres to the clear fibre. The clear fibres are joined together into groups of eight in the multiplex box. These bundles of eight are read out by one pixel on the PMT.*

Figure 4.6: *Soudan Mine and MINOS Far Detector with veto shield.*

multiplier tubes (PMTs) (figure 4.5) from which the signal is read out by the data acquisition (DAQ) system. The vastly different event rates at the two detectors required the use of two different electronics systems, as explained in the following sections.

4.3 The MINOS Far Detector

The MINOS Far Detector is located 705 m underground [90] (2070 meters-water-equivalent) in the Soudan Underground Laboratory in Minnesota, USA. It is made of 486 8 m $\times$ 8 m octagonal planes (of which 484 are instrumented; un-instrumented planes do not have scintillator attached to the steel) arranged into two super-

modules with a total mass of 5,400 tonnes. The first, upstream, super-module is 14.78 m long and is made up of 248 active planes, and one un-instrumented plane (plane 0). The second, downstream, super-module has 236 active planes, with one un-instrumented plane and is 14.10 m long. With a 1.1 m air gap between the two super-modules the total length of the far detector is 30 m. Each super-module is independently magnetised using 15 kA-turn water-cooled coils. The coil runs through the centre of the planes, producing a toroidal magnetic field of mean strength 1.3 T.

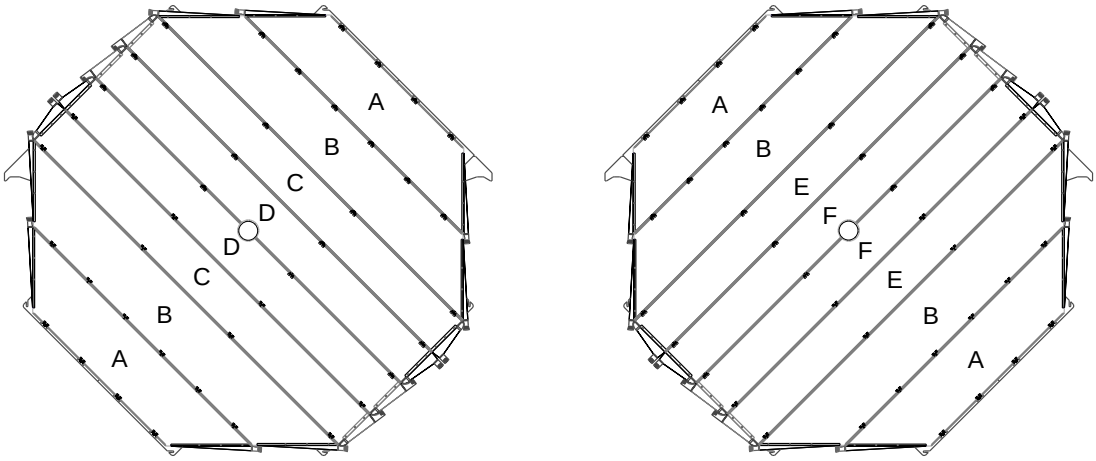

Figure 4.7: *A view of the U (left) and V (right) orientation of scintillator modules looking towards Fermilab.*

Active planes in the FD have 192 scintillator strips arranged into 8 modules (figure 4.7). Each strip is read out at both ends by 16 pixel Hamamatsu M16 PMTs. The signal from each end of a strip can be summed so that the total signal is approximately uniform along the length of the scintillator. As there are a large number of strip ends (185,856), multiplexing is used to reduce the number of PMTs needed for the front-end electronics (FEE). The multiplexing scheme employed requires that one pixel on the PMT reads eight strip ends, which are separated by about 1 m [3]. Each PMT reads out one and a half planes. To correctly reconstruct the strips that have been hit in an event, each strip is connected to a unique pair of pixels on opposite sides of the detector. Another requirement was

[3] one metre is chosen because this is the typical shower width in the far detector

that adjacent strips be read-out by non-adjacent pixels to reduce cross-talk from leakage of charge. The wiring for this pattern is maintained in multiplexing (MUX) boxes. These MUX boxes each hold three PMTs which read out 2 planes. Due to the digitisation of the signal from PMT running at 200 Hz there is 5 μs deadtime after each hit. Each digitised signal has eight possible planes. For muons, only one digitised signal is read out from each side of the plane. In this case, it is relatively easy to reconstruct which strip was hit, using multiplexing maps to see which strip is associated with the two pixels hit. For shower hits which have more than one hit per plane the solution is more complex. In the shower case scenario "The Hypothesis Testing Method" [93] is used the find the strips.

A veto shield is not required for the beam experiment, but it allows the study of atmospheric neutrinos by providing a means of reducing the high level of cosmic muon background. As the FD is optimised for the beam experiment, the planes are hung vertically, so cosmic muons may enter the top of the detector in the gaps between scintillator planes and deposit energy in the scintillator for the first time, deep inside the detector. These cosmic muons give the appearance of an atmospheric neutrino interaction. The veto shield is constructed from overlapping layers of scintillator modules arranged horizontally on top of the detector (figure 4.8). Cosmic muons entering the detector leave energy deposits in one or more of these scintillator layers, which can be used as a veto for these events. The dynode threshold is set to $1-2$ p.e. for the veto shield to reduce tagging inefficiencies due to noise.

4.4 The MINOS Near Detector

The ND (figure 4.9) is 100 m underground and 1 km from the NuMI target within the grounds of Fermilab (figure 4.10) near Chicago.

The MINOS near detector was made functionally similar to the MINOS far detector, so that systematic uncertainties in the properties of neutrino interactions approximately cancel between the two detectors. However, it is not exactly the same as it is nearer the beam source, so the beam is a lot narrower than at the FD, 50 cm diameter compared with 10 km. As well as the higher rate of neutrinos

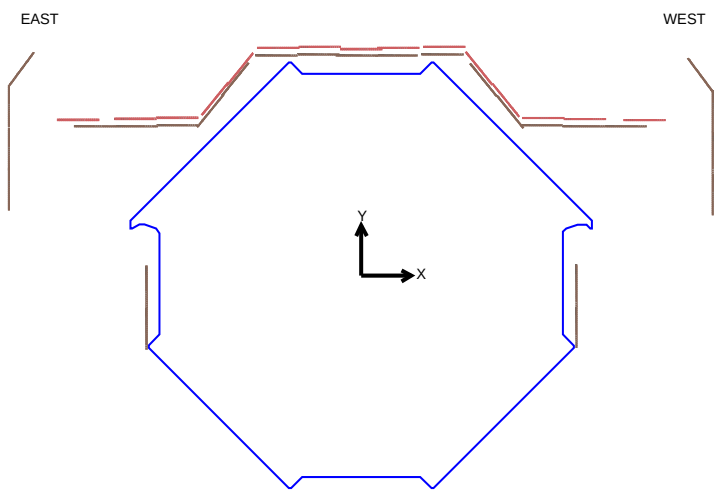

Figure 4.8: *A schematic of the FD with the veto shield in brown.*

from the beam there is a higher rate of cosmic muons due to the near detector not being as deep underground. This means that the detector can be smaller, to keep costs down, but the electronics need to be able to handle the higher event rate. The detector is therefore a "squashed octagon" design 4.8 m wide $\times$ 3.8 m high $\times$16.6 m long (figure 4.11) and is 980 tonnes. The magnetic coil is offset from the centre of the detector by 55.8 cm [90] and the beam is directed to be half way between the hole and the left edge of the detector, in order to contain the neutrino interactions as much as possible. The ND is made from one super-module, made up of 282 steel planes. However the super-module is split into two regions: the colorimeter and the spectrometer. Planes 1 to 120 are called the calorimeter, with plane 0 being just steel. In the calorimeter section every plane is instrumented, but only every 5^{th} is fully instrumented (96 scintillator strips). The other four are only partially instrumented (64 scintillator strips) (figure 4.12), enough to just cover the area where the beam interactions are. The spectrometer region is made up of planes 121 to 281. In this region only the momentum of the muon is calculated. This is determined by how much the muon track curves in the magnetic field. For this purpose it was sufficient to instrument only every 5^{th} plane.

Due to the higher event rate in the ND and its smaller size, a different system of readout is used. Since the scintillator strips are shorter in the ND, they are

Figure 4.9: The MINOS Near Detector. The blue plain is plane zero of the ND with the rest of the detector behind it. The racks holding the electronics are seen on the ground and the walk way on the left of the detector. The white structure in-front of the detector is ArgoNeuT.

read out at a single end by 64-pixel Hammatsu M64 PMTs, with a reflective surface placed at the other end. This gives a similar light yield to the double-sided readout at the FD. Because of this each pixel reads out one strip, so each fully instrumented plane is read out by $1\frac{1}{2}$ PMTs, and a partially instrumented plane is read out by one PMT. The PMT is read out by high-speed QIE (charge integrator and encoder) electronics, that give dead-timeless readout which is digitised into 19 ns buckets. These buckets are recombined at the time of reconstruction to give hits that are like those found in the far detector. In the calorimeter section every anode is read out separately so each strip hit is known. However, the spectrometer section is multiplexed, with four anodes read out together. This means that it is impossible to know exactly which strip has been hit, but information from the calorimeter section gives a “seed” that can be used to reconstruct the track.

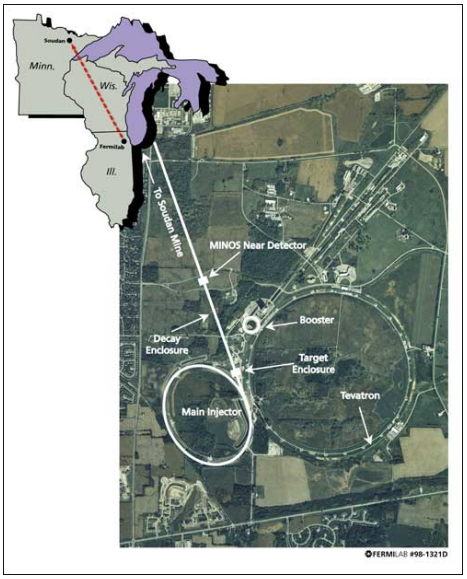

Figure 4.10: *The MINOS control room is on the 12th floor of Wilson Hall at Fermilab. On the right the Main Injector (MI) and Tevatron ring. The MI accelerates protons and sends them to the NuMI target to create neutrinos for the MINOS experiment.*

4.5 Event Topology in the MINOS Detectors

The MINOS detectors are designed to measure Δm^2_{32} and $\sin^2 2\theta_{23}$. This is achieved by looking for a deficit of ν_μ-CC events in the far detector. The signature for this type of event is a μ^- track. As the MINOS detectors are magnetised the μ^- are focused towards the magnetic coil of the detectors (figure 4.13(a)). However, the beam is not pure ν_μ. As part of the NuMI beam 7 % $\overline{\nu}_\mu$ are produced. The $\overline{\nu}_\mu$-CC interaction produces a μ^+. This μ^+ is defocused by the magnetic field, so the track curves away from the coil hole (figure 4.13(b)).The NuMI beam consists of 1.8 % ν_e, which when they interact produce an e, which is identified by a compact electromagnetic shower (figure 4.13(d)). All these neutrinos can interact via the NC interaction, which produces a diffuse shower (figure 4.13(c)).

The MINOS far detector is a compromise between energy resolution and detector mass and cost. It has been designed so that it is very good at identifying μ^- in the range 1 GeV to 30 GeV. Thinner steel in the planes would give better energy resolution at lower energy; however, for the same cost this would reduce the detector mass and so fewer neutrino events would be detected. Having more

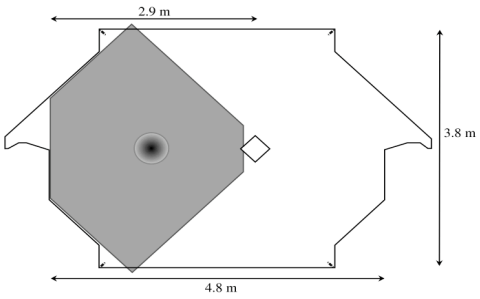

Figure 4.11: The dimensions of a near detector partially instrumented plane. Instrumented region is shown in grey, the beam spot is in black.

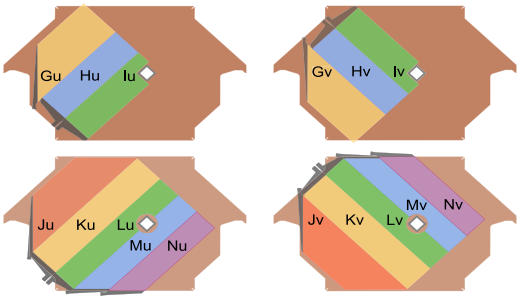

Figure 4.12: *Four different layouts of scintillator modules. The top two U (left) and V (right) are partially instrumented planes. The bottom two are fully instrumented planes. The lettering identifies the different types of module used.*

strips per plane would improve spacial resolution and thus help with the shower shape. The main analysis looks for a deficit of events with tracks at energies below 10 GeV. The peak of the deficit is around 2 GeV; these events produce tracks of about 8 m. Greater energy resolution below 1 GeV would mean that it would be easier to separate tracks from the hadronic shower and thus the oscillation return would be more visible, which in turn would increase the sensitivity to $\sin^2 2\theta_{23}$. However there are few events of this energy in the NuMI beam. For $\overline{\nu}_\mu$ events this is compounded by the fact that the peak energy in the NuMI beam is at a higher energy thus reducing further the benefit of seeing these events. The ν_e analysis would benefit greatly from having thinner planes and less wide strips, as this would allow the shape of the shower to be profiled better, which would assist in the separation of NC events. This would mean that less hard cuts would need to be applied, thereby allowing more events into the signal region. The same argument can also be used for the search for sterile neutrinos via the NC interaction. Better shower shape information would mean that short tracks could be separated out of showers, which would reduce contamination. The MINOS detectors are thus not optimal for searches for ν_e and sterile neutrinos, but well designed for the main ν_μ disappearance analysis.

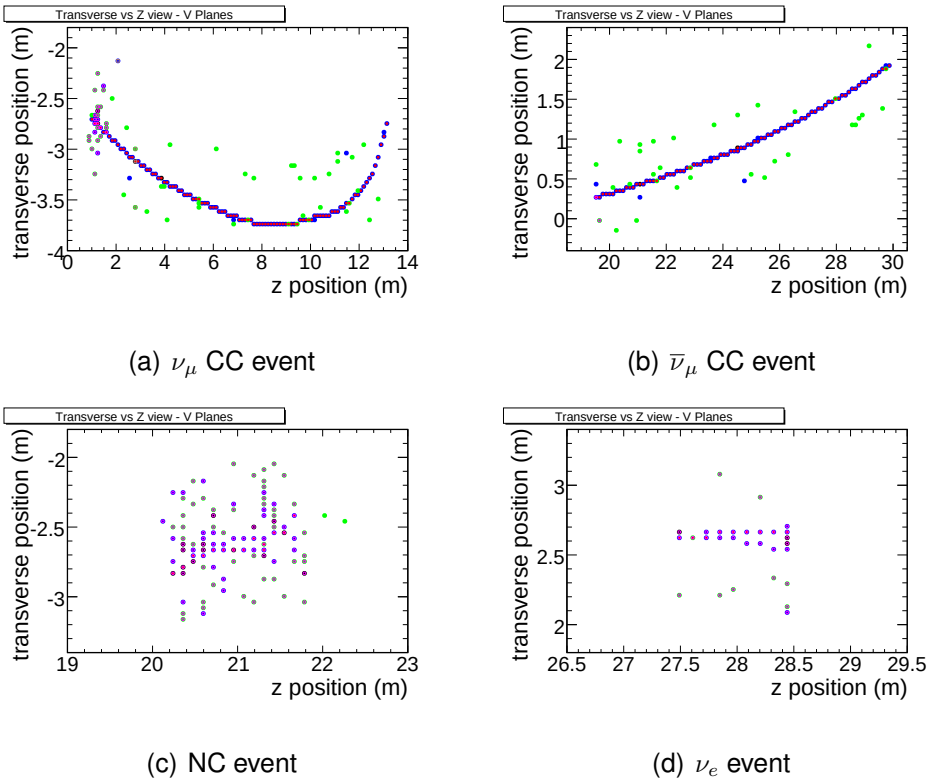

(a) ν_μ CC event

(b) $\overline{\nu}_\mu$ CC event

(c) NC event

(d) ν_e event

Figure 4.13: *How the different beam events look in the MINOS far detector. The ν_μ CC event in a) produces a long track from μ^-, which is focused by the magnetic field towards the coil hole (0 in the U and V planes). The $\overline{\nu}$ CC event in b) produces a long track from μ^+, which is defocused by the magnetic field. The NC events typically produce a diffuse hadronic shower as the only visible signal c). The signature of ν_e-CC events is a compact electromagnetic shower from the e^- created in this interaction.*

4.6 Summary

The MINOS experiment is designed to look for ν_μ disappearance. This is achieved by creating a beam of ν_μ by accelerating protons and colliding them with a graphite target. This beam is directed towards the near and far detectors. These two detectors were designed to be as similar as possible in order to reduce the influence of uncertainties in the neutrino cross-section. However, due to differences in the beam width and event rate at the two detectors they are not identical. The detectors are able to identify μ tracks and determine their energy. They are also able to identify the charge of the μ because the detectors are magnetised; this allows both Δm^2_{32} and $\Delta\overline{m}^2_{32}$ to be determined and thus CPT invariance to be tested

in the neutrino sector. The segmented design also allows the search for sterile neutrinos and ν_e appearance.

Chapter 5

Calibration

> "No, wait a minute. That's gone right up my flagpole, that has, Kryten. I'm saluting that one." (Lister - series 5 Terraform)

This chapter addresses the challenge of calibrating the energy response of two detectors that are underground, separated by 735 km, and of translating the detector response to energy in units of GeV. There is no control source of particles of known energy, and the detectors' environments are different, which could add systematic errors to the energy spectrum. Section 5.1 sets out the reason why it is necessary to calibrate and section 5.2 shows how the calibration is implemented.

Tools used in the MINOS detectors for calibration include the built-in Light Injection (LI) system to measure the gain and the linearity of the response of the PMTs and their electronics; cosmic ray muons are used to determine drift in both detectors' responses, the relative energy scale for the two detectors and for finding interstrip nonuniformities. To determine the absolute energy scale a third smaller calibration detector (CalDet) was built.

Section 5.3 describes a new way of calculating the gains of the PMTs from single-photoelectron spectra, and how they change over time. This method has been used as a cross-check of the gains determined with the LI system.

5.1 Calibration Goals

The main goal of the MINOS experiment is to measure Δm^2_{32} to an accuracy of better than 10 % [90]. MINOS determines the oscillation parameters by studying

ν_μ ($\overline{\nu}_\mu$) disappearance and its energy dependence. Any miscalculation of the ν_μ energy will affect the values assigned to the oscillation parameters. To achieve the required precision in Δm^2_{32} a goal of 2 % relative uncertainty between the detectors and 5 % absolute uncertainty was set. The energy of the neutrino is obtained by adding the muon energy to the shower energy: $E_\nu = E_\mu + E_{shw}$.

The energy of the muon is calculated from a combination of the curvature of the track in the magnetic field and the range in the detector. The calorimetric response of each detector thus does not need to be known very accurately to find the muon's energy, although some calorimetric data is used for rare stochastic energy losses in the muon track. As the MINOS detectors are designed so similarly, a direct range-to-energy conversion can be employed to compare the muon energy between detectors with an error of less than 2 %.

The reconstruction of the shower energy, on the other hand, is achieved by calorimetry, which does require accurate knowledge of the detector response. The calorimetric response of the detector, for an event, is found by summing the amount of light given off by the scintillator strips. However this can vary as a result of: different scintillator strip lengths and light yield; different lengths of WLS and clear fibre; different reflector connectors in the Near Detector; different connector transmission efficiencies; different PMTs and electronics; temperature fluctuations and other time varying processes. All of these effects have to be calibrated out in order to achieve accurate shower energy measurement.

If a detector was not internally calibrated, in time or space, its resolution would degrade, so it would be necessary to collect more events and hence take longer to obtain the same measurement accuracy. Also, if the events are not spread evenly in time or space, this could introduce a bias to the energy spectrum. This in turn would have a direct effect on the measured value of Δm^2_{32}, as the position of the dip in the ratio of the FD spectrum compared to the extrapolated spectrum from the ND would change. Hence a 5 % error was set as the upper limit to minimise the uncertainty in Δm^2_{32} as this would cause the E in equation 2.38 to be wrong. If there was a relative difference between the detectors this would change the position and shape of the dip, and so change $\sin^2 2\theta_{23}$ and Δm^2_{32}. The 2 % error was set so that the change in oscillation parameters would be small compared to

the statistical error, and the shifts on a bin-by-bin basis smaller than the statistical uncertainties, thus keeping the χ^2 small.

5.2 The Calibration Chain

The calibration of the MINOS detectors consists of two branches: the energy branch and the photoelectron branch. The energy branch is a multi-stage process that takes the raw ADC reading $Q_{raw}(s, x, t, d)$ in strip s, position x, time t, and detector d and transforms it into so-called Muon Energy Units (MEUs) (Q_{corr}) by several multiplicative factors, as illustrated in figure 5.1. An MEU is defined as the median response of a scintillator plane to a minimum ionising muon. The photoelectron chain converts ADC units into photoelectron units. This section gives a brief overview of the process and also explains why the gain calculation needed to be checked. A more in-depth review of the chain can be found in [94] and [90]. A raw ADC unit is converted into an MEU by the following operation:

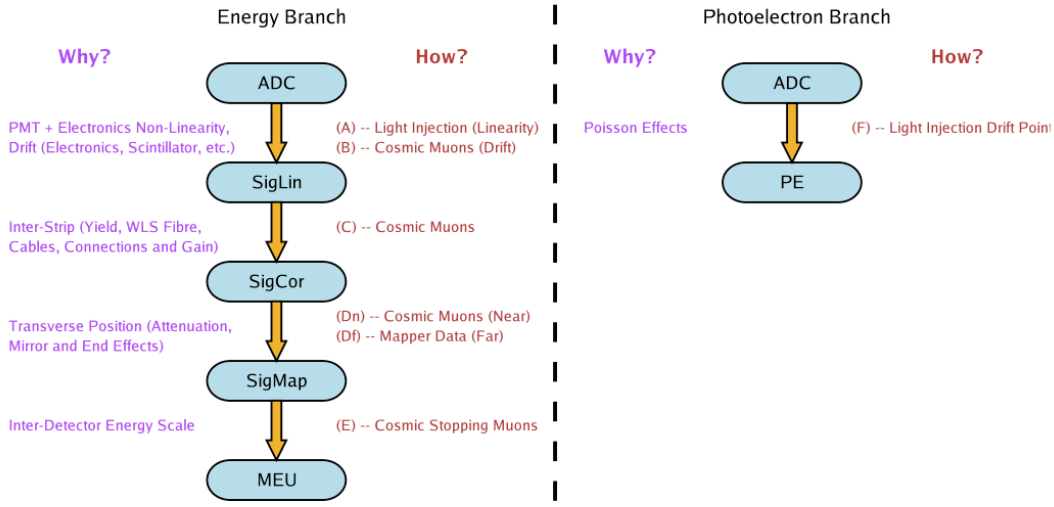

Figure 5.1: *A visual representation of the steps of the calibration chain [95]. The energy branch converts raw ADC counts into calibrated MEU according to equation 5.1. The photoelectron branch converts ADC to p.e. as per equation 5.9.*

$$Q_{corr} = Q_{raw} \times D(d,t) \times L(d,s,Q_{raw}) \times S(d,s,t) \times A(d,s,x) \times M(d), \qquad (5.1)$$

where

D is the drift correction to account for PMT, electronics, and scintillator response changing with temperature and age (section 5.2.2);

L is the function that linearises the response of each channel with pulse-height (section 5.2.3);

S is the strip-to-strip correction that removes differences in response, strip-to-strip and channel-to-channel (section 5.2.4);

A is the attenuation correction, which describes the attenuation of light depending on event position along each strip (section 5.2.5);

M is an overall scale factor that converts corrected pulse height into the same absolute unit for all detectors (section 5.2.6).

However, even after this process all that is known is the ADC response to the scintillator light from a hit. To get the energy of the shower this needs to be converted into GeV (Eq 5.6).

5.2.1 MINOS Calibration Systems

The MINOS calibration system consists of three parts: cosmic ray muons; the LI system; and CalDet.

5.2.1.1 Cosmic Ray Muons

Cosmic ray muons are a vital calibration tool, as they deposit energy at every stage of the readout chain: the light output of the scintillator; the transmission efficiencies of the optical fibres; the gain of the PMTs; and the gain of the electronics. The MINOS detectors are designed to observe muons, which are easy to identify with their long tracks and are well described by the Bethe-Bloch equation 5.2. Thus leaving a well understood energy deposit.

$$-\frac{dE}{dx} = Kz^2\frac{Z}{A}\frac{1}{\beta^2}\left[\frac{1}{2}\ln\frac{2m_ec^2\beta^2\gamma^2T_{max}}{I^2} - \beta^2 - \frac{\delta(\beta\gamma)}{2}\right], \tag{5.2}$$

where T_{max} is the maximum kinetic energy which can be imparted to a free electron in a collision, Z is the atomic number of the absorber, A is the atomic mass of

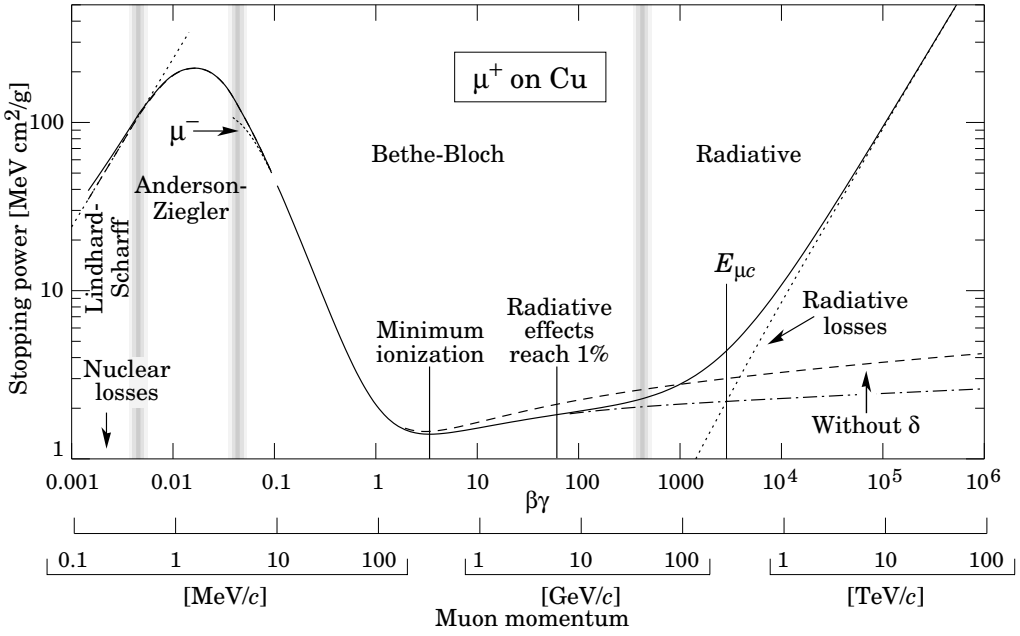

Figure 5.2: *Stopping power for muons in copper as a function of momentum (the stopping power in iron is not much different to copper). The x-axis is in $\beta\gamma$ which is proportional to momentum. The important region for MINOS is between 1 and a few hundred GeV/c, which is quite flat. Figure taken from [11].*

the absorber, z is the charge of incident particle in e, I is the mean excited energy, β is v/c, where v is the particles velocity and c is the speed of light, γ is $1/\sqrt{1-\beta}$ and K is $4\pi N_A r_e^2 m_e c^2$ where N_A is Avagadro's number, r_e is the classical electron radius and $m_e c^2$ is the rest mass of the electron. Figure 5.2 shows the dE/dx of a muon in copper[1]. In order to determine the energy of the muons, the track is found by a pattern-recognition/tracking algorithm. From this the track length in each strip of scintillator can be worked out. The response of the detector is proportional to dE/dx, where dE/dx is the energy loss per unit distance travelled by the muon. Once the track length of the muon is known then the Bethe-Bloch equation is used to calculate the energy deposited in GeV.

[1]MINOS is made from iron which has a similar response to copper. The stopping power of copper is about 3 % lower than for iron, when the μ^+ is minimum ionising $\sim$360 MeV/c. At about 120 GeV/c the stopping power is the same in both, while at high energy energy 100 TeV/c the stopping power of copper is 7 % higher.

5.2.1.2 The Light Injection System

The light-injection system is a hardware based system that is used to check the stability of the PMTs and electronics over time, to map the linearity of the instrumentation and to monitor the optical path. The same-set up was used in the ND, FD and CalDet.

The LI system works by illuminating the WLS fibres embedded in the scintillator strips by ultra-violet (UV) LEDs which are pulsed. The LEDs are housed together in groups of 20 or 40 in "pulser boxes" that reside in racks alongside the detectors. There are 16 pulser boxes at the FD and three at the ND. Each LED illuminates 63 optical fibres simultaneously, which then inject the light into the scintillator modules via light-injection modules (LIMs). These are highly reflective cavities to maximise the amount of light incident on each WLS fibre (figure 5.3) of which there are up to 10 per LIM. The light then takes the same path as the light

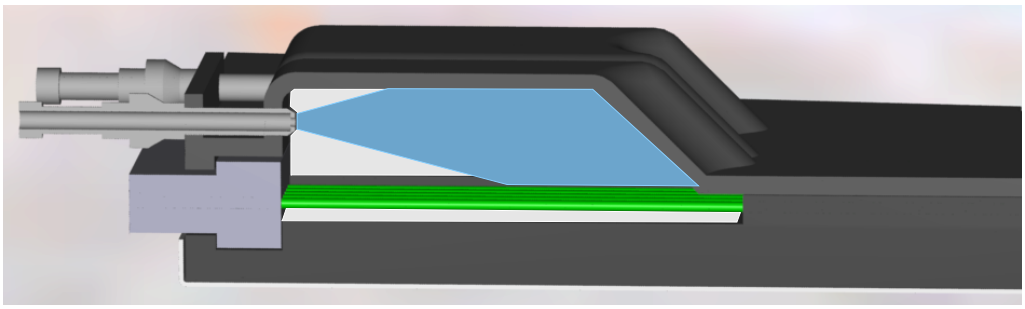

Figure 5.3: *A cutaway of a light-injection module. The green WLS is, at the bottom, and the UV light is injected by the optical fibre from above.*

from the real events to the PMTs, the readout from which is digitised by the FEE. Each strip end is pulsed on average 300 times an hour at the FD, and 1000 times an hour at the ND. The pulses are tuned so that the PMT pixel receives about 50 photoelectrons per pulse.

5.2.1.3 MINOS Calibration Detector

The best way to convert the ADC response into photoelectron (p.e.) counts, would be for a known source of electrons and hadrons to be fired into the ND and FD, but there is no such source. Another way would be to use the decay of the π^0

and reconstruct the invariant mass. However, the steel planes of the MINOS detectors are 1.4 radiation lengths thick, and the scintillator strips are 4.1 cm wide, which leads to poor π^0 identification. We also cannot use stopping μ, as the live time of the electronics at the FD is too short to reconstruct the electron that is emitted from the decay of muons that stop in the detector. In order to address this problem a third, smaller, detector, CalDet, [96] was built to measure the response to individual particles (electrons [97] and hadrons [98]), which were used to tune the MINOS Monte Carlo. This was done by placing CalDet in the PS beamline at CERN and firing various particles of known energy at it. It was made to be as similar to the other detectors as possible; however, the planes were only 2.5 cm thick in CalDet rather than 1" in the ND and FD detectors. This was taken into account in the analysis of the CalDet data. Also, the U and V planes were oriented with the strips running vertically and horizontally rather than at 45°. Both FD and ND electronics were attached to CalDet to check for differences due to the electronics and allow these to be modelled correctly [99].

5.2.2 Drift Calibration

The responses of the scintillator, WLS fibres, PMTs and electronics are not constant over time. This means that as the inter-detector calibration is carried out only once for each detector and run (which covers many months), the energy response calculated is not applicable to the whole data set. A drift in detector response over the run means that none of the energy scale factors are correct, thus degrading the energy resolution. A time-dependent calibration is needed to correct for this. As long as the flux of cosmic-ray muons is constant over time, they provide a good handle to test the whole of the readout system. As the two detectors are at different depths (different overburdens) and different latitudes (different geo-magnetic fields) the through-going muons have different energies ($\sim$ 55 GeV at the ND and $\sim$ 200 GeV at the FD), and different rates ($\sim$ 10 Hz and $\sim$ 0.5 Hz). Although these are different between the detectors they are constant at each detector, and can to be used as a "standard candle":

$$D(d,t) = \frac{\text{Median response}(d,t_0)}{\text{Median response}(d,t)}. \tag{5.3}$$

It takes many months to accumulate enough muons to get the error down to the percent level for individual strips, as the rate is $\sim$500 per strip per month in the FD. However, it is possible to average the whole FD to the 1 % level on the time scale of a day, and shorter for the ND. A more in-depth review of the cosmic-ray muon drift technique is given in [87].

5.2.3 Linearity Calibration

The LI system is used to correct the non-linearity of the PMT response. It is shown in [100, 101] that the PMTs are 5 – 10 % non-linear at light levels of $\mathcal{O}(100)$ p.e. The FD electronics are non-linear at a similar level. Hence, the PMTs and electronics are linearised at the same time. To achieve this, special LI runs are performed every month, where each strip end is flashed 1000 times at various light levels from a few to hundreds of p.e. The correction applied to the FD uses the double-ended readout of the FD scintillator strips, where the average response of the PMT on the far side (which is lower in light-level and thus linear) is taken to correct for the near side PMT.

In the ND, the non-linearity affects low p.e. levels as well. Also, it only has one-sided readout. Hence the method used at the FD cannot be used here. It is shown in [102] that a quadratic equation can be used to correct for non-linearity in the ND.

5.2.4 Strip-to-Strip Calibration

The strip-to-strip calibration takes account of the different responses of each strip end and its readout channel upstream of the photodetectors. These differences come about from differences in the scintillator light output, the WLS fibre light collection efficiency, the transmission efficiency and the PMT gains and quantum efficiencies. As cosmic ray muons take a variety of paths through the detectors, corrections are applied to each hit, such that the mean response is calculated as if the muon travelled horizontally and through the centre of the strip. The number of ADC counts from the muon are used to characterise the response of the readout

channel. This is then corrected to give a uniform response across the detector:

$$S(s,d,t) = \frac{\text{Mean Response of Detector}(d,t)}{\text{Mean Response of the Strip End}(s,d,t)}. \quad (5.4)$$

A more detailed description of the method is given in [103].

5.2.5 Wave Length Shifting Fibre Attenuation

The attenuation in the WLS was determined before the detectors were built. A radioactive source was scanned along each length of scintillator module before it was used in the construction of the detectors. The data from each strip was fitted to a double-exponential

$$A(x) = A_1 e^{-x/L_1} + A_2 e^{-x/L_2} \quad (5.5)$$

where x is the length along the strip, and L_1, and L_2 stand for two attenuation lengths. First the position of the hit along the strip must be determined from the three-dimensional reconstruction, and then the attenuation is applied. The attenuation can make a difference of up to a factor of 5 between the ends of the 8 m strips; however, the rms difference between strips and the average strip is 4%. This has been verified with cosmic ray muons.

5.2.6 Relative Calibration

The inter-detector calibration utilises the fact that the detectors are designed to be as similar as possible, so that muons that stop in each detector will have similar energies. However, the uncertainties in the construction of the detectors means that we cannot use the range of the stopping muon, as the relative accuracy between detectors is about 2 %, but the relative calibration has to be better than 2 %. Instead the "Track Window Technique" [94] was developed. In this, rather than considering the end point of the muon track, one looks at a segment where the muon energy is between 0.5 and 1.1 GeV. This is because the dE/dx of a 1.5 GeV muon increases by a factor of two in the last 10 % of the track, while in the other 90 % of the track the dE/dx changes by only 8 %. 0.0 – 0.5 GeV is discarded in order to avoid the rapid increase in ionisation at the end of the track.

Using the 0.5 – 1.1 GeV part of the track where the dE/dx varies slowly, the 2 % uncertainty in position of the track end-point translates into an approximate 0.2 % error in the energy deposition. The MEU number for each detector is calculated by:

$$\text{MEU} = \text{Median}\left(\left(\frac{1}{\text{N}_\text{p}}\sum_{i=1}^{\text{N}_\text{p}}\frac{S_i}{L_i}\right)_1, \cdots, \left(\frac{1}{\text{N}_\text{p}}\sum_{i=1}^{\text{N}_\text{p}}\frac{S_i}{L_i}\right)_\text{N}\right), \tag{5.6}$$

where S_i is the total detector response in plane i; L_i is the path length through the plane (defined as $\frac{1}{\cos(\theta_z)}$; where θ_z is the angle subtended wrt z-axis); N_p is the number of planes in the track window and N is the number of cosmic muons.

5.2.7 PMT Gain Calibration

The photoelectron branch of the calibration chain is used to calibrate out the gain of the PMTs, which is important for the rejection of cross-talk and for calculations that require a zero-correction procedure. Minimum ionising particles (MIP), such as muons, produce on average between 10 and 20 photons[2] in a MINOS scintillator strip. The photons are attenuated and lost in the transportation to the PMT, so the number of photoelectrons being created at the PMT cathode is low. Cross-talk is typically caused by a photoelectron falling into the wrong dynode chain, which is a result of using multi-anode (MA) PMTs. This mechanism for cross-talk normally takes place at the single-photoelectron (s.p.e.) level, so knowing the gain of the PMT helps with the cross-talk rejection whilst retaining track signals.

A zero-correction is required to adjust the signal of the PMT due to its Poisson nature. At low light levels there is a possibility that no photoelectron is produced when light hits the PMT. As a result, when generating the average response of a scintillator strip such as the muon energy distributions for strip to strip calibration (section 5.2.4), these zero hits need to be accounted for when a signal is generated. For this, the relationship between the ADC and p.e. must be determined.

The calibration of gains is necessitated by the use of multianode PMTs, which have only one high voltage setting per PMT. This leads to a spread in gains on a single PMT of between 15 and 25 % (the M64 PMT); this needs to be calibrated

[2] 50 – 200 for high-energy showers.

out. If single-anode PMTs were used then the high voltage setting could be adjusted in order to obtain uniform gains.

Four techniques for finding the gain have been studied in [104] and [105]. The most robust technique was found to be using the LI system and photoelectron counting. The gain of a PMT is defined as:

$$g = \frac{\mu}{N_{pe} \times e}, \tag{5.7}$$

where g is the gain, μ is the mean charge of repeated light injections, N_{pe} is the number of photoelectrons and e is the charge of the electron. The variance on the average charge is given by:

$$\sigma^2 = \left(\sqrt{N_{pe}} ge\right) + \left(\sqrt{N_{pe}} gew\right)^2 + (\sigma_{ped})^2, \tag{5.8}$$

where w is the fractional width of the s.p.e. spectrum and σ_{ped} is the RMS of the pedestal. The width of the peak is caused by the varying response of the first dynode when being struck by multiple p.e. It can produce a higher or lower secondary number of p.e. than average; therefore one must include the second term, which is dependent on the $\sqrt{N_{pe}}$ in equation 5.8. Rearranging equation 5.8 gives the number of p.e.:

$$N_{pe} = \frac{\mu^2}{\sigma^2 - \sigma^2_{ped}} \times (1 + w^2); \tag{5.9}$$

inserting this into equation 5.7 yeilds the gain

$$g = \frac{1}{\frac{\mu^2}{\sigma^2 - \sigma^2_{ped}} \times (1 + w^2) \times e}. \tag{5.10}$$

The value of w was defined before installation [100], which gave a value of 50 % to w, and verified after installation with low light level flashing of the LED system [105]. A special pedestal run gives the pedestal values. This leaves only μ and σ values in equation 5.10 to be determined with the LI system. This is done by interspersing LI sequences in the normal data taking every two (ND) or three (FD) hours. The LI data are then used to work out the average gains over three day period. A gain increase of 4 % per year has been observed in both detectors [90].

5.3 Gain Calibration with single-photoelectrons

It was found for the first MINOS beam result that the drift in the ND and FD was flat through the first year of running [106]. It was also found that the gain of the PMTs had changed by about 3 %. For this to happen this would mean that the scintillator response was degrading at the same rate as the PMTs' response was increasing. This was within the design studies [107], but was very fortunate. It is not possible to check the scintillator degradation directly in situ, so an alternative method was needed to check that the PMT gains calculated with the method described in section 5.2.7 are correct. One way to do this would be to inject one photon at a time using the LI system and use equation 5.10 to determine the gain. However, it would take a long time to collect the data required, furthermore a completely independent check would carry more weight. There are naturally occurring backgrounds that appear with 1 pe; these are normally discarded in the data-taking process, but may be used to check the PMT gains.

5.3.1 Sources of single-photoelectrons

Each PMT has a background noise rate of 4 – 6.5 kHz. The noise consists mainly of single-photoelectrons, which come principally from three sources:

- **Radioactivity** – This is the natural radioactivity from the rocks in the Soudan mine. It was studied before the building of the Soudan 2 detector in the mid 1980s. The concentration of long-lived radioactive isotopes ^{238}U, ^{232}Th and ^{40}K, which produce a constant flux of γ and β particles that reach the detector, was measured. The resulting concentrations were put into MC to determine the spectrum of these particles coming from the the rock face. These decays also produce ^{222}Rn which escape into the hall and get into the air gaps between the planes. ^{222}Rn has a half-life of 3.8 days. The decay of radon deposits energy directly into the scintillator so is monitored constantly. The detector itself also has radioactive impurities which were studied during the building of each component, the main source being the aluminium cover of each scintillator module. Radioactivity produces an average of 2.5 photoelectrons with a rate of 1.2 kHz per strip;

- **Dark noise** – This is defined as an integrated charge larger than $\frac{1}{3}$ of a single p.e., when the anode records a signal and no input light is present. Thermal emission of electrons from the photo-cathode is the main cause of dark noise. This effect was extensively studied and found to occur at a rate between 350 Hz and 950 Hz per PMT, with an average of 500 Hz per plane side;

- **WLS fibre noise** – This background was unexpected. There is a signal of a single p.e. from the WLS fibre of 1.8 kHz to 4.8 kHz which is due to long-term relaxation of the fibre. The rate is proportional to the temperature.

In normal data-taking these single-photon events, if read out, would induce unacceptable dead-time in the detector. The 2 out of 36 [3] trigger discriminates against single photons, whilst keeping physics recording unaffected, by requiring two channels on a VA readout card (VARC) to be hit within 400 ns of each other. In this study, however, it was precisely these events that were needed. They had to be recorded with special data-taking runs when there was no beam. This limited the data-taking opportunities to only a few occasions. This was not a problem, however, as the s.p.e. method was not used to correct the data on a daily basis but only to check long-term gain stability.

5.3.2 Data Collection

Due to the differences between the near and far detector electronics, the data for this study were collected in different ways for the two detectors. Sparsified data were taken for both; this simply means that events in the pedestal were not read out. This reduces the amount of data that the DAQ is required to handle without significantly affecting the charge distribution proper. Due to the continuos readout at the near detector, the dynode trigger was set to 700 ADC[4]. In the far detector a PMT pixel that is hit is dead for 5 μs afterwards, which splits up the

[3] There are 36 PMTs on a VARC

[4] As there is continuous readout at the near detector a way of splitting the events is needed. The dynode trigger is set so that when the activity is below the set level no charge is recorded. In normal data taking it is set to 1024 ADCs, in this analysis it is set lower to include more low energy events.

events naturally. In the FD the runs were 512 s long and yielded $\mathcal{O}$ (10^5) hits. As the ND is smaller and not multiplexed, the event rate is lower, so the runs were longer, so required 1000 s to yield a similar number of hits.

5.3.3 Fitting the Data

Equation 5.7 shows that the gain is equal to the mean of the single-photoelectron peak. To find the single p.e. peak, several Gaussian distributions are fitted to the charge distribution of a readout channel. The Gaussian fit is centred on one bin of the histogram and covers $\pm$30 % of the central value of the bin, either side of the bin. Each bin from 0 to 300 ADCs is covered in this way. Each mean of each fit is then added to another histogram, with the same binning as the charge distribution (figure 5.4(b)). If the bin with the highest number of mean values is more than double the next highest value, the centre of this bin is taken as the centre of a new Gaussian fit of the charge distribution spectrum. If it is less than double the channel is not fitted. The Gaussian distribution is fitted to $\pm$30 % of this new centre value (figure 5.4(a)). This method achieves a constant value for the s.p.e. peak quickly, so can process many channels without intervention. However, this method ignores the higher p.e. peaks and the pedestal by only fitting to $\pm$30 %, so does not give any further information about the PMT.

5.3.3.1 Justification of Fit Method

Various binnings of the spectrum and ranges of the fit were considered. The fit was optimised to give results as close to the LI as possible for the FD data taken on the 25^{th} June 2007, although some optimisation was made for the ND on the data taken on the 6^{th} June 2008. One date was chosen to optimise in order to get a start value as close as possible for the s.p.e. fit gain and the database gain. The full range of the spectrum could not be used to fit a Gaussian distribution to, as there are peaks associated with two and higher p.e. hits as well as the s.p.e. peak, which pull the mean fit higher. These higher peaks would vary at a different rate to the s.p.e. peak and thus introduce uncertainty to the drift calculation. To counter this only part of the spectrum was fitted. Spectra that have a higher s.p.e. peak

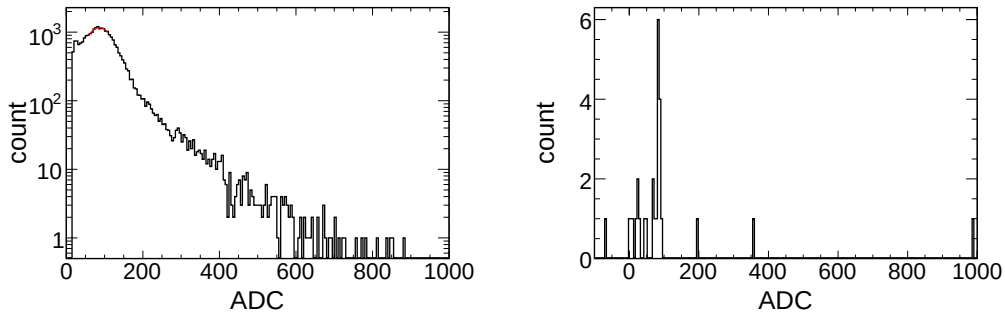

(a) (b)

Figure 5.4: *a) An example of a channel with its final Gaussian fit. The gain is 64.92. b) An example of the distribution of the mean values found by sweeping across the spectrum to find the s.p.e. peak. As the bin with highest frequency is at 64 ADC the final fit (that is shown in figure 5.4(a)) is then centred there on the spectrum and the fit values are found.*

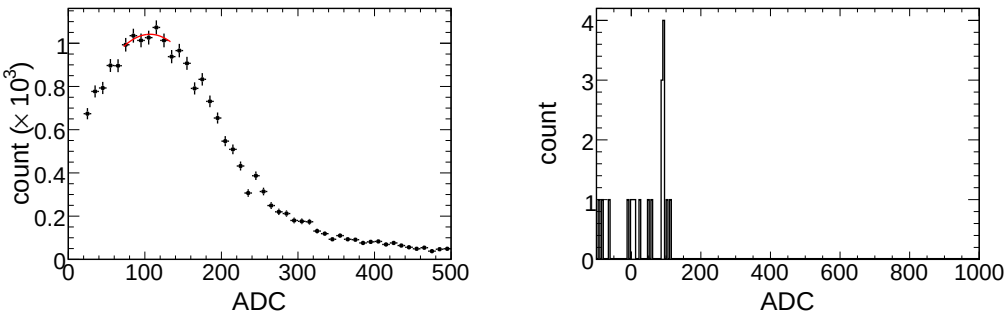

(a) (b)

Figure 5.5: *An example of a good ND channel: a) The fitted spectrum b) histogram of means from sweeping the spectrum.*

have a wider distribution than spectra that have a lower s.p.e. peak value. For this reason, a percentage of where the mean was thought to be was fitted rather than a fixed range. The figure of merit used to distinguish between the methods was to fit a Gaussian distribution to a histogram of (s.p.e.-LI)/(0.5(s.p.e.+LI) and then take the RMS, which is called spread. Table 5.1 shows that 30 % coverage of the central bin value had least spread.

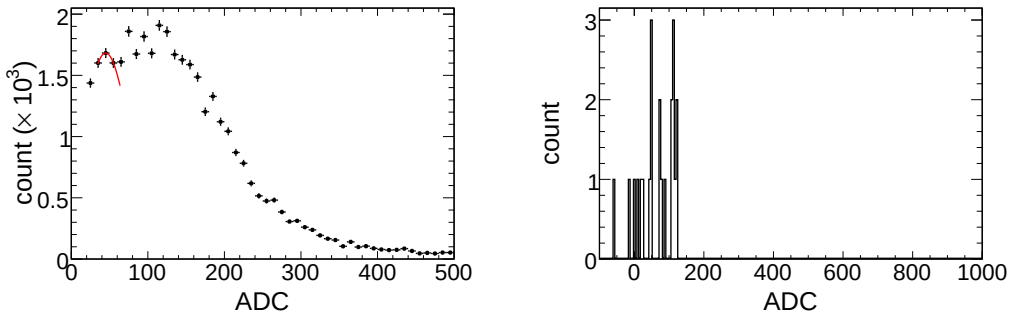

(a) (b)

Figure 5.6: *An example of a rejected ND channel: a) The fitted spectrum b) histogram of means from sweeping the spectrum.*

To find the peak of the spectrum a sweep across the spectrum up to 300 adc, centring on all the bins fitting a Gaussian distribution, and the means of these distributions, were added to a histogram. The median and mode value of this histogram was used to find the centre of the main fit. Table 5.1 shows that the mode had less spread. The width of the s.p.e. peak should not be wider than the mean value of the s.p.e. peak. This made the spread value slightly worse, but made the fit more stable between runs. Table 5.1 shows that the finer the bins used to find the s.p.e. peak the lower the spread value, however, enough statistics need to be acquired with each PMT in each run to make a fit. Five adc counts per bin was chosen for the FD as in later runs not quite enough data was taken for fits to all channels. The final requirement was that the channel had to be good for all dates that were taken. This final requirement tightens the spread in both the ND and FD The fit that was found to work best in the FD was used for the ND. However, some optimisation took place (table 5.2). Ten adc counts per bin, rather than five adc counts per bin, was found to give a lower spread of values due to

Type of fit in FD	Fixed slope	Free slope	Bias	Spread	Number of entrees
Median R30 bin 5	0.999	1.156	0.024	0.0779	3600
Mode R30 bin 5	0.985	1.044	-0.000	0.0609	3600
Mode R20 bin 5	0.974	1.015	0.020	0.0801	3600
Mode R60 bin 5	0.979	1.030	-0.008	0.0634	3600
Mode R30 bin 5 fw	0.984	1.046	0.001	0.0626	3600
Mode R30 bin 2 fw	0.990	1.125	0.000	0.0614	3600
Mode R30 bin 10 fw	0.972	1.053	0.026	0.0774	3600
Mode R30 bin 5 fw height	0.983	1.046	0.001	0.0626	3600
Mode R30 bin 5 fw height all sets		1.100	0.002	0.0542	1501

Table 5.1: *The slope of the profile of the 2D histogram between the s.p.e. gain and the gain found by the LI system in the FD for data taken on the 22/06/2007 (Figure 5.9(a)). The type of fit is described by whether the peak was found by using the median of fits in the first sweep or the mode, and how many adc counts were included in each bin. fw is the Gaussian distribution width has to be less than the found mean of the fitted Gaussian distribution and height is when the mode bin in the first sweep is 100 % more than the next highest bin. The second column shows the value the fit if the profile of the 2D histogram is forced through 0. The third column shows the value if the fit of the profile of the 2D histogram is allowed to float. The bias is the mean of the Gaussian distribution fitted to the distribution (s.p.e.-LI)/(0.5*(s.p.e.+LI)) and the fourth column shows the RMS of the Gaussian distribution (figure 5.9(c)). The lowest spread was chosen for the fit. However, due to limited statistics of later runs the 5 adc counts per bin was used.*

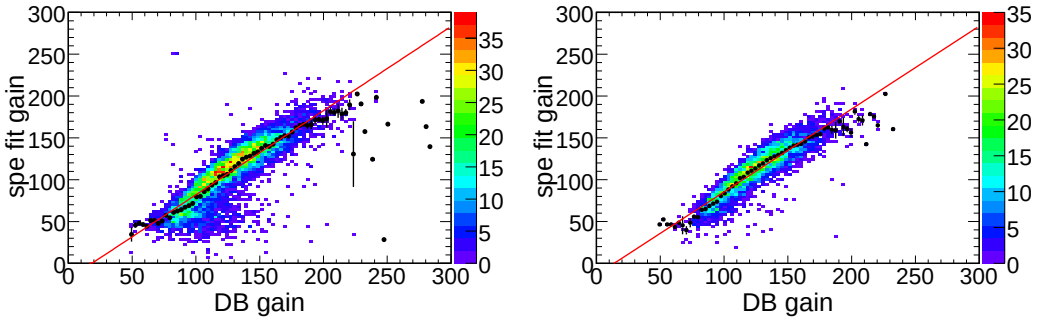

(a) (b)

Figure 5.7: *2D histogram comparing the s.p.e. gain to the LI system gain for the ND. a) Without the requirement that the mode has to be twice the value of the next highest bin. b) With the requirement the mode has to be twice the value the next highest bin. It can be seen that this extra cut cleans up many of the points where the s.p.e gain is low compared to that of the LI system.*

fewer statistics in the ND run. Figure 5.7 shows that there are many PMTs that have low gain for the s.p.e. method. This only affected the ND as the PMTs have a continuos readout, and thus affected by where the trigger is set to separate hits. A trigger level had to be set to distinguish between events which meant on some distributions the peak value was cut so the peak was not clear. To over come this an additional requirement that the bin with the highest number of mean values found had to be 100 % larger than the next highest bin. Figure 5.5 shows a ND channel that meet all requirements. Figure 5.6 show a spectrum that failed the requirement that the mode of the means be 100 % the next highest value. In the far detector this requirement had no effect.

Type of fit in ND	Fixed slope	Free slope	Bias	Spread	Number of entrees
Mode R30 bin 10 fw	0.811	0.861	0.082	0.2251	8012
Mode R30 bin 10 fw height	0.861	0.904	-0.106	0.1084	3341
Mode R30 bin 5 fw height	0.868	0.893	-0.070	0.1305	1454
Mode R30 bin 10 fw height in both sets	0.854	0.886	-0.118	0.1021	1695

Table 5.2: *The slope of the profile of the 2D histogram between the s.p.e. gain and the gain found by the LI system in the ND for data taken on the 06/06/2008. In the ND the mode and 30 % range was used from the FD and the width was limited to less than the mean value of the peak. Ten and five adc counts were included in each bin. Height is when the mode bin in the first sweep is 100 % more than the next highest bin. The second column shows the value of the fit of the profile of the 2D histogram when the fit is forced through 0. The third column shows the value of the fit of the profile of the 2D histogram when the fit is allowed to float. The Bias is the mean of the Gaussian distribution fitted to the distribution (s.p.e.-LI)/(0.5*(s.p.e.+LI)) and the fourth column shows the RMS of the Gaussian distribution (figure 5.9(d)). The fit method with the lowest spread was chosen for the fit.*

5.3.3.2 Other Fit Methods

Another fit was also considered that was used in [101]:

$$f(x) = Ne^{-\lambda}\frac{1}{\sqrt{2\pi}\sigma_{\text{ped}}}e^{-(x-x_{\text{ped}})^2/2\sigma_{\text{ped}}^2} + N(1-d_f) \times \sum_{n=1}^{n=12}\frac{e^{-\lambda}\lambda^n}{n!}\frac{e^{-(x-x_{\text{ped}}-nx_{\text{pe}})^2/2(\sigma_{\text{ped}}^2+n\sigma_{\text{pe}}^2)}}{\sqrt{2\pi(\sigma_{\text{ped}}^2+n\sigma_{\text{pe}}^2)}} + Nd_f(1-e^{-\lambda})\frac{e^{-\frac{(x-x_{\text{ped}}-x_{\text{pe}}/d_s)^2}{2(\sigma_{\text{ped}}^2+\sigma_{\text{pe}}^2/d_s^2)}}}{\sqrt{2\pi(\sigma_{\text{ped}}^2+\sigma_{\text{pe}}^2/d_s^2)}}, \quad (5.11)$$

where x_{ped} is the pedestal mean, σ_{ped} is the pedestal width, λ is the light level (mean number of photoelectrons), x_{pe} is the mean of the s.p.e., σ_{pe} is the width of the s.p.e. peak width, d_f is the fraction of pulses that miss the first dynode and then strike the second dynode first and d_s is the dynode scale (the amount of multiplication they miss). Figure 5.8 shows a result of the fit. The pedestal was fitted separately to help with fitting speed. This method has the advantage of taking account of the Poisson nature of the s.p.e.. However, this method requires the pedestal to be present, which complicates the taking of the data. Also the function takes a lot of computer processing to come to a fit, which often depends on the start values. To decide which of the fits is correct requires human intervention.

5.3.4 Light Injection Gains

Section 5.2.7 explains how the gains are calculated via the light injection system for each strip in the detector. However, in the FD eight strips are read out by one pixel. To compare the gains of the LI system and the gains via the s.p.e. fit, the gains from the strips on one pixel were averaged. In the ND one pixel reads out one strip, so the gains can be compared directly.

5.3.5 Comparison of Light Injection Gain to single-photoelectrons Gain

For the far detector three sets of data, on three different dates, were taken for the single-photoelectron fit (22/06/07, 21/02/08, 28/04/09), which cover 670 days.

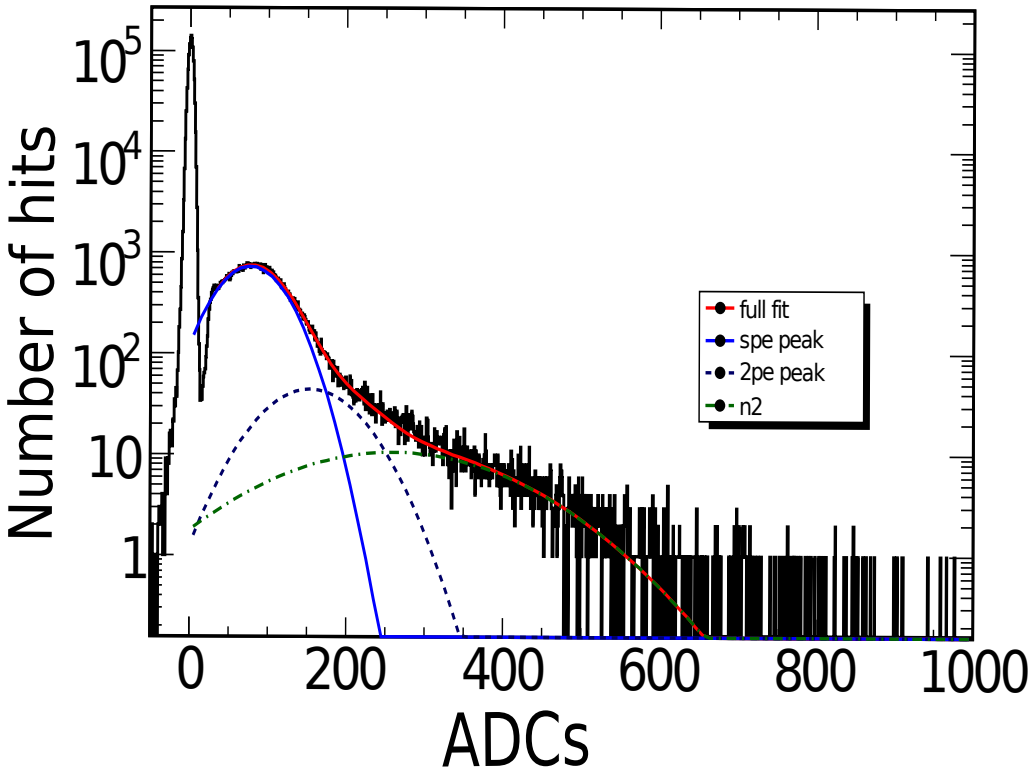

Figure 5.8: *An example of a single-photoelectron charge distribution with the fit given by function 5.11. The pedestal is fitted separately. The x axis is in units of ADC counts. The fit consists of Gaussian distributions weighted by Poisson statistics. Also shown are the first and second p.e. peaks and a term to describe when a photon passes through the photocathode and produces an electron.*

Date taken	DB	DB error	Fit	Fit error	Ratio	Ratio error
25 Jun 07	79.81	0.89	79.09	1.06	1.009	0.030
21 Feb 08	81.05	0.94	80.17	0.40	1.011	0.020
24 Apr 09	82.41	0.97	81.40	0.65	1.012	0.023

Table 5.3: *The gains for the FD, in the database from the LI system and the gains found by the fit to the s.p.e. spectrum in the far detector. It can be seen that they agree to within errors.*

Date taken	DB	DB error	Fit	Fit error	Ratio	Ratio error
6 Jun 08	121.94	1.63	103.80	4.30	1.175	0.087
11 Sep 09	126.55	1.03	112.15	1.72	1.128	0.029

Table 5.4: *The gains for the ND, in the database from the LI system and the gains found by the fit to the s.p.e. in the near detector. It can be seen that they agree to within errors.*

For the near detector only two such datasets were taken and fitted (06/06/08, 10/09/09) covering 461 days. Figure 5.9 shows the gains from the s.p.e. fit method vs. the gains in the database, for each of the two detectors. This shows that the two methods agree well in the FD: there is only a narrow spread of values and the projection of the means in the 2D histogram lies along the best fit line. However, in the ND there is a large spread between the fit gain value and the LI gain value. A projection of the mean value of all the fit values corresponding to a given database gain, shows some structure as these values do not follow that best fit line (figure 5.9(b)). The low gain discrepancy could be coursed by trigger or sparsification efficiencies from crudeness in the electronics. The structure above 110 ADC is likely to be caused from nonlinearity effects that are handled differently between the two methods.

In order investigate whether the gain changes over time by the same amount between the datasets, the mean of the gain values for all channels that were included, in both the database and s.p.e. fit method was calculated for each dataset. Table 5.3 shows that in the FD the two method are in agreement with

each other, while table 5.4 shows that in the ND the database gains found by the LI are consistently higher. This is not unexpected as in the FD there is dead time after every time a PMT records an event, in the ND there is continuous readout so a trigger is set on the number of ADCs. Due to time restraints in taking the data this was not optimised for this investigation. Figure 5.10 gives a graphical representation of these tables.

5.4 Summary

To find Δm^2_{32} and $\sin^2 2\theta_{23}$ the energy of the interacting particles must be known to high precision. The MINOS detectors have been calibrated with cosmic muons, and the built-in light injection system. These systems ensure that the detectors respond in the same way no matter where the interaction happens within them, and also that the response is the same between detectors throughout the running period. The relationship between the response of the detectors and different particles was investigated with the calibration detector. When the first MINOS beam ν_μ-CC result was released [82] the total response remained the same through time. In order to check that the formula that uses high-intensity light from the LI system to find the gains of the PMTs was correct, the single-photoelectron peak was determined from using data from natural s.p.e. scintillation from the detector. This s.p.e. method agreed with the LI method for the far detector. Due to inefficiencies at low light levels for the M64 the methods do not agree for the ND. It needs further investigation to determine whether the change by gain is the same in the two methods. This would be achieved by taking a further high statistics data run in the future.

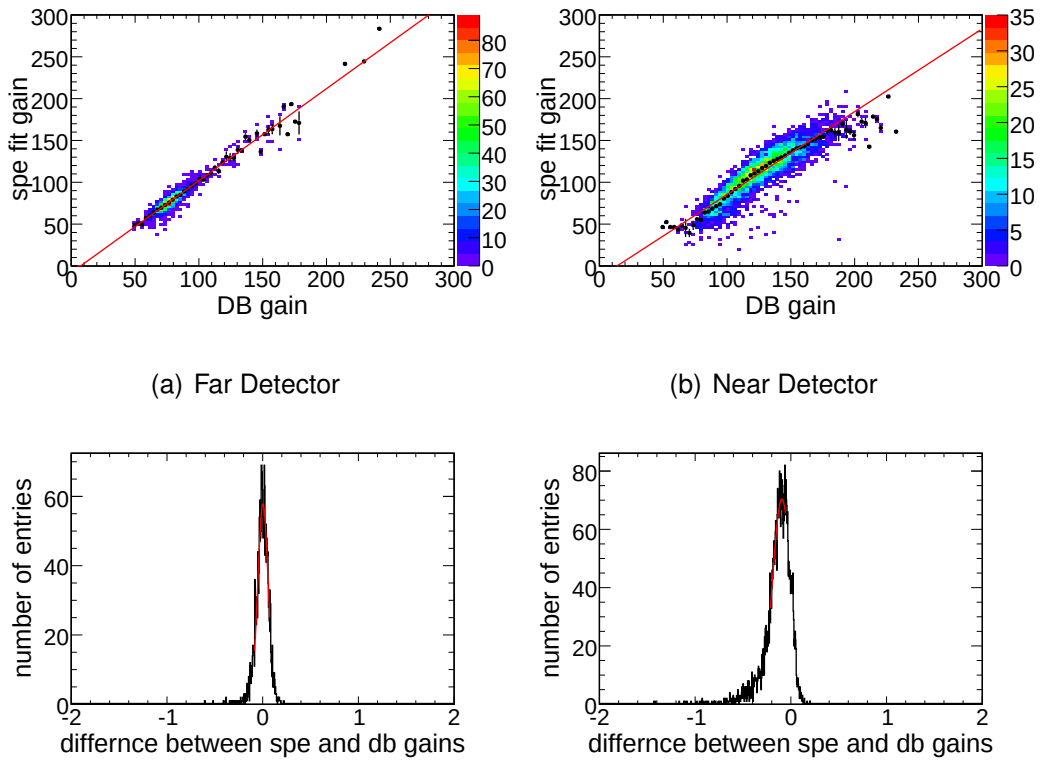

(a) Far Detector

(b) Near Detector

(c) Far Detector spread

(d) Near Detector spread

Figure 5.9: *A comparison of the gains found by the s.p.e. and the LI methods. a) The FD entries have a narrow spread around a straight line. The profile points of the 2D histogram are aligned on the best fit line. b) The ND has a larger spread between the gains found by the two methods. There is also some structure to the distribution of the majority of the points which depends on the gain. c) Shows the distribution of difference in gains between the two methods for the FD. The histogram is centred around zero and has a narrow width, which shows good agreement between the two methods. The red curve is a Gaussian fit made to the data. d) The histogram difference in gains for the ND is offset from zero which shows that the two methods are not in agreement. The broadness of the histogram shows that there is more than just an offset between the two methods. This broadness maybe caused by the inefficiencies in the electronics at low light level.*

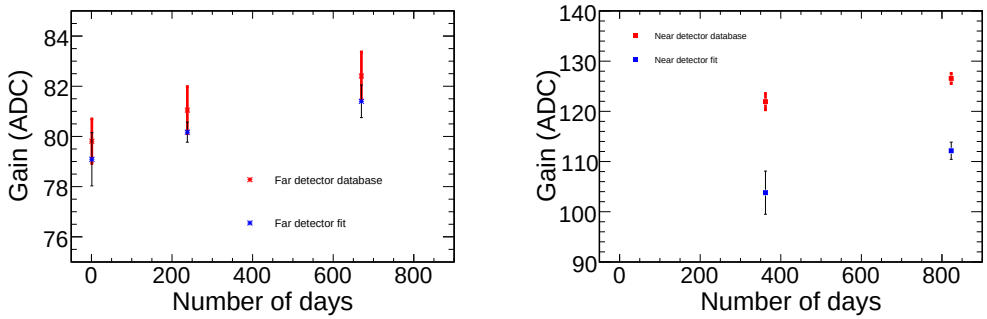

(a) Far Detector

(b) Near Detector

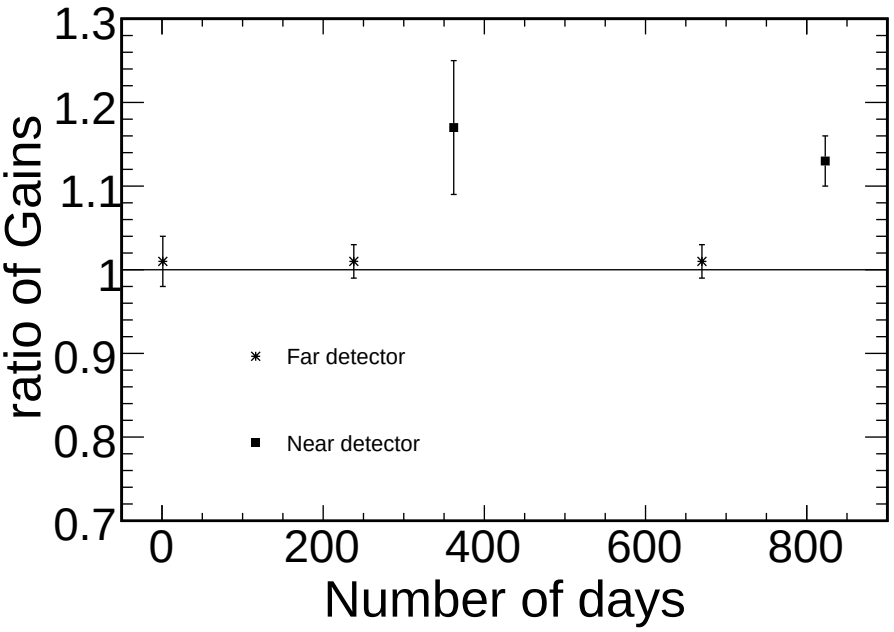

(c) Ratio

Figure 5.10: *Gains from the database and the s.p.e. fit as a function of time. a) It can be seen that the far detector values agree to within errors. b) The near detectors points are quite different for each method. c) It can be seen in the ratio of gains that all points for a given detector are consistent with each other. The ND point on 362 days has large error bars due to lack of statistics in the fit data set.*

Chapter 6

MINOS Analyses

> "All in all, a 100 % successful trip!"
>
> "But, sir, we lost Mr. Rimmer, sir."
>
> "All in all, a 100 % successful trip!" (Cat, Kryten - series 6 Rimmerworld)

The MINOS detectors were designed to make the most precise measurement of Δm^2_{32} and the experiment now has the world-leading result along with the best measurement of $\sin^2 2\theta_{23}$ of a man-made neutrino beam ($\Delta m^2_{32} = 2.43^{+0.13}_{-0.13} \times 10^{-3}$ eV at 68 % C.L., $\sin^2 2\theta_{23} > 0.90$ at 90 % C.L.; see section 6.1). MINOS has also made world-leading, or very competitive, measurements on a range of other topics. It has been able to set a limit on the fraction of ν_μ changing to a sterile neutrino, and it has found no evidence for more than three active neutrino flavours (section 6.2). It has also released results on the measurement of the as yet unmeasured third mixing angle (section 6.3) which suggest a non-zero value for θ_{13}. MINOS has also been able to check CPT invariance by checking that $\Delta\overline{m}^2_{32}$, $\sin^2 2\overline{\theta}_{23}$ are the same as Δm^2_{32}, $\sin^2 2\theta_{23}$ (section 6.4). This chapter gives an overview of beam oscillation results; however, the MINOS detectors have also been used to make a range of other measurements: MINOS has measured the velocity of the neutrinos and thus put limits on its mass [108]. It has also taken data with the far detector that have shed new light on the charge ratio of K and π production at TeV energies by cosmic rays [109]. Furthermore, it has also been used to measure atmospheric temperature change over northern

Minnesota [110]. In addition, MINOS has been able to make a measurement of Δm^2_{32} from atmospheric neutrinos in the far detector and to measure the difference between ν_μ and $\overline{\nu}_\mu$ disappearance and thus able to place a limit on CPT violation in the lepton sector. Data from the near detector has been used to set a limit on Lorentz violation [111] and to make various neutrino cross-section measurements.

6.1 The MINOS Charged Current ν_μ Analysis

The ν_μ-CC analysis is that for which the MINOS detectors were built, namely the measurements of Δm^2_{32} and $\sin^2 2\theta_{23}$. In order to measure these parameters, the energy spectrum of data events in the far detector is compared to a predicted spectrum. This is obtained by extrapolating to the far detector the spectrum measured in the near detector. This relative measurement utilises the two detectors, thus reducing the error from unknown ν cross-sections. A dip in the ratio between the data spectrum and the predicted spectrum provide the values for the oscillation parameters: the depth of the dip gives $\sin^2 2\theta_{23}$; the energy of the dip gives Δm^2_{32} by

$$\frac{E[\,\text{GeV}]}{1.27 \times 735[\,\text{km}]} \simeq \Delta m^2_{32}. \tag{6.1}$$

The latest MINOS result [1] constrains the oscillation parameters to $\Delta m^2_{32} = 2.43^{+0.13}_{-0.13} \times 10^{-3}$ eV^2 at 68 % C.L. and $\sin^2 2\theta_{23} > 0.90$ at 90 % C.L.. It also disfavoured decay and decoherence to 3.7 and 5.7 σ respectively to oscillation.

6.1.1 ν_μ-CC Event Selection

In order to obtain an accurate measurement of the mixing parameters one must select only well constructed beam ν_μ events with a well known energy. This analysis uses only the ν_μ-CC interaction (ν_μ + Fe $\rightarrow \mu^-$ + X), as in this process the neutrino flavour is identifiable, while in the ν_μ-NC interaction (ν_μ + Fe $\rightarrow \nu_\mu$ + X) the neutrino is not.

A pre-selection of events is made in order to ensure: that the beam fired; the beam was of good quality; events are from a period that is being studied; the data

collected were of good quality; the data were collected from part of the detector that is well understood. The pre-selection process, which is common for the ν_μ and $\overline{\nu}_\mu$ analyses, is described in section 7.1.

The muon from the ν_μ-CC events produces a long track which curves towards the coil (as described in section 4.5). Events with a track are selected with an algorithm based on multivariate likelihood, including four variables that characterise a muon track. The four variables are: track length; mean pulse height of track hits; signal fluctuation and transverse track profile. A Kalman filter [112] is used to identify the charge of the track. In the far detector this selects 81.5 % of ν_μ-CC events and has a 0.6 % contamination of NC events.

6.1.2 Extrapolation of Unoscillated Beam

The near detector is used to measure the neutrino flux just after the point of creation of the beam; this is then extrapolated to the far detector. The far detector sees a point source of neutrinos, while the near detector sees an extended source, and also sees them over a larger solid angle. The extrapolation is not a straight conversion of one energy bin in the near detector to one energy bin in the far detector. A method called "the beam matrix method" was developed, which takes into account efficiencies of the detectors and the beam geometry (see chapter 8). The beam matrix prediction has been cross-checked with other methods of calculating the FD spectrum [82]. The flux of neutrinos was constrained in the MC to agree with the near detector data with the NuMI beam in nine different configurations [82], thus reducing errors in the FD prediction.

6.1.3 Charged Current Result

The current charged current analysis includes 3.21 $\times$ 10^{20} POT, collected between 20/5/2005 and 16/7/2007. The far detector data were inspected only after the analysis procedure was fixed. The extrapolation from the near detector predicted 1065^{+60}_{-60}(syst) events for no oscillation (figure 6.1(a)) at the FD. 848 events were observed across all energies between 0 and 120 GeV, with the ratio between the predicted spectrum and the measured spectrum shown in figure 6.1(b).

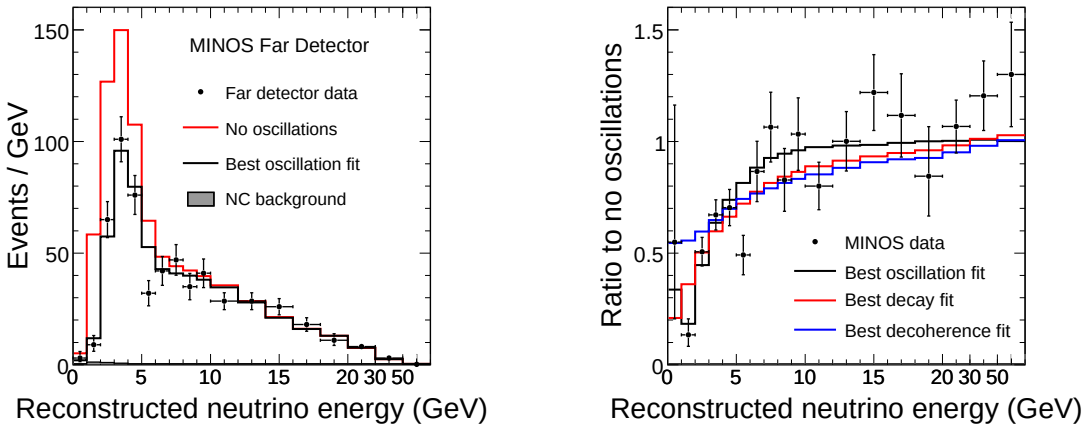

(a) (b)

Figure 6.1: *a) The MINOS FD spectrum with the best fit oscillation and no-oscillation prediction shown. b) The ratio of the data to the predicted no oscillation spectrum. Also shown are the best fit prediction for oscillation and two other models of neutrino flavour disappearance: decay and decoherence.*

The data was fitted to equation equation 2.38 separately, with the largest three systematic errors added to the fit as nuisance parameters. Table 6.1 shows the effect of systematic errors on Δm^2_{32} and $\sin^2 2\theta_{23}$, the largest three are $\pm 10\,\%$ absolute hadronic energy scale, $\pm 4\,\%$ normalisation, $\pm 50\,\%$ NC contamination. The fit was made separately to three different datasets, including one at high energy. Fitting was constrained to the physical region. This gives a best fit of $\Delta m^2_{32} = 2.43^{+0.13}_{-0.13} \times 10^{-3}\,\text{eV}^2$ at 68 % C.L. and $\sin^2 2\theta_{23} > 0.90$ at 90 % C.L. (figure 6.2). The limit on Δm^2_{32} is the world's best limit and the limit on $\sin^2 2\theta_{23}$ is the best measurement for a man-made neutrino beam.

The data were also fitted to alternative neutrino flavour changing methods. Decoherence [113] explains neutrino flavour change by the loss of coherence of the neutrinos' quantum mechanical phase. This would occur in the Standard Model due to the different masses travelling at different velocities and thus separating out over long distances. These distances are of Earth-to-supernovae distances; for decoherence to work over the range of MINOS new physics such as quantum gravity would need to be introduced. Decay [114] is when at least one neutrino can change into a sterile neutrino. Figure 6.1(a) shows the best pure-decay and

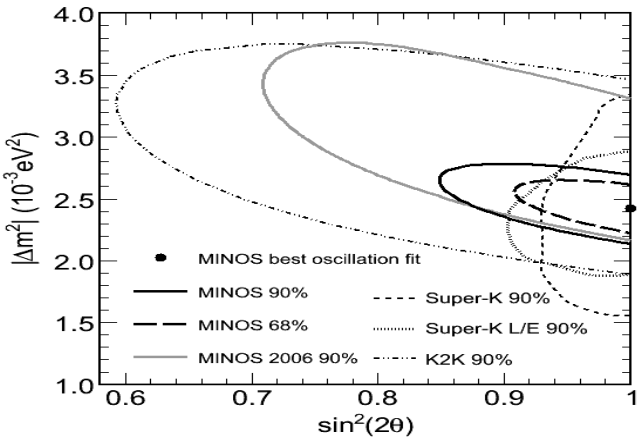

Figure 6.2: *2008 MINOS ν_μ-CC result. It can be seen that MINOS has the worlds best limit for Δm^2_{32}.*

Uncertainty	Δm^2_{32} (10^{-3} eV)	$\sin^2 2\theta_{23}$
i)Abs hadronic E scale ($\pm$ 10.3%)	0.067	0.003
ii)Rel hadronic E scale ($\pm$ 3.3%)	0.035	0.006
iii)Normalisation ($\pm$ 4%)	0.043	0.004
iv)NC contamination ($\pm$ 50%)	0.020	0.017
v)μ momentum (range 2%, curv 3%)	0.032	0.004
vi)CC x-sec $<$ 10 GeV ($\pm$ 12%)	0.012	0.004
vii)Beam uncertainties	0.008	0.001
Total Systematic (sum in quadrature)	0.096	0.019
Expected Statistical Uncertainty	0.19	0.09

Table 6.1: *Sources of systematic uncertainties in the measurements of Δm^2_{32} and $\sin^2 2\theta_{23}$. Correlations are not taken into account. The uncertainty on the absolute hadronic energy scale gives the largest error on Δm^2_{32}, and the uncertainty on NC contamination induces the largest error on $\sin^2 2\theta_{23}$. However, the statistical error has the largest effect on the allowed contour.*

pure-decoherence fits as well as the oscillation best fit. Decay and decoherence are disfavoured by 3.7 σ and 5.7 σ respectively to oscillation.

6.2 The MINOS Neutral Current Analysis

One of the ways in which to reconcile the LSND result (section 3.2.7) with other experiments is to introduce one or more neutrino(s) that do not couple to the Z^0 and are thus called sterile neutrino(s). The SNO experiment has shown that the total flux of active neutrinos from the Sun agrees with the solar model [80], which limits the extent to which the sterile neutrino(s) can interact with the first or second mass eigenstates. Furthermore, Super-K limits the atmospheric oscillation to be predominantly $\nu_\mu \rightarrow \nu_\tau$ [79]. However, this does not rule out $\nu_\mu \rightarrow \nu_s$ as a subdominant oscillation. The MINOS neutral current analysis [115] investigates ν_μ oscillation with a sterile state as well as decay into a sterile state. In both these cases a depletion of NC events in the FD would be observed.

The NC analysis must select events that are well understood beam events, and must ensure that all of the event is accounted for. After the pre-selection events are classified into NC and CC events by a event length cut and assignment by a PID. The predicted FD spectrum is formed by correcting the FD MC in each energy bin by comparing the differences between data and MC at the ND. The main systematic uncertainties for this analysis come from: absolute energy scale; relative calibration of hadronic energy in the two detectors; relative flux normalisation between the two detectors; charged-current contamination of the NC selected events. The results from this analysis are consistent with ν_μ not oscillating, or decaying to a sterile neutrino.

6.2.1 Pre-Selection of Neutral Current Events

The NC analysis is different to the CC ν_μ analysis in that most of the visible energy of the neutrino is in the shower. Rather than following the beam centre in the ND the fiducial volume follows the detector outline. For events to be selected the vertex needs to be 50 cm away from the nearest edge of the partial plane. This enables good containment and reduces contamination from events outside

the detector. A cut of 1.7 m $<$ z $<$ 4.7 m means that the events interact in the fully instrumented section of the ND reduced by 10 planes on either side. Also, as a result of looking for showers, rather than tracks, the NC analysis is more susceptible to: split events; leakage events; incomplete events.

Split events are those where a single neutrino is reconstructed as two or more events. This leads to double counting and reduces the energy of the reconstructed event. If an event is split, two reconstructed events will appear close in time and space. In order to reduce the number of split events, a requirement of Δt $>$ 40 ns is applied. If the separation between events is 40 ns $<$ Δt $<$ 120 ns, a requirement of Δz $>$ 1 m is applied.

One type of leakage events are the vertexing failures, which are events that occur outside the fiducial volume, and are reconstructed inside the fiducial volume. These events are typically cosmic ray events, which have a steep shower. They are removed with a cut on the steepness (S) of the event; this is defined as the ratio of number of strips per plane to the total number of planes in the event. An S of less than one is accepted in the analysis. Another type of leakage event is from secondary particles from interactions outside the fiducial volume migrating into the fiducial volume; these events enter the detector laterally due to sparse instrumentation at the sides. Although the initial event is not reconstructed it will cause extra activity at the edge of the detector, which can be used to veto events within a time window. For events that are less than 5 GeV in energy are selected: if there are less than four strips in the veto region active at the same time as the event; or the energy deposited in the veto is less than 1000 in calibrated pulse height units.

One mode of incomplete events are events where not all the strips hit in an event are assigned to the shower. This is caused by either large gaps in the shower or if the shower is generally sparse. A requirement of an event to be made up of more than four strips cuts these events out.

6.2.2 Event Classification

To get a as pure as possible a selection of NC events, any event that crosses more than 60 planes are classed as CC. If an event crosses less than 60 planes

but has a track that crosses at least five planes more than the shower, the event is passed to the PID as used in the 2006 ν_μ-CC [116][1]. Events that pass the selector are classed as CC; otherwise they are thrown out. All other events i.e., those that have a track that cross less than four planes more than the shower, are classified as NC. The FD prediction was made by extrapolating the ND data to the FD by the "Far over Near (F/N)" method. This corrects the FD MC to make a FD prediction by correcting the ND MC to the ND data and then applying similar shifts to the FD MC on a bin by bin basis. The extrapolation is applied separately to five different classes of event: NC interactions; ν_μ CC interactions; ν_τ CC interactions; ν_e interactions from ν_μ oscillation; ν_e interaction from the beam. The ν_μ-CC events are oscillated with the best fit parameters from the ν_μ-CC analysis[82]. These different extrapolations are combined in the final FD predicted spectrum.

6.2.3 Neutral Currents Systematic Errors

The same systematic errors affect the NC analysis as the CC, with the following exceptions: Absolute hadronic response is 12 %, NC contamination is replaced with CC background and set to 15 %, and muon momentum is replaced with ND selection efficiency which is 15.2 % for $E_{reco} < 0.5$ GeV, 2.9 % for $0.5 < E_{reco} < 1.5$ GeV and negligible for higher energies. CC cross-section (vi) and Beam uncertainties (vii) cancel in the F/N method.

The CC background was estimated by comparing the number of events in the LE beam running (N^{LE}) to number of events in an alternative beam (N^{alt}). The number of events in each beam is described by:

$$N^{LE} = NC^{LE} + CC^{LE}, \tag{6.2}$$

$$N^{alt} = r^{alt}_{NC} \cdot NC^{LE} + r^{alt}_{CC} \cdot CC^{LE}, \tag{6.3}$$

where r^{alt}_{NC} is determined by MC. NC^{LE} is the number of neutral current events in the low energy beam configuration and CC^{LE} is the number of charged current events in the low energy beam configuration, Equations 6.2 and 6.3 have the

[1] also used for the main $\bar{\nu}_\mu$ analysis with a different cut value and other cuts

solution

$$CC^{LE} = (N^{alt} - r^{alt}_{CC}NC^{LE})/(r^{alt}_{CC} - r^{alt}_{NC}) \quad (6.4)$$

$$NC^{LE} = (N^{alt} - r^{alt}_{NC}NC^{LE})/(r^{alt}_{NC} - r^{alt}_{CC}). \quad (6.5)$$

The final estimate of CC^{LE} background is found by weighting the result from the three alternative beam configurations. The final uncertainty in the CC background was calculated from the double ratio of data over MC for CC^{LE} over CC^{alt}.

6.2.4 Neutral Current Result

The results of the NC analysis are presented with the yet unmeasured θ_{13} set to 0° and also at the CHOOZ limit θ_{13} = 12°, with the CP parameter $\delta = 3\pi/2$. The agreement between data and prediction is given by

$$R \equiv \frac{N_{Data} - B_{CC}}{S_{NC}}$$

where B_{CC} is the extrapolated charged current background from all flavours, S_{NC} is the number of neutral current events predicted from the extrapolation of ND data and N_{Data} is the number of events found in the data after cuts. As most ν_μ disappearance is below 6 GeV the data is split into two groups: low energy, $E_{reco} < 3$ GeV, and high energy, 3 GeV $< E_{reco} <$ 120 GeV. The median ν true energy of the low energy group is 3.1 GeV and that of the high energy group is 7.6 GeV. As can be seen in table 6.2 and figure 6.3, R agrees with three active flavours to within errors. To account for three active neutrinos and one sterile neutrino the PMNS matrix needs to be expanded to a 4×4 matrix, where the fourth mass can be either degenerate with the first mass state, or much more massive than the third[2]. The allowed parameter space can be seen in figure 6.4.

Although pure neutrino decay has been ruled out by other analysis, oscillation with decay has not been ruled out. In this analysis this is consistent with zero (figure 6.5 with $\alpha = 0.00^{+0.90} \times 10^{-3}$ GeV/km and a neutrino lifetime $\frac{\tau_3}{m_3} > 2.1 \times 10^{-12}$ s/eV. α is the mass of the neutrino over lifetime.

[2]It could also be degenerate with the third mass state. However, this would mean that there would be no oscillation between active and sterile neutrinos, as the SNO result indicates no oscillation between the first two mass states and the fourth.

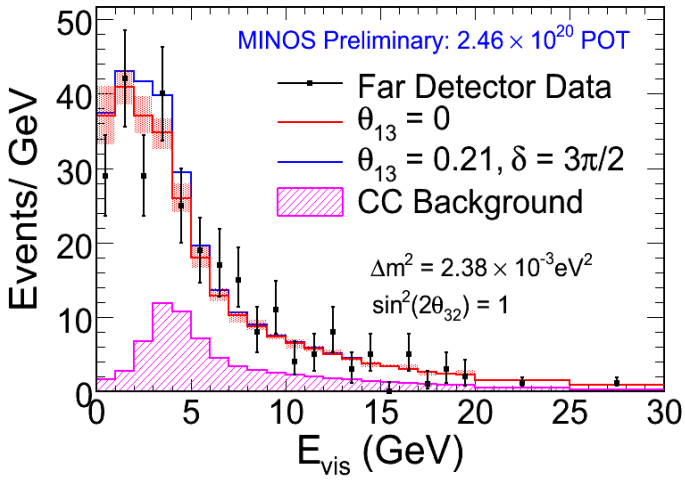

Figure 6.3: *The FD data energy spectrum compared to the prediction for three active neutrino flavours with θ_{13} = 0 (red) and θ_{13} = 12° (blue). Also shown is the ν_μ-CC background.*

6.3 The MINOS Charged Current ν_e Analysis

The last unknown mixing angle is θ_{13}. The current limit on this parameter was set by the Chooz experiment [83] to be $\sin^2 2\theta < 0.15$ at 90 %. A non-zero value of θ_{13} would open up an avenue for observing leptonic CP violation. In MINOS a non-zero θ_{13} would manifest itself as a sub-dominant oscillation of $\nu_\mu \rightarrow \nu_e$. MINOS has observed an excess of events [18] consistent with a non-zero θ_{13} near the Chooz limit.

E_{reco} GeV	N_{Data}	S_{NC}	$B^{\nu_\mu}_{CC}$	$B^{\nu_\tau}_{CC}$	$B^{\nu_e}_{CCn}$
0–3	141	125.1	13.3	1.4	2.3 (12.4)
3–120	247	130.4	84.0	4.9	16.0 (32.8)
0–3	R = 0.99±0.09±0.07-0.08(ν_e)				
3–120	R = 1.09±0.12±0.10-0.13(ν_e)				
0–120	R = 1.04±0.08±0.07-0.10(ν_e)				

Table 6.2: *Number of data events with the predicted MC events for the NC analysis. The ratio of data events to prediction R are in agreement with 3 active flavours*

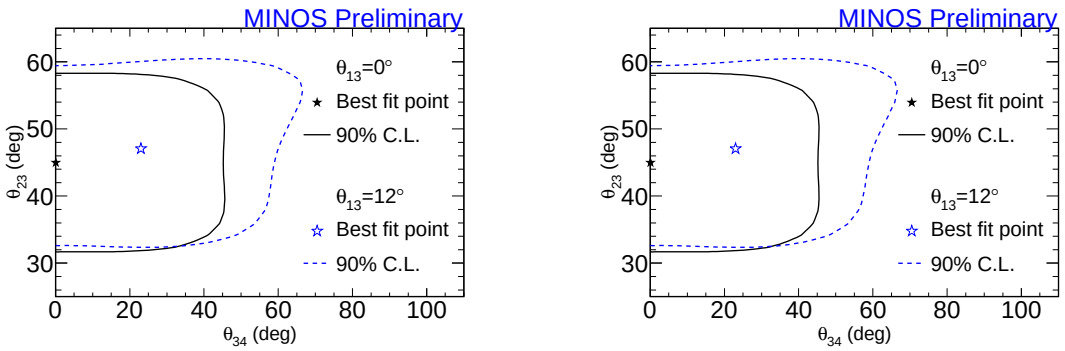

(a) (b)

Figure 6.4: *The MINOS best fit for θ_{23} and θ_{34}. Solid line and filled star are the 90 % contour and best fit point if θ_{13} = 0° and the dashed line and empty star is 90% contour and best fit point if θ_{13} = 12° at the CHOOZ limit. a) $m_4 \equiv m_1$. b) $m_4 \gg m_3$.*

6.3.1 Selecting and Classifying Events

MINOS is able to discover θ_{13} by searching for ν_e appearance in the NuMI beam. As with the ν_μ analysis, only CC interactions allow identification of the neutrino in this analysis via the identification of the e produced in ν_e + Fe $\rightarrow e^-$ + X. Only events with an energy between 1 GeV and 8 GeV are used in this analysis, as this is the energy range where most ν_μ disappear and thus where ν_e appearance is expected to occur due to oscillation. To select ν_e events cuts are made on:

- **Shower** – events are required to have a reconstructed shower and at least five contiguous planes with energy above an energy threshold;

- **Tracks** – tracks longer than 25 planes are rejected.

This increases the ratio of signal to background from 1:55 to 1:12 assuming the Chooz limit of $\sin^2 2\theta_{13}$. To achieve further reduction of the background, an Artifical Neural Network (ANN) with 11 parameters, that characterise the transverse and longitudinal energy deposition of events, is used. The ANN is trained with MC to separate ν_e-CC from NC and ν_μ background events. This increases the signal to background ratio to 1:4.

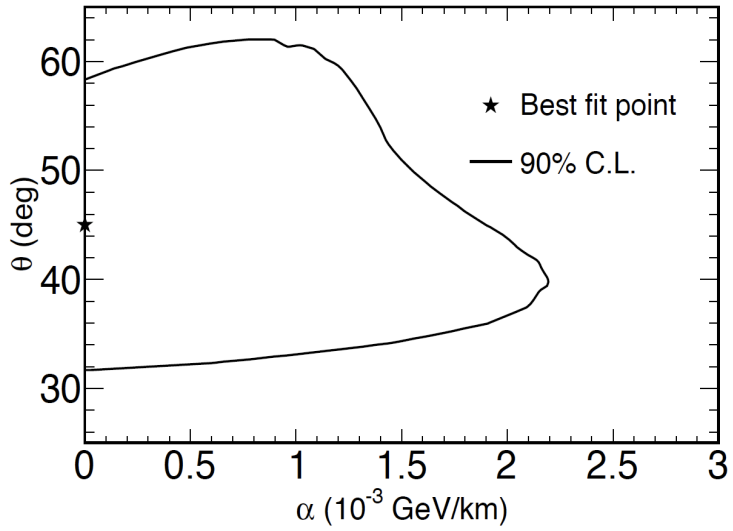

Figure 6.5: *Result of NC analysis with 3.18 $\times$ 10^{20} POT [115]. The best fit point and 90 % contour for the two parameters of neutrino oscillation with decay, where α is the mass of the neutrino over lifetime*

6.3.1.1 Predicting the Far Detector Spectrum

As with the NC analysis, the result of the FD prediction relies on knowing the make-up of events selected in the ND, because different ν backgrounds oscillate with different parameters. When the selection parameters were applied to ND MC and data there was a 20 – 40% discrepancy. The MC is therefore corrected in a similar way to the NC analysis. Horn-on and horn-off data were compared in the ND as these have very different backgrounds. Horn-on data is data collected with the focusing horns powered, and horn-off data is data collected when the focusing horns were switched off. In the horn-off case the low energy peak of CC events disappears so the dominant background is the feed down of higher energy NC events. The number of events in each configuration is given by the following two equations with two unknowns:

$$\begin{aligned} N^{(\text{On Data})} &= N_{NC}^{(\text{On data})} + N_{CC}^{(\text{On Data})} + N_{b\nu_e}^{(\text{On Data})} \\ N^{(\text{Off Data})} &= r_{NC} N_{NC}^{(\text{On Data})} + r_{CC} N_{CC}^{(\text{On Data})} + r_{b\nu_e} N_{b\nu_e}^{(\text{On Data})}, \end{aligned}$$

where $N^{(\text{On Data})}$ and $N^{(\text{Off Data})}$ are the total number of events selected in the ND for horn-on and horn-off respectively. $N_{NC}^{(\text{On data})}$ and $N_{CC}^{(\text{On Data})}$ are the numbers of NC and CC events selected with the horn-on data and are the unknowns. The

number of beam ν_e selected, $N_{b\nu_e}^{(\text{On Data})}$, is taken from the weighted beam fit MC. The r parameters are the ratios between the various component parts between horn-off and horn-on for MC. These are obtained by the following equations:

$$\begin{aligned} r_{NC} &= \frac{N_{NC}^{(\text{Off MC})}}{N_{NC}^{(\text{On MC})}} \\ r_{CC} &= \frac{N_{CC}^{(\text{Off MC})}}{N_{CC}^{(\text{On MC})}} \\ r_{b\nu_e} &= \frac{N_{b\nu_e}^{(\text{Off MC})}}{N_{b\nu_e}^{(\text{On MC})}} \end{aligned}$$

These ratios were checked by creating a CC enhanced sample of data and anti-CC background by applying the PID, from the ν_μ-CC analysis.

6.3.1.2 Backup Far Detector Prediction

A separate method was developed as a check for correcting the ND background. A second set of showers were derived from ν_μ-CC events selected with the CC PID. The hits associated with the muon track were removed and the remaining shower was passed through the reconstruction software to get a clean shower sample. Both data and MC went through this process and then the ν_e selection was applied. The ratio of muon-removed data to muon-removed MC was used to get the relative components of the background for the ν_e analysis. These ratios agree those obtained with the horn-on/horn-off method. The FD prediction is then found by multiplying the component ND data by the ratio between the FD MC spectrum and ND MC spectrum. This gives a prediction at the FD for the background summed over energy to be 18.2 NC events, 5.1 ν_μ-CC events, 2.3 beam ν_e and 1.1 ν_τ events to give a total of 26.6 events.

To test the efficiency for selecting ν_e-CC events the muon-removed sample of events had an electron added, of the same momentum as the removed muon, for both MC and data. The selection efficiency was found to be 41.4$\pm$1.4 %.

6.3.2 Charged Current ν_e Systematic Errors

Systematic errors were worked out by generating modified MC samples and quantifying the change in the background events on the FD prediction. Table

Uncertainty source	Uncertainty on background events (%)
i)Far/Near ratio:	6.4
a)Relative energy scale	3.1
b)PMT gains	2.7
c)PMT crosstalk	2.2
d)Relative event rate	2.4
e)All others	3.7
ii)Horn off (systematic)	2.7
iii)Horn off (statistical)	2.3
Total Systematic (sum in quadrature)	7.3
Expected Statistical Uncertainty	19

Table 6.3: *Breakdown of the percentage change in background in the FD prediction for the ν_e-CC analysis.*

6.3 shows the most important errors that arise from the F/N method, as well as the error from the horn-off method of determining the background. Together they give a systematic uncertainty of 7.3 % on the number of background events. The statistical error is 19 %.

The Far/Near ratio error is made up from multiple sources the most important are a) relative energy scale calibration errors, b) and c) details of the modelling of the photomultiplier gains and crosstalk, d) relative event normalisation.

6.3.3 ν_e Results

The FD data was unblinded in two steps. First the data that passed all cuts except the ANN cut were unblinded. There were 146 data events below the ANN cut of 0.55 compared to the prediction of 132^{+12}_{-12}(stat.)$^{+8}_{-8}$(syst.). After checks on this sample had been completed the signal region was investigated above ANN = 0.7. In this region there were 35 events compared to the prediction of 27^{+5}_{-5}(stat.)$^{+2}_{-2}$(syst.).

A second selection method, Library Event Matching (LEM), was chosen as

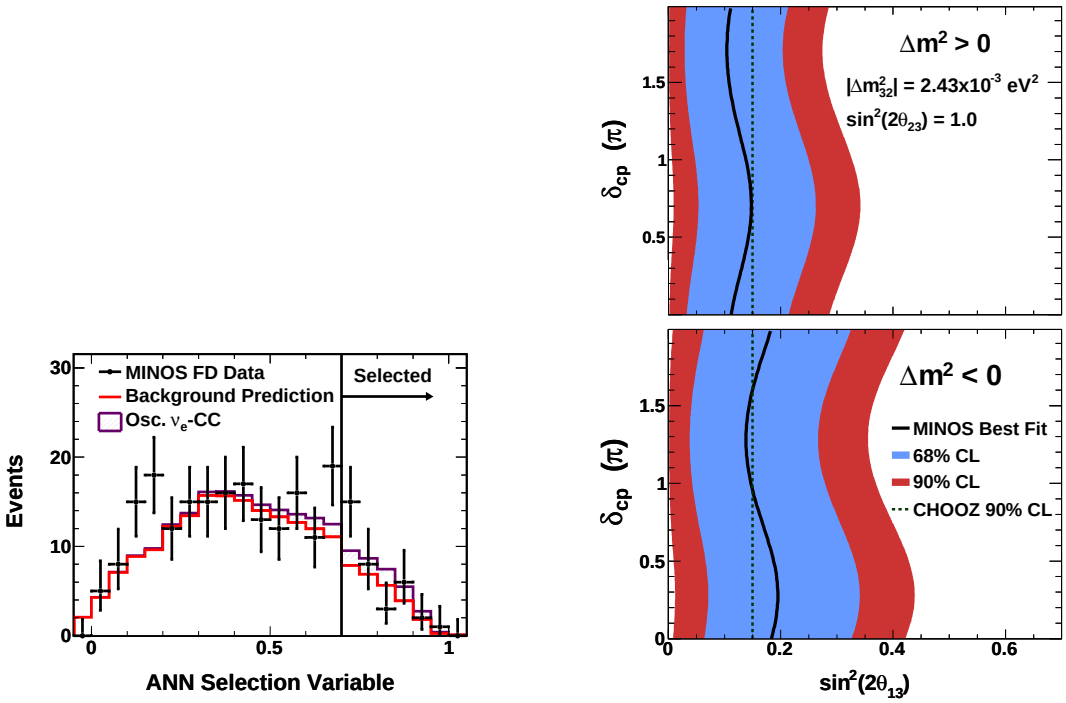

(a) (b)

Figure 6.6: *TThe MINOS FD ANN spectrum with the best fit oscillation and the best confidence levels for normal and inverse hierarchy. a) Distribution of events for the ANN PID. Black points are data with statistical errors and the red line is prediction. b) values of* $\sin^2 2\theta_{13}$ *and* δ_{CP} *the data are consistent with for normal (top) and inverse (bottom) hierarchy.*

a back-up. In the LEM method the data events are compared to a library of MC events. A PID is created from three variables: fraction of 50 best matches that are ν_e CC; mean y of 50 matches that are ν_e CC; mean Q_{frac} of best 50 matches that are ν_e CC, where $Q_{frac} = \frac{Q_{matched}}{Q_{matched}Q_{unmatched}}$. These three parameters are combined into an energy-binned likelihood. The LEM gives a better background rejection and gives a prediction of 22^{+5}_{-5}(stat.)$^{+3}_{-3}$(syst.). The number of data events selected were 28, which, like the ANN selection, is less than a 2σ excess.

Taking the ANN excess and taking $|\Delta m^2|$ = 2.43$\times$ 10^{-3} eV^2 and $\sin^2 2\theta_{23}$ = 1.0, the best fit in normal hierarchy is just below the Chooz limit for full three flavour neutrino oscillation see figure 6.6.

6.4 Charged Current $\overline{\nu}_\mu$ Analysis

MINOS [1], Super-K [57] and K2K [61], have measured the oscillation parameters associated with ν_μ disappearance precisely. However, the oscillation parameters associated with $\overline{\nu}_\mu$ disappearance are less well constrained. The Super-K result is a sum of ν_μ and $\overline{\nu}_\mu$, which needs to assume the initial flux of ν_μ and $\overline{\nu}_\mu$, from which the $\overline{\nu}_\mu$ oscillation parameters can be inferred. Global fits that include pure ν_μ experiments can improve our knowledge of the $\overline{\nu}_\mu$ parameters. The only direct $\overline{\nu}_\mu$ measurement is the MINOS analysis of atmospheric $\overline{\nu}_\mu$ [86], which provides only weak constraints on $\Delta\overline{m}^2_{32}$ and $\sin^2 2\overline{\theta}_{23}$. Observation of P($\nu_\mu \rightarrow \nu_\mu$) $\neq$ P($\overline{\nu}_\mu$ $\rightarrow \overline{\nu}_\mu$) would imply that CPT does not hold and that there must be non-Standard Model physics such as the models discussed in section 2.3.3.

Furthermore if the neutrino is a Majorana particle then the process $\nu_\mu \rightarrow \overline{\nu}_\mu$ could happen at the level $\approx$ (m/E$_\mu$)^2 $\approx$10^{-18} [117]. To parameterise this the term α is added to equation 2.38 so the probability that $\nu_\mu \rightarrow \overline{\nu}_\mu$ becomes:

$$P(\nu_\mu \rightarrow \overline{\nu}_\mu) = \alpha \sin^2 2\theta \sin^2 \left(\frac{1.27\Delta m^2 L}{E} \right). \tag{6.6}$$

Due to the large number of ν_μ being observed to disappear at the far detector by MINOS [1], the fraction α of ν_μ converting to $\overline{\nu}_\mu$ can be constrained.

Chapters 7 – 10 will give an in-depth description of the event selection and extrapolation and the oscillation result. The section below will give a brief overview of an analysis of 3.2 $\times$ 10^{20} POT [88] that will be part of a future analysis of 7.2 $\times$ 10^{20} POT.

6.4.1 Selecting $\overline{\nu}_\mu$-CC events

The events used to determine the oscillation parameters $\Delta\overline{m}^2_{32}$ and $\sin^2 2\overline{\theta}_{23}$ are ($\overline{\nu}_\mu$ + Fe $\rightarrow \mu^+$ + X), as the neutrino flavour is identifiable as $\overline{\nu}_\mu$. As with the ν_μ-CC, the preselection is applied to make sure the events are from the NuMI beam and that the energy of the $\overline{\nu}_\mu$ can be reconstructed. The MINOS detectors are magnetised so that the μ^+ are defocused (figure 4.13(b)); therefore only tracks with positive values found by the Kalman fitter [112] were selected. As the NuMI beam has a lower content and of $\overline{\nu}_\mu$ compared to ν_μ, combined with $\overline{\nu}_\mu$ having a higher

average energy, a different selector was needed. A different NC discriminator was used in combination with two additional selectors which help to remove more of the mis-identified events and NC events. The NC discriminator was a likelihood-based separator that was used in the first MINOS ν_μ-CC analysis [82], but with a different cut value. This discriminator combines three probability distributions: event length; fraction of the total pulse in the reconstructed track; average pulse height per plane in track. The second parameter used is (q/p)/σ(q/p), which says how confident the fitter is of the charge of the track. The third parameter is relative angle, which is the difference between the μ path in free space and its path in the MINOS detector. This is another way of determining the charge of the track. The selected events are 97 % pure and 83 % efficient at the FD, assuming CPT conservation.

6.4.2 Extrapolation

The $\overline{\nu}_\mu$ uses the same beam matrix method as the ν_μ-CC analysis with some slight changes. Neutrinos are extrapolated separately from anti-neutrinos to account for the case where CPT is not conserved. Also the affect that taus have on the result was re-evaluated.

6.4.3 Result for $\overline{\nu}_\mu$-CC analysis

As with the other analysis the full FD energy spectrum was only examined after the analysis had been determined. For CPT conservation $58.3^{+7.6}_{-7.6}$(stat.)$^{+3.6}_{-3.6}$(syst.) events were predicted in the FD in the energy range $0-50$ GeV, from the extrapolation of the near detector. 42 events were observed in energy range $0-50$ GeV (figure 10.1). The confidence level was appraised using a Feldman-Cousins technique [118], with seventeen systematic errors included. The five that had the largest effect on the result are from uncertainties in calculating the muon energy from the track range and the curvature of the track, uncertainties in production of neutrinos in the decay pipe walls, uncertainties in the POT for both detectors and uncertainties in the backgrounds. Systematic errors are discussed further in chapter 9. Figure 10.6 shows that the region $\Delta\overline{m}^2_{32} < 2.0 \times 10^{-3}\,\text{eV}^2$ and $5.0 \times$

10^{-3} $\Delta\overline{m}^2_{32} < 80 \times 10^{-3}$ is excluded to 90 % C.L.. The fraction of ν_μ that disappear reappearing as $\overline{\nu}_\mu$ has been been constrained so that $\alpha < 0.027$.

6.5 Summary

MINOS has measured Δm^2_{32} to the highest precision to date (Δm^2_{32} = $2.43^{+0.13}_{-0.13}$ at 68 % C.L.), and has measured $\sin^2 2\theta_{23}$ with the best precision of a man-made ν_μ beam ($\sin^2 2\theta_{23} > 0.90$ at 90 % C.L.). The NC analysis has yielded results that agree with a three neutrino model to within errors, and other non-oscillation flavour changing processes are also consistent with zero. MINOS has also found the first hints that θ_{13} could be non-zero. Furthermore, it has made the first direct measurement of $\Delta\overline{m}^2_{32}$ and $\sin^2 2\overline{\theta}_{23}$ by a man-made beam. This analysis will be described further in the following chapters.

Chapter 7

$\overline{\nu}_\mu$ Event Selection

> "Causality? Well, okay, you know, one event causes another, okay, but sometimes, you just gotta say: 'The laws of time and space? Who gives a smeg!'" (Kryten - series 7 Tikka To Ride)

In this thesis, the analysis in focus measures the parameters that control the $\overline{\nu}_\mu \leftrightarrow \overline{\nu}_\tau$ oscillation, $\sin^2 2\overline{\theta}_{23}$ and $\Delta\overline{\mathrm{m}}^2_{32}$. The details of this analysis will be described in this and subsequent chapters. The best sensitivity to oscillation is achieved, by making selections to maximise efficiency $\times$ purity in the FD (section 7.2). The ND is used to sample the NuMI beam before any oscillation; this sample is extrapolated to the FD to make a prediction on the assumption of no oscillation (chapter 8). The FD is used to show the effects of any oscillation (chapter 10), and for this analysis, it is important to find beam $\overline{\nu}_\mu$-CC events. Some preselection cuts are required to choose good quality beam events (section 7.1): data quality checks are used to make sure that the detectors are working correctly (section 7.1.1); cuts are made to ensure beam quality (section 7.1.2); the detector live times are from the time period being analysed (section 7.1.3); only the fiducial volume (section 7.1.4) is considered to obtain good energy resolution and remove rock events; timing cuts (section 7.1.5) are applied to find beam events (remove cosmic rays). Alternative selection methods may also be used to be sure the main selector is optimised (section 7.3).

7.1 $\overline{\nu}_\mu$ Pre-Selection

7.1.1 Data Quality Cuts

There are various FD data checks to make sure that the detectors are running properly and to ensure that all of an event is reconstructed:

- All parts of the detector and readout channels are working;
- The HV supplies that supply power to the PMTs are working. Any trip would lead to a large area of detector being down. A trip is detected if 20 or more PMTs go cold. A cold PMT is defined as having a singles rate of less than 50 Hz;
- The detector needs to be magnetised with the normal coil current 80$\pm$1A with a forward field that focuses μ^-;
- The GPS system used to correlate the detectors to the beam spills has an error of less than 1000 ns;
- The LI system which is used to test the gain of the PMTs was not injecting any light into the detector.

A full report can be found in [119]. The ND's only automated check is that the coil current is working correctly, with other cuts made by hand. A more automated approach is currently in development [120].

7.1.2 Selection of Good Beam

To understand the neutrino beam produced, a selection was based upon when the beam was good. The selection was chosen from the results of scanning the proton beam across the target, and analysing the muon and hadrons produced. If the numbers of muons and hadrons are stable it is considered a good beam [121]. With the position cuts varied throughout the runs to optimise the data collection a typical cut would be:

$$
\begin{array}{rcccl}
-2.0\,\text{mm} & < & \text{Beam spot mean x position} & < & -0.01\,\text{mm} \\
0.01\,\text{mm} & < & \text{Beam spot mean y position} & < & 2.0\,\text{mm} \\
0.1\,\text{mm} & < & \text{RMS of beam spot x position} & < & 1.5\,\text{mm} \\
0.1\,\text{mm} & < & \text{RMS of beam spot y position} & < & 2.0\,\text{mm}
\end{array}
$$

Other selections were applied to ensure that the POT were between 0.5×10^{12} and 50×10^{12} in each spill (so as to avoid any abnormal POT counting), that the horns had a current between -200kA and -155kA to focus π^+ correctly, and also that the NuMI target is at the LE-10 position. Any data taken at any other target position would have to be extrapolated separately due to different π decay kinematics.

7.1.3 Runs

The analysis presented here used data from Run I and Run II. Run I is from 20/5/2005 after the initial start up of the beam, in which it ran in LE-10 beam configuration. Run I finished when the accelerator shut down for general maintenance on the 26/2/2006. In this period, a problem occurred with the movement of the NuMI target. The target had to be replaced as different beam energies were required for testing the high energy tail of the LE beam. After the higher energy running the target was returned to the LE-10 position and Run II started on the 12/9/2006 and ran till 16/7/2007. It was noticed that the beam energy spectrum was not the same as it had been in Run I. From analysis of the data, it was concluded that the Run I target was at LE-9, the horns are in the low energy configuration with the target 9 cm from the stop closest to the horn. Figure 7.1 shows how the POT accumulated through the runs. Run III has now been taken and contains as much data as Run I and Run II, thus doubling the data. Run III covers the period 17/11/2007 to 13/6/2009. However, the ND has a much higher event rate; furthermore it is only used to track changes in the beam's energy and composition. Therefore, the lower live time (1.20 $\times$ 10^{20} and 1.74 $\times$ 10^{20} POT, compared to 1.27 $\times$ 10^{20} and 1.94 $\times$ 10^{20} for the FD) does not affect the result.

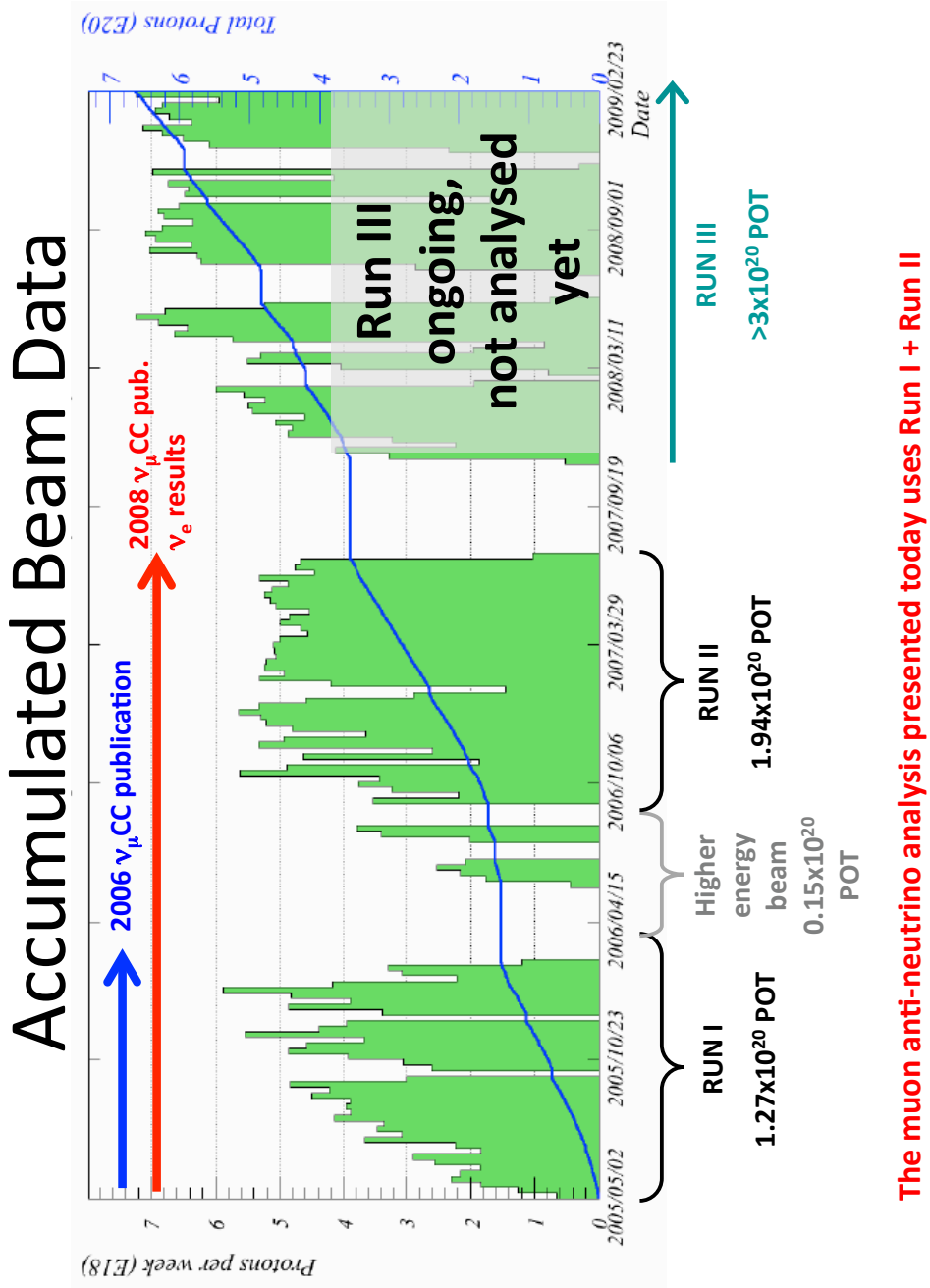

Figure 7.1: *The number of POT per week and the accumulated total for runs I,II and III. Only Run one and two (3.21 $\times$ 10^{20} POT) are used in this analysis. Taken from [88].*

7.1.4 Cuts on Fiducial Volume

To get a good measure of the energy of the neutrino it is required that the hadronic shower is contained within the fully instrumented region of the detectors. For this reason the ND fiducial volume starts at the 14^{th} plane and finishes at the 68^{th} plane, rejecting any events that started in the rock. The ND fiducial volume leaves 3 m of the fully instrumented region for the hadronic shower to develop in, which allows good calorimatic calculation of the energy of the shower. A cylinder of radius 0.8 m, centred on the beam centre, is used to minimise energy lost out of the sides and ensures that instrumentation is uniform. The fiducial volume is shown in figure 7.2. In the FD, as the beam neutrino flux is lower, more of the detector is included in the fiducial volume. The fiducial volume starts at the 4^{th} plane and the last plane in the fiducial volume is the 464^{th} plane. Planes 240 to 252 are excluded as they surround the gap between the super modules in which energy from the hadronic shower may be lost. A cylinder of radius $\sqrt{14}$ m centred on the coil hole is used to contain the events. A second cylinder of radius 0.4 m centred on the coil hole is excluded to avoid losing the hadronic shower in the coil hole. The fiducial volume for the far detector is shown in figure 7.3.

7.1.5 Timing Cuts

To include only beam events the detectors, data is only recorded when the "kicker" is fired. A signal is sent to the kicker magnet 20 cycles before the magnet is fired. The ND receives this signal and starts to record data 1.5 μs before the neutrinos arrive and records for 13 μs. The event is timestamped by the GPS at the ND and is sent via TCP/IP to the FD. The FD then reads out a ± 50 μs window around when the neutrinos are predicted to arrive. Although the signal from the GPS arrives after the neutrino beam, there is enough buffering for the FD to hold the event signal until the GPS signal is received. The period 30 μs before the trigger is read out as well to see if any previous activity in the detector has caused any dead time in the electronics. To test detector backgrounds, fake triggers can be generated.

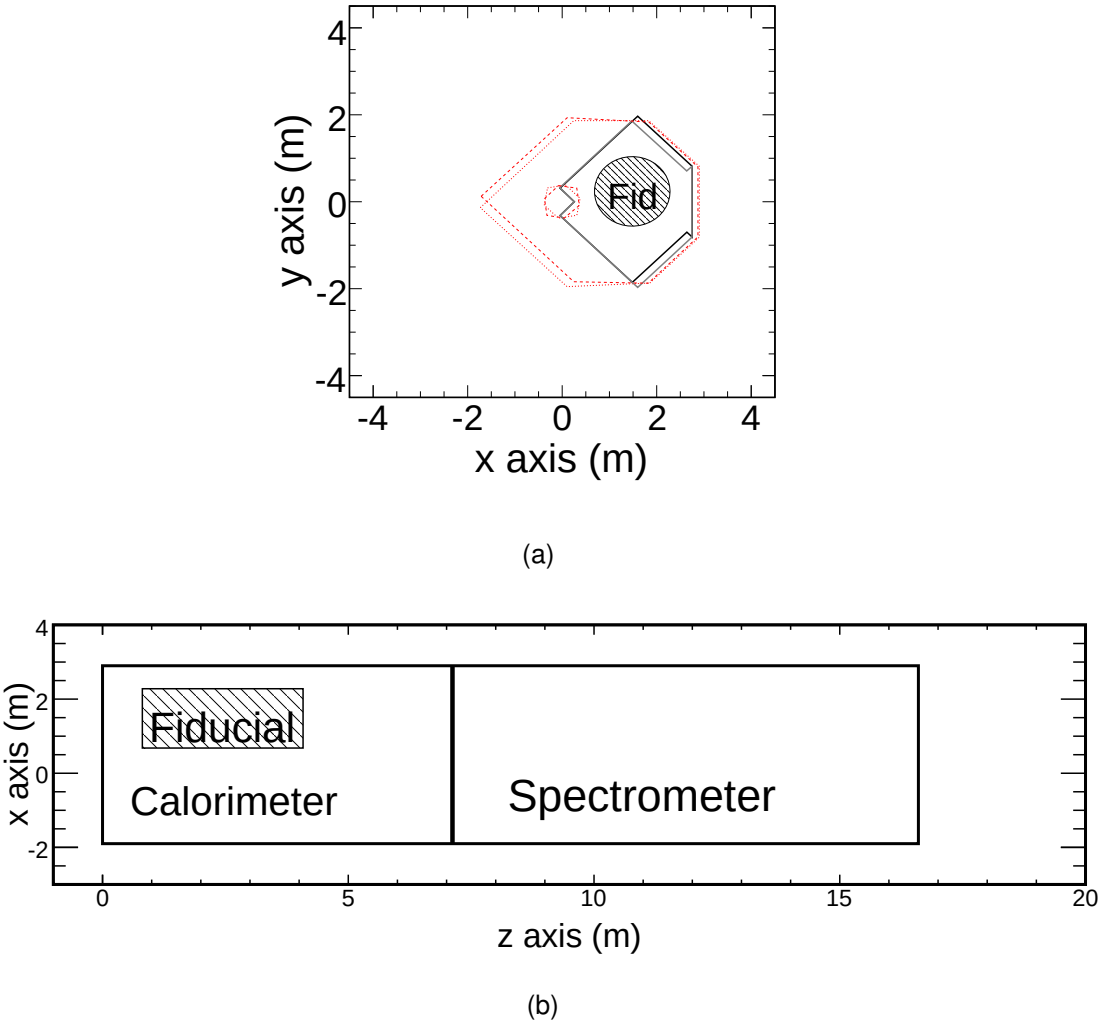

Figure 7.2: *The fiducial volume of the near detector. a) The fiducial volume, shaded, shown face on looking towards the beam source. Shown also are the instrumented parts of the plane. The red dotted lines are the U and V fully instrumented planes, and the black and grey lines are the partially instrumented planes. b) The fiducial volume, shaded, shown looking down. Also shown is the near detector outline and the calorimeter and spectrometer sections.*

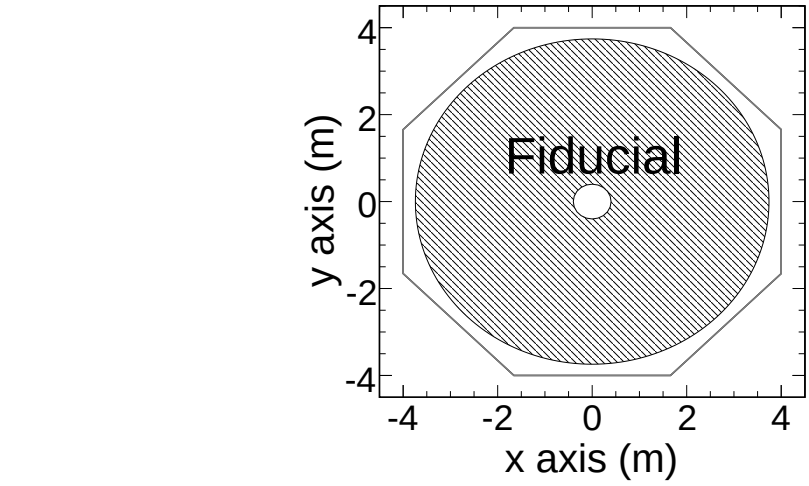

(a)

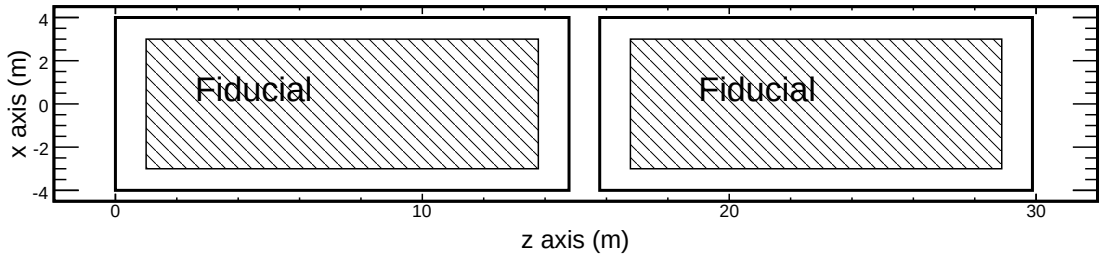

(b)

Figure 7.3: *The fiducial volume of the far detector. a) The fiducial volume, shaded, shown face on looking towards the beam source. Shown also are the instrumented parts of the plane. b) The fiducial volume, shaded, shown looking down. Also shown are the two super modules of the far detector outline.*

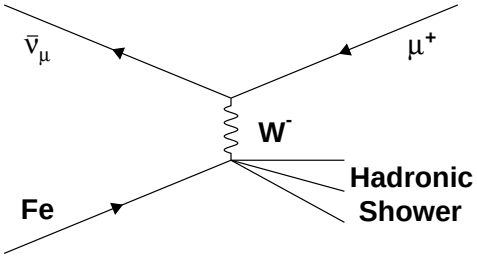

(a) CC interaction

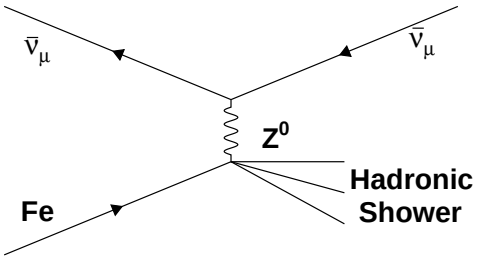

(b) NC interaction

Figure 7.4: *The Feynman diagrams for $\overline{\nu}_\mu$ interactions.*

7.2 Selecting $\overline{\nu}_\mu$-CC Events

After these cuts, the data consist only of beam neutrinos which interact with the MINOS detectors, either through the charged current (CC) interaction (figure 7.4(a)) or the neutral current (NC) interaction (figure 7.4(b)). In this analysis we are looking for $\overline{\nu}_\mu$ disappearance, so it is necessary to identify the neutrino involved via the charged lepton produced. Section 4.5 described how these events look in the MINOS detectors in this a typical NC interaction (figure 4.13(c)) is a large defuse shower. However, if a $\pi^\pm$ is produced this will cause a track which is difficult to distinguish from a $\mu^\pm$ track. The different ν flavours have different CC interactions. The ν_e produces an electron in the CC interactions which produces a more compact shower than the NC interactions, which have no track (Figure 4.13(d)). A ν_τ produces a τ. A ν_τ would appear in the NuMI beam only through the flavour change of a ν_μ neutrino. As such the ν_τ would have the same energy as the ν_μ that changed flavour. At the energies associated with a Δm^2_{32} of 2.5×10^{-3} eV^2 the taus produced decay within the plane they are produced in and hence not detected. A μ is produced 17 % of the time in these decays, and look

like a CC event from a ν_μ. A ν_μ-CC event produces a μ which appears as a track in the MINOS detector (figure 4.13(a)). The MINOS detectors are magnetised, so μ^- and μ^+ curve in opposite directions. In normal $\mathbf{B}$-field running, the μ^- curve towards the coil and the μ^+ curve away from the coil. This has the effect that the μ^+ spends less time in the detector; therefore it is harder to detect the curvature of the track and thus to measure their energy (figure 4.13(b)).

7.2.1 Contamination Events

In addition to signal events in the MINOS detectors there are other events that may bias the measurement. Rock muons are muons that are produced in the rock surrounding the detectors by neutrinos from the NuMI beam; these are removed by the fiducial volume cuts described in section 7.1.4. Rock muons cause a problem, as not all the energy is deposited in the detector, so the energy of the neutrino that caused the rock muon is unknown. Cosmic ray muons and atmospheric $\overline{\nu}_\mu$ would add extra events that may wash out any disappearance from the beam, they are removed by the timing cuts (section 7.1.5). Any other events produced in the detector, for example light injection leakage, would appear like a shower and be removed by cuts designed to remove NC interactions.

7.2.2 Finding a μ Track

The main feature of a $\overline{\nu}_\mu$-CC event is a track curving away from the coil hole, which shows that the μ is positively charged. Any event reconstructed without a track is rejected. To get the charge of the track a Kalman filter is used [112], which returns a parameter q/p where q is the charge, and p is the momentum. The Kalman fitter takes into account both the bending of the muon track in the magnetic field, the muon energy loss and deflections from Coulomb scattering. All tracks with a q/p $<$0 are rejected as these curve towards the coil hole and thus are negatively charged.

The pre-selection and track selection are applied to data and high statistic MC (2.6 $\times$ 10^{23} POT). Using the truth information of the MC it was calculated that, using purity as defined in equation 7.1, the selection is 23.3 $\%$ pure and by

definition (equation 7.2) 100 % efficient.

$$\text{purity} = \frac{\text{Number of selected } \overline{\nu}_\mu \text{ events}}{\text{Total number of selected events}} \tag{7.1}$$

$$\text{efficiency} = \frac{\text{Number of selected } \overline{\nu}_\mu \text{ events}}{\text{Total number of } \overline{\nu}_\mu \text{ events after pre-cuts}} \tag{7.2}$$

After the pre-selection has been made, a large background of non-$\overline{\nu}$ events remains; these are mainly NC events (figure 7.5). In some of the NC events there are hadronic tracks from π^+ or protons which the track finder correctly identifies as a positive track. In addition, ν_μ events that have been mis-identified, due to scattering, makes up the contamination. Mis-identified charge is more of a problem in this $\overline{\nu}_\mu$ study than in the ν_μ study, as there are many more ν_μ than $\overline{\nu}_\mu$ in the beam (91.7 % ν_μ, 7.0 % $\overline{\nu}_\mu$). Even though mis-identified ν_μ are a small fraction of total events they outnumber $\overline{\nu}_\mu$ events. Mis-identified and NC events are minimised with further cuts.

7.2.3 CC/NC PID Parameter

One way of identifying NC events was developed for the first MINOS NuMI beam oscillation search [82, 116]. In a real $\overline{\nu}_\mu$ event the track is formed by a μ^+ which is a minimally ionising particle and curves smoothly, whereas the track formed in a NC event is from a π or proton, which is not minimally ionising. To find these NC events, three parameters are combined to form a new Particle Identification parameter (PID). The NC events can then be removed by a cut on this parameter. The three parameters are:

- **Event length (in planes)** – NC events are shorter;
- **Fraction of total pulse in the reconstructed track** – NC events have a large hadronic shower associated with them;
- **Average pulse height per plane in track hits** – NC tracks are produced by non-MIP particles.

These parameters are normalised to act as probability density functions (pdfs) for the data events and are filled with MC events using truth information. A set of pdfs are created for all CC and NC interactions separately. It should be noted that ν_e interactions are not included in the construction of the PID. The PID is calculated from six pdfs, two for each parameter (one CC and one NC). Each data event is then compared to the pdfs. The product of the CC pdfs is used to assess how likely a data event is to be a CC event and the same for the NC pdfs. The probabilities of an event being a CC event (P_{CC}) or an NC event (P_{NC}) are defined as:

$$P_{CC} = \prod_{i}^{3} f_i(CC) \tag{7.3}$$

$$P_{NC} = \prod_{i}^{3} f_i(NC) \tag{7.4}$$

where i is the number of the pdf and f is the value taken from the pdf. The two probabilities (equation 7.3, equation 7.4) are then combined to form the PID parameter:

$$PID = -(\sqrt{-\ln P_{CC}} - \sqrt{-\ln P_{NC}}). \tag{7.5}$$

The more positive the PID the more CC-like the event. In the MINOS ν_μ analysis [82, 116], values of -0.2 (FD) and -0.1 (ND) were used. In this analysis, the same value of CC/NC PID cut is used in both detectors in order to utilise the similarities between the detectors. As there are significantly fewer $\overline{\nu}_\mu$ in the NuMI beam compared to ν_μ, combined with the fact that there is just as much chance of a NC event being classified as a positive event as a negative event, a harder cut is required on the PID.

7.2.4 Removal of Mis-Identified Events

It is possible that ν_μ events may be assigned the wrong sign q/p < 0 if the muon scatters off a nucleus in the detector. The removal of mis-id events is more important in this $\overline{\nu}_\mu$ analysis than in the ν_μ analysis, as 8 % mis-identified ν_μ events is a significant proportion of signal events due to the larger number of ν_μ events. Most of the mis-id events have shorter track lengths and look like NC events, and are therefore removed by the NC PID (table 7.1). To remove remaining mis-id

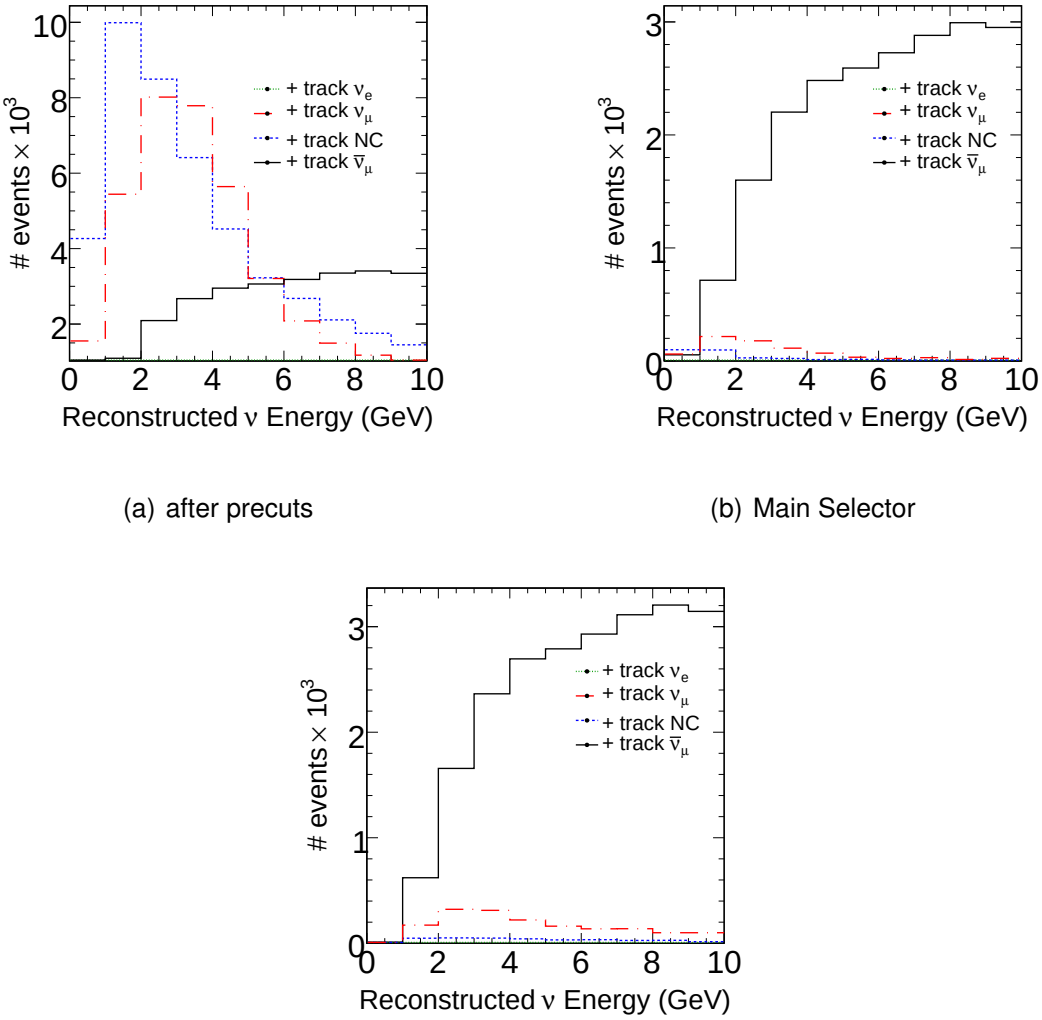

(a) after precuts

(b) Main Selector

(c) Backup Selector

Figure 7.5: *The number of events in for full MC, POT 2.7 $\times 10^{23}$: a) after pre-cuts have been applied; b) after pre-cuts and the Main Selector cuts have been applied; c) and after pre-cuts and the Backup Selector cuts have been applied.*

events, a further two cuts are applied on different parameters, the relative angle parameter and qp_sigmaqp.

7.2.4.1 Relative Angle Parameter

The relative angle parameter [122] was designed as an alternative to the charge-to-moment q/p, parameter. It is based on a calculated trajectory of the μ in free space, without material or magnetic field, and is compared to the actual trajectory through the detector. The detectors are magnetised, so that μ^- bend towards the coil, while μ^+ curve away from the coil, which is defined as the "forward" field. The muon momentum is taken at the track vertex, V, and the momentum vector is projected to a point, P, in the plane where the last hit, E, in the track was recorded. P is the centre of a two-dimensional Cartesian right-handed co-ordinate system. The x-axis in this co-ordinate system goes radially outwards parallel to a line that passes from the coil through the point V (figure 7.6). The relative angle is the angle ϕ PE and the x-axis. Negative tracks are peaked around π and positive tracks are peaked round 0 and 2π. To make only one cut the absolute value of $\phi - \pi$ is used, thus negative tracks are peaked at 0 and positive tracks are peaked around π. Negatively charged events mis-identified as positive events are caused by the μ^- scattering off a nucleus; however, as some of the curvature is towards the coil, they will not have a very large relative angle.

7.2.4.2 qp_sigmaqp Parameter

The track fitter in section 7.2.2 also returns a value on how likely an event is to contain a track, $\sigma\left(\frac{q}{p}\right)$. The parameter qp_sigmaqp is defined as:

$$\text{qp\_sigmaqp} = \frac{\frac{q}{p}}{\sigma\frac{q}{p}}. \tag{7.6}$$

Most of the remaining mis-id and NC backgrounds have a large uncertainty ($\sigma\left(\frac{\mathrm{q}}{\mathrm{p}}\right)$) in the track identification and are removed by cutting on low values of qp_sigmaqp. Short track $\overline{\nu}_\mu$ events also have a high uncertainty but also have a large $\frac{q}{p}$.

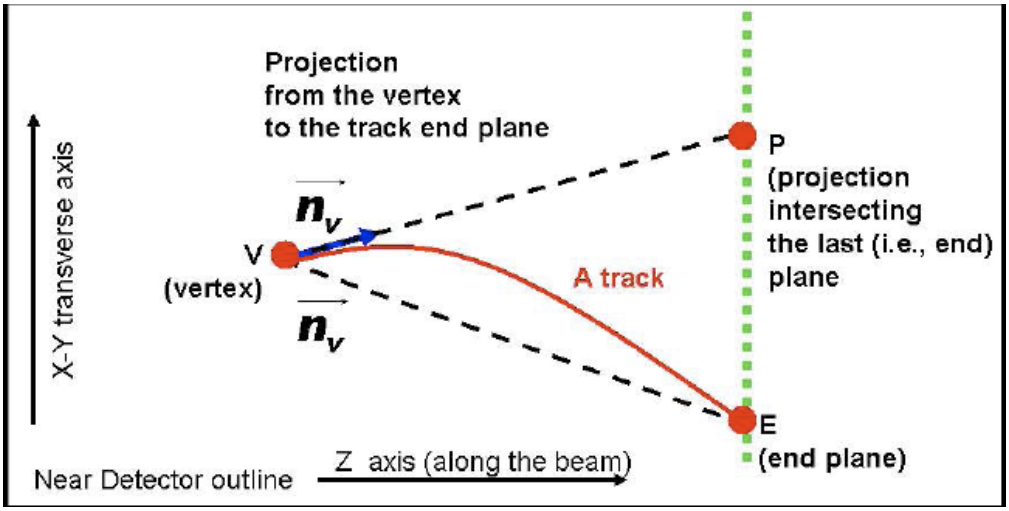

(a)

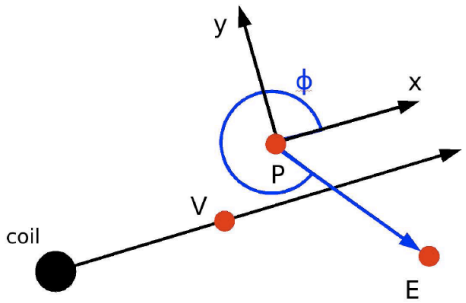

(b)

Figure 7.6: *Illustration of the definition of the relative angle parameter (from [122]), where V is the vertex of the track, E is the end of the track. A straight line is drawn from V along the direction of travel of n_v to P in the last plane of the track a). Thus P becomes the centre of a right hand 2D Cartesian co-ordinate system, where the x-axis points radially outward parallel to the line that connects the coil and V. The y-axis is orthogonal to the x-axis. b) The relative angle (ϕ) is the angle between the x-axis and the vector to point E from point P.*

7.2.5 The $\overline{\nu}_\mu$ Main Selector

The selection criteria were chosen by optimising the value of efficiency $\times$ purity for ν energies below 10 GeV [123]. Studying purity $\times$ efficiency in the FD at reconstructed neutrino energies of less than 10 GeV was preferred to studying the sensitivity directly, as efficiency $\times$ purity gives a good figure of merit (FOM) and takes vastly less time to calculate than sensitivity. Other parameters than those included here were considered, but were rejected due to higher systematic errors and poorer sensitivity [124, 125]. The Main Selector is defined as:

Parameter	Values selected
CC/NC PID	> 0.25
qp_sigmaqp	> 3.5
$\lvert\phi - \pi\rvert$	> 2.08

The efficiency, purity and purity $\times$ efficiency for each cut parameter, with the other cuts applied, is shown in figure 7.7 for the FD. Table 7.1 shows the effect of each cut as it is applied along with the type of events selected. The selection was the same in both detectors in order to take advantage of the similarities in the detectors; this removes some systematic error. An unfortunate result of using the same selection is that the ND cuts were not optimised. The final purity $\times$ efficiency for the Main Selector is 0.796. Figures 7.8(a) and 7.8(b) show

FD selector	No $\overline{\nu}$	No ν_e	No NC	No CC	Eff	Pur	Eff*Pur
after precuts	25348	1021	44902	37423	1.000	0.233	0.233
CC/NC PID	21998	6	701	3307	0.868	0.846	0.734
CC/NC PID and $\lvert\phi - \pi\rvert$	21895	6	580	1404	0.864	0.917	0.792
Main Selector	21196	5	297	757	0.836	0.952	0.796
Backup selector	22544	13	328	1686	0.889	0.918	0.816

Table 7.1: *The number of events below 10 GeV after each additional cut. The $\overline{\nu}_\mu$ efficiency, purity and efficiency $\times$ purity are also shown. The values were determined using high statistic MC.*

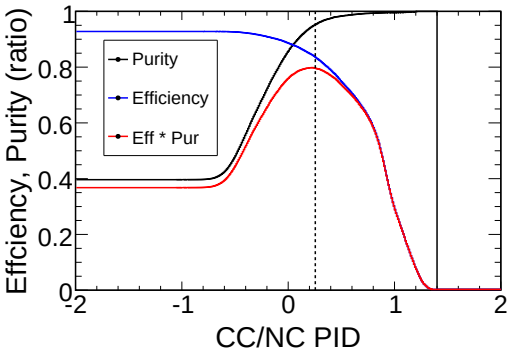

(a)

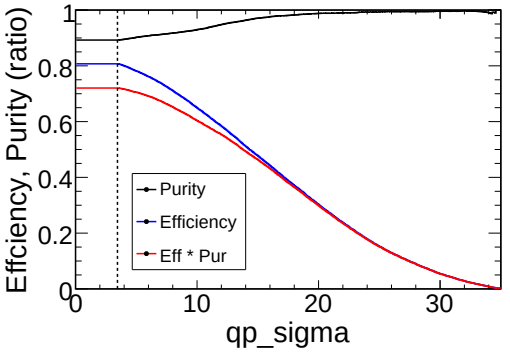

(b)

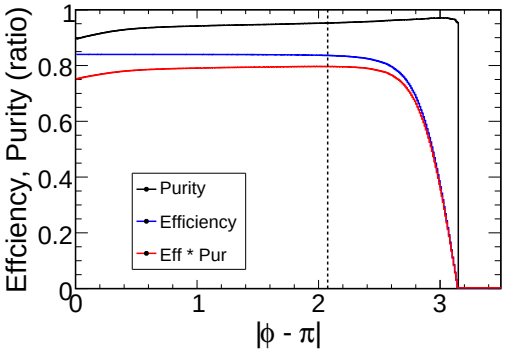

(c)

Figure 7.7: *The efficiency, purity and efficiency $\times$ purity for the parameters that are cut on in the Main Selector. Shown are each parameter with the other cuts applied. The line marked is the cut value, which is the peak of the efficiency $\times$ purity, everything to the right of the line is included. a) CC/NC PID, b)qp_sigmaqp, c) relative angle.*

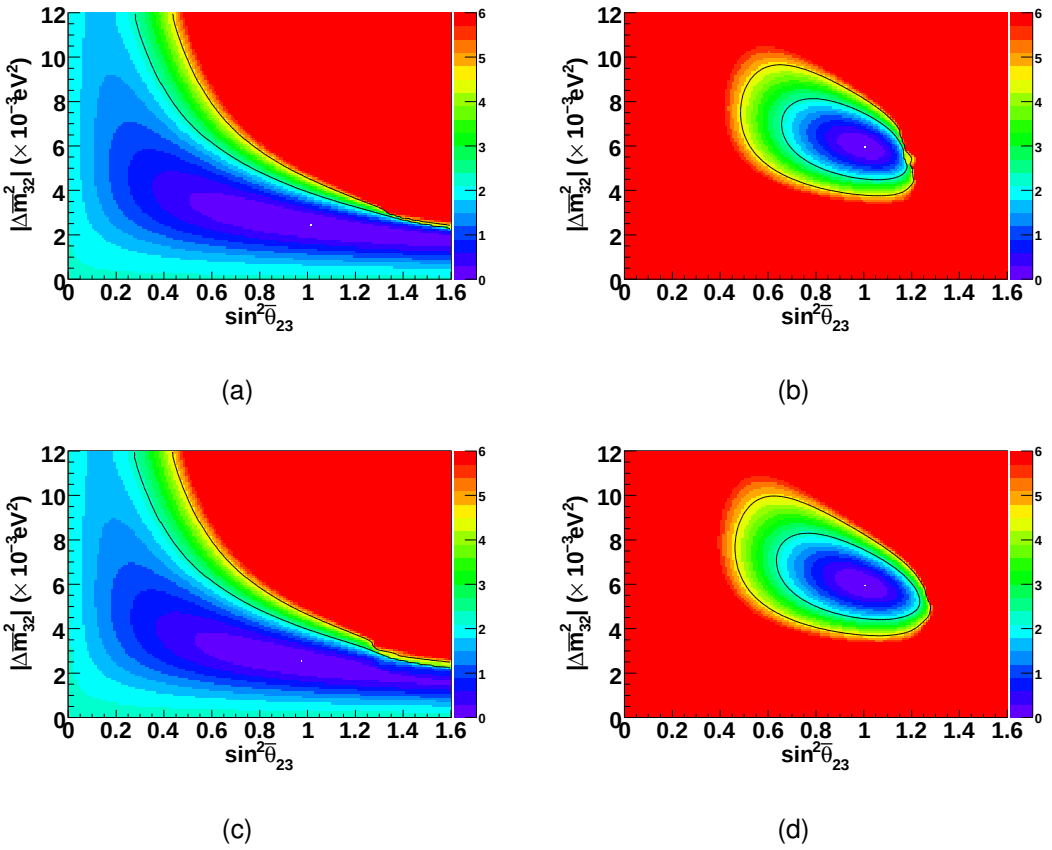

Figure 7.8: *The Gaussian sensitivities for the Main Selector at a) $\Delta\overline{m}^2_{32}$ 2.5 = $\times$ 10^{-3} eV^2 b) $\Delta\overline{m}^2_{32}$ = 6.0 $\times$ 10^{-3} eV^2 and Backup selector c) $\Delta\overline{m}^2_{32}$ = 2.5 $\times$ 10^{-3} eV^2 d) $\Delta\overline{m}^2_{32}$ 6.0 = $\times$ 10^{-3} eV^2. The two back lines are the 68 % and 90 % contours*

the Gaussian sensitivities of the Main Selector for CPT conservation and a non-CPT conserving case of $\Delta\overline{m}^2_{32}$ = 6.0 $\times$ 10^{-3} eV^2 and $\sin^2 2\overline{\theta}_{23}$ = 1. It can be seen that this analysis is more sensitive to the higher $\Delta\overline{m}^2_{32}$ than CPT conserving values, due to the NuMI focusing positive mesons, which decay to neutrinos, and defocusing negative mesons, which, in turn, decay to give anti-neutrinos. Only negative particles that go through the centre of the horns (and thus feel no $\mathbf{B}$-field) make up part of the NuMI beam. As a result, $\overline{\nu}_\mu$ have higher energies than ν_μ, with a peak around 8 GeV. CPT conserving value of $\Delta\overline{m}^2_{32}$ causes a dip, due to oscillation, on the rising slope of the NuMI $\overline{\nu}_\mu$ energy spectrum while the $\Delta\overline{m}^2_{32}$ = 6.0 $\times$ 10^{-3} eV^2 would result in a dip due to oscillation at energies in the peak of the spectrum.

7.3 Selector Checks

The Main Selector was chosen using the best efficiency $\times$ purity for events below 10 GeV as the figure of merit (FOM). Section 7.3.1 investigates whether choosing the cuts by directly studying the sensitivity in $\Delta\overline{m}^2_{32}$ and $\sin^2 2\overline{\theta}_{23}$ would affect the result. The CC/NC PID was trained on all CC interactions as signal, and NC interactions as only background. In section 7.3.2 retraining the PID for different signal and backgrounds are investigated. Section 7.3.3 investigates the use of the PID that is used in the 2008 ν_μ-CC paper [1] as a parameter to cut on and only one other cut to make a backup selector.

7.3.1 Best Sensitivity Search

As explained in section 7.2.5, the optimisation of the Main Selector was done based upon efficiency $\times$ purity for events below 10 GeV rather than on sensitivity directly. A separate study was carried out in order to check whether efficiency $\times$ purity gives the best sensitivity. The cut values of the Main Selector were varied and a set of likelihood surfaces created. For each additional cut of the selector, the difference in $\Delta\chi^2$ between the best fit value and no oscillation ($\Delta\overline{m}^2_{32}$ = 0), and also the best fit value and $\Delta\overline{m}^2_{32}$ = 10.0$\times$10^{-3} eV^2, was calculated as a function of the cut. If the $\Delta\chi^2$ was found to be greater than the Main Selector's $\Delta\chi^2$, the difference between them was plotted in a 2D histogram (figure 7.9) as a function of how much the $\Delta\chi^2$ was higher in the new selector over the Main Selector. Figure 7.9, shows that the Main Selector cut does not produce optimum sensitivity; however, there is no great improvement to be made in $\Delta\chi^2$ by excluding no oscillation, or by excluding a $\Delta\overline{m}^2_{32}$ of 10 $\times$ 10^{-3} eV^2. The Main Selector is thus essentially at the optimal value. The best $\Delta\chi^2$ using the cuts as in the Main Selector, and the best cuts for excluding zero oscillation (Main Selector0) and $\Delta\overline{m}^2_{32}$ 10 $\times$ 10^{-3} eV^2 (Main Selector10), are shown in Table 7.2. Table 7.3 shows how these new selectors score on the efficiency $\times$ purity scale.

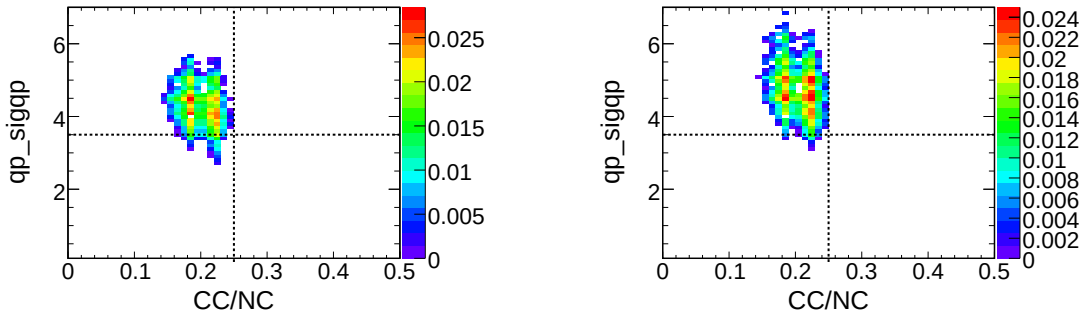

(a) excluding No Osc

(b) excluding $\Delta\overline{m}^2_{32}$ = 10 eV^2

Figure 7.9: *Values of CC/NC PID and qp_sigmaqp which exclude a) $\Delta\overline{m}^2_{32}$ = 0 b) $\Delta\overline{m}^2_{32}$ = 10 eV^2 at a greater $\Delta\chi^2$ than the standard main selector cut.*

7.3.2 Retraining CC/NC PID

The CC/NC PID was trained on all CC events as signal and only NC events as background. Due to the different interaction kinematics of $\overline{\nu}_\mu$ to ν_μ, it would be reasonable to assume that training the PID, using only $\overline{\nu}_\mu$-CC as signal events, and all other events as background would improve the selection. The PID was therefore re-trained with a signal sample that had been classified as $\overline{\nu}_\mu$ and reconstructed with a positive track while the background sample consisted each of the following separately:

a Nominal (NC only).

b NC events with a positive reconstructed track.

c NC and ν_e events with a positive reconstructed track.

d NC and all non-$\overline{\nu}_\mu$ events with a positive reconstructed track.

Using these new NC PID samples the best efficiency $\times$ purity was found for each case, keeping the other cuts the same. It was found that efficiency $\times$ purity curve broadened but the actual best value was unchanged (Figure 7.10). It maybe reasonable to assume that different interaction kinematics would result in a different PID. However, the sample of ν_μ-CC that appear in the non-signal region are high y events, events where most E$_\nu$ is transferred to the nucleon which produces high energy showers compared to the μ track. The most events in both ν_μ and $\overline{\nu}_\mu$ sample are track like, so have the same characteristics.

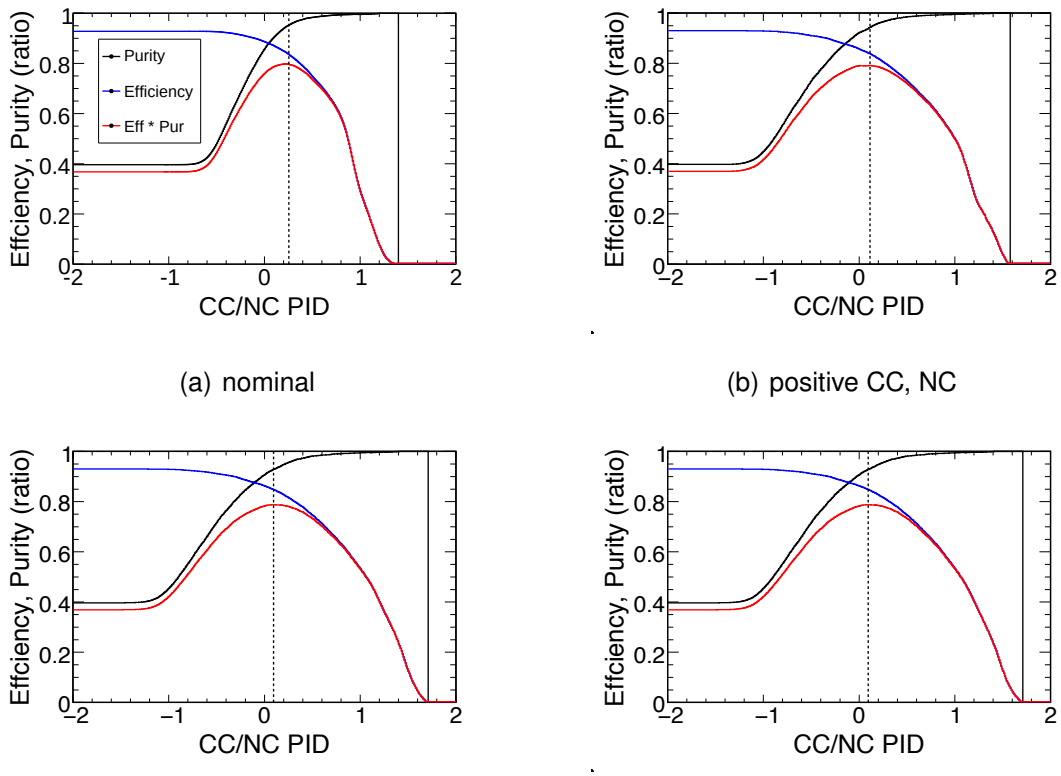

(a) nominal

(b) positive CC, NC

(c) positive CC, NC ν_e

(d) positive CC and all none CC

Figure 7.10: *The purity (blue) efficiency (black) and efficiency $\times$ purity red for different trainings of the CC/NC pid. a) Is the original PID values, all CC-interaction are included as signal and only NC-events are classed as background. b) Only positive CC-interactions are included as signal and only NC-events are classed as background. c) Only positive CC-interactions are included as signal, NC and ν_e interactions are classed as background. d) Only positive $\overline{\nu}_\mu$-CC interactions, anything that is not $\overline{\nu}_\mu$-CC interaction is classed as background.*

selector	($\Delta\chi^2$ w.r.t best fit) $\Delta\overline{m}^2_{32}$ = 0	($\Delta\chi^2$ w.r.t bestfit) $\Delta\overline{m}^2_{32}$ = 10$\times10^{-3}$ eV^2
Main Selector	2.029	1.283
Main Selector0	2.057	1.308
Main Selector10	2.052	1.308
Backup Selector	2.016	1.335
Backup Selector0	2.054	1.321

Table 7.2: *Comparing the best exclusion for $\Delta\overline{m}^2_{32}$ = (0 and 10)$\times10^{-3}$ eV^2. Main Selector0 is the best set of cuts, using the Main Selector parameters, at excluding no oscillation. Main Selector10 is the best set of cuts, using the Main Selector parameters, at excluding $\Delta\overline{m}^2_{32}$ = 10. Backup Selector0 is the best set of cuts, using the Backup Selector parameters, at excluding no oscillation.*

7.3.3 The $\overline{\nu}_\mu$ Backup Selector

The Main Selector for the main MINOS $\overline{\nu}_\mu$ result was announced in 2009 [88]. It was chosen because it has the best efficiency $\times$ purity below 10 GeV and small systematic errors. In this thesis, as well as evaluating this selector, a backup selector was created using the CC/NC PID that is used in the 2008 ν_μ result [1]. This PID is called k-nearest neighbour PID (kNN PID), where k stands for the number of nearest neighbours. The Backup Selector makes use of fewer cuts, as this reduces the error in the MC data comparison. The new kNN PID is made of four variables:

- **Number of track scintillator planes** - muons usually have a longer tracks.
- **Mean pulse height of track hits** - muons are MIP particles so have a low pulse height
- **Signal fluctuation** - muons deposit a consistent amount of energy along their track
- **Transverse track profile** - muons usually only hit one scintillator strip per plane

Selector	Purity	Efficiency	Efficiency*Purity
Main Selector	0.926	0.855	0.792
Main Selector0	0.943	0.832	0.785
Main Selector10	0.952	0.825	0.785
Backup selector	0.918	0.889	0.816
Backup Selector0	0.896	0.905	0.811

Table 7.3: *Efficiencies and purities for different selectors. Main Selector0 is the best set of cuts, using the Main Selector parameters, at excluding no oscillation. Main Selector10 is the best set of cuts, using the Main Selector parameters, at excluding* $\Delta\overline{m}^2_{32}$ *= 10*

Two training sets were created in MC for signal (CC) interactions and background (NC). These were then used to create a pdf for the four variables. The event to be classified was compared to these pdfs using the k-nearest neighbour algorithm [126]. The kNN algorithm uses the training sets to estimate the density of the signal and background events of the nearest k events,

$$\mathrm{k} = \mathrm{k_s} + \mathrm{k_B}, \tag{7.7}$$

where $\mathrm{k_s}$ is the number of signal events and $\mathrm{k_B}$ is the number of background events. The probability of an event being signal ($\mathrm{P_s}$) is then:

$$\mathrm{P_s} = \frac{\mathrm{k_s}}{\mathrm{k}}. \tag{7.8}$$

To work out the nearest neighbours a distance function D is found. A vector X_i is constructed using the values of the event i:

$$D = \left(\sum_{i=1}^{d} |X_i^T - X_i^Q|^2 \right)^{\frac{1}{2}}, \tag{7.9}$$

where d is the number of variables, X_i^T are the values from the training set and X_i^Q are the vales of the event to be classified. For this analysis k = 80. A more detailed description of this method is found in [122].

In addition, the Backup Selector uses relative angle to remove further background events. The oscillation dip for CPT conserving $\Delta\overline{\mathrm{m}}^2_{32}$ appears at 1.5 GeV.

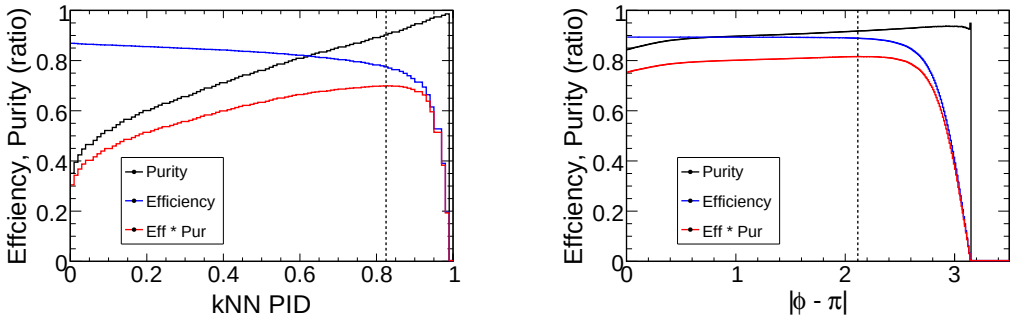

(a) (b)

Figure 7.11: *The efficiency, purity and efficiency $\times$ purity for the parameters make up the Backup Selector. Shown are each parameter with the other cuts applied. The line marked is the cut value, which is the highest efficiency $\times$ purity, everything to the right of the line is included.*

So the best efficiency $\times$ purity was studied $\overline{\nu}_\mu$ energies below 5 GeV in addition to below 10 GeV. It was found that for the kNN PID it did not change, although it did change slightly the relative angle cut. Moreover, when the sensitivity for CPT oscillations was checked the cuts giving the best efficiency $\times$ purity below 10 GeV was found to be best for sensitivity. The Backup Selector is defined as:

$$\begin{aligned} \text{kNN PID} &> 0.826 \\ |\phi - \pi| &> 2.120. \end{aligned}$$

Figure 7.11 shows the parameters as a function of one cut, with the other cut applied. The selected events are those to the right of the cut. Table 7.1 shows the events that are selected in high-statistic unoscillated FD MC. As with the Main Selector (section 7.3.1), the kNN PID parameter cut was varied to see if the sensitivity could be improved. A marginal improvement in disfavouring no oscillation was found; however, with these values, $\Delta\overline{m}^2_{32}$ = 10 $\times$ 10^{-3} eV^2 has a smaller $\Delta\chi^2$, so the value found by efficiency $\times$ purity was used. Figures 7.8(c) and 7.8(d) show the Gaussian sensitivities for this selector. It can be seen that at CPT conservation the sensitivity is about the same as the Main Selector, while at $\Delta\overline{m}^2_{32}$ = 6.0 $\times$ 10^{-3} eV^2 and $\sin^2 2\overline{\theta}_{23}$ = 1 the Main Selector performs better. It can be seen from figure 10.1 and figure 10.3 that there is more contamination at higher energy, which will affect the higher $\Delta\overline{m}^2_{32}$ while at the CPT conserving

value the contamination is the same as the energies of the dip from oscillation.

7.4 Summary

In order to measure the neutrino oscillation parameters the type of interaction in the events must be identified correctly. Therefore, only events that took place within a part of the detectors that is well understood, and when the beam was good, are included in this analysis. The investigation of the $\Delta\overline{m}^2_{32}$ and $\sin^2 2\overline{\theta}_{23}$ oscillation parameters requires the selection of $\overline{\nu}_\mu$-CC events. The event selection for this analysis was made with the Main Selector which cuts on a CC/NC PID to select CC events and qp_sigma and relative angle to select only well reconstructed tracks.

The Main Selector was optimised for efficiency $\times$ purity below 10 GeV. In order to verify that this gave the best sensitivity to $\overline{\nu}_\mu$ oscillations combinations of cuts on the Main Selector parameters were tested to see whether any were better at excluding no oscillation or $\Delta\overline{m}^2_{32} = 10\times10^{-3}$. Some of those other cuts were found to be marginally better than the Main Selector at excluding one or the other but not both.

The Main Selector includes the CC/NC PID used in the first MINOS ν_μ-CC paper [82]. Training this CC/NC PID on $\overline{\nu}_\mu$-CC interactions only, rather than on all CC events, was has been shown not to make a difference to the final sensitivity.

A Backup Selector has also been created; this uses fewer parameters and the same PID as the 2008 ν_μ-CC [1] analysis. This Backup Selector has a slightly better efficiency $\times$ purity at energies less than 10 GeV; however, the overall sensitivities are the same at CPT conserving values, while at higher $\Delta\overline{m}^2_{32}$, the new selector has slightly worse sensitivity. This is due to the Backup Selector being more efficient, but having larger contamination at higher energies. This contamination is at higher energies than the expected oscillation dip for CPT conserving values, however there are few events at low energy so the higher efficiency doesn't gain anything.

Chapter 8

Extrapolation of $\overline{\nu}_\mu$ Events

> "Mark my words: time is a great healer. Unless you've got a rash, in which case you're better off with ointment." (Holly - series 8 Krytie TV)

The measurement of the $\overline{\nu}_\mu$ oscillation parameters requires an accurate knowledge of the un-oscillated spectrum in the far detector. In the $\overline{\nu}_\mu$ analysis the near detector is used to correct for uncertainties in the knowledge of this spectrum, for example the $\overline{\nu}_\mu$ cross-section with steel and the beam flux (section 8.1). The neutrino energy spectrum of actual event energy is then compared to a predict neutrino energy spectrum (section 8.2). The dominant oscillation is $\overline{\nu}_\mu$ to $\overline{\nu}_\tau$. The $\overline{\nu}_\tau$ are mostly of too low energies to interact. However, when a $\overline{\nu}_\tau$ does interact with the detector via the CC interaction a τ^+ is produced which can decay into a μ^+. The $\overline{\nu}_\mu$ analysis measures a deficit of μ^+ in the far detector, so "extra" μ^+ in the far detector would reduce this deficit. The affect of μ^+ from τ^+ decay on the extrapolation is investigated for different $\Delta\overline{m}^2_{32}$ in section 8.3. Furthermore, events in the ND extrapolate differently depending on the type of interaction. Sections 8.4,8.5 explore what happens if the interactions are not well modelled.

8.1 Extrapolation Method

To make an accurate measurement of $\Delta\overline{m}^2_{32}$, the prediction of an un-oscillated spectrum at the FD is of utmost importance. The FD MC gives a crude prediction using current knowledge of ν ($\overline{\nu}$) cross-sections, beam flux and the detector

acceptance, however there are large errors associated with these. With the two-detector design of the MINOS experiment, the ND can be used to correct for some of these uncertainties and these corrections can be carried over to the FD. The ND was placed close to the beam source so that the beam can be sampled before oscillation has a chance to take effect[1]. The spectrum measured at the ND can then be used to get a more accurate prediction at the FD; the detectors were made to be as similar as possible, so that uncertainties in the knowledge of cross-sections etc. would cancel. This cancellation only works if the flux is the

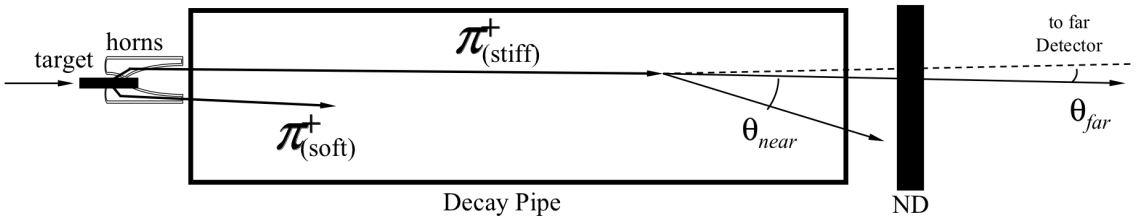

Figure 8.1: π *decay in the decay-pipe. The ND and FD have different* ν *spectra due to the different solid angles subtended by the detectors. The ND has a larger angular acceptance than the FD, due to the difference in distance between the decay point and each detector. Also the ND sees a line source compared to the point source of the FD.*

same in both. However, this is not strictly true for the MINOS detectors as the FD is 735 km away, so only sees a point source which covers a small angle of the beam. The ND is much closer to the decay pipe and therefore subtends a much larger solid angle (figure 8.1). Furthermore, the parent particles decay at different points within the decay pipe, with higher-energy parents decaying closer to the ND, thus allowing the ND to record a wider range of angles for higher energy parents, which outweighs the increase in Lorentz boost which would narrow the angle in the laboratory frame. This has the effect of lowering the typical event energy in the ND compared to the FD. Figure 8.2 shows how three different neutrino energies in the ND extrapolate to the FD with a greater spread of energies at higher energy. To account for this, four methods of extrapolation were studied [116]. The beam matrix method, which was also used in the ν_μ-CC analysis

[1] At the energies that the MINOS detectors can detect. Neutrinos with an energy of around 3.1 MeV would oscillate over this distance, using the oscillation parameters from [1].

of the second-run data [1], was chosen. The method gets its name from the "beam matrix" B_{ij} (figure 8.3), a 2-D matrix that associates the ND reconstructed energy with a FD reconstructed energy. The ND events are transformed via the Beam Matrix, they must be converted to an spectrum of true energies. This is achieved by first stripping the ND spectrum of background (NC) events. Then the reconstructed energy is converted to true energy via a non-diagonal matrix. Next an efficiency correction is made to take out the effect of the cuts and reconstruction inefficiencies. The efficiencies and purities are worked out via a near detector helper file. The helper file is a high-statistic MC simulation of the ND data. This leaves a pure true energy spectrum of events in the ND fiducial volume. The neutrino flux in the ND is obtained by dividing by neutrino cross section and by the mass of the fiducial volume.

Monte Carlo simulations of the neutrino flux are then used to convert this ND flux into a FD flux. The beam matrix is formed by splitting the parents of the neutrinos into separate representative sets, one set for each ND energy bin, and then scaling these until they match the ND neutrino flux. The contribution of each of these scaled sets is then calculated for the FD and summed to give the flux at the FD. This information is stored in a file called a flux file. The procedure is then reversed: the cross-sections, and the mass of the fiducial volume are multiplied back in, to produce an energy spectrum of all events interacting in the fiducial volume. Reconstruction and selection efficiencies are then applied to give the energy spectrum of selected events. Oscillations are then applied to the true spectrum as a function of energy. Finally a non-diagonal matrix transforms the remaining true energy spectrum to reconstructed energy and the NC events are then inserted to give a prediction of the FD energy spectrum. In this analysis neutrinos and anti-neutrinos may have different oscillation parameters; therefore, the ν_μ and $\overline{\nu}_\mu$ events are extrapolated separately [87] (figure 8.5) which allows for different oscillation parameters and thus non-CPT conserving oscillations.

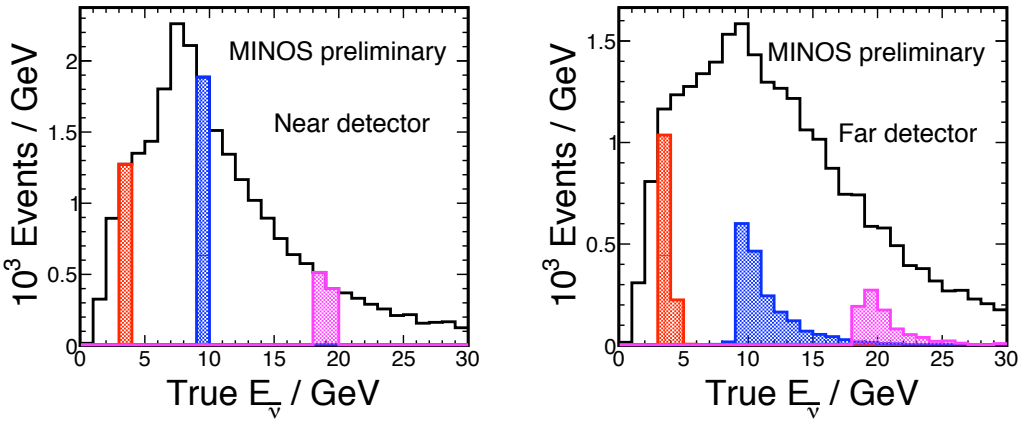

Figure 8.2: *Energies in the ND extrapolated to energies in the FD. The black line is the total energy spectrum. The coloured columns show events in the ND with the same energy. The high-energy ν are affected more by the different solid angle covered by the ND and so spread out more [127].*

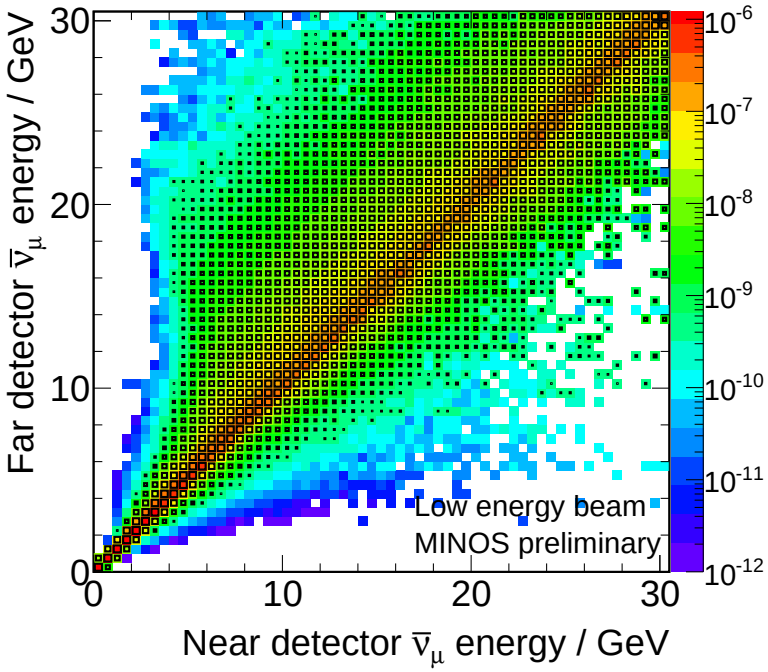

Figure 8.3: *The mean distribution of events in the FD for one event in the ND, as a function of the energy of that event [127].*

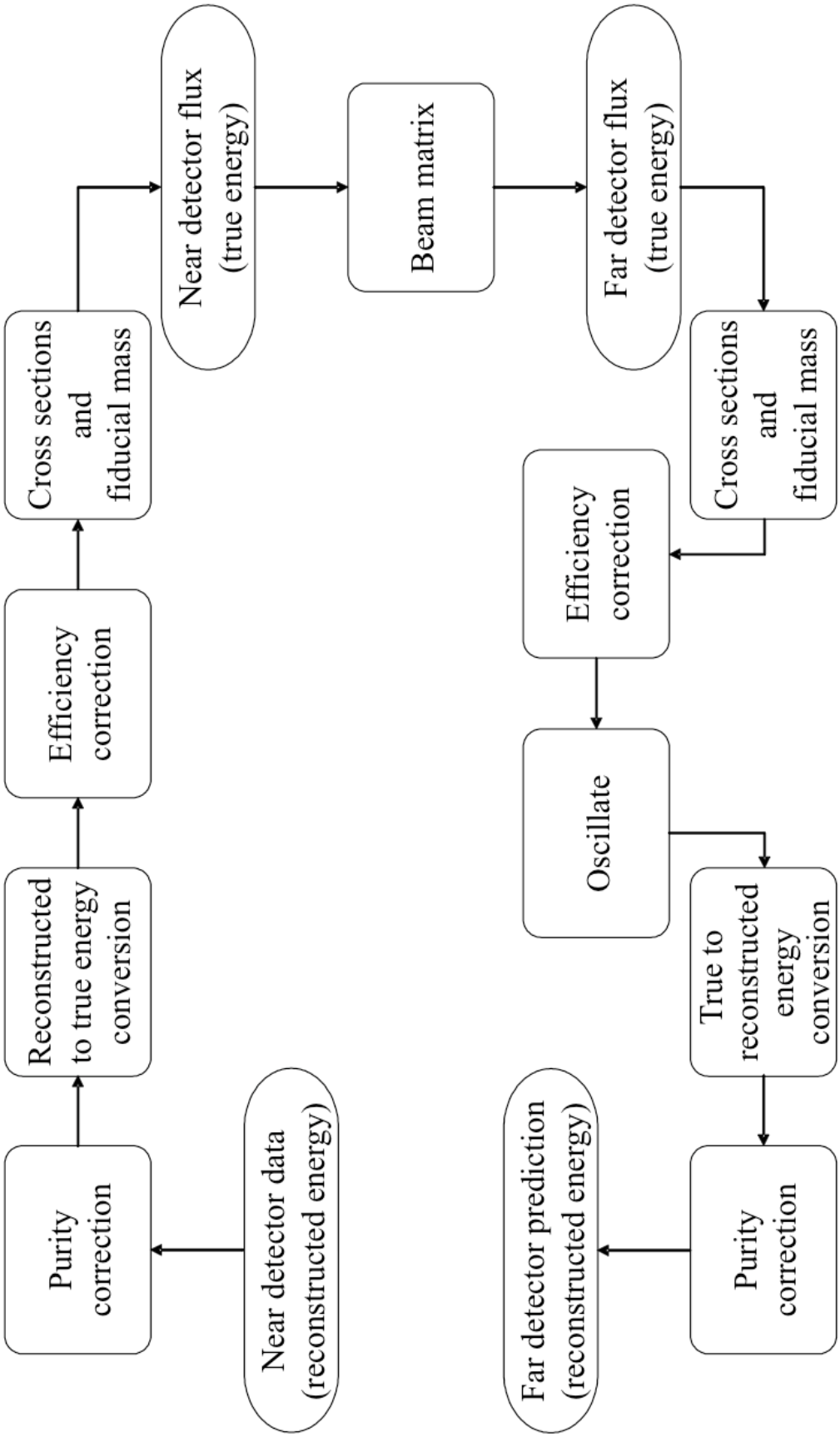

Figure 8.4: *The steps involved in the matrix method, used in the ν_μ analysis [82, 116]*

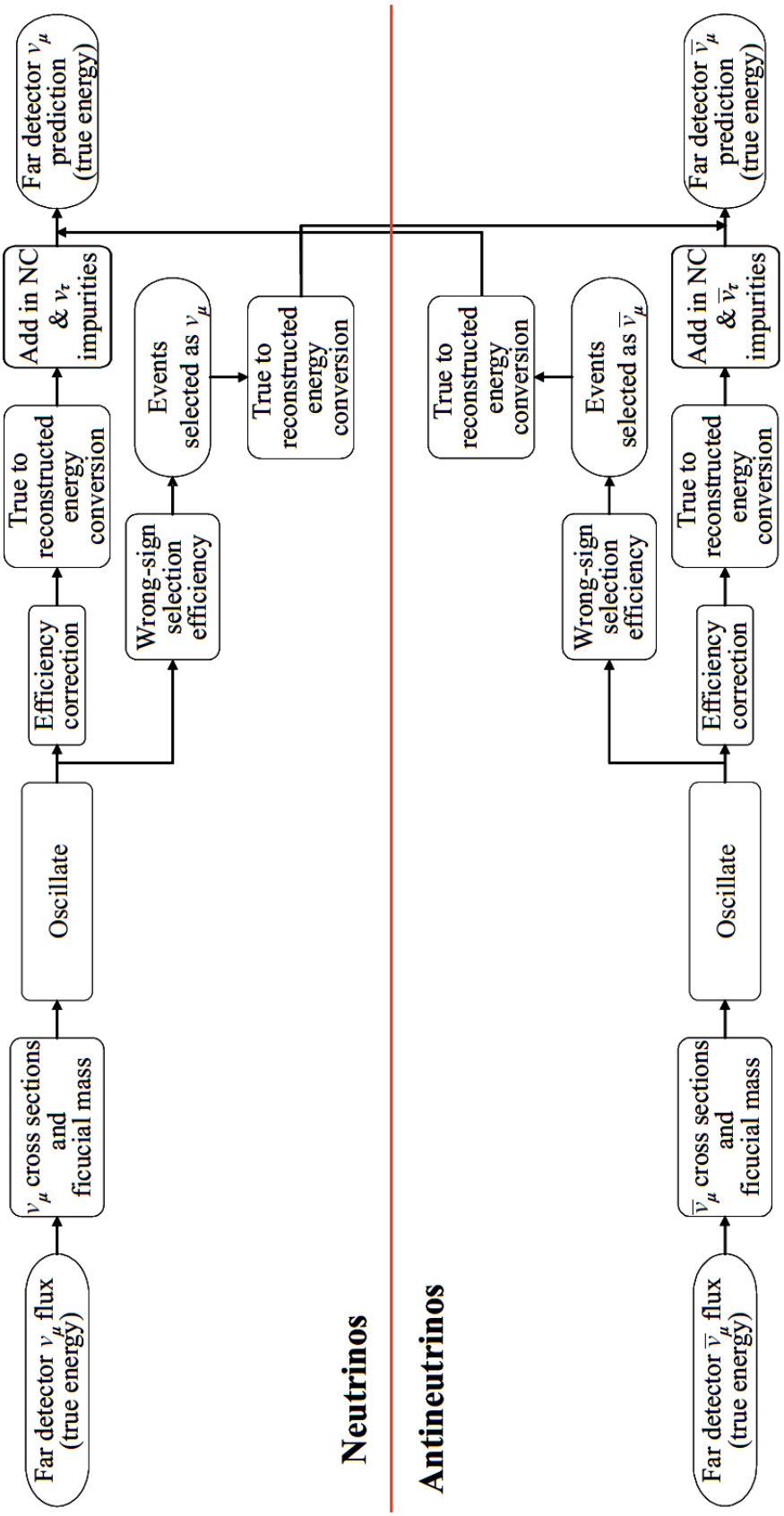

Figure 8.5: *The steps added to the ν_μ matrix (shown in figure 8.4) for the $\overline{\nu}_\mu$ analysis [87].*

8.2 Fitting Events

In order to accounts for the differing beam conditions between the runs, each run is extrapolated and compared to the corresponding FD data separately. The predicted spectrum is compared to the FD data using the likelihood function [11]:

$$-2\ln\lambda(P) = 2\sum_{i=1}^{N}\left[E_i(P) - n_i + n_i\ln\frac{n_i}{E_i(P)}\right], \tag{8.1}$$

where n_i is the number of data events in the i^{th} bin, $E_i(P)$ corresponds to the predicted number of events in the i^{th} bin from the extrapolation and P represents the combination of oscillation parameters being used. This likelihood is then maximised using the MINUIT package [128].

8.3 Tau Background

In the oscillation model, the muon neutrinos disappear because they have changed into tau neutrinos, which means that the number of ν_τ can be worked out by equation 2.38. This causes another background that has not been considered so far. It comes from ν_τ interacting with the detector to produce a τ which can decay to μ. It does this mainly through

$$\begin{aligned} {}^{56}Fe + \nu_\tau \rightarrow X + \quad & \tau^- \\ & \tau^- \rightarrow \mu^- + \overline{\nu}_\mu + \nu_\tau \end{aligned} \tag{8.2}$$

with a similar process for $\overline{\nu}_\tau$. Both processes have a branching ratio of 17.4% [11]. As the taus have a lifetime of only 290 $\times$ 10^{-15} s they decay in the steel, so cannot be identified by kinks in the track. A special study investigated this background could affect the measurement of the parameters, and whether it could be separated out from the signal. Due to the mass of the τ, at low energy the interaction equation 8.2 is suppressed. The tau decays via a three-body decay (figure 8.6), so the muon can have a range of energies. The rest of the energy is taken away by the neutrinos so the reconstructed energy is lower than that of the interaction neutrino. This means that the tau events are not necessarily reconstructed with the same energy as the neutrino that disappeared in the original oscillation. This has the effect of increasing events at lower energy. $\Delta\overline{m}^2_{32}$ has

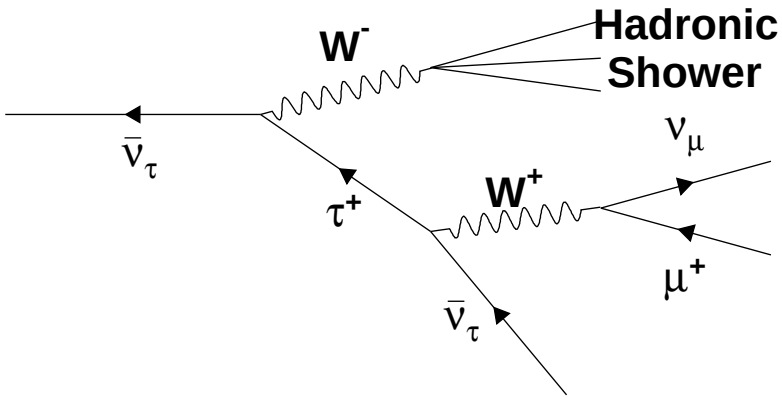

Figure 8.6: *Feynman diagram of a $\overline{\nu}_\tau$-CC interaction in the MINOS detector. The μ^+ produced in this reaction will be at lower energy than the neutrino that oscillated due to the energy taken away by the out going ν_μ, and thus more events appear in the oscillation dip.*

been constrained to $<$10 eV^2 by the Super-K experiment through their analysis of atmospheric neutrinos. Super-K is not able to measure $\Delta\overline{m}^2_{32}$ directly as it cannot separate μ^- and μ^+, but a third of its events would be $\overline{\nu}_\mu$. To determine how the taus would affect the reconstructed energy spectrum and thus the measurement of the oscillation parameters, a range of $\Delta\overline{m}^2_{32}$ were studied at with high-statistic MC. The reconstructed energy spectrum, with and without taus (figure 8.7), and the ratio to the non-oscillated spectrum, were plotted. At CPT-conserving value even with high-statistic MC the difference in the energy spectrum with and without taus is within an error bar, so if $\Delta\overline{m}^2_{32}$ conserves CPT it is not expected to make much difference to the final result. However, if CPT is not conserved and $\Delta\overline{m}^2_{32}$ is higher than Δm^2_{32}, then the taus do make a noticeable difference to the reconstructed energy spectrum. These MC fake data can then be fitted to see if the oscillation parameters change as a result of the differences. Table 8.1 shows that at CPT-conservation the result is the same whether taus are included in the extrapolation or left out. However, at non-CPT values the effect on $\sin^2 2\overline{\theta}_{23}$ is considerable, over 10 error bars, although $\Delta\overline{m}^2_{32}$ is stable. This is a result of the $\overline{\nu}_\mu$ oscillating to $\overline{\nu}_\tau$ being above the rest mass of the tau. When the tau decays, it produces muons of that appear in the part of the spectrum where there is a lack of muons from $\overline{\nu}_\mu$ oscillation so "fill in" the dip. This means that if $\Delta\overline{m}^2_{32}$ is not at

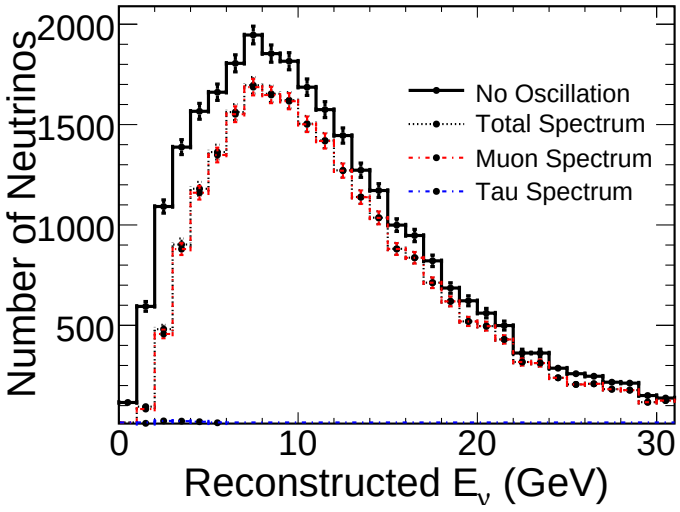

(a)

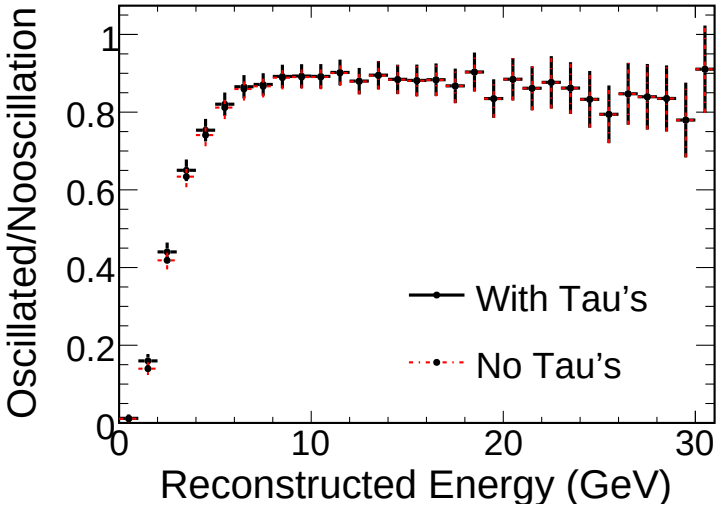

(b)

Figure 8.7: *The spectrum of muons detected after pre cuts for* $\Delta\overline{m}^2_{32}$ *= 2.5* $\times$ *10*$^{-3}$ *eV*^{2} *and* $\sin^2 2\overline{\theta}_{23}$ *= 1 for full MC POT. In figure a) the thick black line shows the total* $\overline{\nu}_\mu$ *energy spectrum without oscillation detected. The dashed black line is the total energy spectrum detected after oscillation. The blue dashed line is the* $\overline{\nu}_\mu$ *energy spectrum detected after oscillation. The red dashed line is the energy spectrum of* $\overline{\nu}_\tau$ *after detected after oscillation. Figures b)show the ratio of the total energy to the total energy spectrum after oscillation in black and the ratio of the un-oscillated energy spectrum to the* $\overline{\nu}_\mu$ *spectrum after oscillation in blue. It can be seen that for* CPT*-conserving value of* $\Delta\overline{m}^2_{32}$ *the ratio plots are within an error bar. For greater* $\Delta\overline{m}^2_{32}$ *the* $\overline{\nu}_\tau$ *have a greater affect due to the oscillation occurring above the energy needed to create taus.*

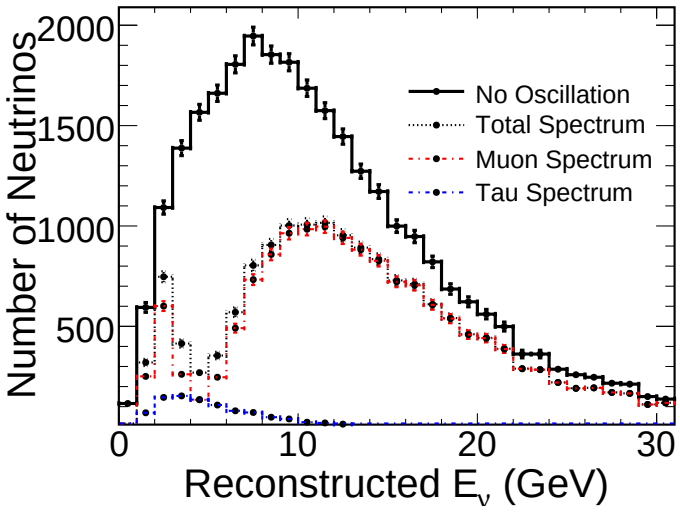

(a)

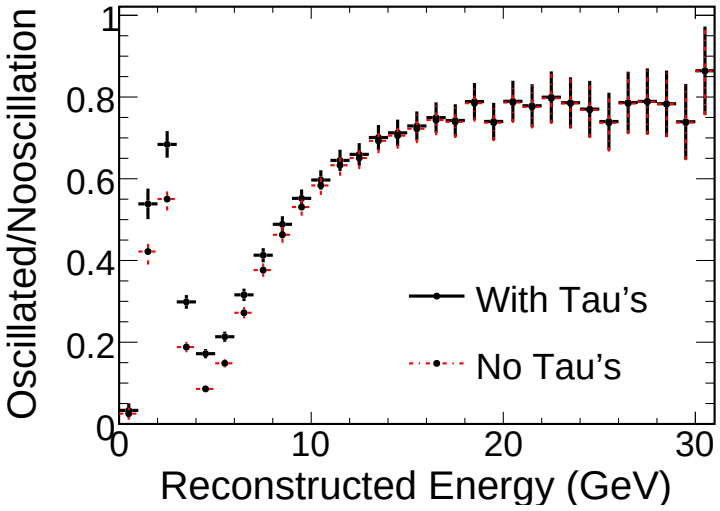

(b)

Figure 8.8: *The spectrum of muons detected after pre cuts for* $\Delta\overline{m}^2_{32}$ *= 7.5* $\times$ *10*$^{-3}$ *eV*^{2} *and* $\sin^2 2\overline{\theta}_{23}$ *= 1 or full MC POT. For further description see figure 8.7.*

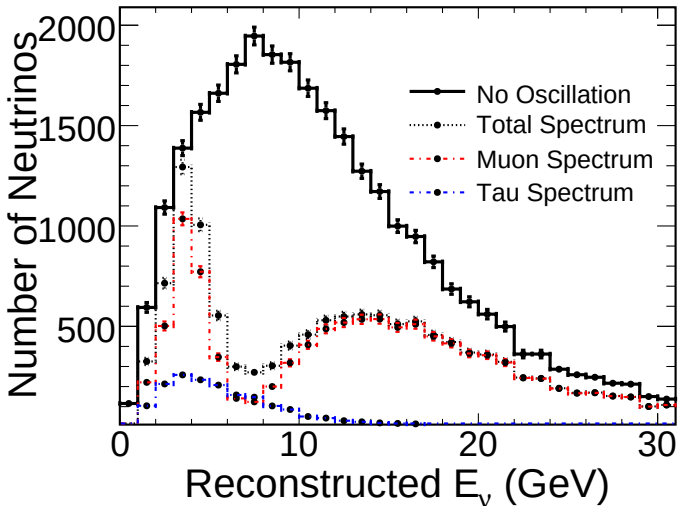

(a)

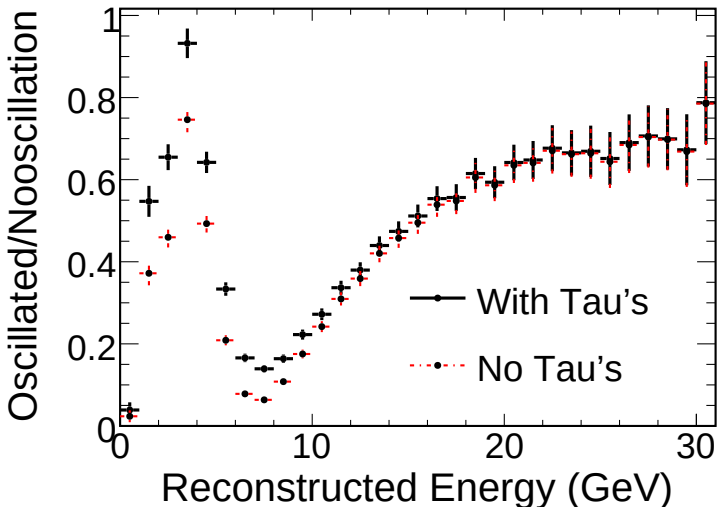

(b)

Figure 8.9: *The spectrum of muons detected after pre cuts for* $\Delta\overline{m}^2_{32}$ *= 12* $\times$ *10*$^{-3}$ *eV*^{2} *and* $\sin^2 2\overline{\theta}_{23}$ *= 1 or full MC POT. For further description see figure 8.7.*

CPT-conserving value to get the correct $\sin^2 2\overline{\theta}_{23}$ $\overline{\nu}_\tau$ need to be included in the extrapolation.

	Entered values	Fake Data $\overline{\nu}_\mu$ only	Fake Data including $\overline{\nu}_\tau$	Fake Data including $\overline{\nu}_\tau$
		Extrapolation $\overline{\nu}_\mu$ only	Extrapolation $\overline{\nu}_\mu$ only	Extrapolation including $\overline{\nu}_\tau$
$\sin^2 2\overline{\theta}_{23}$	1	1.007	0.996	1.005
$\Delta\overline{m}^2_{32} \times 10^{-3}$ eV^2	2.5	2.46	2.46	2.47
$\sin^2 2\overline{\theta}_{23}$	1	0.995	0.953	0.989
$\Delta\overline{m}^2_{32} \times 10^{-3}$ eV^2	7.5	6.97	7.06	6.98
$\sin^2 2\overline{\theta}_{23}$	1	1.000	0.964	1.000
$\Delta\overline{m}^2_{32} \times 10^{-3}$ eV^2	12.0	11.98	12.15	11.97

Table 8.1: How including taus affect the found best fit value for different entered $\Delta\overline{m}^2_{32}$. The second column are the values the fake data were oscillated with. The third column contains the found values of fit when only $\overline{\nu}_\mu$ are included in the fake data and the extrapolation only extrapolates $\overline{\nu}_\mu$. The forth column contains the values of the fit when the fake data includes $\overline{\nu}_\tau$ from oscillation of $\overline{\nu}_\mu$, but the extrapolation only includes $\overline{\nu}_\mu$. The fifth column contains the values of the fit when the fake data includes $\overline{\nu}_\tau$ from oscillation of $\overline{\nu}_\mu$ and the extrapolation includes $\overline{\nu}_\tau$ from oscillation of $\overline{\nu}_\mu$.

8.4 Effects of Cuts on the Extrapolation

The selector was chosen to maximise the value of efficiency $\times$ purity in the region below 10 GeV in reconstructed neutrino energy [123]. To study the effect of data-MC differences on the extrapolation, the cuts in the ND was varied simultaneously in the ND MC, which went into the extrapolation helper, and the ND data. The flux and FD files were unchanged [129]. The ND data was then extrapolated un-oscillated to the FD. This prediction was then compared to the nominal prediction. If there was good agreement between data and MC the prediction would

not change as a result of the shifted cuts. On cut at a time was shifted so that the purity $\times$ efficiency changed by a relative 3 % in each direction. Figure 8.10 shows the efficiency $\times$ purity as a function of each cut value, with the other cuts remaining unchanged. Table 8.2 shows the nominal cut values as well as those corresponding to the $\pm$ 3 % shift in efficiency $\times$ purity obtained from figure 8.10.

For the extrapolation, only Run I data and MC weights were used. Run I I data

Variable	Nominal	Value +	Value −
CC/NC PID	> 0.25	> 0.44	> 0.1
$\lvert\phi - \pi\rvert$	> 2.08	> 2.38	> 0.78
(q/p)/σ(q/p)	> 3.5	> 5.7	> 0

Table 8.2: *Main Selector Near Detector cut values: nominal as well as those corresponding to +3 % and -3 %.*

were not included in this study because the difference in the ratio of the differences between data and MC between the runs is small. Figure 8.11 displays the predicted un-oscillated FD $\overline{\nu}_\mu$ spectrum with the shifted efficiency $\times$ purity ND cuts, applied as well as the ratio to the nominal prediction. The largest departure from the nominal prediction comes from CC/NC PID where the deviation reaches 14 % below 1 GeV. The changes in the other cuts cause a difference of less than 5 % over the whole energy range. These discrepancies are smaller than the differences caused by changing the CC, NC backgrounds by 50 % which is the uncertainty on the background (section 9.1.4). If the differences are caused by incorrect simulation of the background, and not by incorrect simulation of $\overline{\nu}_\mu$, the uncertainty due to a difference between data and MC is already covered by the 50 %.

8.5 Spatial Variations in the Data/MC Agreement

Another test performed was to see if the difference between high statistic MC and data was the same in all regions of the ND fiducial volume. If the difference between data and MC vary over the detector volume then this difference could

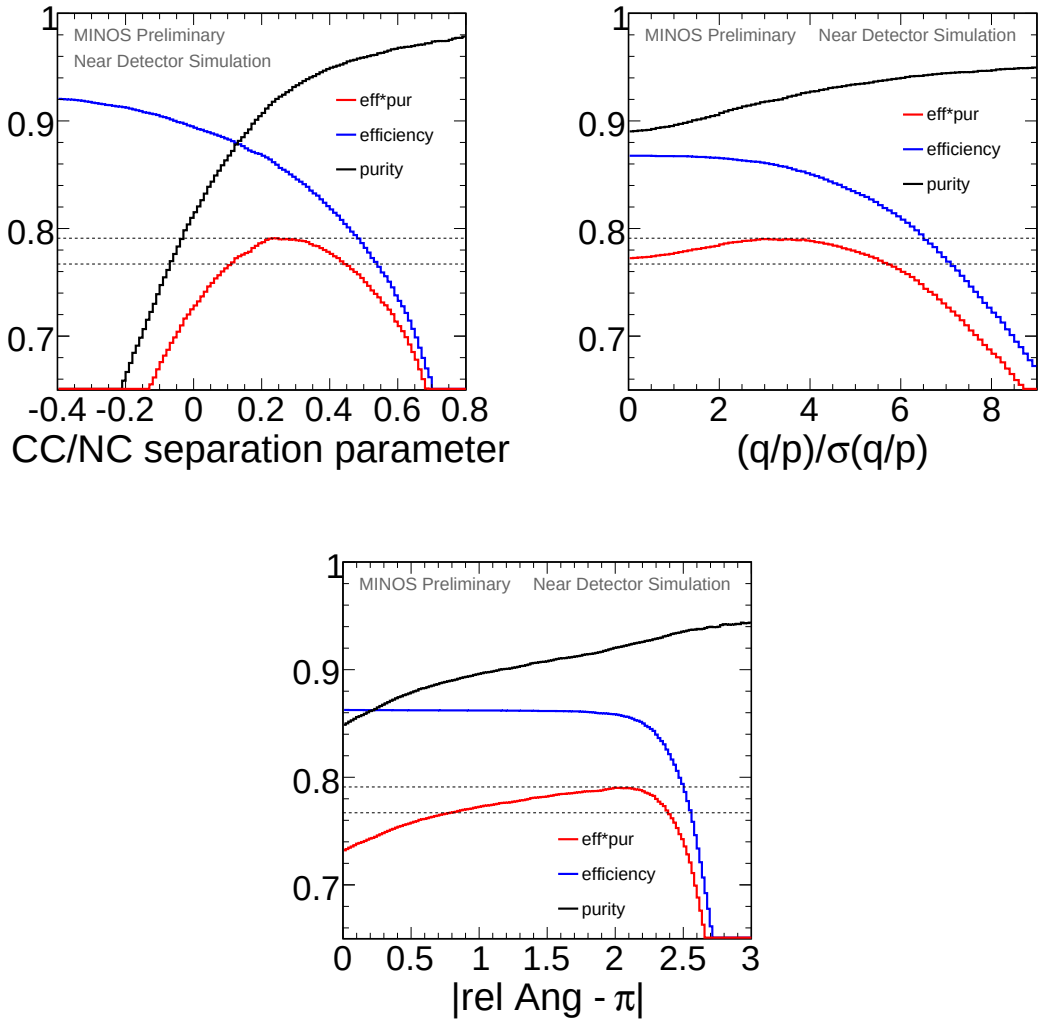

Figure 8.10: *Efficiency (blue), purity (black), and efficiency × purity (red) as a function of the cut on each variable in the Main Selector. The cuts on the other variables are kept at their nominal values. The dashed lines mark the highest efficiency × purity and 3 % below the highest value.*

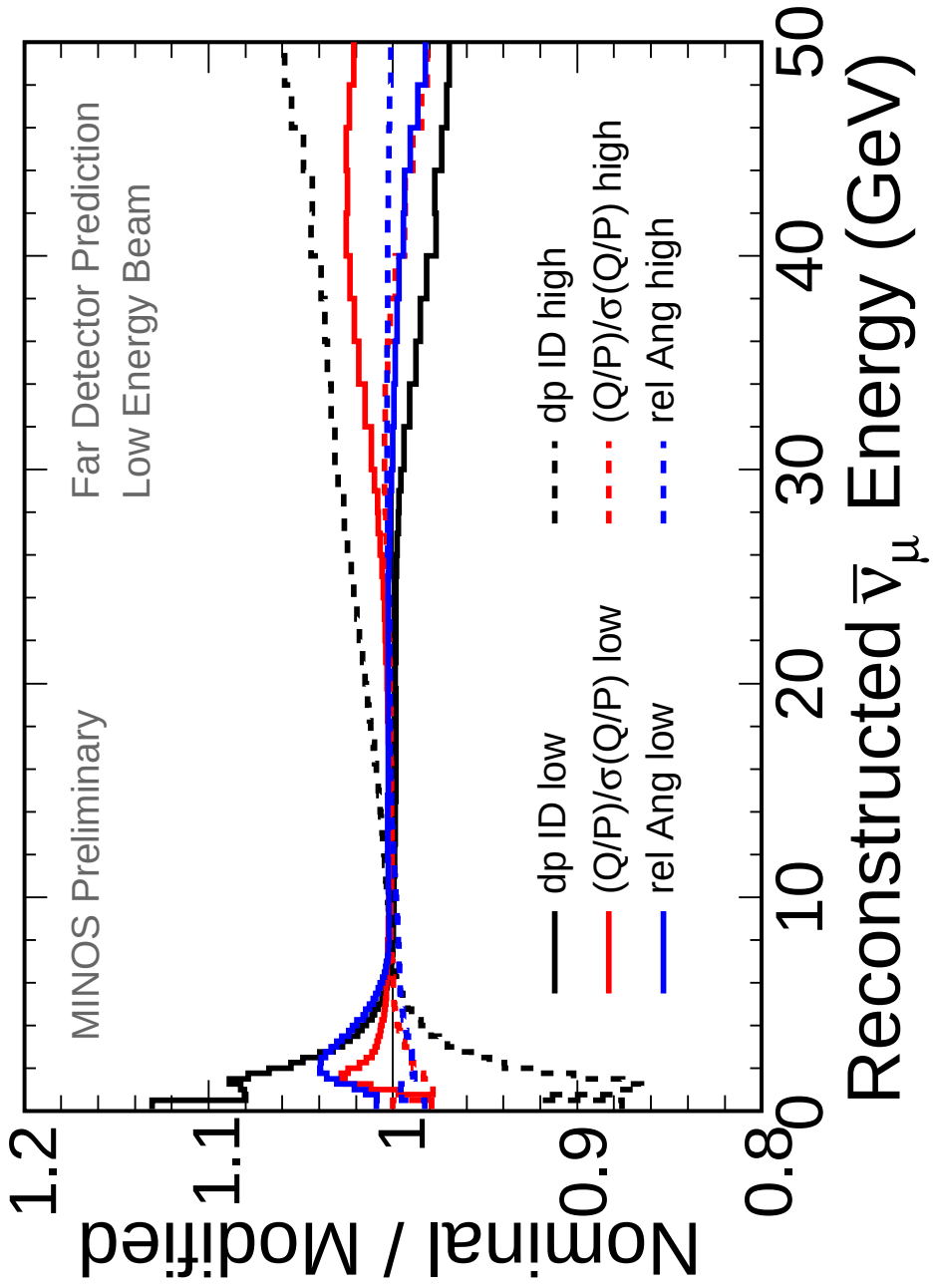

Figure 8.11: *Ratio of predicted un-oscillated FD $\overline{\nu}_\mu$ spectra shifted cuts to nominal, for the three Main Selector cuts. dpID is CC/NC PID which has the largest variation of 14 % below 1 GeV. As there are few events here it does not change the predicted spectrum too much.*

affect the extrapolation because it would point to a problem with the ND acceptance or beam positioning. This would manifest in the data/MC being different for different regions. Therefore, a study was performed in order to investigate non-uniformities in the data/MC agreement. The ND fiducial volume was divided into 10 regions as shown in figure 8.12.The MC truth information was used to obtain a baseline for the predicted differences in the data/MC between different regions. Then the ratio of data to MC was taken for each region, and the ratio of this and that of the opposite region was taken. Figure 8.13 shows that there are variations between regions; however for these sections are within statistical errors, and so showing that the beam position and detector acceptance are well modelled. Between the left and right regions there is a 2σ difference in the lowest energy bin. This difference is noticeable in both Run I and Run I I.

The 2σ discrepancy was investigated by studying the single ratios data left/data right and MC left/MC right, as functions of reconstructed energy. The MC predicts more events in the lowest-energy bin on the right side than the left (figure 8.14). At all other energies both data and MC show more events on the left. The excess of MC events on the right-hand side in the lowest-energy bin comes from mis-identified events as shown in figure 8.15. Both CC-$\overline{\nu}_\mu$ and NC events have more events on the left (figure 8.15). The reason why the MC predicts more low-energy mis-identified events on the right is because the $\mathbf{B}$-field decreases away from the coil, thus scattered events less likely to be curved in the correct direction. At higher energies the tracks are longer, and so the lower $\mathbf{B}$-field is not an issue; there are simply fewer events on the right. To investigate whether this caused a problem with the FD spectrum, the different regions of the fiducial volume of the ND were extrapolated to the FD. Both the ND MC helper file and the ND data file had the same fiducial cut applied and extrapolated to give a FD spectrum. It can be seen in figure 8.16 that the variations in the predicted FD spectrum is less than 6 % except in the lowest energy bin. This disagreement is less than the uncertainties in the CC, NC which is set to be 50 % [130] which is the uncertainty in background investigated in section 8.4.

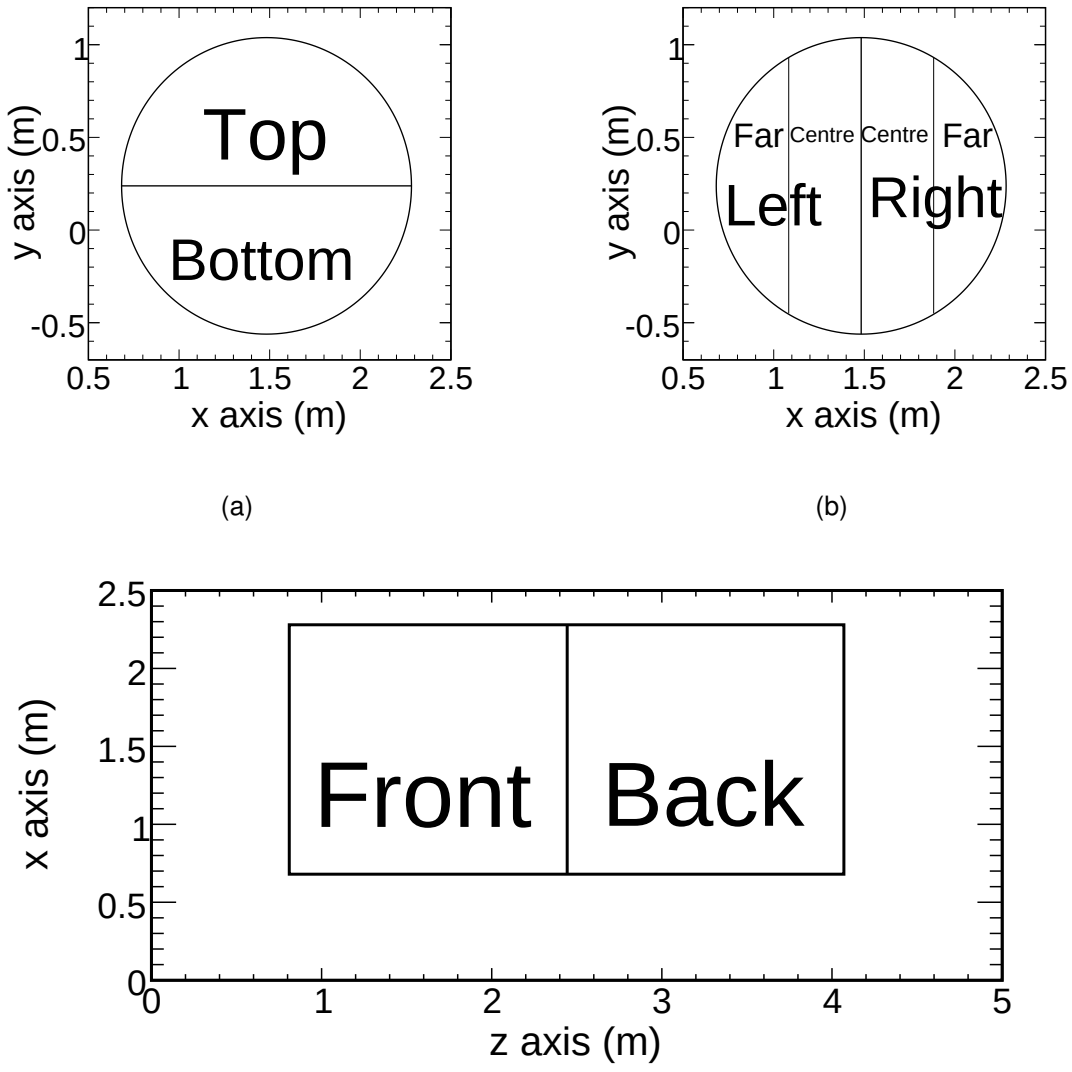

Figure 8.12: *Division of the fiducial volume of the near detector into different regions, for the study of the data/MC difference. In this study the data/MC for each region was compared to that of the opposite region. The magnetic coil located at (0,0) in x and y. The first plane of the detector nearest the beam source is 0 in the z-axis.*

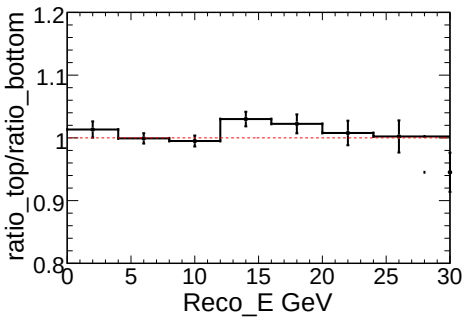

(a) Top/bottom

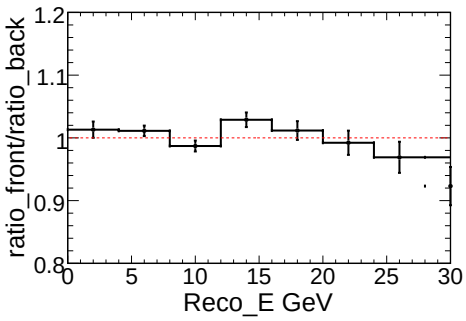

(b) Front/back

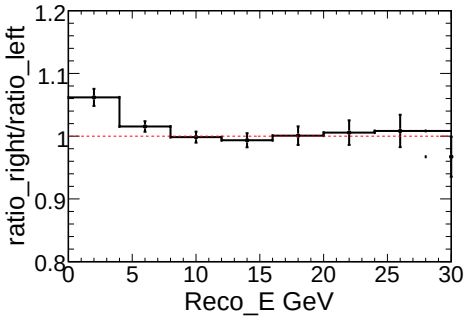

(c) Right/left

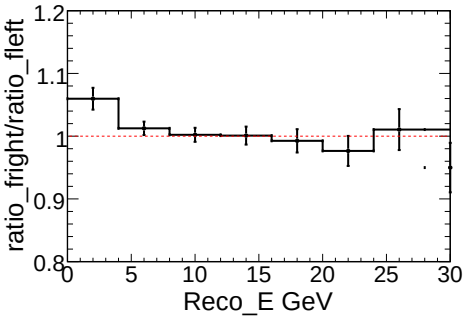

(d) Centre right/left

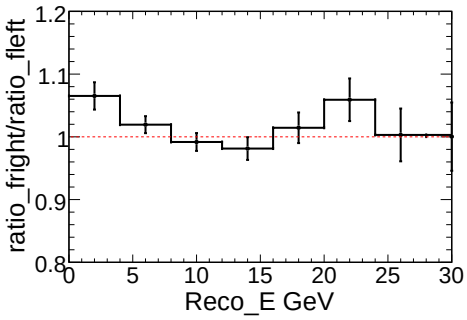

(e) Far right/left

Figure 8.13: *Double ratios of Run I and Run I I data/MC as a function of reconstructed energy for different regions of the ND fiducial volume after Main Selector cuts.*

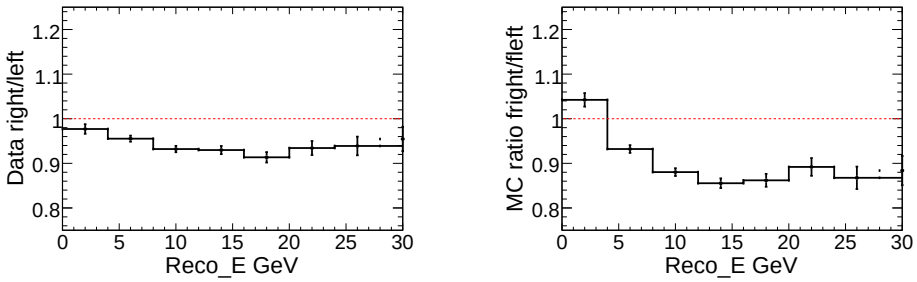

(a) Data (b) MC

Figure 8.14: *Ratio of far right to far left side of the ND fiducial volume a)shows data and b) Monte Carlo. There is disagreement at below 4 GeV due to less events in the right side of the detector in data than MC.*

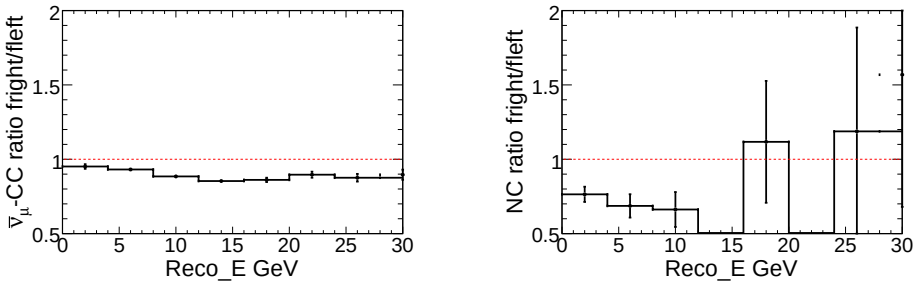

(a) $\overline{\nu}_\mu$ (b) NC

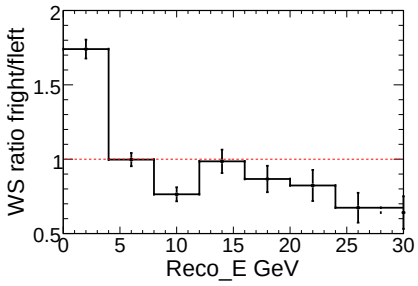

(c) WS

Figure 8.15: *The ratio of MC events far right to far left side of the ND fiducial volume as a function of energy: a) CC-$\overline{\nu}_\mu$ events b) neutral current events and c) mis-identified events. The MC predicts more events on the left side (near to coil) for $\overline{\nu}_\mu$-CC and NC events, while there is an excess of mis-identified events at low energies on the right side (far from coil).*

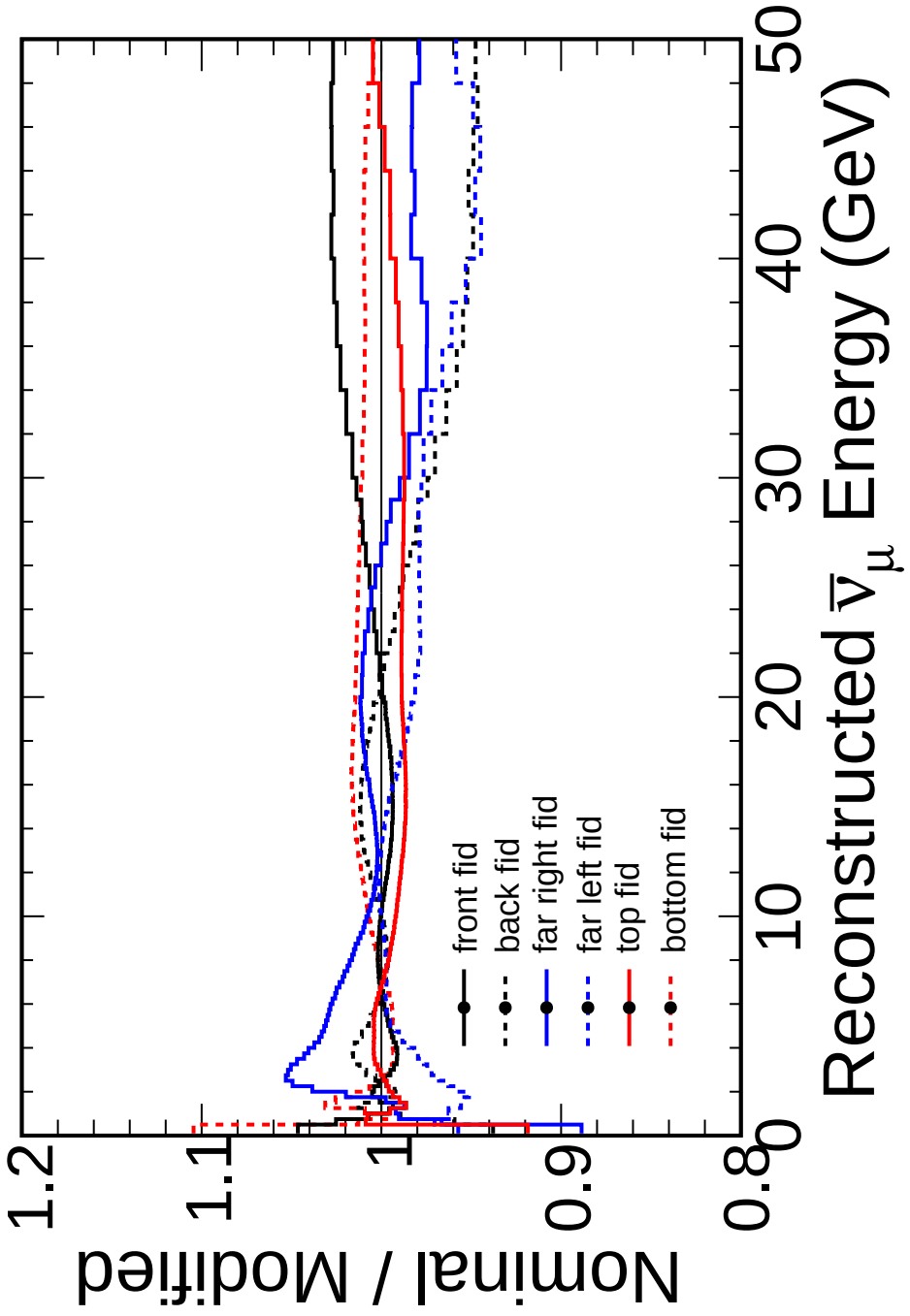

Figure 8.16: *How different cuts on the ND fiducial volume extrapolate toe the FD. The largest discrepancy between data/MC was between the far part of the ND fiducial volume between left and right (figure 8.13 and figure 8.14). It can be seen that change of the ND region extrapolated has little effect on the FD predicted spectrum.*

8.6 Summary

The energy spectrum of reconstructed data in the near detector is used to make a prediction of the unoscillated spectrum in the far detector. The standard extrapolation used in the CC ν_μ analysis [1] was adapted to take into account CPT non-conserving oscillation parameters by oscillating ν_μ and $\overline{\nu}_\mu$ separately. Neutrinos that have oscillated from $\overline{\nu}_\mu$ to $\overline{\nu}_\tau$ affect the energy spectrum in the far detector by τ^+ decaying intoμ^+ at a lower energy. The affect of this on the measurement of the oscillation parameters was investigated by extrapolating fake ND data with certain oscillation parameters to make far detector predicted spectra. It was found that τ^+ decaying into μ^+ has a non-negligible effect on the oscillation parameters at CPT non-conserving values of $\Delta\overline{\mathrm{m}}^2_{32}$. The $\overline{\nu}_\tau$ events must therefore be identified and extrapolated separately. The stability of the extrapolation was studied by varying the cuts in the Main Selector at the near detector while holding the far detectors cuts the same. At low energy there is a 14 % variation in the energy spectrum which is within the systematic error assigned to the NC-CC errors. Furthermore, a study of the acceptance of events in the near detector and beam direction shows that the MC predicts more mis-identified events than are observed in data. The study of the stability of the extrapolation demonstrates, however, that the effect of this discrepancy is negligible, and thus that the extrapolation is robust.

Chapter 9

Studies of Systematic Uncertainties

> "That's Dave Lister's bath from season 9. Best season ever, if you ask me. Awesome season. Best by miles." (Noddy - Back to Earth)

Systematic uncertainties have several different sources. The main source in an experiment like MINOS arise from the limited precision with which the neutrino production and interactions can be modelled; not collaborating the detector correctly; and a finite precision in measuring the detector properties. Biases in these quantities could manifest themselves in a fake oscillation signal or change the measured oscillation parameters. In MINOS, some of these uncertainties are cancelled out by the use of two functionally identical detectors. The effect of the remaining uncertainties on the oscillation parameters was studied, both in the case of a CPT conserving value of $\Delta\overline{m}^2_{32}$ = 2.5 $\times$ 10^{-3} eV^2 and in the case of a non-CPT conserving value of $\Delta\overline{m}^2_{32}$ = 6.0 $\times$ 10^{-3} eV^2. This chapter does not consider all systematic errors in detail, but only the five that affect the oscillation parameters the most. Furthermore, it is only concerned with the affect of the systematic error on the oscillation parameters, not the magnitude of the error itself. The magnitudes of the errors have been determined in [87]. An additional two systematic errors are considered in this chapter but not included in the final systematic error on the result are the alignment of the scintillator strips and a different way of calculating the error on the muon track. In future analyses the systematics studies will need to be expanded as the statistical errors come down. The alignment error is unimportant, while it is likely the new way of calculating the uncertainty in the muon track energy would make the likelihood contour to be

reduced.

9.1 Systematic Errors

The five most important systematic uncertainties, which will be discussed below, are: the energy of the muon from curvature as well as from range (section 9.1.1); relative normalisation between detectors (section 9.1.2); the production of neutrinos from decay of parents in the decay pipe (section 9.1.3); and uncertainties on the background interactions (section 9.1.4).

9.1.1 Muon Energy Error

An error in the energy of the final-state muon would result in a corresponding error in the total energy of the incident neutrino. If it was systematically overestimated the dip in the energy spectrum would be shifted upwards, thus giving a larger $\Delta\overline{m}^2_{32}$, while systematically low muon energies would make $\Delta\overline{m}^2_{32}$ smaller. The muon energy is determined in two ways: if the muon is contained within the detector then the energy is determined by range; if the muon exits the detector the energy is worked out by the curvature of the track. A comparison of the MC to the calibration detector [131] showed a difference of $3-4\,\%$. Some of this difference has been attributed to the uncertainty of the muon beam energy at the calibration detector, which is the same for both ND and FD, so a compromise of $2\,\%$ error was settled on and applied wholly to the far detector. The energy of a muon can only be determined by its range for muons that stop in the detector. For a muon that exit the detector its energy is determined by its curvature in the magnetic field. The accuracy of the energy determined by curvature is compared to the energy determined by range. Thus the error in curvature and range are fully correlated. Another uncertainty is brought in by not knowing the magnetic field accurately, which results in a $3\,\%$ error for the whole detector. This is added in quadrature with the $2\,\%$ error from range to give a total error of $4\,\%$. A possible improvement of the magnetic field accuracy is investigated in section 9.3.

9.1.2 Relative Normalisation Error

The number of POT is normalised to the live time for both the ND and FD, so that the ND energy spectrum can be extrapolated to the FD to use the whole FD dataset, as the near detector has a lower live time. An error in this relative normalisation would manifest itself as either: too few events in the FD prediction, which would mean a low measurement of $\sin^2 2\overline{\theta}_{23}$; or too many events in the prediction, which would cause the measurement of $\sin^2 2\overline{\theta}_{23}$ to be high. Too many events in the FD may also cause $\Delta\overline{\mathrm{m}}^2_{32}$ to be overestimated; this is because the fit may attribute this to fast oscillation. The error in the normalisation is caused by: uncertainty in the number of protons on target for the ND compared to the FD (1 %); uncertainty in the fiducial mass of the FD is uncertain (2 %); and a difference in track reconstruction efficiency in MC and data (3 %). These errors are added in quadrature to give an error of 4 %.

9.1.3 Decay Pipe Error

Neutrinos originating from parents produced in the decay pipe have a different acceptance in the ND compared to the FD because of the differing solid angle covered by each. This is of particular importance to the $\overline{\nu}_\mu$ search: π^- and K^- produced in the target are defocused, and so only $\overline{\nu}_\mu$ of parents travelling down in the middle of the horns, where the magnetic field is zero, make it into the NuMI beam. At the ND 17 % of $\overline{\nu}_\mu$ events are from parents produced in the decay pipe while at the FD 8.4 % of $\overline{\nu}_\mu$ events are produced in the decay pipe. For ν_μ production, only 4.2 % events in the ND and 1.6 % in the FD are from the decay pipe. As a consequence, any mis-modelling in the production would have a much a much greater effect on the extrapolation for $\overline{\nu}_\mu$ than for ν_μ.

The decay pipe has little affect on the ν_μ. In the runs included in this study the decay pipe was evacuated; however for Run III the decay pipe was filled with helium to relieve the pressure on the aluminium window that was found to be corroding. This gave a handle on how to estimate the systematic error. The ratio of the ND $\overline{\nu}_\mu$-energy spectrum when helium filled the decay pipe was compared to the runs when it was evacuated, for data and MC. The MC was then adjusted

until it matched the data. The uncertainty in the make up of particles that interact in the decay pipe needed to be taken into account in this estimation. This was done by adding five penalty terms to the fit. The five terms are: P2; P3; P4; H3 and H4 where P stands for protons and H for hadrons, and the number denotes the generation in which the neutrino was created; for example:

$$\begin{aligned} \text{P2:} \quad & \text{p} + \text{He} \rightarrow \pi^- + \text{X} \\ & \pi^- \rightarrow \overline{\nu}_\mu + \mu^- \\ \text{H3:} \quad & \text{p} + \text{C} \rightarrow \pi + \text{X} \\ & \pi + \text{He} \rightarrow \pi^- + \text{X} \\ & \pi^- \rightarrow \overline{\nu}_\mu + \mu^-. \end{aligned}$$

The MC was fitted to the data and by minimising χ^2 defined as:

$$\chi^2 = \sum_{i@1\,\text{GeV}}^{14\,\text{GeV}} \frac{\left(\text{data}_i^{\text{He}}/\text{data}_i^{\text{Vac}} - \text{MC}_i^{\text{He}}/\text{MC}_i^{\text{Vac}}\right)^2}{\sigma_i^2} + \sum_{j=1}^{N} \frac{\epsilon_j^2}{(1.0)^2} \tag{9.1}$$

where i counts in 1 GeV energy bins[1], j counts over N fitting parameters and ϵ_j is the j$^{\text{th}}$ fitting parameter, which is defined so ϵ_j = 0 is no shift. The fit resulted in 7 % more decay pipe production than the standard MC, with 30 % statistical uncertainty giving an 37 % error [132] [2].

9.1.4 Error on Backgrounds

In the ν_μ MINOS paper [1] the background mis-modelling was calculated by looking at the CC/NC PID discrepancy between data and MC in the region that is rejected. This region selects NC events, so to correct any differences it is presumed the difference is from NC events. The NC events are scaled till there is data MC agreement and this scaling is taken to be the NC systematic error. A

[1] Only includes up to 14 GeV as this covers 70 % of the beam flux. Higher energies have a large discrepancy which has not been understood yet.

[2] It was then decided, after the studies presented here had been completed, that it was not possible to extrapolate the result of helium to iron and a new method of calculating the systematic error was found. The new method assumes that all the difference between the data and MC in the ND is from the decay pipe, with the other systematic errors added in quadrature for positive and negative shifts. This new method provides a limit of $^{+60\,\%}_{-100\,\%}$

similar procedure was used for $\overline{\nu}_\mu$ but only the region just next to the CC/NC PID cut was used (0 – 0.25). Also misidentified events are a larger proportion of the background, as ν_μ make up a larger proportion of the NuMI beam than $\overline{\nu}_\mu$. It is not possible to tell if a background is from NC or a misidentified event, so the scaling was applied to both. This gives an error of 50 % [130].

9.1.5 Other Systematic Uncertainties

Other uncertainties that have a smaller effect on the oscillation parameters and so not included in this study, but are included in the final systematic error are:

- ν_μ interaction cross-section [133];
  - M_A quasi-elastic 15 %;
  - M_A resonance 15 % (shape);
  - deep-inelatic R_{ijk} parameters k=2 $\pm$ 0.1, k = 3 $\pm$ 0.2;
  - total cross section 3.5 %;
- $\overline{\nu}_\mu$ interaction cross-section [133];
  - M_A quasi-elestic 8 % (shape);
  - M_A resonance 8 % (shape);
  - deep-inelatic R_{ijk} parameters k=2 $\pm$ 0.2, k = 3 $\pm$ 0.2;
  - total cross section 4.0 %;
- Absolute hadronic energy measurement 10 %(8.2 % intranuke [134], 5.7 % CalDet [95]);
- Relative hadronic energy scale 3.3 % (2.4 % FD, 2.3 % ND [95]);
- SKZP beam re-weighting (varies with energy)[135].

9.2 Applying the Systematic Shifts

The systematic shifts described above were applied to high statistic Monte Carlo: 2.55 $\times$ 10^{23} POT for nominal FD MC files combined with 3.85 $\times$ 10^{23} POT tau

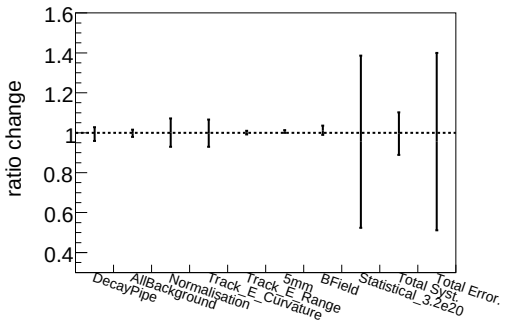

(a) $\Delta\overline{m}^2_{32}$ = 2.5 $\times$ 10^{-3} eV^2 $\sin^2 2\overline{\theta}_{23}$ = 1

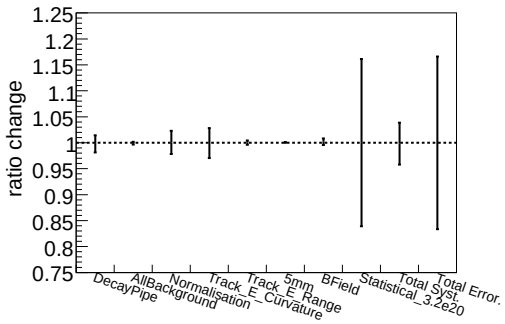

(b) $\Delta\overline{m}^2_{32}$ = 6.0 $\times$ 10^{-3} eV^2 $\sin^2 2\overline{\theta}_{23}$ = 1

Figure 9.1: *The one-parameter systematic errors for the Main Selector expressed as a percentage of the best-fit value for a) $\Delta\overline{m}^2_{32}$ = 2.5 $\times$ 10^{-3} eV^2, b)$\Delta\overline{m}^2_{32}$ = 6.0 $\times$ 10^{-3} eV^2, $\sin^2 2\overline{\theta}_{23}$ fixed to 1.*

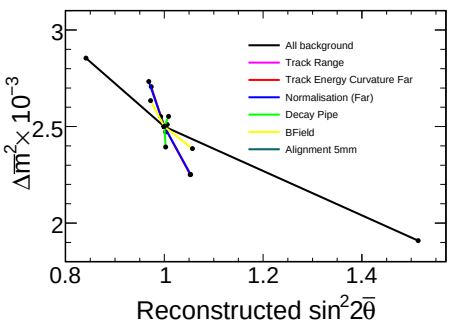

(a) $\Delta\overline{m}^2_{32}$ = 2.5 $\times$ 10^{-3} eV^2 $\sin^2 2\overline{\theta}_{23}$ = 1

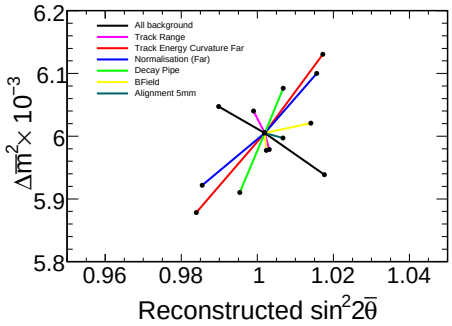

(b) $\Delta\overline{m}^2_{32}$ = 6.0 $\times$ 10^{-3} eV^2 $\sin^2 2\overline{\theta}_{23}$ = 1

Figure 9.2: *The two-parameter systematic errors for the Main Selector. They are expressed as shifts are shown in oscillation parameters away from the best fit value. The nominal values are a)$\Delta\overline{m}^2_{32}$ = 2.5 $\times$ 10^{-3} eV^2 b)$\Delta\overline{m}^2_{32}$ = 6.0 $\times$ 10^{-3} eV^2. The statistical error is much larger and thus not shown.*

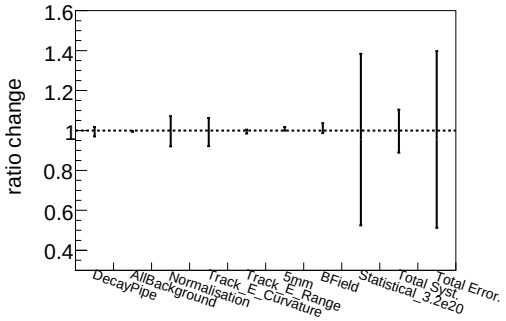

(a) $\Delta\overline{m}^2_{32}$ = 2. $\times$ 10^{-3} eV^2 $\sin^2 2\overline{\theta}_{23}$ = 1

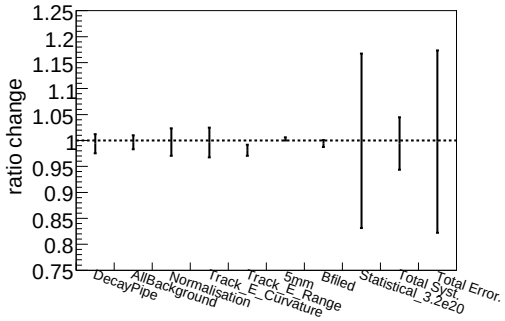

(b) $\Delta\overline{m}^2_{32}$ = 6.0 $\times$ 10^{-3} eV^2 $\sin^2 2\overline{\theta}_{23}$ = 1

Figure 9.3: *The one-parameter systematic errors for the Backup Selector expressed as a percentage of the best-fit value for a) $\Delta\overline{m}^2_{32}$ = 2.5 $\times$ 10^{-3} eV^2. b)$\Delta\overline{m}^2_{32}$ = 6.0 $\times$ 10^{-3} eV^2, with $\sin^2 2\overline{\theta}_{23}$ is fixed to 1.*

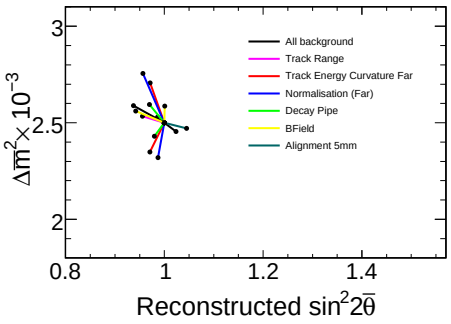

(a) $\Delta\overline{m}^2_{32}$ = 2.5 eV^2 $\sin^2 2\overline{\theta}_{23}$ = 1

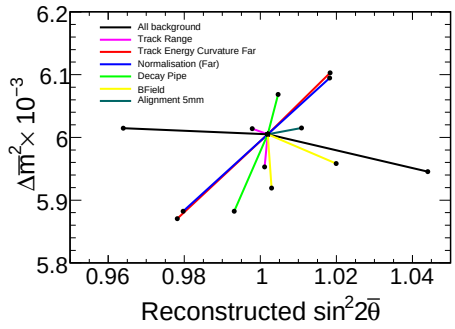

(b) $\Delta\overline{m}^2_{32}$ = 6.0 eV^2 $\sin^2 2\overline{\theta}_{23}$ = 1

Figure 9.4: *The two-parameter systematic errors for the Backup Selector. They are expressed as shifts are shown in oscillation parameters away from the best fit value. The nominal values are a)$\Delta\overline{m}^2_{32}$ = 2.5 $\times$ 10^{-3} eV^2 b)$\Delta\overline{m}^2_{32}$ = 6.0 $\times$ 10^{-3} eV^2. It can be seen that the All Background systematic error for 2.5$\times$$10^{-3}$ eV^2 a) is a lot smaller than the Main Selector 9.2. The statistical error is much larger and thus not shown.*

MC files and 4.38 $\times$ 10^{20} POT ND files. The selector cuts were made to these files to create helper files for the extrapolation and combined with the flux files. Fake data was then created from these files with two oscillations applied: $\Delta\overline{m}^2_{32}$ = 2.5 $\times$ 10^{-3} eV^2 CPT conserving and $\Delta\overline{m}^2_{32}$ = 6.0 $\times$ 10^{-3} eV^2 CPT non-conserving, with $\sin^2 2\overline{\theta}_{23}$ set equal to 1, for both sets the neutrino oscillation were set to the parameters found in the latest MINOS paper [1]. After these nominal files were made each systematic was added individually, and new fake data files were created for each shift, by shifting the reconstructed quantities. The fake data were then fitted by the beam matrix as if it were data, and the fitted points found. The fits were performed twice, once forcing $\sin^2 2\overline{\theta}_{23}$ = 1 and letting the fit change $\Delta\overline{m}^2_{32}$, and once letting both $\sin^2 2\overline{\theta}_{23}$ and $\Delta\overline{m}^2_{32}$ vary. In the two-parameter case there were no constraints on the best fit to be physical; the neutrino oscillation parameters in the fit were fixed to the entered values. The difference between the nominal value and the shifted value is then called the systematic shift. A list of these values are shown in tables 9.1, and 9.2, and they are shown graphically in figures 9.1 and 9.2. From these it can be seen that the systematic errors (at 2.5$\times$$10^{-3}$ eV^2; $\Delta\overline{m}^2_{32}$ $^{+0.475}_{-0.697}\times10^{-3}$ eV^2, $\sin^2 2\overline{\theta}_{23}$ $^{+0.5195}_{-0.1641}$: at 6.0$\times$$10^{-3}$ eV^2; $\Delta\overline{m}^2_{32}$ $^{+0.181}_{-0.193}\times10^{-3}$ eV^2, $\sin^2 2\overline{\theta}_{23}$ $^{+0.0481}_{-0.0510}$) have a negligible effect compared to the statistical error (at 2.5 $\times10^{-3}$ eV^2 ∞; at $\Delta\overline{m}^2_{32}$ 6.0$\times$$10^{-3}$ eV^2: $\Delta\overline{m}^2_{32}$ $^{+2.13}_{-1.52}\times10^{-3}$ eV^2, $\sin^2 2\overline{\theta}_{23}$ $^{+0.182}_{-0.343}$). Of the systematic errors, uncertainties on the background have the largest effect on $\sin^2 2\overline{\theta}_{23}$ (+0.514, -0.159), and $\Delta\overline{m}^2_{32}$ (+0.355$\times$$10^{-3}$ eV^2, -0.592$\times$$10^{-3}$ eV^2), for CPT oscillations. At the non-CPT value, the systematic error that has the largest affect on both $\Delta\overline{m}^2_{32}$ and $\sin^2 2\overline{\theta}_{23}$, is the uncertainty on the energy of the muon found from curvature (+0.126$\times$$10^{-3}$ eV^2, -0.127$\times$$10^{-3}$ eV^2, +0.015, -0.018).

This process was repeated for the Backup Selector (figures 9.3, 9.4). It can be seen that the statistical error is a lot larger (at $\Delta\overline{m}^2_{32}$ = 2.5, ∞: at 6.0 $\times10^{-3}$ eV^2; $\Delta\overline{m}^2_{32}$ $^{+2.30}_{-1.59}\times10^{-3}$ eV^2, $\sin^2 2\overline{\theta}_{23}$ $^{+0.234}_{-0.365}$) than the systematic error (at 2.5$\times$$10^{-3}$ eV^2 $\Delta\overline{m}^2_{32}$ $^{+0.354}_{-0.250}\times10^{-3}$ eV^2, $\sin^2 2\overline{\theta}_{23}$ $^{+0.0234}_{-0.0785}$: at $\Delta\overline{m}^2_{32}$ 6.0; $\Delta\overline{m}^2_{32}$ $^{+0.148}_{-0.233}\times10^{-3}$ eV^2, $\sin^2 2\overline{\theta}_{23}$ $^{+0.0481}_{-0.0510}$). Furthermore, for CPT the background systematic is a lot smaller, thus bringing down the overall systematic error compared to the Main Selector. At $\Delta\overline{m}^2_{32}$ = 6.0 $\times$ 10^{-3} eV^2 the Backup Selector has larger systematic error than the

Uncertainty	Input $\Delta\overline{m}^2_{32}$ = 2.5$\times10^{-3}$ eV^2 + change in $\Delta\overline{m}^2_{32}$ $\times10^{-3}$ eV^2	+ change in $\sin^2 2\overline{\theta}_{23}$	- change in $\Delta\overline{m}^2_{32}$ $\times10^{-3}$ eV^2	- change in $\sin^2 2\overline{\theta}_{23}$
Decay pipe ($\pm$37%)	0.0523	0.0084	-0.1059	0.0027
Background ($\pm$50%)	0.3548	-0.1588	-0.5915	0.5141
Normalisation ($\pm$4%)	-0.2482	0.0530	0.2331	-0.0316
Track Energy Curvature ($\pm$4%)	0.2060	-0.0264	-0.2494	0.0524
Track Energy Range ($\pm$2%)	0.0102	0.0056	-0.0277	0.0027
Total Systematic Error	0.4749	0.5195	-0.6969	-0.1641
Statistical Error	∞	∞	∞	∞

Table 9.1: *Absolute shift of nominal fit point from true input value, for input* $\Delta\overline{m}^2_{32}$ *of 2.5*$\times$ *10*$^{-3}$ *eV*^{2} *and* $\sin^2 2\overline{\theta}_{23}$ *= 1.0, for the Main Selector. The largest systematic error in* $\Delta\overline{m}^2_{32}$ *and* $\sin^2 2\overline{\theta}_{23}$ *is the uncertainty in the background events.*

Main Selector. The reason for the larger effect at the higher $\Delta\overline{m}^2_{32}$ is the same as the reason why as the Backup Selector not being as sensitive at the higher $\Delta\overline{m}^2_{32}$. There are more background events at higher energies in the Backup Selector compared to the Main Selector, where the oscillation dip occurs for $\Delta\overline{m}^2_{32}$ = 6.0 $\times$ 10^{-3} eV^2. However, at CPT oscillation these extra background events act as a normalisation that fixes the lower energy events, so the variation in the lower events can be better accounted for.

9.3 Estimation of the B-Field Error

In the main analysis the error on the muon energy determined by curvature was estimated at 2 % which was translated into a 2 % error on the nominal field. In the study described here a more sophisticated technique was used based on the B-field calculated in [136]. The B-field maps were calculated using finite element analysis (FEA), which varies the B-field across the detector. This in part relies

	Input $\Delta\overline{m}^2_{32}$ = 6.0$\times10^{-3}$ eV^2			
	+		-	
	change in		change in	
Uncertainty	$\Delta\overline{m}^2_{32}$ $\times10^{-3}$ eV^2	$\sin^2 2\overline{\theta}_{23}$	$\Delta\overline{m}^2_{32}$ $\times10^{-3}$ eV^2	$\sin^2 2\overline{\theta}_{23}$
Decay pipe ($\pm$37%)	0.0713	0.0048	-0.0947	-0.0066
Background ($\pm$50%)	0.0423	-0.0121	-0.0666	0.0157
Normalisation ($\pm$4%)	-0.0833	-0.0165	0.0951	0.0136
Track Energy Curvature ($\pm$4%)	0.1256	0.0153	-0.1268	-0.0180
Track Energy Range ($\pm$2%)	0.0351	-0.0029	-0.0262	0.0012
Total Systematic Error	0.1815	0.0262	-0.1927	-0.0282
Statistical Error	2.13	0.182	-1.52	-0.343

Table 9.2: *Absolute shift of nominal fit point from true input value, for input $\Delta\overline{m}^2_{32}$ of 6.0$\times$ 10^{-3} eV^2 and $\sin^2 2\overline{\theta}_{23}$ = 1.0, for the Main Selector. The largest systematic error in $\Delta\overline{m}^2_{32}$ and $\sin^2 2\overline{\theta}_{23}$ is in the uncertainty in the muon energy found from the track energy found from curvature.*

	Input $\Delta\overline{m}^2_{32}$ = 2.5$\times 10^{-3}$ eV^2			
	+		-	
	change in		change in	
	$\Delta\overline{m}^2_{32}$	$\sin^2 2\overline{\theta}_{23}$	$\Delta\overline{m}^2_{32}$	$\sin^2 2\overline{\theta}_{23}$
Uncertainty	$\times 10^{-3}$ eV^2		$\times 10^{-3}$ eV^2	
Decay pipe ($\pm$37%)	0.0950	-0.0302	-0.0695	-0.0204
Background ($\pm$50%)	0.0885	-0.0627	-0.0458	0.0234
Normalisation ($\pm$4%)	-0.1809	-0.0127	0.2550	-0.0433
Track Energy Curvature ($\pm$4%)	0.2064	-0.0289	-0.1518	-0.0293
Track Energy Range ($\pm$2%)	0.0295	-0.0136	0.0338	-0.0444
Total Systematic Error	0.3540	0.0234	-0.2503	-0.0785
Statistical Error	∞	∞	∞	∞

Table 9.3: *Absolute shift of nominal fit point from true input value, for input $\Delta\overline{m}^2_{32}$ of 2.5$\times 10^{-3}$ eV^2 and $\sin^2 2\overline{\theta}_{23}$ = 1.0, for the Backup Selector. The largest systematic in $\Delta\overline{m}^2_{32}$ is in the uncertainty in the normalisation, and uncertainty in the background events gives the largest error in $\sin^2 2\overline{\theta}_{23}$.*

	Input $\Delta\overline{m}^2_{32}$ = 6.0$\times10^{-3}$ eV^2			
	+		-	
	change in		change in	
Uncertainty	$\Delta\overline{m}^2_{32}$ $\times10^{-3}$ eV^2	$\sin^2 2\overline{\theta}_{23}$	$\Delta\overline{m}^2_{32}$ $\times10^{-3}$ eV^2	$\sin^2 2\overline{\theta}_{23}$
Decay pipe ($\pm$37%)	0.0633	0.0027	-0.1226	-0.0088
Background ($\pm$50%)	0.0098	-0.0380	-0.0596	0.0421
Normalisation ($\pm$4%)	-0.1227	-0.0223	0.0895	0.0162
Track Energy Curvature ($\pm$4%)	0.0979	0.0164	-0.1345	-0.0238
Track Energy Range ($\pm$2%)	0.0089	-0.0041	-0.0519	-0.0008
Total Systematic Error	0.1476	0.0481	-0.2332	-0.0510
Statistical Error	2.30	0.234	-1.59	-0.365

Table 9.4: *Absolute shift of nominal fit point from true input value, for input $\Delta\overline{m}^2_{32}$ of 6.0$\times10^{-3}$ eV^2 and $\sin^2 2\overline{\theta}_{23}$ = 1.0, for the Backup Selector. The largest systematic in $\Delta\overline{m}^2_{32}$ is in the uncertainty in muon energy found from the track energy found from curvature, and the uncertainty in background events gives the largest error in $\sin^2 2\overline{\theta}_{23}$.*

on the input magnetisation ("$\mathbf{B}$-$\mathbf{H}$") curve which was calculated using six testing toruses made from five of the 45 batches that made the planes[3]. The hysteresis loops were calculated for two different $\mathbf{H}$-fields. One, at 50 Oe (Oersted), provides fine sampling for low fields, where the FEA is affected more by variations at low $\mathbf{H}$-fields, and the other, at 500 Oe, for studying the behaviour at higher driven fields. The responses for these two tests were combined to get the final behaviour. The batch with the median response was taken to be the nominal field. The batches with the highest and lowest fields were given the labels bhhi and bhlo respectively. The difference between the nominal field and bhhi (bhlo) was 1.31 % (-0.64 %) at 2 m from the coil and 2.63 % (-1.97 %) at r = 3.5 m. The MC used in this study was the same as the MC used for the other systematic errors, but differs in that the systematic shift was applied before reconstruction. This was then weighted with the oscillation parameters above and then fitted with the matrix method. The result was then compared to the nominal fit.

9.3.1 The effect on the oscillation parameters of B-Field Error

Varying the $\mathbf{B}$-field was studied for two different nominal $\Delta\overline{\mathrm{m}}^2_{32}$. This was then compared this result to the track energy from curvature. From table 9.5 one can see that varying the $\mathbf{B}$-field across the FD reduces the total systematic error in the one parameter fits. However, a higher $\mathbf{B}$-field than nominal affects $\Delta\bar{m}^2_{32}$ more than a lower map. This is expected as bhlo map is closer to the median map than the bhhi map. The two-parameter fits Figure 9.2 show the same pattern in that the $\mathbf{B}$-field has a smaller effect on both $sin^2 2\bar{\theta}_{23}$ and $\Delta\bar{m}^2_{32}$ than track energy from curvature with the $\mathbf{B}$-field high having more of an effect than the lower $\mathbf{B}$-field. The errors are not symmetric about $sin^2 2\bar{\theta}_{23}$; this may be due to the change in $\mathbf{B}$-field affecting the number of tracks interacting with the coil hole which would affect the normalisation. Figures 9.5 and 9.6 show that in the region where oscillation is expected to occur the difference between bhhi and bhlo is within 2 $\%$ from range and 4 $\%$ from curvature for most points, which suggests that the 4 $\%$ should cover it. Once you get past 15 GeV/c^2 there is more variation as these are longer tracks that exit the detector. From this study I would suggest using the error in the $\mathbf{B}$field

[3]The five were spread evenly through time to get a representative sample.

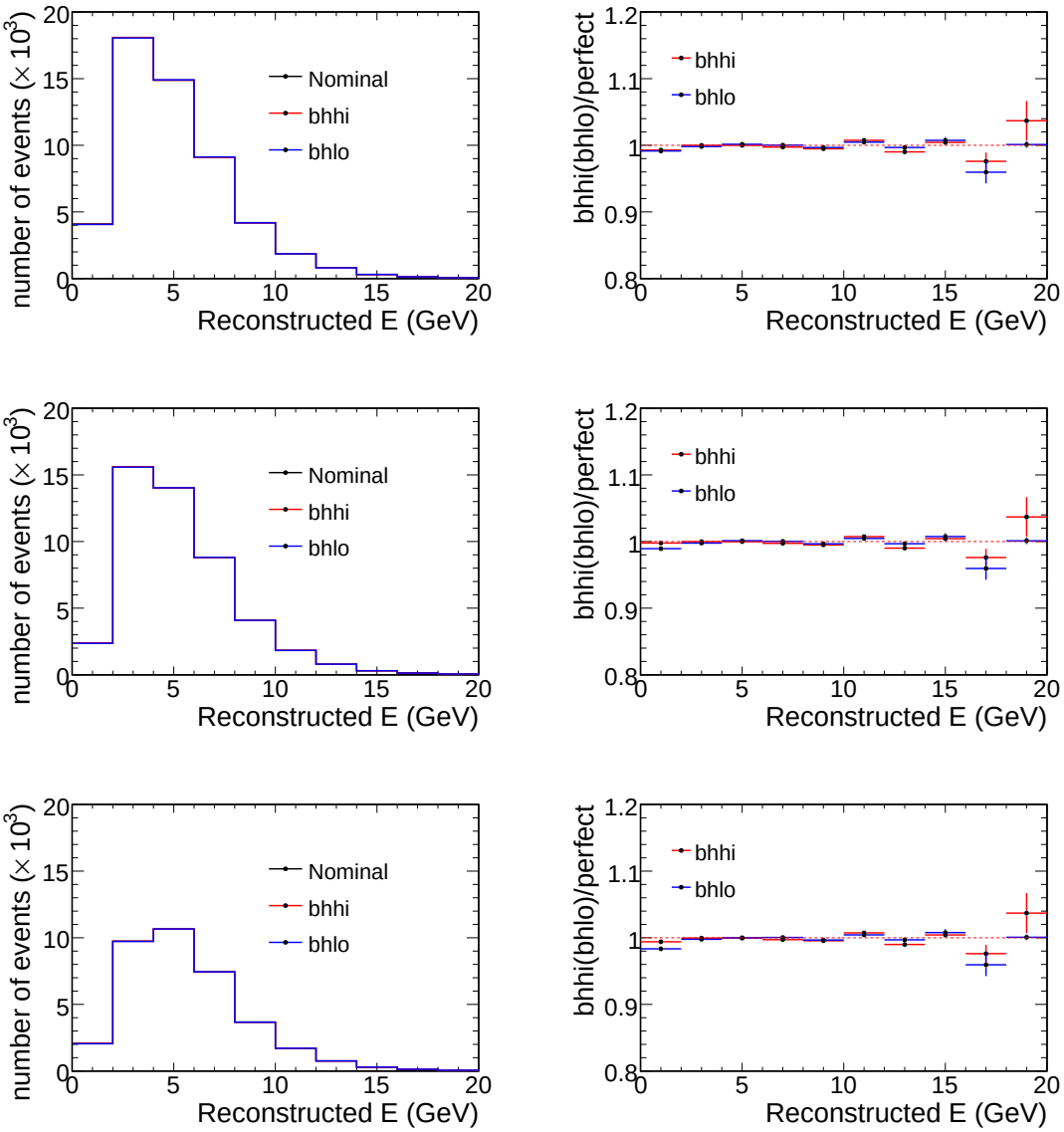

Figure 9.5: *The reconstructed energy of the muon track from range using the Main Selector for nominal, bhhi (*$\mathbf{B}$*-field from the toroid that gives the highest response for given* $\mathbf{H}$*-field) and bhlo (*$\mathbf{B}$*-field from the toroid that gives the lowest response for given* $\mathbf{H}$*-field) fields on the left. On the right is the ratio of bhhi(bhlo) to nominal field.True value* $\Delta\overline{m}^2_{32} = 0 \times 10^{-3}$ *eV*^{2} *top* $\Delta\overline{m}^2_{32} = 2.5 \times 10^{-3}$ *eV*^{2} *middle* $\Delta\overline{m}^2_{32} = 6.0 \times 10^{-3}$ *eV*^{2} *bottom.*

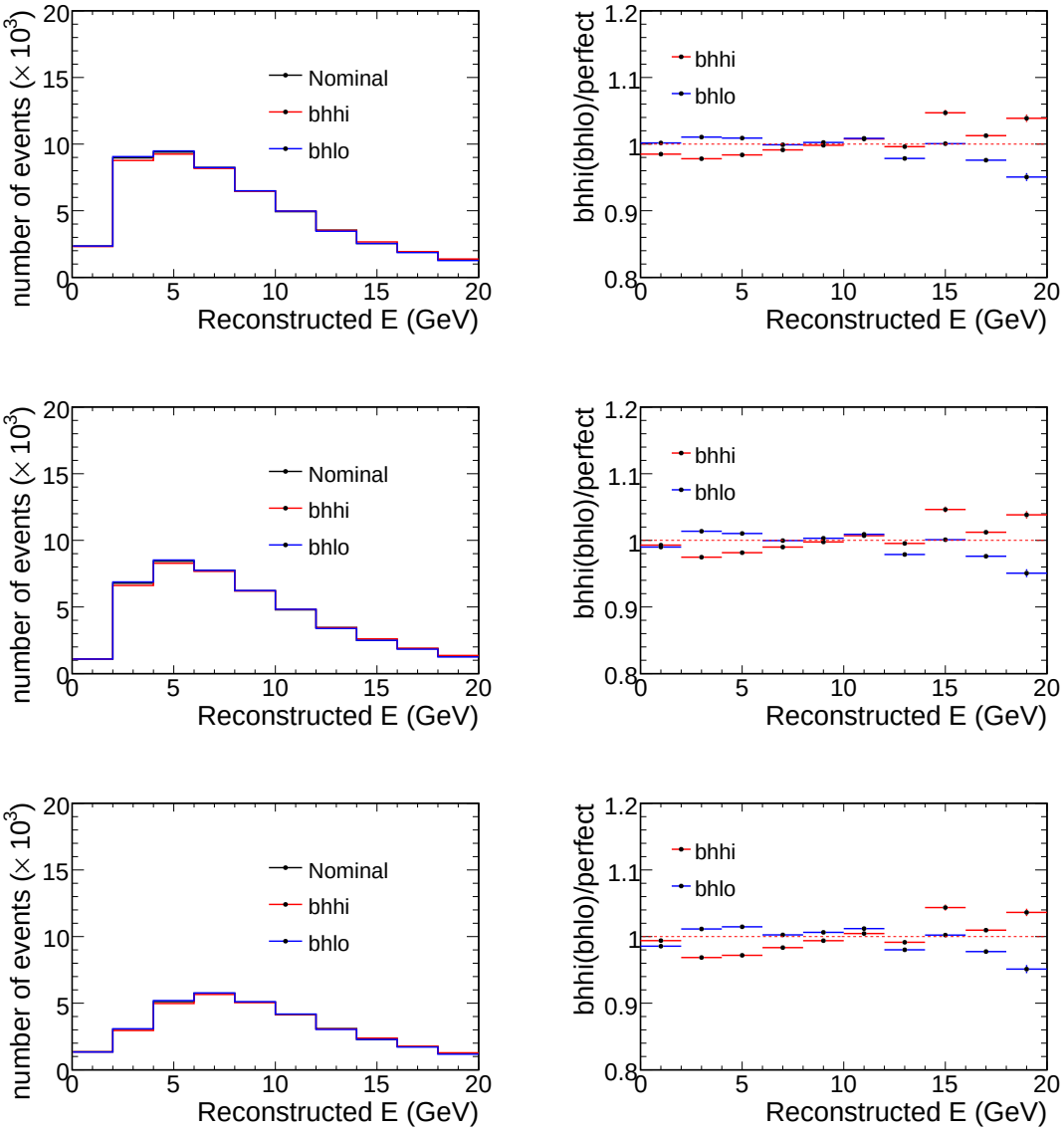

Figure 9.6: *The reconstructed energy of the muon track from curvature using the Main Selector for nominal bhhi and bhlo fields on the left. On the right is the ratio of bhhi(bhlo) to nominal field.True value* $\Delta\bar{m}^2_{32}$ *= 0* $\times 10^{-3}$ *eV*^{2} *top* $\Delta\bar{m}^2_{32}$ *= 2.5* $\times 10^{-3}$ *eV*^{2} *middle* $\Delta\bar{m}^2_{32}$ *= 6.0* $\times 10^{-3}$ *eV*^{2} *bottom.*

to find the total systematic error rather than TrackEnergyCurvatureFar as it gives a lower error where we contain events and where the oscillation is, but it also takes into account the uncertainly in the curvature of longer tracks.

9.4 Alignment Uncertainty Error

The positions of the scintillator modules were measured to a precision of 3 mm via a Vulcan Spatial Measurement system; a description can be found the MINOS detector paper [90]. This was then checked with cosmic muons in unmagnetised detector [137, 138], by looking at high energy cosmic rays passing through the detector. These travel in straight lines, so with enough statistics the alignment from one scintillator to the next can be worked out, and the alignment determined to better than 1 mm. However, in the 2007 charge ratio[4] analysis [139] a number of bias effects were seen. To account for this bias, M Goodman [140] investigated the cause and concluded that it was not caused by uncertainties in the magnetic field, but with small errors in the alignment.

Presented here we investigated the effects of misalignments of 2 mm and 5 mm on the oscillation parameters and various reconstructed quantities used in the analysis.

9.4.1 Effect of Alignment on Reconstructed Parameters

The Monte Carlo was adjusted to investigate how mis-measuring the position of the scintillator strips would affect the found oscillation result (appendix B.2 gives a description of the MC used). Misalignment of scintillator strip positions (with respect to their real location in the experimental setup, which is recorded in the relevant database files) was achieved by introduction of small shifts (2mm or 5mm) imposed on the transverse positions of scintillator modules in both MINOS detectors. These displacements were randomised using a flat square distribution of shift values in the range $\pm$ 2 mm and $\pm$ 5 mm. The displacements were inserted into database ascii files, which were used to control the geometry chosen for particular simulation cases:

[4] number of μ^- / number of μ^+

- Perfect, where the positions of strips are determined purely from ideal Monte-Carlo geometry setup-up;

- Aligned, where strip positions are taken from real measurements of modules' placement in the experimental setup, including alignment constants.

The reconstructed events were produced for several geometry cases:

1. Simulated: with "**Perfect**" case. Reconstructed: with "**Perfect**" case.

2. Simulated: with "**Aligned**" case. Reconstructed: with "**Aligned**" case.

3. Simulated: with "**Aligned**" case. Reconstructed: with "**2mm**" random shifts.

4. Simulated: with "**Aligned**" case. Reconstructed: with "**5mm**" random shifts.

The corresponding statistics of produced events are: 1.34×10^6 negatively and 52986 positively charge muons in the Far Detector.

Figures 9.7 – 9.11 are selected highlights of the distributions in appendix C. These distributions show, as expected, the high energy positive $\overline{\nu}_\mu$ events have the greatest deflection[5], however, these are changes are $< 15\,\%$ in all energy specta as shown in figure 9.7. Mis-identified events (figure 9.8) vary by up to 15 % at energies above 10 GeV. This difference is because events of this energy exit the detector so the energy is wholly by "curvature". Mis-identified events often scatter so the curvature will change and thus the energy worked out from curvature will change greatly. The position of the events reconstructed in x vary by less than 4 % (figure 9.9). Track fit probability (figure 9.10) is the probability that a found μ track is actually a μ track which if the planes were not aligned would get worse. Relative angle has large change (figure 9.11) however these are in the tails, were there are not many events, so would not affect the result of finding events.

[5]High energy events are not deflected much by the magnetic field. Misalignment of scintillator strips could introduce a greater curvature to the track

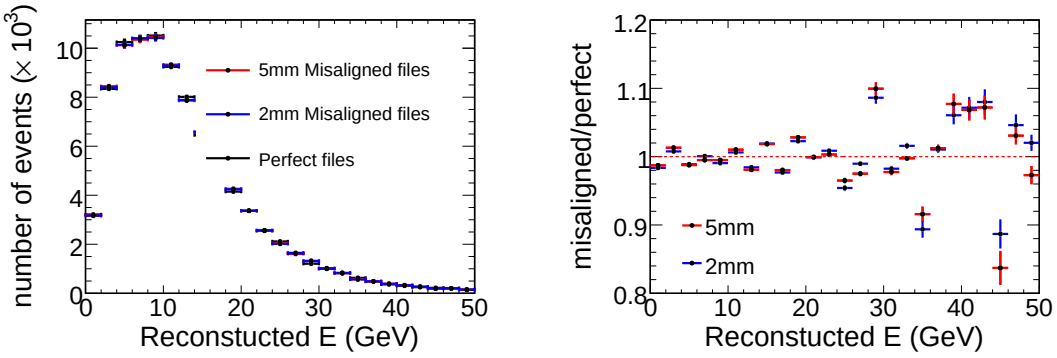

Figure 9.7: The reconstructed $\bar{\nu}_\mu$ energy spectra for events that are reconstructed with a positive charge, with perfect or misaligned geometry (left) and their ratio (right) of the misaligned files to the perfect file. The reconstruction of tracks are affect by less than 5 % below 30 GeV.

9.4.2 Alignment Change Effect on Oscillation

The change to the oscillation parameters was checked by oscillating the perfect MC with values of $\Delta\overline{m}^2_{32}$ = 2.5 $\times$ 10^{-3} eV^2 and $\Delta\overline{m}^2_{32}$ = 6.0 $\times$ 10^{-3} eV^2. This was then compared to the oscillated misaligned files of 2 mm and 5 mm. The difference between the found best fit points for the misaligned files and the perfect files is the systematic error. Figures 9.1, 9.2, 9.3 and 9.4 show that the alignment does not make a large difference to the found oscillation parameters ($\Delta\overline{m}^2_{32}$ +0.0517$\times10^{-3}$ eV^2, $\sin^2 2\overline{\theta}_{23}$ -0.007 at CPT). This two percent change in $\Delta\overline{m}^2_{32}$ and point seven percent change in $\sin^2 2\overline{\theta}_{23}$ is much smaller than the other systematic errors that it can be ignored.

9.5 Summary

The effects of systematic errors associated with the detection of $\overline{\nu}_\mu$ have been investigated. In particular their effects on the measured oscillation parameters for CPT conserving and non-CPT conserving values of $\Delta\overline{m}^2_{32}$ for two selectors were studied. The systematic errors were themselves calculated in the same way as in the 2008 ν_μ-CC study [1]. It was found that the error in the background has the largest effect on $\Delta\overline{m}^2_{32}$ (+14 %, -24 %) and $\sin^2 2\overline{\theta}_{23}$ (+51 %, -16 %) for

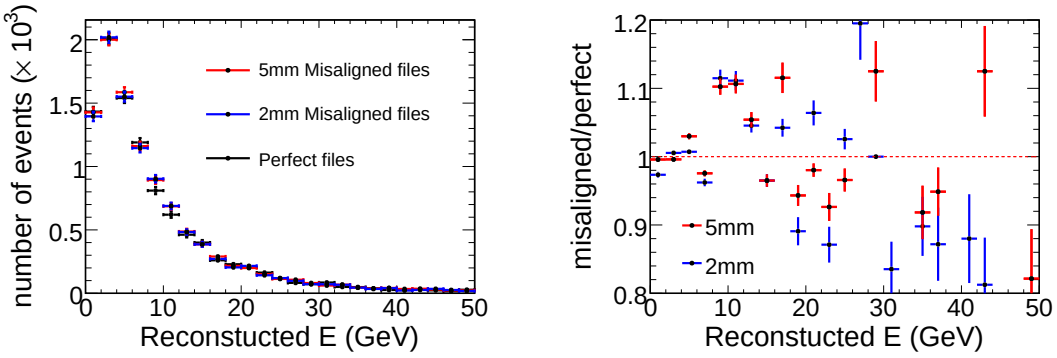

Figure 9.8: The reconstructed $\bar{\nu}_\mu$ energy spectra for events that are reconstructed with a negative charge, with perfect or misaligned geometry (left) and their ratio (right) of the misaligned files to the perfect file. There are large affects above 10 GeV. These are signal events that are cut figure 9.7 shows this does not effect the result.

$\Delta\overline{m}^2_{32}$ = 2.5 $\times$ 10^{-3} eV^2 and $\sin^2 2\overline{\theta}_{23}$ = 1. For $\Delta\overline{m}^2_{32}$ = 6.0 $\times$ 10^{-3} eV^2 and $\sin^2 2\overline{\theta}_{23}$ = 1 the largest effect on $\Delta\overline{m}^2_{32}$ (+2 %, -2 %) and $\sin^2 2\overline{\theta}_{23}$ (+2 %, -2 %) comes from the uncertainty in the track energy from curvature in the FD.

Furthermore, an alternative way of calculating the systematic error due to the magnetic field was investigated. In this study the $\mathbf{B}$-$\mathbf{H}$ curves of the highest and the lowest curve, of $\mathbf{B}$-field response to a given $\mathbf{H}$ field, for toroids made from the same batches as the MINOS planes were used to investigate the change in the measured oscillation parameters. The oscillation parameters changed less than the the flat 2 % error applied across the detector but was not used for this analysis as more study was needed. The affect of detector misalignment on the reconstructed parameters and the oscillation parameters has also been investigated.

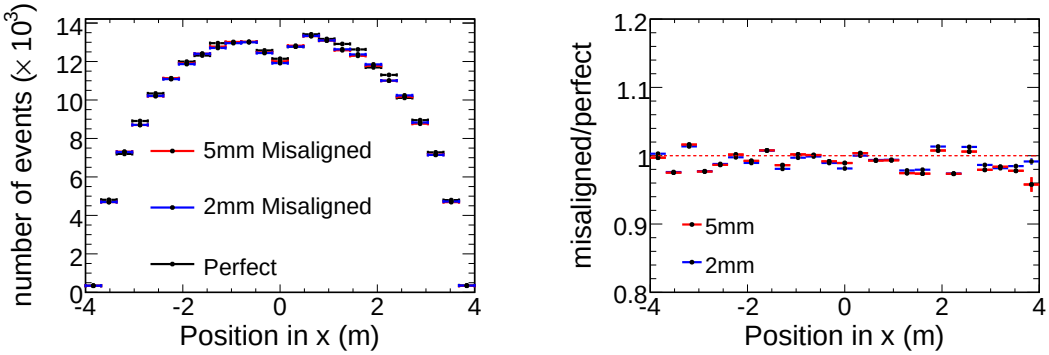

Figure 9.9: The reconstructed track vertex x position for events that are reconstructed with a positive charge, with perfect or misaligned geometry (left) and the ratio (right) of the misaligned files to the perfect file. The misalignment of scintillator strips does not affect the reconstructed position in x.

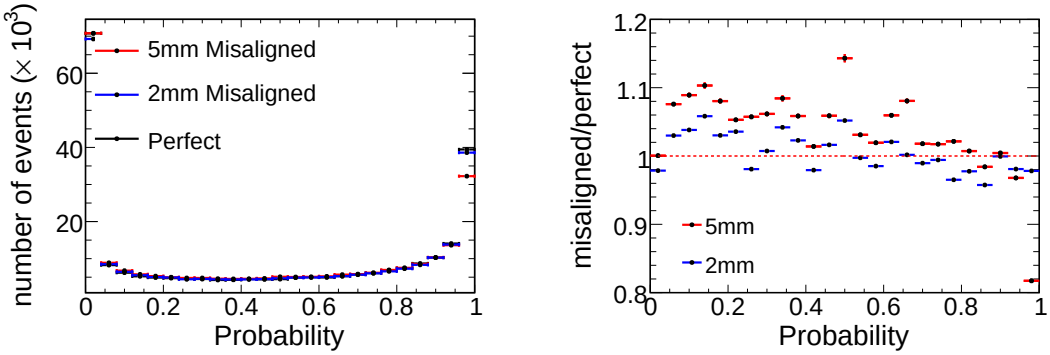

Figure 9.10: Track fit probability in positive charge events with perfect or misaligned geometry (left) and their ratio (right) of the misaligned files to the perfect file. Where the cut is applied in the Main Selector alignment does not make a difference.

$\Delta\bar{m}^2_{32} \times 10^{-3} eV^2$					
Input $\Delta\bar{m}^2_{32}$	Systematic + no curvature	Systematic - no curvature	Systematic + inc Bfield	Systematic - inc Bfield	Systematic + inc TrackEnergyCurvature	Systematic - inc TrackEnergyCurvature
2.5	0.193	-0.207	0.213	-0.206	0.254	-0.269
6.0	0.165	-0.175	0.172	-0.177	0.237	5.249

Table 9.5: *Table showing total systematic error calculated without using a curvature variable and including* B*field and including TotalEnergyCurvature.*

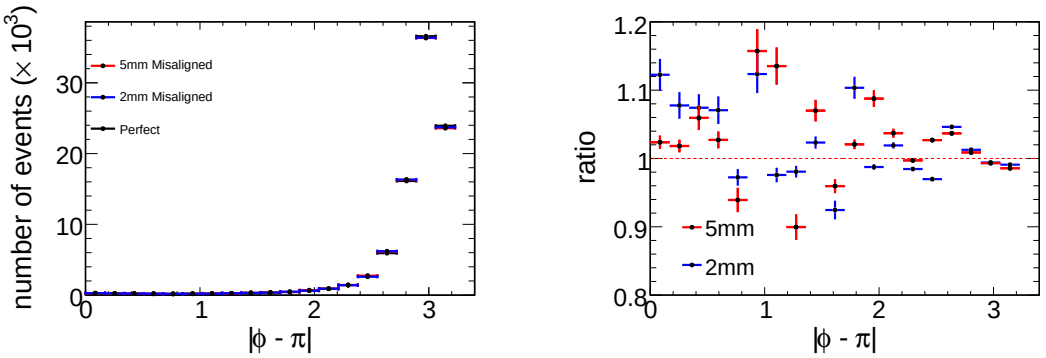

Figure 9.11: The relative angle variable, for exiting events that are reconstructed with a positive charge, with perfect or misaligned geometry (left) and their ratio (right) of the misaligned files to the perfect file.

Chapter 10

Results

> "Spaghettification. Let me guess. I can see only two options: one – due to the bizarre effects of the intense gravitational pull, and because we're entering a region of time and space where the laws of physics no longer apply, we all of us inexplicably develop an irresistible urge to consume vast amounts of a certain wheat-based Italian noodle conventionally served with Parmesan; or two – we the crew, get turned into spaghetti. I have a feeling we can eliminate option one." (Rimmer - book Better Than Life)

The analysis of $\overline{\nu}_\mu$-CC events followed a "blind" procedure: the data were looked at only after the cuts had been defined and the systematic errors calculated using MC. The data events were then fitted for oscillation and compared to the prediction for no oscillation and for CPT-conserving[1] oscillation (Main Selector section 10.1.1, Backup Selector section 10.1.2). After the data had been fitted the previously "blinded" parameters were checked for any anomalies (section 10.1.1). The best fit oscillation parameters for each selector, along with the confidence level contours, were produced using the Feldman Cousins technique (section 10.2). This analysis is not very sensitive to $\sin^2 2\overline{\theta}_{23}$, so fits were also made to $\Delta\overline{\mathrm{m}}^2_{32}$ only, with $\sin^2 2\overline{\theta}_{23}$ fixed to 1, as suggested by other experiments. This constrains $\Delta\overline{\mathrm{m}}^2_{32}$ better (section 10.3). Both the two-parameter and one-

[1] In this chapter where I have used the term"CPT-conserving" I mean the value that is the same as the MINOS 2008 ν_μ [1] analysis value. Any difference between $\overline{\nu}_\mu$ and the ν_μ value could be down to some other unknown physics i.e. no standard interaction of $\overline{\nu}_\mu$

parameter fits were then compared to the global limits.

10.1 Data Selected

The $\overline{\nu}_\mu$ analysis was a "blind" analysis which means that the far detector data were not looked at until the selector had been chosen and all the MC/data checks had been finalised. The MC/data checks were performed on the ND data and MC and on quantities in the FD that do not rely on oscillation parameters. The data used in this analysis were collected from Run I and Run II with the beam in the low-energy configuration, and have 3.21×10^{20} POT (1.27×10^{20} POT during Run I and 1.94×10^{20} POT during Run I I). These runs were extrapolated separately to account for the change of ν spectrum due to the replacement of the target between runs. Muons with energy above 50 GeV do not bend in the MINOS detectors, it is therefore not possible to distinguish $\overline{\nu}_\mu$ from ν_μ events. Therefore, only the energy range 0 – 50 GeV was investigated.

10.1.1 Main Selector Results

The expected number of events with the Main Selector for no oscillation is $64.6^{+8.0}_{-8.0}$ (stat.)$^{+3.9}_{-3.9}$ (syst.). For CPT-conserving oscillations, $58.3^{+7.6}_{-7.6}$ (stat.)$^{+3.6}_{-3.6}$ (syst.) events were expected. The number of events found in the data was 42 (figure 10.1). This is a 1.9 σ deficit of events compared to CPT conservation, with the best fit at $\Delta\overline{m}^2_{32}$ = 18 $\times$ 10^{-3} eV^2 and $\sin^2 2\overline{\theta}_{23}$ = 0.55. The deficit shows across the entire spectrum, which gives a good χ^2/N$_{\text{dof}}$ = 4.38/5. This best fit point is at variance with the region excluded by the global 90 % contour. Extensive checks were made on the data to see if there were detector effects, such as dead areas of the detector, or beam effects, or errors in the calculation of the POT for normalisation [141]. These checks were performed on $\overline{\nu}_\mu$ data and on data from other analyses. The only distribution that looked abnormal was the track vertex distribution (figure 10.2): there were far fewer events in the right-hand half of the detector. The asymmetry (A) is defined as,

$$A = \frac{R - L}{L + R}, \tag{10.1}$$

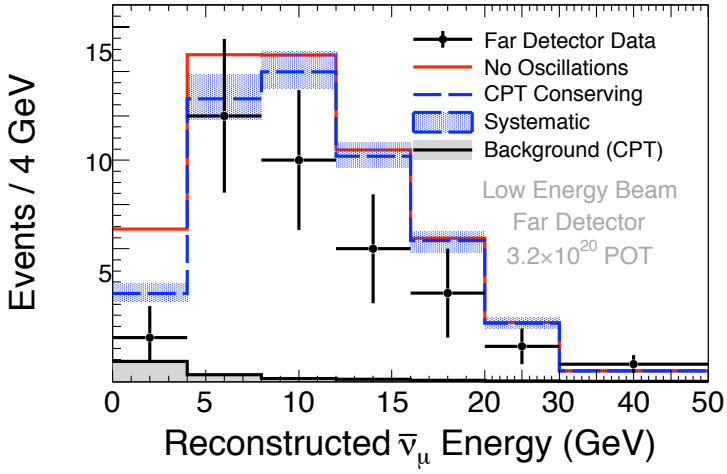

Figure 10.1: *Energy spectrum of $\overline{\nu}_\mu$ events selected in the Far Detector with the Main Selector. The black points are the data, the red line is the predicted spectrum if no oscillation took place and the blue hash line is the CPT-conserving spectrum with systematic error, and the grey shaded area is the background expected with mis-identified events oscillated with the MINOS [1] result.*

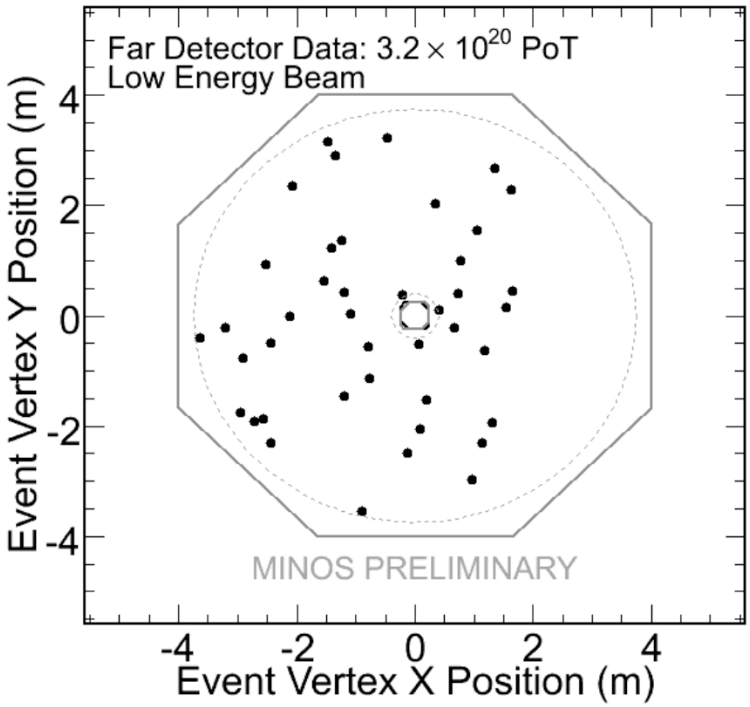

Figure 10.2: *Distribution of selected $\overline{\nu}_\mu$ events in the Far Detector. There are more events on the left-hand side of the detector than on the right at 3.4σ level. This amount of asymmetry is expected in at least one distribution, of the 20 distributions checked, 40 % of the time for 42 events.*

where L is number of events on the left and R is the number of events on the right. The asymmetry A = -0.19. For the CPT-conserving expectation of 58 events, an asymmetry of this amount or more would occur 8 % of the time. The number of events that were seen in this analysis, 42, has an asymmetry of $\pm$ 0.19 or greater 14 % of the time. However, looking at all distributions a 3.4 σ or larger asymmetry would occur about 40 % of the time in one distribution [142], from the 20 distributions checked as part of the box opening procedure [143]. This effect was not seen in the ν_μ-CC analysis or in positive cosmic muons, which seemed to rule out any detector efficiency effect. Moreover, as the POT counting and extrapolation used were the same for the ν_μ-CC result, it rules out a miscalculation of the flux as a cause. A further check was made on Run III data, which is almost the same size as this study, to see if the asymmetry was present there. If the effect is a statistical anomaly then it should not be seen in the Run III data. Histograms of the Run III dataset were area normalised to the MC prediction to preserve the blindness condition, so absolute numbers could not be counted. The asymmetry was not seen in Run III data [144].

10.1.2 Backup Selector Results

The expected number of events with the Backup Selector for no oscillation is $69.7^{+8.4}_{-8.4}$ (stat.)$^{+4.2}_{-4.2}$ (syst.). For CPT-conserving oscillation parameters it is $65.1^{+8.1}_{-8.1}$ (stat.)$^{+3.9}_{-3.9}$ (syst.). The observed number of events in data was 50 (figure 10.3). This is a 1.7 σ deficit of events compared to CPT conservation, with the best fit at 101.2$\times 10^{-3}$ eV^2, $\sin^2 2\overline{\theta}_{23}$ = 0.73. Table 10.1 compares the prediction of this selector with that of the Main Selector. Table 10.2 compares the Backup Selector's best fit to that of the Main Selector's. All the events that were selected by the Main Selector were also selected with the Backup Selector. The extra 8 events selected by the latter have energies greater than 9.5 GeV. This would be expected, as the Backup Selector has higher contamination at higher energies. However, for CPT-conserving values of $\Delta\overline{\mathrm{m}}^2_{32}$, a greater number of $\overline{\nu}_\mu$ events should be observed at these energies than were observed with the Main Selector. The asymmetry is A = -0.16; this is lower than for the Main Selector, and would be expected if the asymmetry was down to statistics.

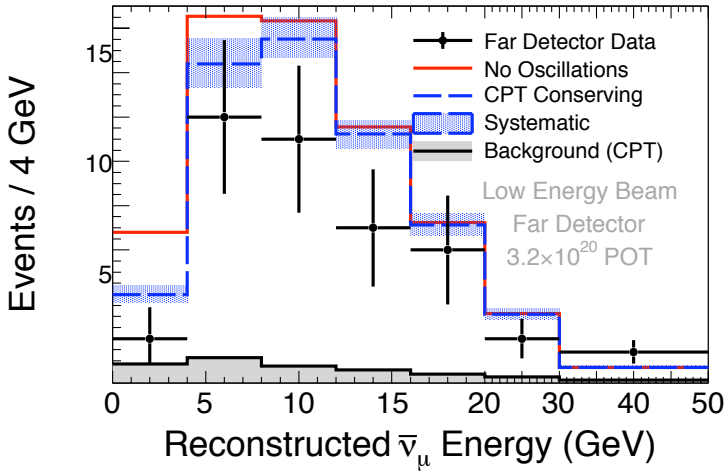

Figure 10.3: *Energy spectrum of $\overline{\nu}_\mu$ events selected in the Far Detector with the Backup Selector. The black points are the data, the red line is the predicted spectrum if no oscillation took place and the blue hash line is the CPT-conserving spectrum with systematic error, and the grey shaded area is the background expected with mis-identified events oscillated with the MINOS [1] result.*

Selector	Predicted No Oscillation	Predicted CPT Oscillation	Data events	CPT excluded
Main Selector	$64.6^{+8.0}_{-8.0}$ (stat.)$^{+3.9}_{-3.9}$ (syst.)	$58.3^{+7.6}_{-7.6}$ (stat.)$^{+3.6}_{-3.6}$ (syst.)	42	1.9σ
Backup Selector	$69.7^{+8.4}_{-8.4}$ (stat.)$^{+4.2}_{-4.2}$ (syst.)	$65.1^{+8.1}_{-8.1}$ (stat.)$^{+3.9}_{-3.9}$ (syst.)	50	1.7σ

Table 10.1: *Predicted number of events for the two selectors, and the number of events selected. The number of events selected by the Main Selector is 1.9 σ, and the Backup Selector is 1.7 σ away from CPT-conservation by pure counting.*

Selector	Best Fit	
	$\Delta\overline{m}^2_{32}$	$\sin^2 2\overline{\theta}_{23}$
CPT-conserving	2.48×10^{-3} eV^2	1.0
Main Selector	18×10^{-3} eV^2	0.55
Backup Selector	101×10^{-3} eV^2	0.73

Table 10.2: *Best fits of the the two selectors and the CPT value from the 2008 MINOS ν_μ-CC result [1]*

10.2 Finding the $\overline{\nu}_\mu$ Contours

In the ν_μ-CC MINOS analysis [82, 1] the confidence levels were worked out using Gaussian statistics, and with systematic errors added as nuisance parameters. Since $\sin^2 2\theta > 1$ has no physical meaning, the best fit was restricted to the physical region of parameter space. To find the 68 % (90 %) C.L. contour, the $\Delta\chi^2$ between each point in the parameter space and the best fit point is calculated; the contour is drawn through all the points that have a $\Delta\chi^2$ of 2.3 (4.61). This is problematic in that the confidence contours rely on the best fit point found. The non-Gaussian nature of errors near the physical boundary has caused the 2008 ν_μ CC result to have confidence levels greater than the sensitivity [1], as the best fit was found in the unphysical region: with the low statistics of the $\overline{\nu}_\mu$ analysis, this will be enhanced. To avoid this problem, a Feldman Cousins (FC) technique [118] was developed for this analysis.

10.2.1 Feldman Cousins Technique For Finding Contours

The FC technique is based on a large number of generated fake experiments with different oscillation parameters. The oscillation parameters cover the parameter space in a likelihood grid. Each experiment is fitted in such a way that the fit is required to be physical. Then the difference in the χ^2 with the best-fit point is used to construct the correction grid, which in turn is used to correct the sensitivity contours. Figure 10.4(a) shows the range of $\Delta\chi^2$ for 35,000 fake experiments with the oscillation parameters $\Delta\overline{m}^2_{32}$ = 2.5$\times$10^{-3} eV^2 and $\sin^2 2\overline{\theta}_{23}$ = 1.0. The $\Delta\chi^2$ of the 68th (90th) quantile is then used to create a correction grid to find the 68 % (90 %) correction grid.

10.2.1.1 Including Systematic Errors in the Contour

Another advantage to the FC approach is that systematic errors can be included directly in the fake experiments using the FD MC [146], rather than adding a nuisance parameter to the fit. To add the systematic errors to the FC correction grid one uses the “sampling” method to create the fake experiments. The simplest and fastest way of generating a FC point would be to just apply Poisson-fluctuations

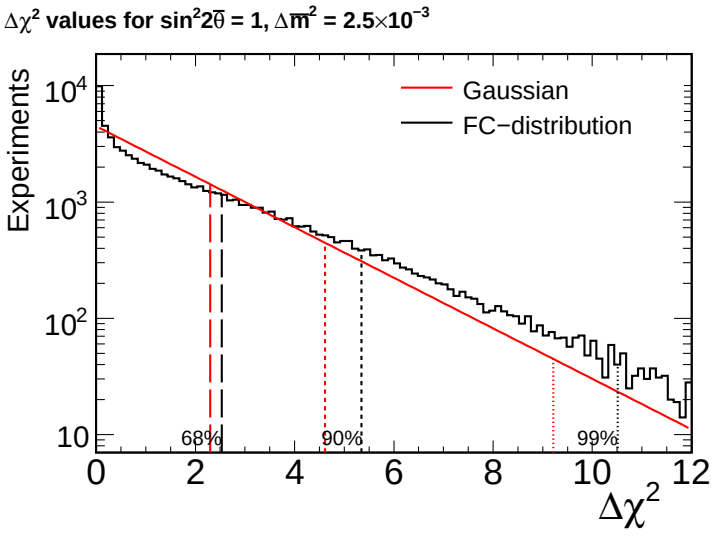

(a)

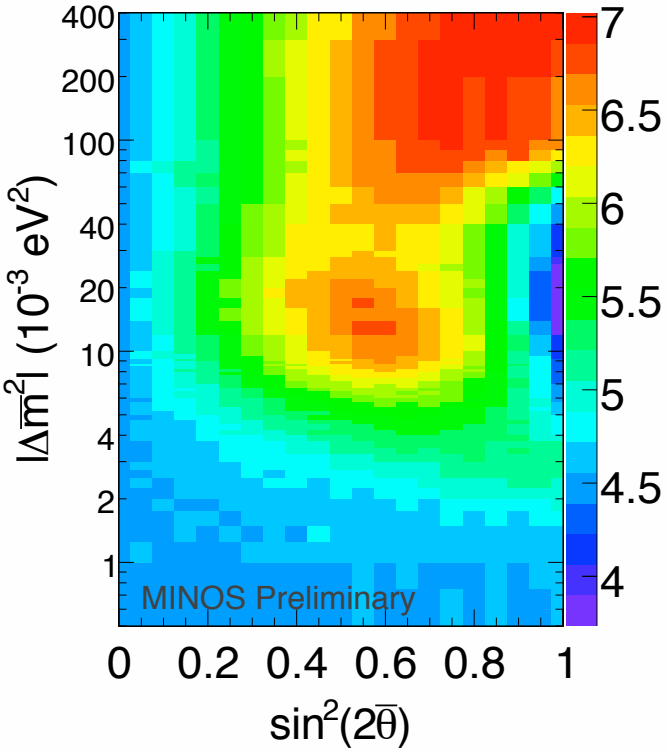

(b)

Figure 10.4: *Feldman Cousins grid: a) Distribution of $\Delta\chi^2$ of best fit point to the inputted value of $\Delta\overline{m}^2_{32}$ = 2.5 × 10^{-3} eV^2 and $\sin^2 2\overline{\theta}_{23}$ =1.0 [145].The red line is the Gaussian values and the black line is the FC values. b) 90% correction grid made with 35,000 fake experiments at each point [146]. Blue regions mean sensitivity is greater than Gaussian and red are areas that have less sensitivity than Gaussian.*

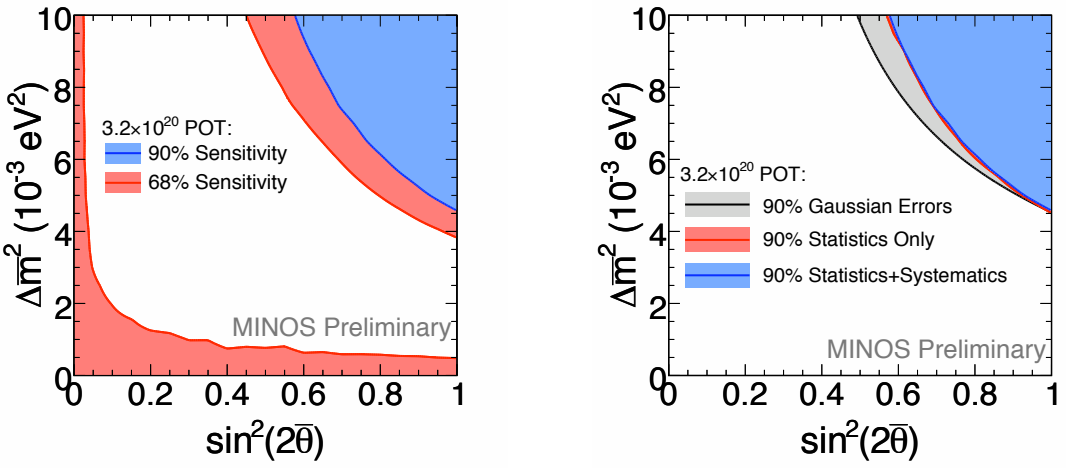

(a) (b)

Figure 10.5: *a) Sensitivity to $\overline{\nu}$ oscillations for a two-parameter oscillation fit with $\Delta\overline{m}^2_{32}$ =2.5×10^{-3} eV^2, $\sin^2 2\overline{\theta}_{23}$ = 1 for 3.2×10^{20} POT. b) The solid curve shows the 90 % confidence exclusion region expected (neglecting systematic uncertainties) [146].*

to each bin of the FD pdf, and then use this distribution as the experiment that is being fitted. However, with such a simple approach it is difficult to apply the systematic errors. In the sampling method the FD spectrum of selected $\overline{\nu}_\mu$ from the FD MC is separated into different samples: signal; mis-identified ν_μ; NC; ν_τ. For each of these samples the true energy is predicted separately using the Matrix Method [147]. From these true energy spectra the total number of events to be used is determined by Poisson-fluctuating the integral of each spectrum. The events are then selected randomly by rejection sampling [11] until the desired number of events is obtained.

10.2.1.2 The Feldman Cousins Correction Grid

In the Gaussian case of a $\Delta\chi^2$ of 2.3 (4.61) covers more than 68 % (90 %) of experiments. Figure 10.4(b) shows the 90 % C.L. FC correction grid: very little of the parameter space has a $\Delta\chi^2$ of the expected 4.61. Moving up in $\Delta\overline{m}^2_{32}$ from no oscillation the $\Delta\chi^2$ is less than the expected Gaussian $\Delta\chi^2$. This is because experiments whose best fit points are lower than zero are forced to be on the physical boundary so the $\Delta\chi^2$ is between the best fit point and the entered value

is lower than if the fit had been free to range over all points. This is also the reason for the small $\Delta\chi^2$ at small $\sin^2 2\overline{\theta}_{23}$. When analysing data the confidence contours in this area would be tightened after the FC correction. This low $\Delta\chi^2$ continues for $\Delta\overline{m}^2_{32}$ up to 2.5 $\times$ 10^{-3} eV^2: no events are expected in the region of the oscillation, so the likelihood surface is flat. This effect combines with the difficulty of seeing a fraction of an event in oscillation for low $\sin^2 2\overline{\theta}_{23}$ to create the large region of low $\Delta\chi^2$ in the lower left region of the plot. There is a spur centred round $\Delta\overline{m}^2_{32}$ = 3 $\times$ 10^{-3} eV^2 and $\sin^2 2\overline{\theta}_{23}$ = 1, this is caused by the NuMI beam spectrum predicting a fraction of an event in the affected energy bin, so an event/no event in this part of the energy spectrum here causes a big difference in the χ^2 surface. The oscillation peak at energies of $\Delta\overline{m}^2_{32}$ = (4−50) $\times 10^{-3}$ eV^2 is in agreement with the peak of the NuMI beam anti-neutrino contamination. This means that a $\sin^2 2\overline{\theta}_{23}$ = 1 would create a clear dip, which like the $\sin^2 2\overline{\theta}_{23}$ = 0 is a physical boundary. So experiments whose best fit point would go non-physical migrate to the boundary, reducing the $\Delta\chi^2$ between the best fit and the entered value. However, when $\sin^2 2\overline{\theta}_{23}$ is a fraction the fit would predict a fraction of an event to disappear at the entered value. As data only occurs at integer values, $\sin^2 2\overline{\theta}_{23}$ which predict integer values of events are likely to fit more experiments. As there are few events there are large $\Delta\chi^2$ between the entered value and best fit. Having a larger $\Delta\chi^2$ than the Gaussian case means that the sensitivity would be less for FC corrected sensitivity compared to a Gaussian sensitivity. At high $\Delta\overline{m}^2_{32}$ oscillations would appear in the tail of the spectrum where natural fluctuation outweighs oscillation signal disappearance, and thus the top right corner of figure 10.4(b) has a high $\Delta\chi^2$ correction.

10.2.1.3 Applying the Feldman Cousins Correction

The FC correction grids are then subtracted from the likelihood surface. Where the grid equals zero is where the contour is drawn. Figure 10.5 shows the sensitivity for the FC corrected contours and how the 90 % contour compares to the Gaussian contour at $\Delta\overline{m}^2_{32}$ = 2.5 $\times$ 10^{-3} eV^2 and $\sin^2 2\overline{\theta}_{23}$ = 1. This technique was then applied to the likelihood surface found using the data. Figure 10.6(a) shows the 68 %, 90 % and 99.7 % C.L. contours. Figure 10.6(b) shows these limits with

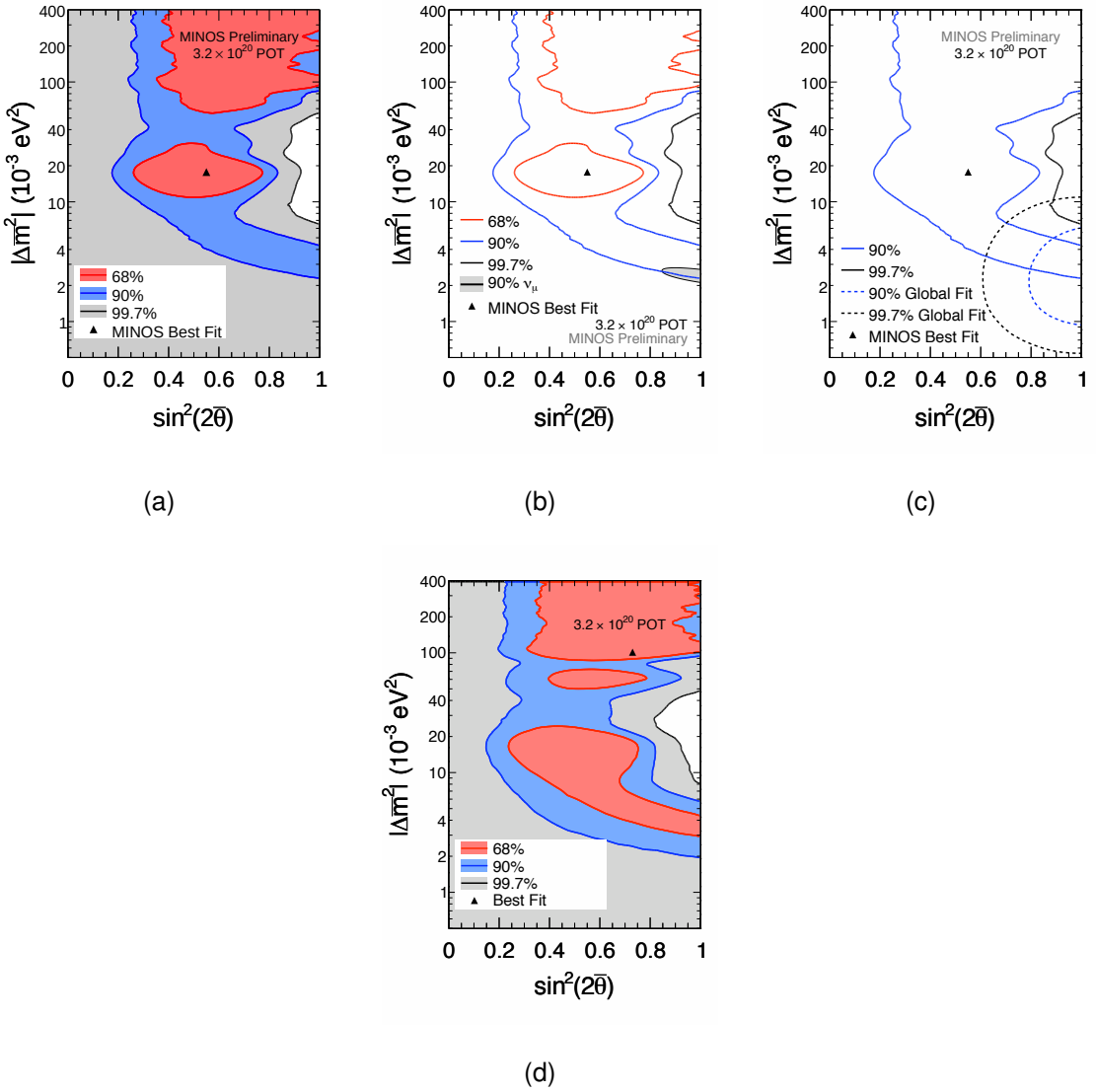

Figure 10.6: *a), b) and c) shows the 68% (red), 90% (blue) and 99.7% (black) C.L. contours for the MINOS 3.2 $\times$ 10^{20} POT analysis. b) Also shows the MINOS ν_μ analysis 90 % result (shaded grey). c) has the 90 % and 99.7 % C.L. contours of a global fit (dashed lines) [127]. d) Contours for Backup Selector selection. It can be seen that both the Main Selector and Backup Selector exclude the region around maximal mixing, the Main Selector $\Delta\overline{m}^2_{32}$ = (7−55)$\times$ 10^{-3} eV^2, $\sin^2 2\overline{\theta}_{23}$ 0.85−1, and the Backup selector $\Delta\overline{m}^2_{32}$ = (8−50)$\times$ 10^{-3} eV^2, $\sin^2 2\overline{\theta}_{23}$ = 0.8−1. This region also excludes at 3 σ some of the allowed region for the world limit [148]. As can be seen by b) the $\overline{\nu}_\mu$ result from this analysis agrees with the oscillation parameters found by the 2008 MINOS ν_μ [1] analysis at 90 %.*

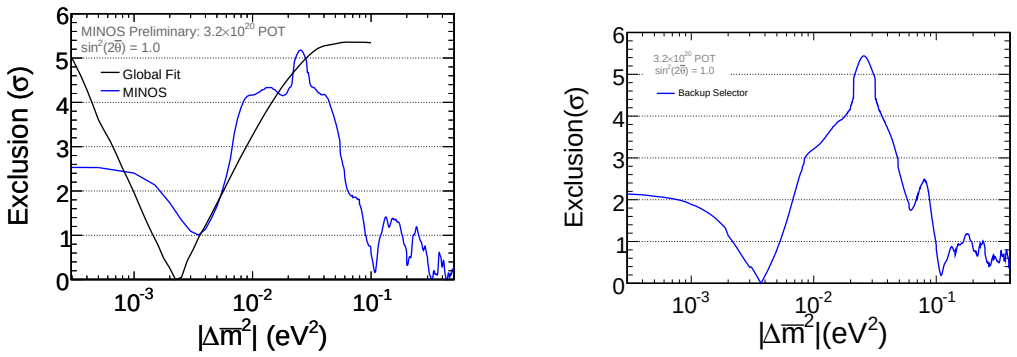

(a) (b)

Figure 10.7: *a) MINOS best fit $\Delta\overline{m}^2_{32}$ at maximal mixing (blue) and global best fit (black) [127]. b) The Backup Selector best fit $\Delta\overline{m}^2_{32}$ at maximal mixing (blue). The Main Selector has a best fit at high $\Delta\overline{m}^2_{32}$. MINOS is not sensitive to values above 50$\times 10^{-3}$ eV^2 due to the lack of $\overline{\nu}_\mu$ at high energy in the NuMI beam. The dip near 3.4$\times 10^{-3}$ eV^2 agrees with the global limits. The Backup Selector best fit is at 3.7$\times 10^{-3}$ eV^2 with the neutrino best fit value within 1σ [1] of 2.43Δm^2_{32}.*

the ν_μ 90 % C.L. contour [1]. It can be seen that the CPT-conserving value of Δm^2_{32} = 2.43$\times 10^{-3}$ eV^2, $\sin^2 2\theta_{23}$ = 1 is within the 90 % C.L. contour but outside the 68 % C.L. contour. Plot 10.6(c) shows the world limit for the 90 % and 99.7 % C.L. contours. This shows that this result agrees with a small region of the world limit so is able to exclude the high $\Delta\overline{m}^2_{32}$ allowed by the world limit at maximal mixing.

Backup Selector contours were made in the same way, and it can be seen that they give a similar confidence level (figure 10.6(d)) to the Main Selector. Aside from the Backup Selector yielding a higher best fit point the contours are similar. However, the Main Selector excludes more of the phase space at maximal mixing.

10.3 One Parameter Fit

With the low statistics in this analysis $\sin^2 2\overline{\theta}_{23}$ is not well constrained. If $\sin^2 2\overline{\theta}_{23}$ = 1, which is the ν_μ best fit value, $\Delta\overline{m}^2_{32}$ can be constrained a lot better by a single-parameter fit (figure 10.7). The minimum found in the likelihood surface for the main selector is at $\Delta\overline{m}^2_{32}$ = 326.6 $\times$ 10^{-3} eV^2. However, there is a minimum that is

close to the CPT-conserving value and also consistent with the global best fit at $\Delta\overline{m}^2_{32}$ = 3.4$\times 10^{-3}$ eV^2. A similar pattern is shown in the Backup Selector except that the minimum is at $\Delta\overline{m}^2_{32}$ = 3.7 $\times$ 10^{-3} eV^2 and other troughs are of the order of $\Delta\overline{m}^2_{32}$ = 100 $\times$ 10^{-3} eV^2. The more interesting result from the Main [Backup] selector one-parameter fit is the fact that the region $\Delta\overline{m}^2_{32}$ <2.0 $\times$ 10^{-3} eV^2 [$\Delta\overline{m}^2_{32} <$ 1.4 $\times 10^{-3}$ eV^2 and (6.2 $< \Delta\overline{m}^2_{32} <$ 91) $\times$ 10^{-3} eV^2] {(6.7 $< \Delta\overline{m}^2_{32} <$ 55) $\times 10^{-3}$ eV^2 [(8.5 $< \Delta\overline{m}^2_{32} <$ 48) $\times 10^{-3}$ eV^2]} is excluded to greater than 90 % $\{3\,\sigma\}$, thus excluding previously allowed CPT violating regions of parameter space.

10.4 Summary and the Future

In this chapter the data events chosen by the main MINOS $\overline{\nu}_\mu$ selector has been presented and fitted to oscillation parameters along with a Backup Selector made of fewer cuts and using the same CC/NC PID as the main CC ν_μ analysis. A brief analysis of how likely the data event distributions are was also discussed. The Feldman Cousins method of calculating confidence level contours, which is independent of the calculated best fit point, and which takes into account the physical boundaries, was also introduced. This method leads to a natural way of including the systematic errors when determining the confidence levels. The CPT-conservation oscillation parameters within the 90 % C.L. contour. A one-parameter fit fixing $\sin^2 2\overline{\theta}_{23}$ to 1 was also carried out, due to the lack of sensitivity to $\sin^2 2\overline{\theta}_{23}$ in this analysis. The one-parameter fit excludes to 3σ a previously allowed CPT-violating region of $\Delta\overline{m}^2_{32}$.

A data sample twice as large as that used in this analysis have been collected and are ready to be analysed. Furthermore, between September 2009 data and March 2010 were collected in a dedicated $\overline{\nu}_\mu$ run where the currents in the magnetic horns were reversed so that $\overline{\nu}_\mu$ rather than ν_μ were focused. The projected sensitivities can be seen in figure 10.8. In Run IV 1.7 $\times$ 10^{20} POT was taken.

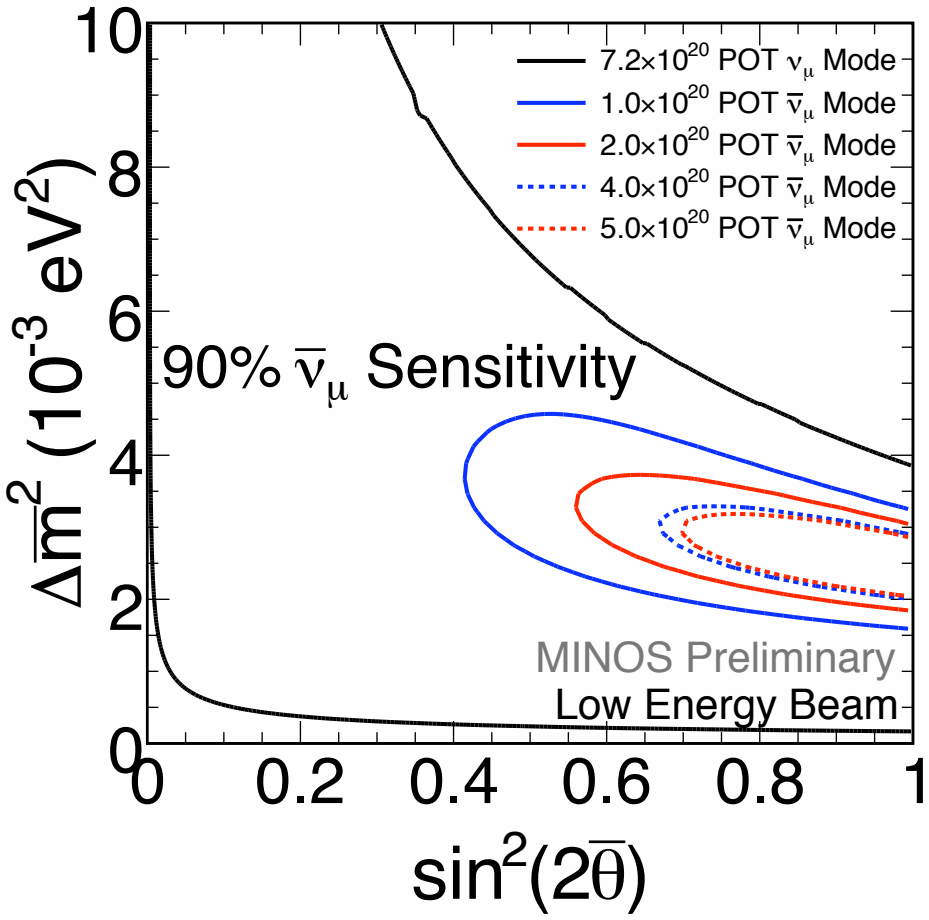

Figure 10.8: *Expected sensitivities with double the statistics of the current data set (black solid line) and running with reverse horn current (red line expected sensitivity) [127].*

Chapter 11

Conclusion

> "Well, the thing about a black hole - it's main main distinguishing feature - is it's black. And the thing about space, your basic space colour is black. So how are you supposed to see them?" (Holly - series 3 Marooned)

In this thesis various studies towards the 3×10^{20} POT $\overline{\nu}_\mu$-CC analysis, using the MINOS detectors and the NuMI beam, have been presented. It has shown how to select $\overline{\nu}_\mu$-CC events to investigate the first oscillation parameters $\Delta\overline{m}^2_{32}$ and $\sin^2 2\overline{\theta}_{23}$ for a man-made ν-beam. Although the limited statistics meant that the 68 %, and 90 % C.L. do not close, in combination with the global fit it has been able to exclude previously allowed values of $\Delta\overline{m}^2_{32}$.

Chapter 7 showed how only well reconstructed events selected were coincident with coming from the NuMI beam 7.1. Further cuts were added to these to select $\overline{\nu}_\mu$ events specifically. The Main Selector was chosen as the best combination of cuts on three parameters which gave the best efficiency $\times$ purity below 10 GeV. Various checks were made on this selector to see if the sensitivity could be improved. Section 8.4 showed that efficiency $\times$ purity below 10 GeV was a good figure of merit as changing the values on each parameter did not improve sensitivity, while section 7.3.2 showed that training the CC/NC PID on a sample of $\overline{\nu}_\mu$ MC did not improve efficiency $\times$ purity. The final part of chapter 7 (section 7.3.3), looked into creating another selector that cut on fewer parameters and used the same CC/NC PID as the 2008 ν_μ-CC analysis [1], which is called the Backup Selector. This selector had slightly greater efficiency $\times$ purity below

10 GeV than the Main Selector. This leads to the Backup Selector excluding $\Delta\overline{m}^2_{32}$ = 10$\times$10^{-3} eV^2 with more certainty and the Main selector excluding $\Delta\overline{m}^2_{32}$ = 0 with more certainty. Although neither is excluded by 3σ.

In chapter 8 explained the way the ND spectrum was used to give a prediction of the FD. The explanation for $\overline{\nu}_\mu$ oscillation is that they change into $\overline{\nu}_\tau$. Section 8.3 investigated what effect tau appearance would make to the $\overline{\nu}_\mu$ energy spectrum at the FD. This studied showed that at CPT for the statistics of this analysis tau appearance does not change the found oscillation. However, for higher $\Delta\overline{m}^2_{32}$ tau appearance makes a significant contribution to the energy spectrum and thus changes the found fit values. Section 8.4 showed that changing the cuts in the ND for both data and MC did not change the FD prediction by much, showing good data/MC agreement. This was further confirmed by section 8.5 which showed that the difference between data and MC is the same in different regions of the ND.

Chapter 9 investigated the systematic uncertainties affecting the oscillation parameters found by the fit, for CPT conserving and CPT non-conserving values of $\Delta\overline{m}^2_{32}$. It investigated whether a more sophisticated way of calculating the systematic error for the muon energy found from curvature would reduce the systematic error. The sophisticated method used the **B** maps of the highest **B**$-$**H** curve and the lowest, rather than applying a flat 2 % shift across the detector. These different **B** values were then entered into the MC rather than shifting MC by an amount with a nominal **B** (section 9.3). It found that this new method reduced the systematic error. However, for this analysis it was decided that old method would be used, as it is statistic limited and the flat 2 % has been justified for other analyses. The misalignment of the strips was looked at (section 9.4) and how this affected various reconstructed quantities as well as the oscillation parameters. Although some of these varied by up to 20 % in low statistic regions, so did not affect the final result.

The results of the oscillation study are presented in chapter 10 which gave a best fit to $\Delta\overline{m}^2_{32}$ = 18$\times$10^{-3} eV^2, $\sin^2 2\overline{\theta}_{23}$ = 0.55 for the Main Selector and 101.2$\times$10^{-3} eV^2, $\sin^2 2\overline{\theta}_{23}$ = 0.73 for the Backup Selector. Due to the low statistics and due to the physical boundaries the statistics are not distributed in a Gaussian

way. A Feldman-Cousins approach was developed for calculating the coverage is explain (section 10.2). The low statistics combined with the beam spectrum $\sin^2 2\overline{\theta}_{23}$ is not constrained in the 2-D fit. A one parameter fit at constraining $\sin^2 2\overline{\theta}_{23}$ = 1 is described in section 10.3 with a best fit for the Main Selector 326.6$\times 10^{-3}$ eV^2 and Backup Selector 3.7$\times 10^{-3}$ eV^2. MINOS is now running with an anti-neutrino beam and section 10.4 showed that with the reverse horn current running the $\overline{\nu}_\mu$ oscillation parameters will be constrained a lot better. In both the 2-D fit and the 1-D fit the ν_μ oscillation parameters are within 90 % C.L.. The best fit values of the anti-neutrino analyses are well away from the neutrino best fit. However, the MINOS neutrino contour is within the 90 % contour of these anti-neutrino analyses. From this it is difficult to tell whether CPT [1] is conserved or not, more data needs to be taken to answer this question. Twice the data set has now been taken in the same beam configuration has now been taken, but not analysed yet. A dedicated $\overline{\nu}_\mu$ run has also been taken of 1.7 $\times$ 10^{20} POT. Analysis of these data sets will clarify whether this result is a statistical fluctuation or whether $\Delta\overline{\text{m}}^2_{32}$ is different to Δm^2_{32}.

As well as these physics analyses, the method of calibrating the MINOS detectors was looked at (chapter 5). A different, independent way of checking the PMT gains was described. The gains that were worked out via this single-photoelectron method were then compared to the high intensity light injection method in section 5.3.5. It was found that the two methods gave similar results for the overall gains of the PMTs when the whole detector was looked at. The difference in the change of the gains was 3.3 % over a period of 670 days.

[1] Again any unknown physics will show itself as a difference in Δm^2_{32}, $\sin^2 2\theta_{23}$ and $\Delta\overline{\text{m}}^2_{32}$, sinb.

Bibliography

[1] P. Adamson et al, "Measurement of Neutrino Oscillations with the MINOS Detectors in the NuMI Beam," *Phys. Rev. Lett.*, vol. **101**, no. **13**, 2008.

[2] G. Giunti and C. Kim, *Fundamentals of Neutrino Physics and Astrophysics*. Oxford University Press, 2007.

[3] S. L. Glashow, "Partial-symmetries of weak interactions," *Nuclear Physics*, vol. **22**, no. **4**, pp. 579 – 588, 1961.

[4] A. Salam, "Elementary Particle Theory: Relativistic Groups and Analyticity. Stockholm," in *1969 Proceedings of the 8th Nobel Symposium* (N. Svartholm, ed.), pp. 367 – 377, 1968.

[5] S. Weinberg, "A Model of Leptons," *Phys. Rev. Lett.*, vol. **19**, pp. 1264 – 1266, Nov 1967.

[6] S. N. Bose, "Plancks Gesetz und Lichtquantenhypothese," *Zeitschrift für Physik A Hadrons and Nuclei*, vol. **26**, no. **1**, pp. 178 – 181, 1924.

[7] A. Einstein, "Quantentheorie des einatomigen idealen Gases," *Zeitschrift für Physik A Hadrons and Nuclei*, vol. **25**, no. **1**, pp. 37 – 41, 1924.

[8] A. Zannoni, "On the Quantization of the Monoatomic Ideal Gas (Translation of [9]," 1999.

[9] E. Fermi, "Sulla quantizzazione del gas perfetto monoatomic," *Rend Lincei*, vol. **3**, pp. 145 – 1949, 1926.

[10] *Proceedings of the Royal Society of London. Series A, contain papers of a Mathematical and Physical Character*, vol. **112**, The Royal Society, 1926.

[11] C. P. D. G. Amsler et al, "Review of Particle Physics," *Phys. Lett. B*, vol. **667**, no. **1**, 2008.

[12] C. S. Wu, E. Ambler, R. W. Hayward, D. D. Hoppes, and R. P. Hudson, "Experimental Test of Parity Conservation in Beta Decay," *Phys. Rev.*, vol. **105**, pp. 1413–1415, Feb 1957.

[13] P. W. Higgs, "Broken Symmetries and the Masses of Gauge Bosons," *Phys. Rev. Lett.*, vol. **13**, pp. 508–509, Oct 1964.

[14] K. Zuber, "Neutrinoless Double Beta Decay Experiments," *Acta Physica Polonica B*, vol. **37**, pp. 1905 – 1921, 2006.

[15] C. Arnaboldi et al, "Results from a search for the $0\nu\beta\beta-$decay of ^{130}Te," *Phys. Rev. C*, vol. **78**, 2008.

[16] N. Cabibbo, "Unitary Symmetry and Leptonic Decays," *Phys. Rev. Lett.*, vol. **10**, pp. 531–533, Jun 1963.

[17] Z. Maki, M. Nakamura, and Sakata, "Remarks on the Unified Model of Elementary Particles," *Prog. Theor. Phys*, vol. **28**, no. **5**, pp. 870 – 880, 1962.

[18] P. Adamson et al, "Search for muon-neutrino to electron-neutrino transitions in minos," *Phys. Rev. Lett.*, vol. **103**, p. 261802, Dec 2009.

[19] J. H. Christenson, J. W. Cronin, V. L. Fitch, and R. Turlay, "Evidence for the 2π Decay of the $K2$ Meson," *Phys. Rev. Lett.*, vol. **13**, pp. 138–140, Jul 1964.

[20] B. Aubert et al, "Observation of CP Violation in the B Meson System," *Phys. Rev. Lett.*, vol. **87**, p. 091801, Aug 2001.

[21] B. Aubert et al, "Observation of CP Violation in B^0 –> K$^+$ π^- and B^0 –> π^+ π^-," *Physical Review Letters*, vol. **99**, no. **2**, p. 021603, 2007.

[22] K. Abe et al, "Observation of Large CP Violation in the Neutral B Meson System," *Phys. Rev. Lett.*, vol. **87**, p. 091802, Aug 2001.

[23] H. Ishino et al, "Observation of Direct CP Violation in B^0 –> π^+ π^- Decays and Model-Independent Constraints on the Quark-Mixing Angle ϕ_2," *Physical Review Letters*, vol. **98**, no. **21**, p. 211801, 2007.

[24] A. Angelopoulos et al, "First direct observation of time-reversal non-invariance in the neutral-kaon system," *Physics Letters B*, vol. **444**, no. **1 – 2**, pp. 43 – 51, 1998.

[25] C. A. Baker et al, "Improved Experimental Limit on the Electric Dipole Moment of the Neutron," *Physical Review Letters*, vol. **97**, no. **13**, p. 131801, 2006.

[26] G. Luders, "Proof of the TCP theorem," *Annals of Physics*, vol. **2**, no. **1**, pp. 1 – 15, 1957.

[27] D. Colladay and V. A. Kostelecký, "cpt violation and the standard model," *Phys. Rev. D*, vol. **55**, pp. 6760–6774, Jun 1997.

[28] D. Colladay and V. A. Kostelecký, "Lorentz-violating extension of the standard model," *Phys. Rev. D*, vol. **58**, p. 116002, Oct 1998.

[29] V. A. Kostelecký and M. Mewes, "Lorentz and CPT violation in neutrinos," *Phys. Rev. D*, vol. **69**, p. 016005, Jan 2004.

[30] V. A. Kostelecký and M. Mewes, "Lorentz and CPT violation in the neutrino sector," *Phys. Rev. D*, vol. **70**, p. 031902, Aug 2004.

[31] T. Katori, V. A. Kostelecký, and R. Tayloe, "Global three-parameter model for neutrino oscillations using Lorentz violation," *Phys. Rev. D*, vol. **74**, p. 105009, Nov 2006.

[32] A. A. Aguilar-Arevalo et al, "Unexplained Excess of Electronlike Events from a 1-GeV Neutrino Beam," *Phys. Rev. Lett.*, vol. **102**, p. 101802, Mar 2009.

[33] J. S. Díaz, V. A. Kostelecký, and M. Mewes, "Perturbative Lorentz and CPT violation for neutrino and antineutrino oscillations," *Phys. Rev. D*, vol. **80**, p. 076007, Oct 2009.

[34] V. A. Kostelecký and N. Russel, "Data Tables for Lorentz and CPT Violation," *arXiv:0801.0287v3*, 2010.

[35] W. Pauli, "a letter to the Tübingen Conference on radioactivity," Dec 1930.

[36] J. Chadwick, "POSSIBLE EXISTENCE OF A NEUTRON," *Nature*, vol. **129**, p. 312, 1932.

[37] E. Fermi, "An attempt of a theory of beta radiation," *Z phys*, vol. **88**, no. **161**, p. 177, 1934.

[38] F. Reines and C. L. Cowan, "The neutrino," *Nature*, vol. **178**, pp. 446–449, 1956.

[39] M. Goldhaber, L. Grodzins, and A. W. Sunyar, "Helicity of Neutrinos," *Phys. Rev.*, vol. **109**, pp. 1015–1017, Feb 1958.

[40] G. Danby et al, "Observation of high-energy neutrino reactions and the existence of two kinds of neutrinos," *Phys. Rev. Lett.*, vol. **9**, no. **1**, pp. 36–44, 1962.

[41] B. Pontecorvo, "Electron and muon neutrinos," *Sov. Phys. JETP*, vol. **10**, pp. 1236–1240, 1960.

[42] M. Schwartz, "Feasibility of Using High-Energy Neutrinos to Study the Weak Interactions," *Phys. Rev. Lett.*, vol. **4**, pp. 306–307, Mar 1960.

[43] B. Adeva et al, "A determination of the properties of the neutral intermediate vector boson Z0," *Phys. Lett. B*, vol. **231**, pp. 509–518, Nov 1989.

[44] M. Nakamura, "Results from DONUT," 2000. Prepared for 30th International Conference on High-Energy Physics (ICHEP 2000), Osaka, Japan, 27 Jul - 2 Aug 2000.

[45] J. N. Bahcall, A. M. Serenelli, and S. Basu, "New solar opacities, abundances, helioseismology, and neutrino fluxes," *Astrophys. J.*, vol. **621**, pp. L85–L88, 2005.

[46] J. N. Bahcall, M. H. Pinsonneault, and S. Basu, "Solar Models: Current Epoch and Time Dependences, Neutrinos, and Helioseismological Properties," *Astrophys. J.*, vol. **555**, pp. 990–1012, Jul 2001.

[47] J. N. Bahcall, "Chemical controversy at the solar surface," *Physics World*, vol. **February**, p. 26, 2005.

[48] J. R. Wilson, *A Measurement of the* ^{8}*B Solar Neutrino Energy Spectrum at the Sudbury Neutrino Observatory*. PhD thesis, Oxford, 2004.

[49] R. Davis, "A review of the Homestake solar neutrino experiment," *Progress in Particle and Nuclear Physics*, vol. **32**, pp. 13 – 32, 1994.

[50] J. N. Abdurashitov et al, "Measurement of the solar neutrino capture rate by the Russian-American gallium solar neutrino experiment during one half of the 22-year cycle of solar activity," *J. Exp. Theor. Phys.*, vol. **95**, pp. 181–193, 2002.

[51] W. Hampel et al, "GALLEX solar neutrino observations:results for GALLEX IV," *Phys. Lett. B*, vol. **1-2**, no. **447**, pp. 127 – 133, 1999.

[52] T. Webweavers, "What is dark matter made of?." http://www.scienzagiovane.unibo.it/English/darkmatter/3-dark-composition.html, 08 2009.

[53] K. Arisaka et al, "KAMIOKANDE (KAMIOKA Nucleon Decay Experiment)," *LICEPP preprint*, vol. **82-04**, 1982.

[54] R. Clark et al, "Atmospheric Muon Neutrino Fraction above 1 GeV," *Phys. Rev. Lett.*, vol. **79**, pp. 345–348, Jul 1997.

[55] Y. Ashie et al, "Measurement of atmospheric neutrino oscillation parameters by Super-Kamiokande I," *Phys. Rev. D*, vol. **71**, p. 112005, Jun 2005.

[56] Y. Fukuda et al, "Evidence for Oscillation of Atmospheric Neutrinos," *Phys. Rev. Lett.*, vol. **81**, pp. 1562–1567, Aug 1998.

[57] Y. Ashie et al, "Evidence for an Oscillatory Signature in Atmospheric Neutrino Oscillations," *Phys. Rev. Lett.*, vol. **93**, p. 101801, Sep 2004.

[58] B. Aharmim et al, "Electron energy spectra, fluxes, and day-night asymmetries of ^{8}**B** solar neutrinos from measurements with NaCl dissolved in the heavy-water detector at the Sudbury Neutrino Observatory," *Physical Review C (Nuclear Physics)*, vol. **72**, no. **5**, p. 055502, 2005.

[59] S. Fukuda et al, "Determination of solar neutrino oscillation parameters using 1496 days of Super-Kamiokande-I data," *Phys. Lett. B*, vol. **539**, pp. 179–187, July 2002.

[60] S. Abe et al, "Precision Measurement of Neutrino Oscillation Parameters with KamLAND," *Phys. Lett.*, vol. **100**, no. **221803**, 2008.

[61] M. H. Ahn et al, "Measurement of neutrino oscillation by the K2K experiment," *Phys. Rev. D*, vol. **74**, no. **072003**, 2006.

[62] M. Apollonio et al, "Limits on neutrino oscillations from the CHOOZ experiment," *Phys. Lett. B*, vol. **466**, pp. 415–430, Nov 1999.

[63] A. . Aguilar et al, "Evidence for neutrino oscillations from the observation of $\bar{\nu}_e$ appearance in a $\bar{\nu}_\mu$ beam," *Phys. Rev. D*, vol. **64**, p. 112007, Nov 2001.

[64] B. Achkar et al, "Search for neutrino oscillations at 15, 40 and 95 meters from a nuclear power reactor at Bugey," *Nucl.Phys B*, vol. **434**, pp. 503 – 532, Jan 1995.

[65] A. A. Aquilar-Arevalo et al, "Search for Electron Neutrino Appearance at the Δ m^2 1 eV^2 Scale," *Phys. Rev. Lett.*, vol. **98**, Jun 2007.

[66] F. Ardellier et al, "Double Chooz, A Search for the Neutrino Mixing Angle θ_{13}," *arXiv:hep-ex/0606025v4*, 2006.

[67] M. Goodman, "World nu's," *Doc-db*, vol. 7021, 2010.

[68] D. B. Collaboration, "A Precision Measurement of the Neutrino Mixing Angle θ_{13} Using Reactor Antineutrinos At Daya Bay," *arXiv:hep-ex/0701029v1*, 2007.

[69] M. Mezzetto, "Next Challenge in Neutrino Physics: the theta(13) Angle," *arXiv:0905.2842*, 2009.

[70] P. Huber, M. Lindner, and W. Winter, "Superbeams vs. neutrino factories," *Nuclear Physics B*, vol. **645**, no. **1-2**, pp. 3 – 48, 2002.

[71] Y. Itow et al, "The JHF-Kamioka neutrino project," *arXiv:hep-ex/0106019v1*, 2001.

[72] "T2K first event detected." http://www.kek.jp/intra-e/press/2010/T2KfirstEvent.html.

[73] D. Ayres et al, "Proposal to Build a 30 Kiloton Off-Axis Detector to Study $\nu_\mu \rightarrow \nu_e$ Oscillations in the NuMI Beamline," tech. rep., 2006.

[74] S. Geer, "Neutrino beams from muon storage rings: Characteristics and physics potential," *Phys. Rev. D*, vol. **57**, pp. 6989 – 6997, Jun 1998.

[75] P. Zucchelli, "A novel concept for a neutrino factory: the beta-beam," *Physics Letters B*, vol. **532**, no. **3 – 4**, pp. 166 – 172, 2002.

[76] K. Eguchi et al, "First Results from KamLAND: Evidence for Reactor Antineutrino Disappearance," *Phys. Rev. Lett.*, vol. **90**, p. 6, Jan 2003.

[77] T. Bruce et al, "Measurement of the Solar Electron Neutrino Flux with the Homestake Chlorine Detector," *Astrophys. J.*, vol. **496**, no. **1**, p. 505, 1998.

[78] J. N. Abdurashitov et al, "Measurement of the solar neutrino capture rate with gallium metal," *Phys. Rev. C*, vol. **60**, p. 055801, Oct 1999.

[79] S. Fukuda et al, "Solar B^8 and hep Neutrino Measurements from 1258 Days of Super-Kamiokande Data," *Phys. Rev. Lett.*, vol. **86**, pp. 5651–5655, Jun 2001.

[80] S. N. Ahmad et al, "Measurement of the Total Active $B8$ Solar Neutrino Flux at the Sudbury Neutrino Observatory with Enhanced Neutral Current Sensitivity," *Phys. Rev. Lett.*, vol. **92**, p. 181301, May 2004.

[81] E. Aliu et al, "Evidence for Muon Neutrino Oscillation in an Accelerator-Based Experiment," *Phys. Rev. Lett.*, vol. **94**, p. 081802, 2005.

[82] D. G. Michael et al, "Observation of Muon Neutrino Disappearance with the MINOS Detectors in the NuMI Neutrino Beam," *Physical Review Letters*, vol. **97**, no. **19**, p. 191801, 2006.

[83] M. Apollonio et al, "Search for neutrino oscillations on a long base-line at the CHOOZ nuclear power station," *Eur. Phys. J. C*, vol. **27**, pp. 331–374, 2003.

[84] M. C. Gonzalez-Garcia and M. Maltoni, "Atmospheric neutrino oscillations and new physics," *Phys. Rev. D*, vol. **70**, p. 12, Aug 2004.

[85] S. Antusch and E. Fernandez-Martinez, "Signals of CPT violation and non-locality in future neutrino oscillation experiments," *Physics Letters B*, vol. **665**, no. **4**, pp. 190 – 196, 2008.

[86] J. D. Chapman, *Atmospheric neutrino observations in the MINOS far detector*. PhD thesis, University of Cambridge, 2007. FERMILAB-THESIS-2007-29.

[87] J. J. Evans, *Measuring Antineutrino Oscillations with the MINOS Expriment*. PhD thesis, University of Oxford, 2008.

[88] J. Hartnell, "Muon Anti-Neutrinos in MINOS," *Doc-db*, vol. **5938**, 2009.

[89] B. Aharmim et al, "An Independent Measurement of the Total Active ^{8}B Solar Neutrino Flux Using an Array of ^{3}He Proportional Counters at the Sudbury Neutrino Observatory," *Phys. Rev. Lett.*, vol. **101**, p. 111301, 2008.

[90] M. C. D. G. Michael, "The magnetized steel and scintillator calorimeters of the MINOS experiment," *NUCL.INSTRUM.METH.A*, vol. **596**, p. 190, 2008.

[91] R. M. Zwaska, *Accelerator Systems and Instrumentation for the NuMI Neutrino Beam*. PhD thesis, University of Texas in Austin, 2005.

[92] A. Himmel, "Private comunication."

[93] B. J. Rebel, *Neutrino-Induced Muon in the MINOS Far Detector*. PhD thesis, Indiana University, August 2005.

[94] J. Hartnell, *Measurement of the Calorimetric Energy Scale in MINOS*. PhD thesis, University of Oxford, 2005.

[95] T. M. Calibration, "January 2008 Position Paper on Calibration of the Pre-Shutdown Data," *Doc-db*, vol. **3941**, 2008.

[96] P. Adamson et al, "The MINOS calibration detector," *NUCL.INSTRUM.METH*, vol. **A**, no. **556**, pp. 119–133, 2006.

[97] P. L. Vahle, *Electromagnetic Interactions in the MINOS Detectors*. PhD thesis, University of Texas in Austin, 2004.

[98] M. A. Kordosky, *Hadronic Interactions in the MINOS Detectors*. PhD thesis, University of Texas in Austin, 2004.

[99] A. E. Cabrera Serra, *Systematic Comparison of the MINOS Near & Far Detector readout systems*. PhD thesis, Oxford, 2005.

[100] N. Tagg et al, "Performance of Hamamatsu 64-anode photomultipliers for use with wavelength-shifting fibres," *NUCL.INSTRUM.METH.A*, vol. **539**, pp. 668 – 678, 2005.

[101] K. Lang et al, "Characterization of 1600 Hamamatsu 16-anode photomultipliers for the MINOS Far detector," *Nuclear Instruments and Methods in Physics Research Section A: Accelerators, Spectrometers, Detectors and Associated Equipment*, vol. **545**, no. **3**, pp. 852 – 871, 2005.

[102] T. M. C. Group, "Position Paper on Calibration, for the June 2007 Box Opening," Tech. Rep. , various, 2007.

[103] P. S. Symes, *First Preliminary Measurment Of Neutrino Oscillation Paramerters By NuMu/MINOS A Calibrations Studies For Improving This Measurement*. PhD thesis, University of Sussex, 2005.

[104] P. Adamson et al, "Photoelectron Counting by Several Methods," Tech. Rep. **NuMI-L-661**, FNAL, 2000.

[105] R. Nichol, *Calibration of the MINOS Detectors*. PhD thesis, University College London, 2003.

[106] T. M. C. Group, "Position Paper on Calibration, for the Jan 2006 Box Opening," Tech. Rep. **DocDB 1289**, various, 2006.

[107] B. C. Choudhary, "Extruded Polystyrene Scintillator for MINOS," Tech. Rep. **NuMI-not-676**, California Institute of Technology, 2000.

[108] P. Adamson et al, "Measurement of neutrino velocity with the MINOS detectors and NuMI neutrino beam," *Phys. Rev. D*, vol. **76**, no. **072005**, 2007.

[109] P. Adamson et al, "Measurement of the Atmospheric Muon Charge Ratio at TeV Energies with MINOS detectors," *Phys. Rev. D*, vol. **76**, no. **052003**, 2007.

[110] S. Osprey et al, "Sudden stratospheric warmings seen in MINOS deep underground muon data," *Geophys. Res Lett*, 2009.

[111] P. Adamson et al, "Testing Lorentz Invariance and CPT Conservation with NuMI Neutrinos in the MINOS Near Detector," *Physical Review Letters*, vol. **101**, no. **15**, p. 151601, 2008.

[112] J. S. Marshall, *A study of muon neutrino disappearance with the MINOS detectors and the NuMI beam*. PhD thesis, Cambridge, 2008.

[113] E. Lisi, A. Marrone, and D. Montanino, "Probing Possible Decoherence Effects in Atmospheric Neutrino Oscillations," *Phys. Rev. Lett.*, vol. **85**, pp. 1166 – 1169, Aug 2000.

[114] T. Kajita, "Atmospheric neutrinos and the implications to cosmic ray interactions," *Nuclear Physics B - Proceedings Supplements*, vol. **175 – 176**, pp. 301 – 306, 2008. Proceedings of the XIV International Symposium on Very High Energy Cosmic Ray Interactions.

[115] P. Adamson et al, "Search for active neutrino disappearance using neutral-current interactions in the MINOS long-baseline experiment," *Phys. Rev. Lett.*, vol. **101**, no. **221804**, 2008.

[116] P. Adamson et al, "Study of muon neutrino disappearance using the Fermilab Main Injector neutrino beam," *Physical Review D (Particles and Fields)*, vol. **77**, no. **7**, p. 072002, 2008.

[117] B. Kayser, "Neutrino Intrinsic Properties: The Neutrino-Antineutrino Relation," *Physica Scripta*, vol. **T121**, pp. 156 – 160, 2005.

[118] G. J. Feldman and R. D. Cousins, "Unified approach to the classical statistical analysis of small signals," *Phys. Rev. D*, vol. **57**, no. **7**, 1998.

[119] A. Blake, "Far Detector Data Quality Software," *Doc-db*, vol. **3486**, 2007.

[120] D. Petyt, "Update on ND data quality checks," *Doc-db*, vol. **3883**, 2007.

[121] S. Kopp and L. Loiancono, "Beam Quality Cuts," *Doc-db*, vol. **2747**, 2007.

[122] R. Ospanov, *A measurement of muon neutrino disappearance with the MINOS detectors and NuMI Beam*. PhD thesis, University of Texas in Austin, 2008.

[123] I. Danko, "Effect of qp/sigqp on NuMubar selection," *Doc-db*, vol. **4483**, 2008.

[124] M. Artamendi Tavera, D. Auty, and N. Devenish, "Selector Evaluation," *Doc-db*, vol. **4839**, 2008.

[125] M. Artamendi Tavera et al, "NuMuBar Selector Evaluation," *Doc-db*, vol. **4829**, 2008.

[126] T. Hastie, R. Tibshirami, and J. Friedman, *The Elements of Statistcal Learning: Data Mining, Inference, and Prediction*. Springer, 2001.

[127] A. Himmel, "Plots for the NuMuBar Blessing Package," *Doc-db*, vol. **5404**, 2009.

[128] F. James and M. Roos, "A System for function minimization and analysis of teh parameter errors and correlations," *Comput. Phys. Commun.*, 1975.

[129] D. Auty and I. Danko, "Effect of Near Detector Data-Monte Carlo discrepancies on the Far Detector Extrapolation," *Doc-db*, vol. **5259**, 2008.

[130] J. Evans, "NC and CC Background Systematic," *Doc-db*, vol. **5237**, 2008.

[131] J. Musser, "Range/Energy Task Force Position Paper," *Doc-db*, vol. **3134**, 2007.

[132] A. Himmel, M. Ishitsuka, and D. Jaffe, "Systematic Error on Antineutrino from the Decay Pipe," *Doc-db*, vol. **4584**, 2008.

[133] C. A. et al, "Updated Cross Section Model Uncertainties for the Charged Current Analysis," *Doc-db*, vol. **2989**, 2007.

[134] H. Gallagher, "Shower Energy Scale Uncertainty For the Run I+II Analysis," *Doc-db*, vol. **4287**, 2008.

[135] B. Armstong, "K/pi ratio uncertainties update," *Doc-db*, vol. **5305**, 2008.

[136] S. Coleman, "High Low Bfield Maps," *Doc-db*, vol. **4160**, 2008.

[137] B. Becker et al, "Alignment of the MINOS FD," *FERMILAB-TM-2410-E*, 2004.

[138] R. Ospanov and K. Lang, "Alignment of the Near Detector Scintillator Modules Using Cosmic ray Muons," *FERMILAB-TM-2411-E*, 2005.

[139] P. Adamson et al, "Measurement of the atmospheric muon charge ratio at TeV energies with the MINOS detector," *Phys. Rev. D*, vol. **76**, no. **5**, 2007.

[140] M. Goodman, "Cosmic Ray muon analysis of Magnet off data or why we think errors in the magnetic field didn't cause the charge ratio biases," *Doc-db*, vol. **4104**, 2008.

[141] J. Evans, J. Hartnell, and D. Naples, "Cross Checks of the 3.2×10^{20} PoT $\overline{\nu}_{\mu}$ Analysis," *Doc-db*, vol. **5968**, 2009.

[142] A. Himmel, "How Likely is Our Data," *Doc-db*, vol. **5690**, 2009.

[143] Z. Isvan, "Far Detector Data/MC Plots," *Doc-db*, vol. **5531**, 2008.

[144] A. Himmel, "Run III Blinded Geometrical Distributions," *Doc-db*, vol. **5611**, 2009.

[145] N. Devenish, "NuMuBar 2nd Apr 09," *Doc-db*, vol. **5876**, 2009.

[146] A. Himmel and N. Devenish, "Feldman-Cousins for the Antineutrino Analysis," *Doc-db*, vol. **5209**, 2008.

[147] J. Evans, J. Hartnell, A. Himmel, and P. Rodrigues, "Matrix Method extrapolation for $\overline{\nu}_\mu$ analyses," *Doc-db*, vol. **4462**, 2008.

[148] M. Gonzalez-Garcia and M. Maltoni, "Phenomenology with massive neutrinos," *Physics Reports*, vol. **460**, no. **1-3**, pp. 1 – 129, 2008.

[149] S. Kasahara, "Status of PTSim and GeoGeometry," *Doc-db*, vol. **2524**, 2006.

Appendix A

Glossary of Acronyms

Below is a list of the most commonly used acronyms in this thesis.

CalDet	=	CALibration DETector
FD	=	Far Detector
FEE	=	Front End Electronics
Fermilab	=	FERmi national accelerator LABoratory
F/N	=	Far over Near
HE	=	High Energy
LE	=	Low Energy
LEM	=	Library Event Matching
LI	=	Light Injection
LIM	=	Light Injection Module
ME	=	Medium Energy
MEU	=	Muon Energy Unit
ND	=	Near Detector
NuMI	=	Neutrinos at the Main Injector
POT	=	Protons On Target
spe	=	Single PhotoElectron

VARC = VA Readout Card

VFB = Va Front end Board

VMM = Va Mezzanine Module

WLS = WaveLength Shifting fibre

Appendix B

Monte Carlo Sets Used

B.1 General

The Monte Carlo used in the $\overline{\nu}_\mu$ charged-current analysis in this thesis is the forth version of the so-called Daikon Monte Carlo reconstructed with the Cedar version of the reconstruction software. The calibration constants applied to the MC set were derived from physics datasets RunI – RunII. A corrected magnetic field was also apply to the reconstruction. In the MINOS collaboration these files have the tag D04_cedar_phy_bhcurv included in the file name.

B.2 Alignment

For the mis-alignment studies the MINOS Monte Carlo framework, using PTSim[149], was used to simulate events in the Far Detectors. The MINOS software release R1.26 (snapshot S07-10-22-R1026) was used for event simulation purposes. Reconstruction of simulated events has been done with the software release R1.24.3 using cedar_phy production scripts.

Appendix C

Alignment Plots

This appendix displays a gallery of plots from the study of the systematic due to the detector alignment uncertainty (section 9.4.1). They are included here to show the effect of the two misalignments, of 2 mm and of 5 mm, on all the reconstructed parameters investigated. Overall they show that in the high statistic regions of the parameters there is less than a 5 % error. There are however, large variations of greater than 20 % in the tails of the parameters.

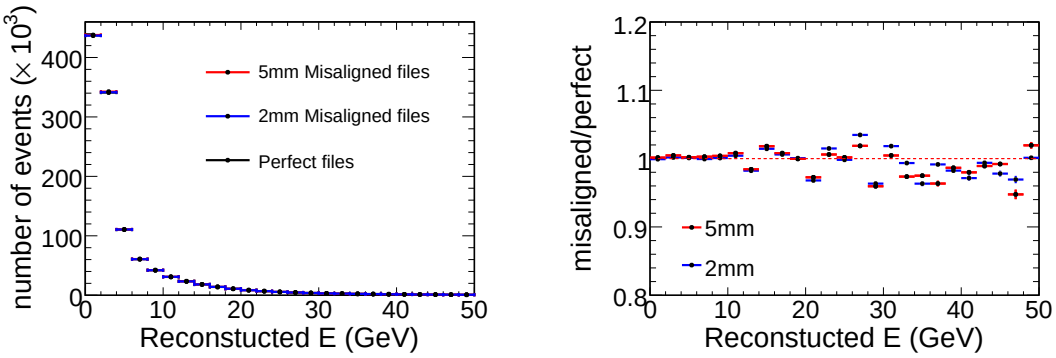

Figure C.1: The reconstructed muon track energy spectra in negatively charged events with perfect or misaligned geometry (left) and their ratio (right).

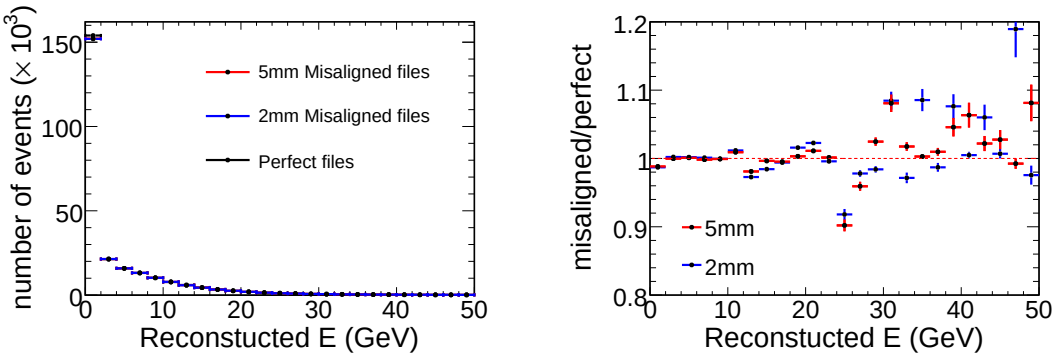

Figure C.2: The reconstructed muon energy spectra in positively charged events with perfect or misaligned geometry (left) and their ratio (right).

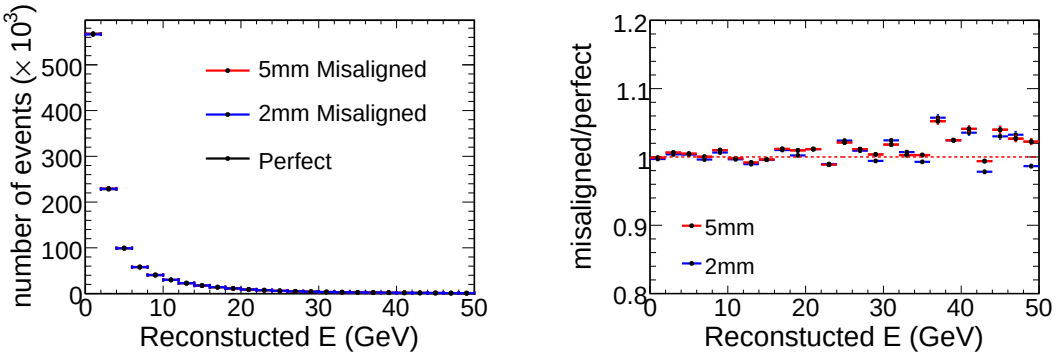

Figure C.3: The reconstructed shower energy spectra in negatively charged events with perfect or misaligned geometry (left) and their ratio (right).

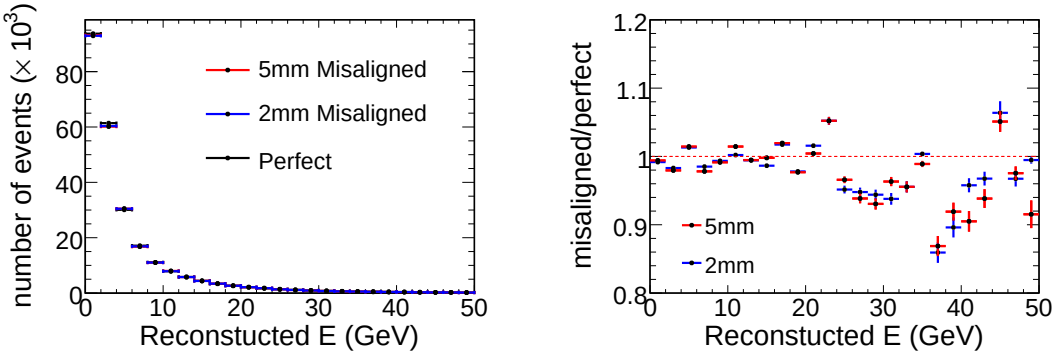

Figure C.4: The reconstructed shower energy spectra in positively charged events with perfect or misaligned geometry (left) and their ratio (right).

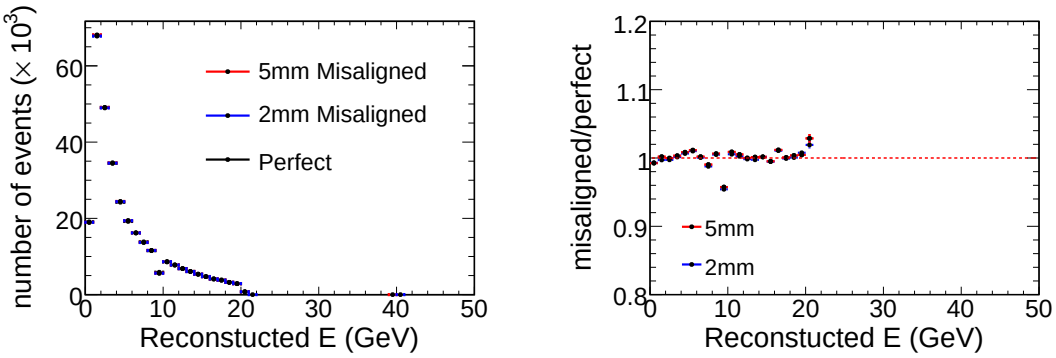

Figure C.5: The track energy range with reweight variable for exiting negatively charged track events with perfect or misaligned geometry (left) and their ratio (right).

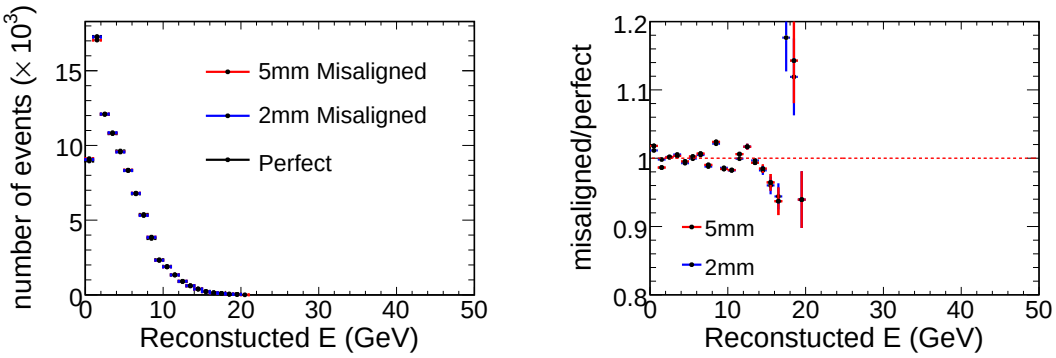

Figure C.6: The track energy range with reweight variable for exiting positively charged track events with perfect or misaligned geometry (left) and their ratio (right).

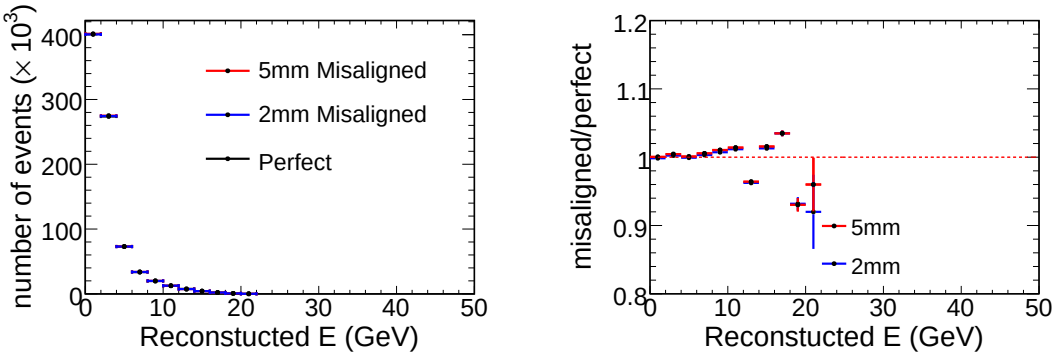

Figure C.7: The track energy range with reweight variable for contained negatively charged track events with perfect or misaligned geometry (left) and their ratio (right).

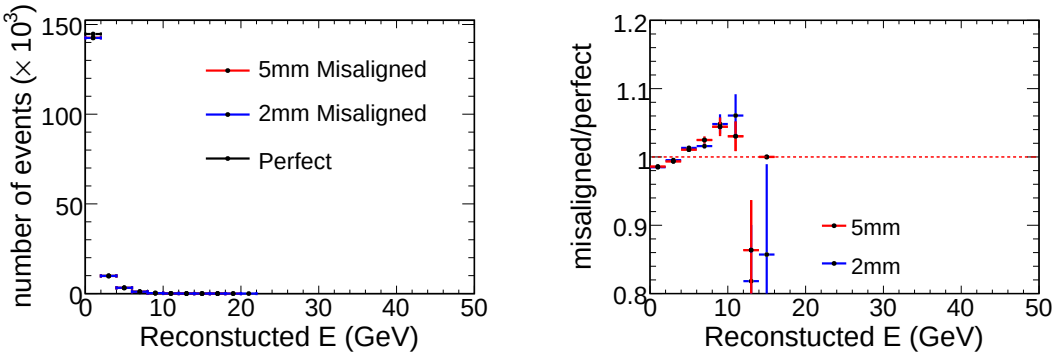

Figure C.8: The track energy range with reweight variable for contained positively charged track events with perfect or misaligned geometry (left) and their ratio (right).

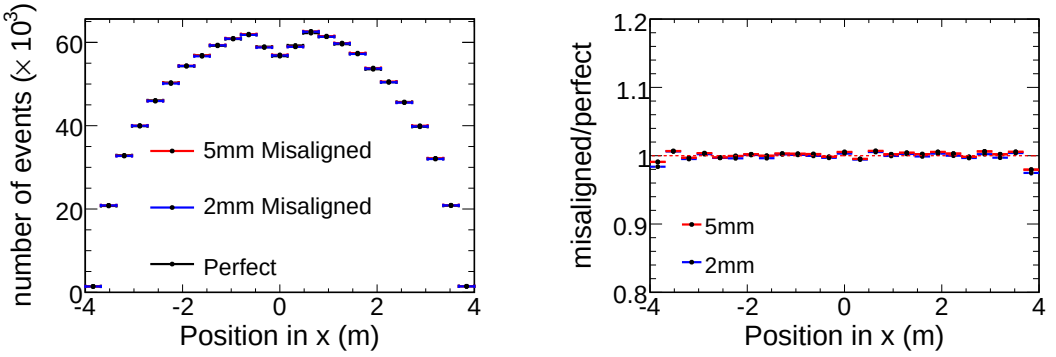

Figure C.9: The reconstructed track vertex x position in negatively charged events with perfect or misaligned geometry (left) and their ratio (right).

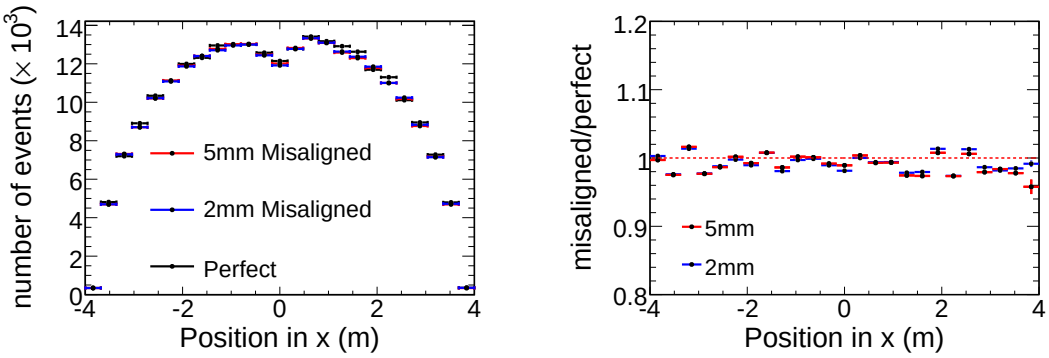

Figure C.10: The reconstructed track vertex x position in positively charged events with perfect or misaligned geometry (left) and their ratio (right).

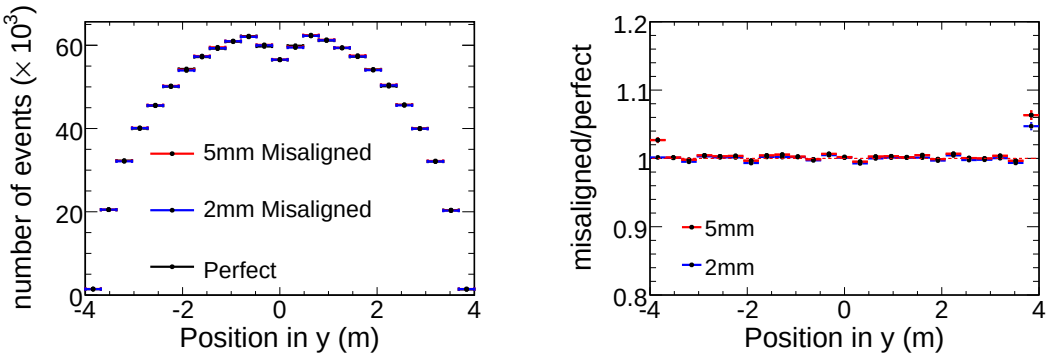

Figure C.11: The reconstructed track vertex y position in negatively charged events with perfect or misaligned geometry (left) and their ratio (right).

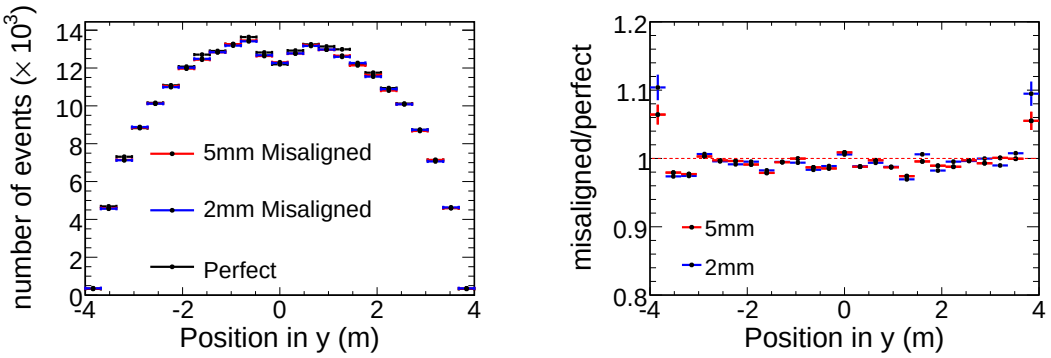

Figure C.12: The reconstructed track vertex y position in positively charged events with perfect or misaligned geometry (left) and their ratio (right).

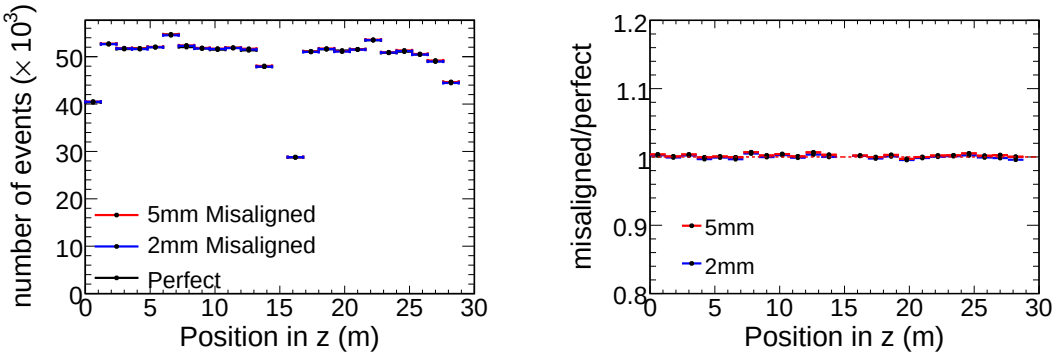

Figure C.13: The reconstructed track vertex z position in negatively charged events with perfect or misaligned geometry (left) and their ratio (right).

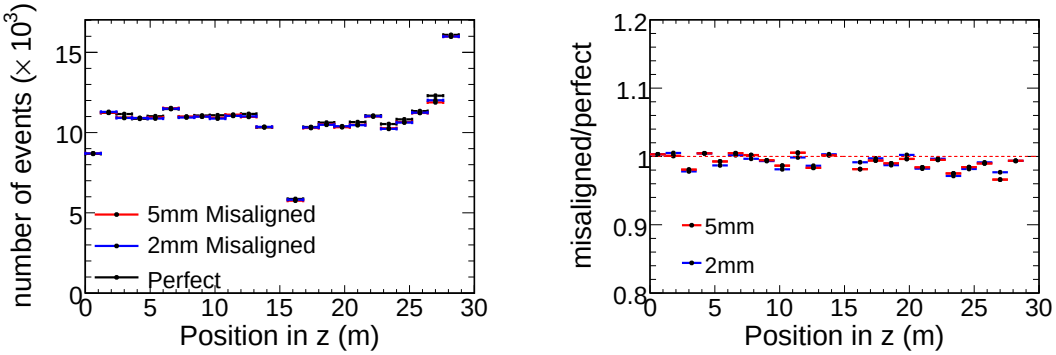

Figure C.14: The reconstructed track vertex z position in positively charged events with perfect or misaligned geometry (left) and their ratio (right).

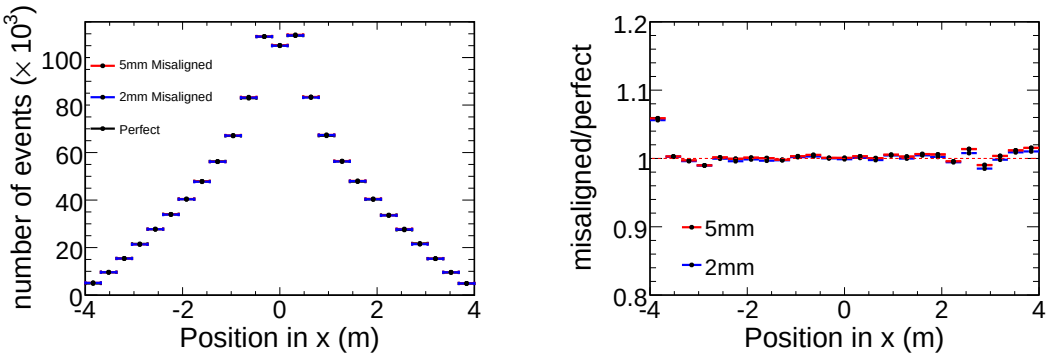

Figure C.15: The reconstructed track end x position in negatively charged events with perfect or misaligned geometry (left) and their ratio (right).

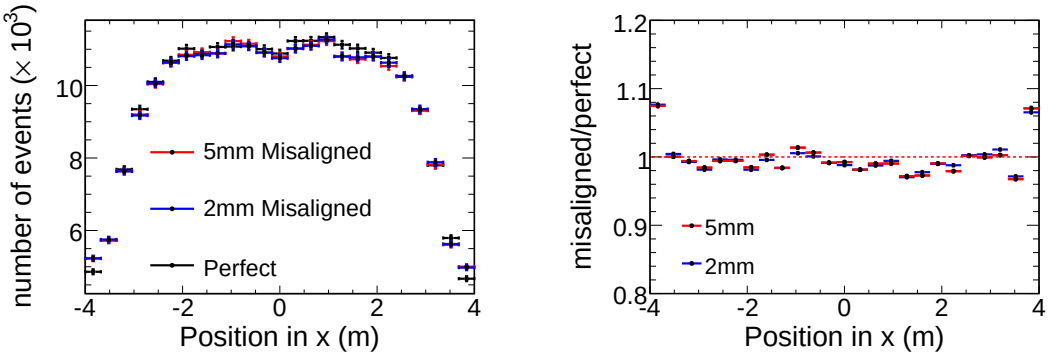

Figure C.16: The reconstructed track end x position in positively charged events with perfect or misaligned geometry (left) and their ratio (right).

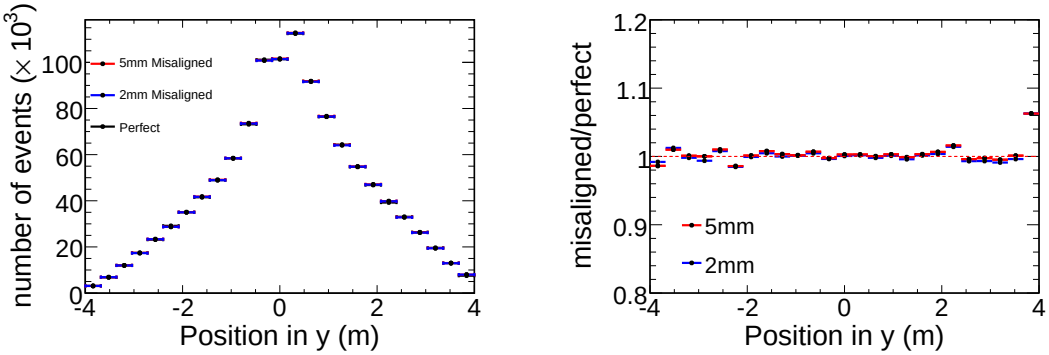

Figure C.17: The reconstructed track end y position in negatively charged events with perfect or misaligned geometry (left) and their ratio (right).

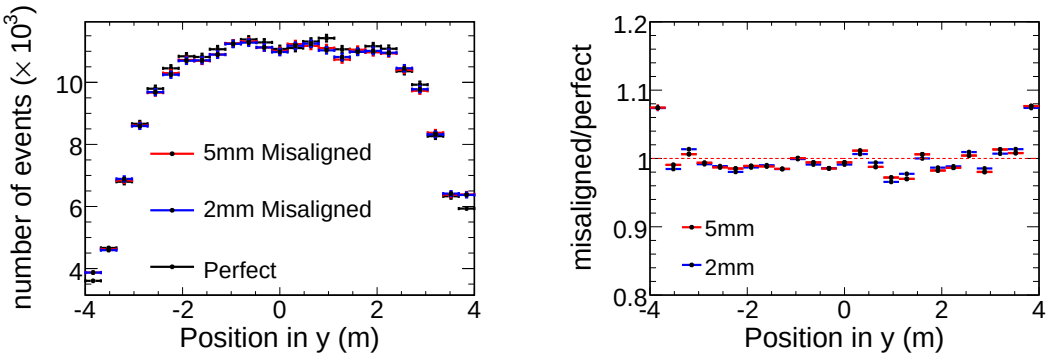

Figure C.18: The reconstructed track end y position in positively charged events with perfect or misaligned geometry (left) and their ratio (right).

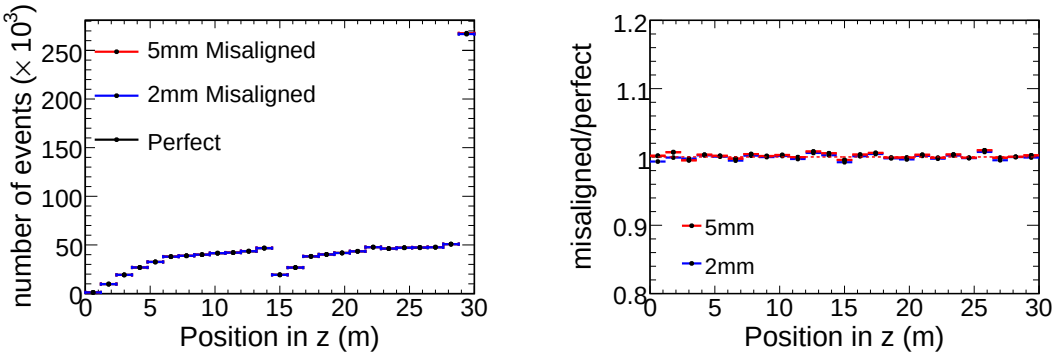

Figure C.19: The reconstructed track end z position in negatively charged events with perfect or misaligned geometry (left) and their ratio (right).

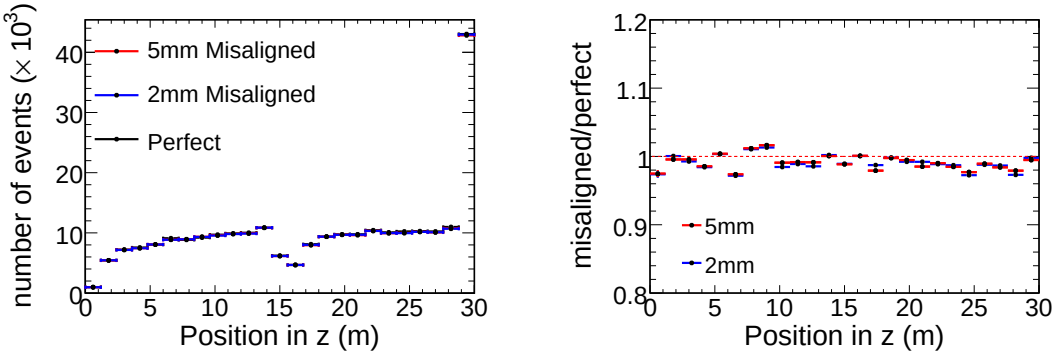

Figure C.20: The reconstructed track end z position in positively charged events with perfect or misaligned geometry (left) and their ratio (right).

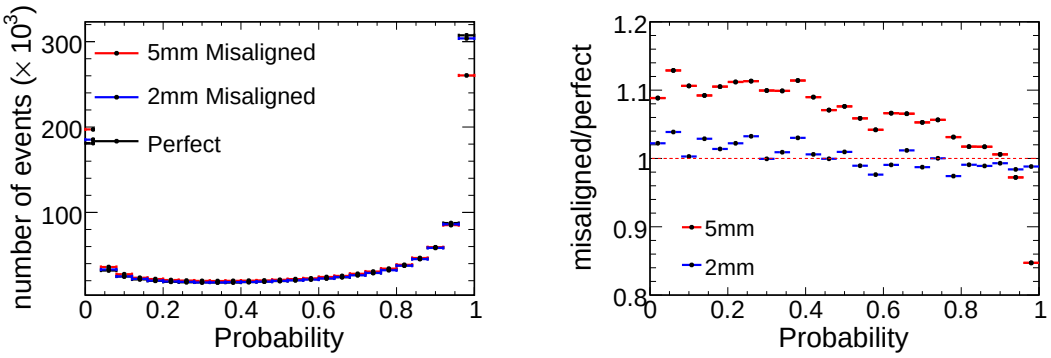

Figure C.21: Track fit probability in negatively charged events with perfect or misaligned geometry (left) and their ratio (right).

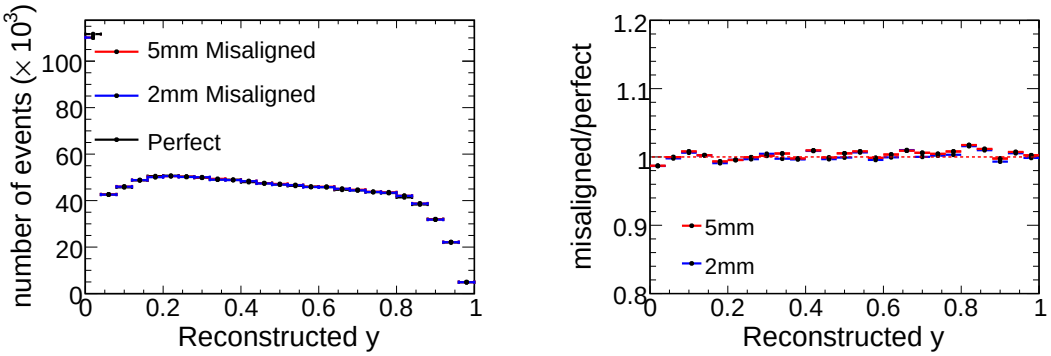

Figure C.22: The reconstructed y in negatively charged events with perfect or misaligned geometry (left) and their ratio (right).

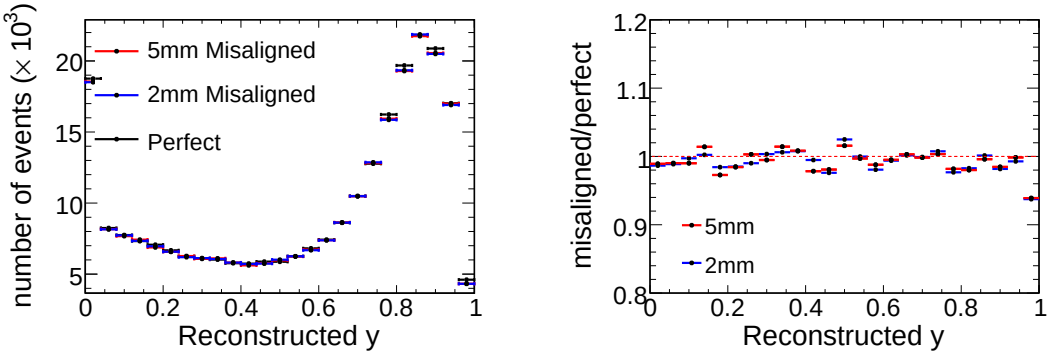

Figure C.23: The reconstructed y in positively charged events with perfect or misaligned geometry (left) and their ratio (right).

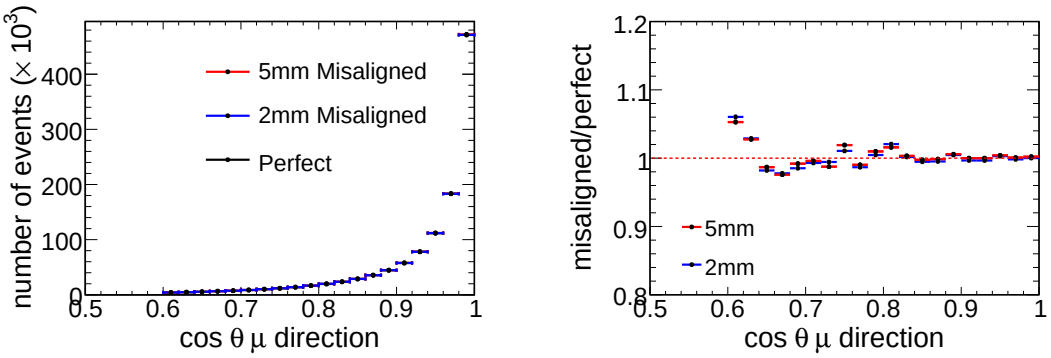

Figure C.24: The direction cosine of track (with respect to the beam) in negatively charged events with perfect or misaligned geometry (left) and their ratio (right).

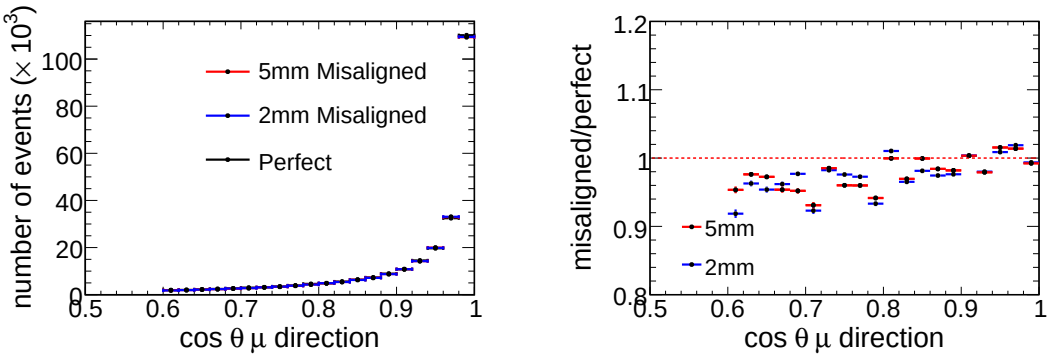

Figure C.25: The direction cosine of track (with respect to the beam) in positively charged events with perfect or misaligned geometry (left) and their ratio (right).

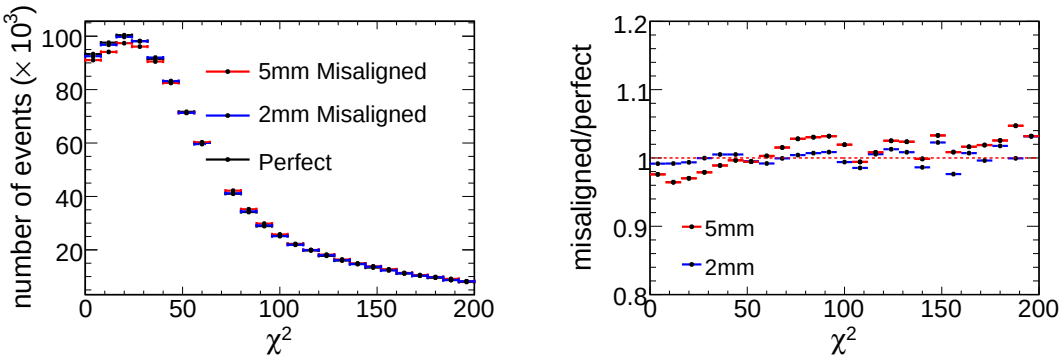

Figure C.26: The track fit χ^2 in negatively charged events with perfect or misaligned geometry (left) and their ratio (right).

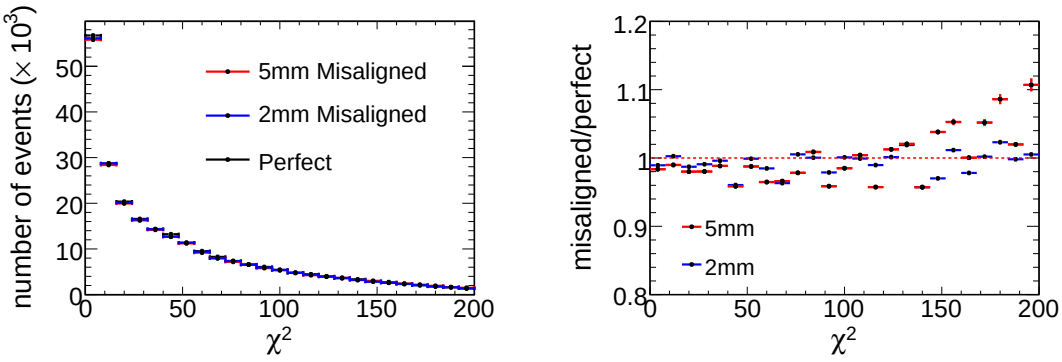

Figure C.27: The track fit χ^2 in positively charged events with perfect or misaligned geometry (left) and their ratio (right).

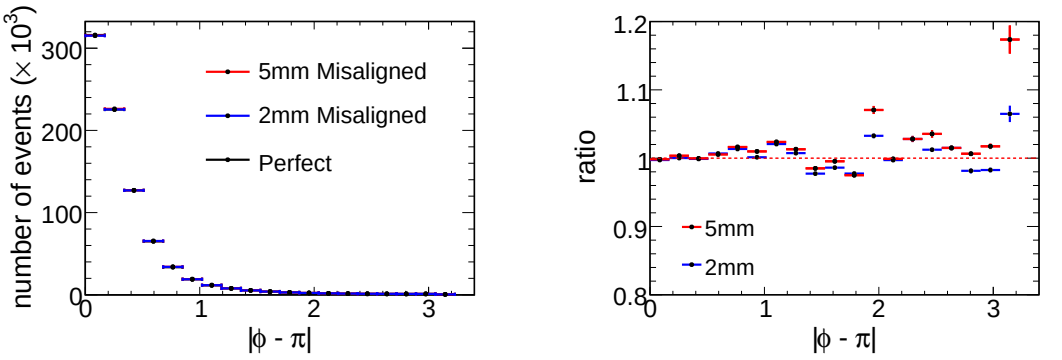

Figure C.28: The relative angle variable for contained negatively charged events with perfect or misaligned geometry (left) and their ratio (right).

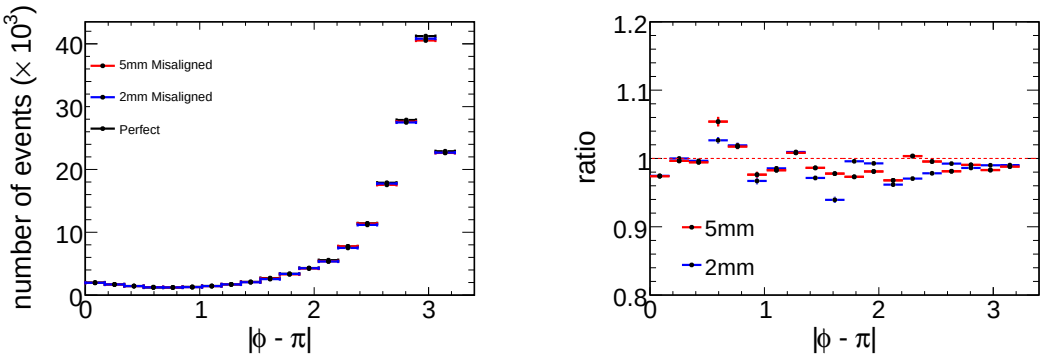

Figure C.29: The relative angle variable for contained positively charged track events with perfect or misaligned geometry (left) and their ratio (right).

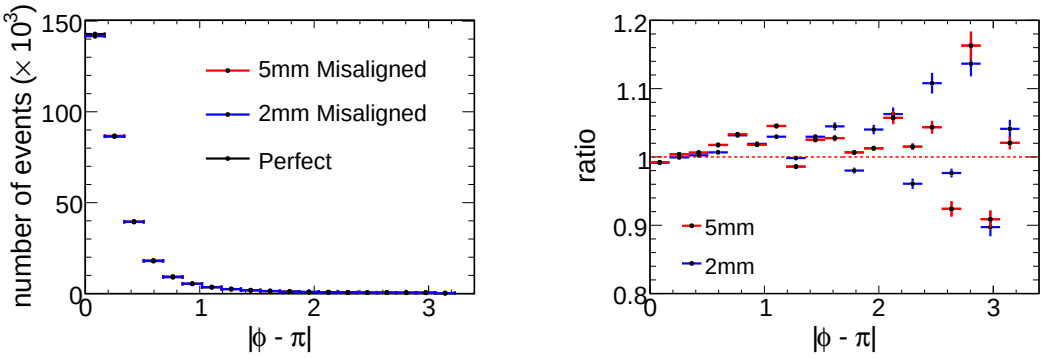

Figure C.30: The relative angle variable for exiting negatively charged track events with perfect or misaligned geometry (left) and their ratio (right).

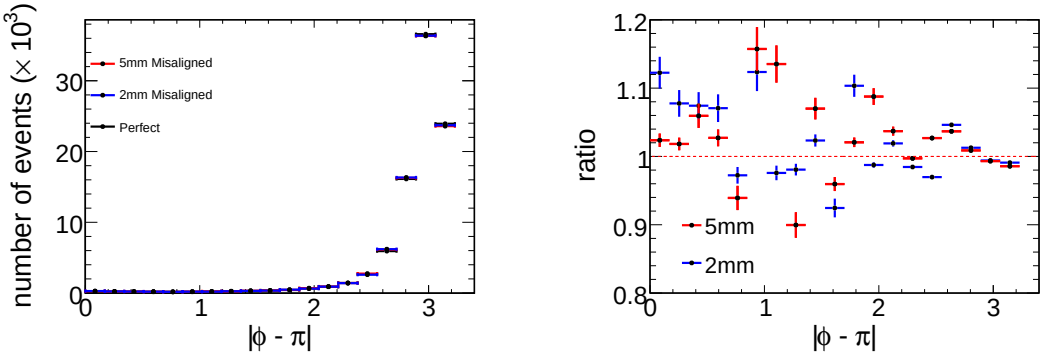

Figure C.31: The relative angle variable for exiting positively charged track events with perfect or misaligned geometry (left) and their ratio (right).

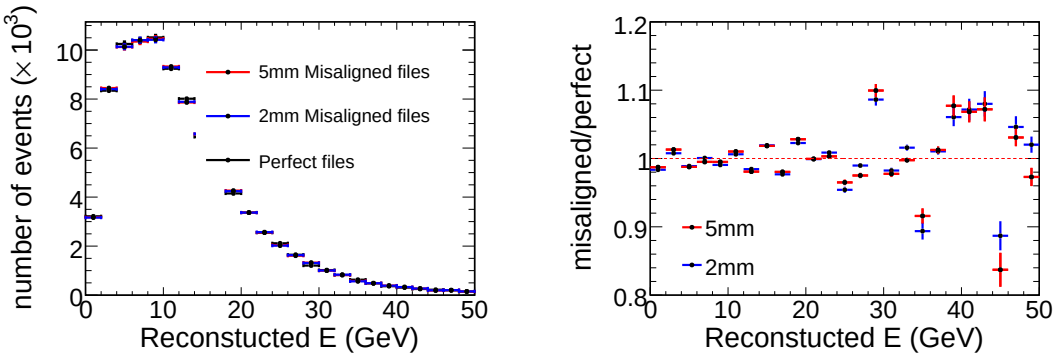

Figure C.32: The reconstructed $\bar{\nu}_\mu$ energy spectra in positively charged events with perfect or misaligned geometry (left) and their ratio (right) of the misaligned files to the perfect file. The reconstruction of tracks are affect by less than 5 % below 30 GeV.

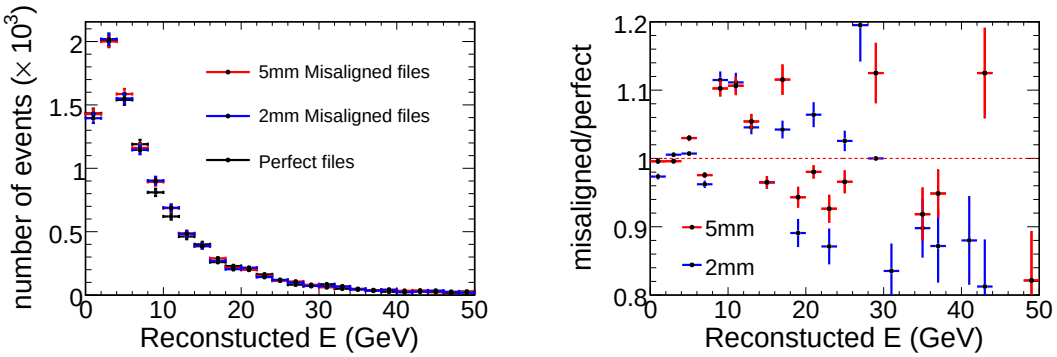

Figure C.33: The reconstructed $\bar{\nu}_\mu$ energy spectra in negatively charged events with perfect or misaligned geometry (left) and their ratio (right) of the misaligned files to the perfect file. There are large affects above 10 GeV. These are signal events that are cut figure C.32 shows this does not effect the result.

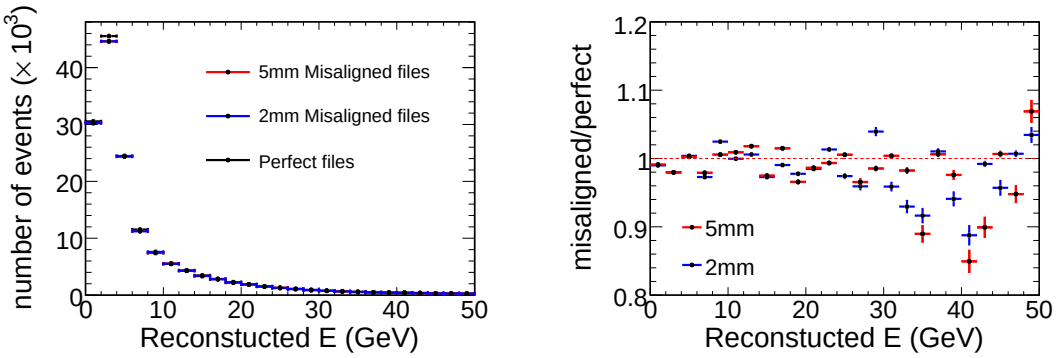

Figure C.34: The reconstructed ν_μ energy spectra in positively charged events with perfect or misaligned geometry (left) and their ratio (right) of the misaligned files to the perfect file. The reconstruction of tracks are affect by less than 5 % below 30 GeV.

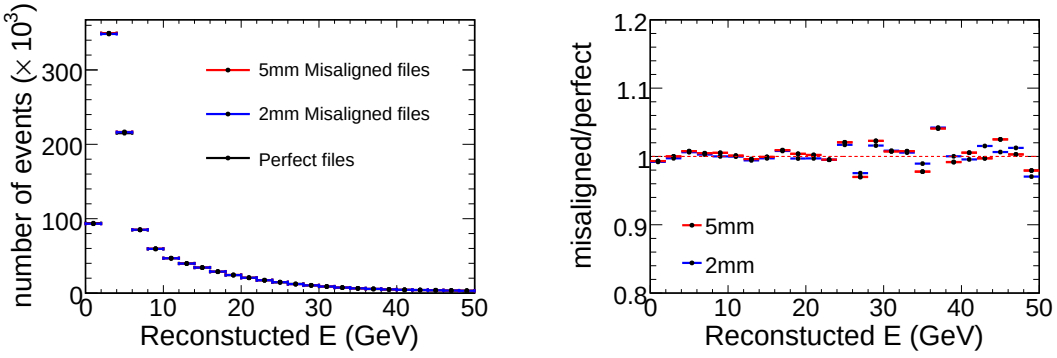

Figure C.35: The reconstructed ν_μ energy spectra in negatively charged events with perfect or misaligned geometry (left) and their ratio (right) of the misaligned files to the perfect file. There are large affects above 10 GeV. These are signal events that are cut figure C.34 shows this does not effect the result.